



The  
University  
Of  
Sheffield.

THE RING VORTEX FLOW PHANTOM:  
CHARACTERISATION, OPTIMISATION  
AND EXPANSION.

Alana S. Matthews

A thesis submitted for the degree of Doctor of  
Philosophy

May 2023

# Abstract

The field of cardiovascular diagnostic imaging is rapidly evolving, with emerging state-of-the-art medical flow visualisation technologies demonstrating superior quantitative abilities. These techniques require rigorous QA through flow phantoms which generate well-characterised and challenging flows, a requirement not met by current flow test objects. The ring vortex complex flow phantom is a prototype device designed and manufactured in previous work, intended to challenge and assess these next-generation technologies and enable comparison between modalities. The ultrasound-compatible phantom generates ring vortices over a range of Reynolds numbers. These vortices were previously visualised using Laser-PIV and noted for their reproducibility at the macro-scale.

This work strove to continue the development of this device, by optimising the device, characterising its functionality (both in device and flow) and expanding its modality compatibility. Achieving these objectives would produce a pre-commercial device compatible with both US and MRI, where high confidence is held in its capabilities.

Firstly, the phantom vortices were characterised at the micro-scale, with stability of 80% and reproducibility of 10% found for a range of generating conditions. These thresholds established the levels to which this device and its flows can perform. A QA tool was manufactured to ensure these behaviours were met, with device and flow behaviour tracked in real-time to heighten confidence in correct functionality. The device was optimised to ensure efficient and consistent behaviour, through refinement of the device components and flow generating conditions.

Phantom vortices were then further characterised in the context of analytical models, with vortices found to behave according to the Kaplanski-Rudi viscous vortex ring model. Updated experimental visualisation was performed on the optimised phantom version, with the vortices found to retain their high stability and reproducibility, and low stroke-ratio rings acting according to Kaplanski-Rudi. This consistent agreement established Kaplanski-Rudi model as a useful tool for analytical ground-truth datasets for flow characterisation.

With the ultrasound-compatible phantom suitable for more widespread use, its restriction to US modalities was addressed, and an MRI-compatible version was manufactured. High stability and reproducibility were observed at the macro-scale, and micro-scale analysis revealed Kaplanski-Rudi behaviour despite the significant design change. This proved the consistency of vortex behaviour over a wide range of generating conditions, and its robustness to design changes.

This project significantly improved confidence in the ring vortex phantom, through characterising its vortices' behaviour (experimentally and analytically), demonstrating device functionality in real-time, and retaining its abilities through a significant re-design for MRI application. The ring vortex phantom is now equipped for the final pre-commercial stage, where widespread imaging through clinical and pre-clinical technologies will demonstrate its usefulness and potential.

## Publications and Presentations

The work presented in this thesis is complemented by the following publication and presentations:

1. Publication: A.S.Matthews, K.Simatwo, A. Narracott, S. Ambrogio, A. Walker, J.W.Fenner (2023) Quality Assuring a Ring Vortex Flow Phantom in Real-time. *Open Journal of Medical Imaging*
2. Conference Poster Presentation: Vortex Ring Classification for Improved Flow Phantom Design. *BioMedEng21, Sheffield*
3. Conference Poster Presentation: An MRI-Compatible Ring Vortex Complex Flow Phantom. *BioMedEng22, UCL*
4. Conference Poster Presentation: Ultrasound Imaging and the Ring Vortex Phantom: Initial Experience. *BMUS 2023*

## Covid Impact

This project was undertaken over 2019-2023, in part affected by the COVID-19 pandemic and its associated safety regulations. Due to lockdown and lack of lab access, the project was reordered, with experimental work taking place in later years. The opportunity to perform theoretical work was enhanced, which informed and improved the experimental work presented in later chapters. Timelines are indicated below for the material presented in each chapter:

Chapter 1 - 2019-2023

Chapter 2 - Spring 2020-Winter 2020

Chapter 3 - Spring 2022 - Winter 2022

Chapter 4 - Spring 2021 - Winter 2021

Chapter 5 - Winter 2020 - Autumn 2021

Chapter 6 - Spring 2023

Chapter 7 - Summer 2022 - Spring 2023

## Acknowledgements

First and foremost I am grateful to Dr John Fenner for his supervision and guidance through the years. Your support and understanding throughout this project, and particularly through the unprecedented times of 2020/21 made it possible to finish this PhD. Your immense knowledge and passion for medical physics has been truly inspiring since I joined the university, and I am very proud of the work we have achieved.

Thank you also to Dr Andrew Narracott for providing valuable guidance, and for thorough and insightful feedback throughout the project. I would like to thank Leeds Test Objects for their support to the phantom research and valuable feedback. Additionally thank you to our clinical collaborators Jasmine Lister and Dr Prashant Verma for their expertise and time investment for after-hours phantom experiments.

This PhD would not have been possible without my parents, who created a learning-friendly environment to grow up in and provided support through every stage of my education. To Dad, your practical expertise and engineering insights have been invaluable, and your famous ‘The best way to eat a dinosaur? Small bites!’ philosophy was called upon countless times throughout this process. To Mum, you have been my first point of call at the end of long days in the lab or library and you were so integral to this achievement, both through confidence growth and support. To all of my family - thank you.

Thank you to Abdulaziz Al Baraikan, my colleague and friend, you kept me going during never-ending lockdowns and empty labs. I will miss both our 8-hour image-processing silences, too-long conversations putting the world to rights, and excellent snacks. Congratulations on your PhD, it is so well-deserved. Thank you also to Laura Grocott, I could always count on you for excellent advice and emotional support, and the PGR students of Keele are lucky to have you! A final thank you to Joe, Rebecca, Leila, Owen, Tom and April for your constant support and understanding throughout the process.

# Contents

|          |  |           |
|----------|--|-----------|
| <b>1</b> | <b>Introduction</b>  | <b>23</b> |
| 1.1      | Background and Motivation . . . . .  | 23        |
| 1.2      | Thesis Aims . . . . .  | 24        |
| 1.3      | Thesis Structure . . . . .   | 25        |
| 1.4      | Medical Imaging Technology for Cardiovascular Flow - Angiography and<br>Ultrasound . . . . . | 26        |
| 1.4.1    | Introduction . . . . .   | 26        |
| 1.4.2    | Angiography . . . . .  | 26        |
| 1.4.3    | Doppler Ultrasound - Basic Principles . . . . .  | 27        |
| 1.4.4    | Doppler Imaging - Clinical Techniques . . . . .  | 28        |
| 1.4.5    | Doppler Imaging - State-of-the-Art . . . . .   | 30        |
| 1.4.6    | Doppler Imaging Conclusion . . . . .   | 32        |
| 1.5      | Medical Imaging Technology for Cardiovascular Flow - Magnetic Resonance<br>Imaging . . . . . | 33        |
| 1.5.1    | Magnetic Resonance Imaging - Basic Principles . . . . .                                      | 33        |
| 1.5.2    | Magnetic Resonance Imaging- Clinical Techniques . . . . .                                    | 33        |
| 1.5.3    | Magnetic Resonance Imaging - State-of-the-Art . . . . .                                      | 35        |
| 1.5.4    | Discussion - Gold-Standard Quantitative Flow Imaging . . . . .                               | 36        |
| 1.6      | Flow Phantoms for Medical Imaging Assessment . . . . .                                       | 39        |
| 1.6.1    | Phantom Introduction . . . . .   | 39        |
| 1.6.2    | Other Phantom Applications . . . . .   | 40        |
| 1.6.3    | 1-D and 2-D Phantoms . . . . .   | 40        |
| 1.6.4    | 3-D Flow Phantoms . . . . .  | 43        |
| 1.6.5    | Phantom Findings . . . . .   | 45        |
| 1.7      | Discussion - Phantom Design for Next-Generation Flow Imaging . . . . .                       | 46        |
| 1.8      | Conclusion . . . . .   | 46        |
| <b>2</b> | <b>The US-Compatible Ring Vortex Phantom: Unit-O</b>   | <b>48</b> |
| 2.1      | Introduction . . . . .   | 48        |
| 2.2      | The Ring Vortex . . . . .  | 48        |
| 2.2.1    | Basics of the Ring Vortex and Characteristics . . . . .                                      | 49        |
| 2.2.2    | Formation . . . . .  | 50        |
| 2.2.3    | Evolution . . . . .  | 52        |
| 2.2.4    | Turbulent Rings . . . . .  | 54        |

|          |   |           |
|----------|---|-----------|
| 2.2.5    | Intracardiac Vortices . . . . .   | 55        |
| 2.2.6    | Discussion - The Ring Vortex as a Phantom Reference Flow . . . . .                  | 57        |
| 2.3      | The Ring Vortex Phantom - Historical Context . . . . .                              | 58        |
| 2.3.1    | Technical Specification . . . . .   | 58        |
| 2.3.2    | Phantom Workflow and Vortices . . . . .   | 63        |
| 2.3.3    | Flow-Field Visualisation . . . . .  | 64        |
| 2.3.4    | Project Outcomes . . . . .  | 66        |
| 2.4      | Ring Vortex Phantom Unit-0 Micro-Analysis (Present Day) . . . . .                   | 67        |
| 2.4.1    | Ring Speed . . . . .  | 68        |
| 2.4.2    | Ring Diameter . . . . .   | 71        |
| 2.4.3    | Core Diameter . . . . .   | 72        |
| 2.4.4    | Circulation . . . . .   | 74        |
| 2.4.5    | Vector Reproducibility . . . . .  | 77        |
| 2.4.6    | CentVect . . . . .  | 81        |
| 2.5      | Discussion - Suitability of Ring Vortex Configurations as Reference Flows . . . . . | 82        |
| 2.5.1    | Phantom Flow Analysis . . . . .   | 82        |
| 2.5.2    | Ring Behaviour and Stability . . . . .  | 84        |
| 2.6      | Conclusions . . . . .   | 86        |
| <b>3</b> | <b>Optimising the US-Compatible Ring Vortex Phantom: Unit-1</b>                     | <b>87</b> |
| 3.1      | Introduction . . . . .  | 87        |
| 3.2      | Device Optimisation I - Piston Re-Design . . . . .                                  | 87        |
| 3.2.1    | Introduction . . . . .  | 87        |
| 3.2.2    | Effect on Piston Velocity Profile . . . . .   | 88        |
| 3.2.3    | Effect on Vortex Flow - Ring Speed . . . . .  | 90        |
| 3.2.4    | Effect on Vortex Flow - Energetics . . . . .  | 91        |
| 3.2.5    | Conclusion - Piston Re-Design . . . . .   | 93        |
| 3.3      | Device Optimisation II - Piston Response to Motor Sequence . . . . .                | 93        |
| 3.3.1    | Ideal Piston Profile . . . . .  | 93        |
| 3.3.2    | Piston Oscillation and Cause . . . . .  | 94        |
| 3.3.3    | Phantom Base Reinforcement . . . . .  | 96        |
| 3.4      | Device Optimisation III - Refined Motor Pulse Sequence . . . . .                    | 99        |
| 3.4.1    | Refined Pulse Sequence for Trapezoidal Piston Response . . . . .                    | 99        |
| 3.4.2    | Full Input Profile Pulse Sequence . . . . .   | 101       |
| 3.5      | Flow Optimisation . . . . .   | 103       |
| 3.5.1    | Introduction . . . . .  | 103       |
| 3.5.2    | Method - Ring Vortex Landscape . . . . .  | 104       |
| 3.5.3    | Results I - Ring Vortex Landscape (Controllability) . . . . .                       | 105       |
| 3.5.4    | Results II - Ring Vortex Landscape (Stability, Reproducibility) . . . . .           | 107       |
| 3.6      | Discussion . . . . .  | 110       |
| 3.6.1    | Suitability of Optimised Ring Vortices for Phantom Flow Use . . . . .               | 110       |
| 3.7      | Conclusions . . . . .   | 113       |

|          |  |            |
|----------|--|------------|
| <b>4</b> | <b>Quality Assuring the Ring Vortex Phantom in Real-Time</b>                                   | <b>115</b> |
| 4.1      | Introduction . . . . .   | 115        |
| 4.2      | Background - Phantom Quality Assurance in the Literature . . . . .                             | 116        |
| 4.2.1    | Device QA . . . . .  | 116        |
| 4.2.2    | Flow QA . . . . .  | 117        |
| 4.2.3    | Phantom QA and Flow Complexity . . . . .   | 119        |
| 4.2.4    | Ring Vortex Phantom QA Procedures . . . . .  | 119        |
| 4.3      | Methods - Instrumentation Pack . . . . .   | 120        |
| 4.3.1    | Linear Encoder- Device QA . . . . .  | 120        |
| 4.3.2    | Laser-Photodiode Array - Flow QA . . . . .   | 120        |
| 4.3.3    | Doppler Probe - Flow QA . . . . .  | 122        |
| 4.3.4    | User Interface and Combined Code . . . . .   | 124        |
| 4.3.5    | Validation Experiment . . . . .  | 126        |
| 4.4      | Results - Instrumentation Pack . . . . .   | 126        |
| 4.4.1    | Linear Encoder . . . . .   | 126        |
| 4.4.2    | Laser-Photodiode Array . . . . .   | 128        |
| 4.4.3    | Doppler Probe . . . . .  | 129        |
| 4.5      | Discussion - Instrumentation Pack . . . . .  | 129        |
| 4.5.1    | Results Assessment . . . . .   | 129        |
| 4.5.2    | Instrumentation Requirements for End-Users . . . . .   | 130        |
| 4.5.3    | Commercialisation . . . . .  | 131        |
| 4.6      | Conclusions . . . . .  | 132        |
| <br>     |  |            |
| <b>5</b> | <b>Analytical Classification of the Ring Vortex</b>  | <b>133</b> |
| 5.1      | Motivation . . . . .   | 133        |
| 5.2      | Analytical Rings in the Literature . . . . .   | 134        |
| 5.2.1    | The Basis of Analytical Models . . . . .   | 134        |
| 5.2.2    | Steady State Inviscid Models . . . . .   | 137        |
| 5.2.3    | Viscous Ring Vortex Models . . . . .   | 139        |
| 5.2.4    | Conclusion . . . . .   | 142        |
| 5.3      | Methods I - Formation of Analytical Vector Fields . . . . .                                    | 143        |
| 5.3.1    | Experimental Ring Sampling . . . . .   | 143        |
| 5.3.2    | Hill's Spherical Vortex Formulation . . . . .  | 144        |
| 5.3.3    | Lamb-Oseen Ring Vortex Formulation . . . . .   | 145        |
| 5.3.4    | Kaplanski-Rudi Formulation . . . . .   | 146        |
| 5.3.5    | Conclusion . . . . .   | 147        |
| 5.4      | Methods II - Comparison between Experimental and Analytical Ring Vortex Formulations . . . . . | 148        |
| 5.4.1    | Method A: Ring Vortex Properties . . . . .   | 148        |
| 5.4.2    | Method B: Local Velocity Vector Agreement . . . . .  | 149        |
| 5.4.3    | Method C: Streamline Spherical Harmonics . . . . .   | 153        |
| 5.5      | Results . . . . .  | 157        |
| 5.5.1    | Method A: Ring Vortex Properties . . . . .   | 157        |
| 5.5.2    | Method B: Local Velocity Vector Agreement . . . . .  | 159        |

|          |   |            |
|----------|---|------------|
| 5.5.3    | Method C: Spherical Harmonics . . . . .                               | 161        |
| 5.6      | Discussion . . . . .  | 162        |
| 5.6.1    | Results Analysis . . . . .  | 162        |
| 5.6.2    | Are the Phantom Ring Vortices Kaplanski-Rudi? . . . . .               | 164        |
| 5.6.3    | Agreement in Phantom Context . . . . .                                | 165        |
| 5.6.4    | Method Limitations . . . . .  | 166        |
| 5.7      | Conclusions . . . . .   | 167        |
| <b>6</b> | <b>Micro-Analysis of the Unit-1 US-Compatible Ring Vortex Phantom</b> | <b>168</b> |
| 6.1      | Introduction . . . . .  | 168        |
| 6.2      | Methods . . . . .   | 169        |
| 6.2.1    | Ring Selection Procedure for Laser PIV . . . . .                      | 169        |
| 6.2.2    | PIV Methodology . . . . .   | 170        |
| 6.3      | Results I - Suitability as a Phantom Reference Flow . . . . .         | 172        |
| 6.3.1    | Circulation - Stability and Reproducibility . . . . .                 | 172        |
| 6.3.2    | Ring Radius - Stability and Reproducibility . . . . .                 | 173        |
| 6.3.3    | Core Radius - Stability and Reproducibility . . . . .                 | 174        |
| 6.3.4    | Vector Agreement - Stability and Reproducibility . . . . .            | 175        |
| 6.3.5    | Discussion - Phantom Flow Suitability . . . . .                       | 178        |
| 6.4      | Results II - Agreement with Kaplanski-Rudi Model . . . . .            | 180        |
| 6.4.1    | Integral Parameters . . . . .   | 180        |
| 6.4.2    | Local Vector Agreement . . . . .                                      | 183        |
| 6.4.3    | Streamline Harmonics . . . . .  | 185        |
| 6.4.4    | Discussion - Are the Rings Kaplanski-Rudi? . . . . .                  | 186        |
| 6.4.5    | Discussion - Relation to Generating Conditions . . . . .              | 188        |
| 6.5      | Discussion - Phantom Context . . . . .                                | 190        |
| 6.6      | Conclusions . . . . .   | 190        |
| <b>7</b> | <b>Design and Development of an MRI-Compatible Phantom</b>            | <b>191</b> |
| 7.1      | Introduction . . . . .  | 191        |
| 7.2      | Background - MRI Considerations for Phantom Design . . . . .          | 191        |
| 7.2.1    | MRI Clinical Safety Regulations . . . . .                             | 191        |
| 7.2.2    | Standard Clinical Phantoms . . . . .                                  | 194        |
| 7.3      | Design Concepts for the MRI-Compatible Ring Vortex Phantom . . . . .  | 195        |
| 7.3.1    | Concepts and Hydraulic System . . . . .                               | 195        |
| 7.3.2    | Previous work . . . . .   | 197        |
| 7.4      | Materials and Methods - MRI Phantom Manufacturing . . . . .           | 197        |
| 7.4.1    | MRI-Unsafe Motor/Piston Input . . . . .                               | 197        |
| 7.4.2    | MRI-Safe Plate/Tank Output . . . . .                                  | 198        |
| 7.4.3    | Coupling Pipe and Connectors . . . . .                                | 199        |
| 7.4.4    | Full Device and Initial Observations . . . . .                        | 200        |
| 7.5      | Device Assessment - Characterising Device Functionality . . . . .     | 202        |
| 7.5.1    | Method - Tracking Plate Motion . . . . .                              | 202        |
| 7.5.2    | Results - Piston Profiles . . . . .                                   | 204        |

|          |   |            |
|----------|---|------------|
| 7.5.3    | Results - Plate Profiles . . . . .  | 208        |
| 7.5.4    | Piston-to-Plate Relationship . . . . .  | 211        |
| 7.5.5    | Discussion - Phantom Sensitivity . . . . .  | 214        |
| 7.5.6    | Discussion - Phantom Functionality . . . . .  | 216        |
| 7.6      | Flow Assessment - Characterising the MRI-Phantom Vortices . . . . .                   | 217        |
| 7.6.1    | Methods - Ring Vortex Analysis . . . . .  | 217        |
| 7.6.2    | Results - Ring Vortex Analysis . . . . .  | 218        |
| 7.6.3    | Discussion I - Suitability of MRI-P ring vortices as reference phantom flow . . . . . | 221        |
| 7.6.4    | Discussion II - Micro-Analysis . . . . .  | 223        |
| 7.7      | Conclusion . . . . .  | 225        |
| <b>8</b> | <b>Future Work and Thesis Conclusions</b>   | <b>226</b> |
| 8.1      | Review of the Thesis . . . . .  | 226        |
| 8.2      | Future Work - Phantom Refinement . . . . .  | 227        |
| 8.2.1    | US-Phantom Redesign . . . . .   | 227        |
| 8.2.2    | Phantom Commercialisation . . . . .   | 228        |
| 8.2.3    | Instrumentation Pack Commercialisation . . . . .                                      | 229        |
| 8.2.4    | MRI-Compatible Phantom Improvements . . . . .   | 230        |
| 8.3      | Future Work - Imaging . . . . .   | 230        |
| 8.3.1    | Clinical Ultrasound Experiments . . . . .   | 231        |
| 8.3.2    | Proposed Experiments . . . . .  | 232        |
| 8.4      | Thesis Conclusion . . . . .   | 232        |
|          | <b>References</b>   | <b>234</b> |
| 8.4.1    | Incompressible Fluids . . . . .   | 247        |
| 8.4.2    | Streamfunction and Velocity Components . . . . .                                      | 247        |
| 8.4.3    | Stokes Streamfunction . . . . .   | 248        |

# List of Figures

|     |  |    |
|-----|--|----|
| 1.1 | Example angiography of the coronary artery. Image from [9] . . . . .   | 27 |
| 1.2 | Examples of conventional CW and PW Doppler spectral outputs, supplemented with Colour Doppler. Images are annotated to show the types of Doppler imaging in use. Images from [14]. . . . .   | 29 |
| 1.3 | Examples of VFI imaging dataset. Both the Colour Doppler and VFI vector flow field are presented to compare visualisation approaches. Arrow colours are encoded according to velocity magnitude. Image is from [22]. . . . .   | 31 |
| 1.4 | An example 2D PC-MRA image of the ascending and descending aorta. Image from [40] . . . . .  | 34 |
| 1.5 | A 4D-MRI scan of the heart, visualising the intracardiac flow. Streamlines are visible, with colours encoded according to velocity direction and magnitude. Image from [44]. . . . .   | 35 |
| 1.6 | Examples of 1D and 2D phantom flow profiles. (a.) presents the flow of Sun Nuclear 1430 Doppler phantom [70], a straight tube phantom example used often in regular clinical QA and research. (b.) presents the flow of Vali [73], an example of a rotating gel phantom. (c.) presents the flow of Yiu [32], a novel spiral phantom . . . . .  | 42 |
| 1.7 | Examples of 3D flow phantoms. (a.) presents the stenosed bifurcation phantom of Chee et al. [77]. (b.) presents the helical toroid phantom, also from Chee et al[80] . . . . .   | 44 |
| 2.1 | Schematic of the ring vortex using the cylindrical coordinate system. Ring radius ( $R$ ), core radius ( $a$ ), circulation ( $\Gamma$ ) and direction of propagation are annotated. The radial velocity and vorticity distribution across the core centre are also presented, demonstrating the Gaussian-like properties. . . . .   | 50 |
| 2.2 | A schematic of ring vortex formation using the piston/orifice experimental setup. The first pane defines key parameters for ring vortex generation. Panes (a)-(b) presents the propulsion of a slug of fluid through a circular orifice, forming a jet. Pane (c) demonstrates the bending of peripheral fluid layers due to friction, causing the accumulation of a vortical core in pane (d). Pane (e) then presents the formed ring vortex propagating away from the orifice. All panes represent a ‘slice’ across a circular orifice and piston, axisymmetric around the horizontal central axis. . . . . | 51 |

|      |   |    |
|------|---|----|
| 2.3  | A schematic presenting the stages of initially-laminar ring vortices, with laminar, transitional and turbulent stages listed. Key properties of the ring in each regime is included. . . . .  | 54 |
| 2.4  | Digital Particle Imaging Velocimetry visualisations of the ring vortex at stroke ratios of 2, 3.8, and 14.5 respectively. Laminar and turbulent ring vortex behaviour is visible. Image from [105] . . . . .  | 55 |
| 2.5  | Ultrasound Echo-PIV images of the intracardiac ring vortex, in late diastole and onset systole. Image from [111] . . . . .  | 56 |
| 2.6  | Photograph of the assembled Unit-0 ring vortex phantom in 2019 with components annotated for clarity. Image is from [119] . . . . .   | 58 |
| 2.7  | A schematic presenting the square wave mode of bipolar linear motor motion. The <i>SetDisplacement</i> and <i>SetSpeed</i> variables are annotated, with the calculations used to determine average piston speed and displacement. . . . .  | 59 |
| 2.8  | A schematic of the ring vortex phantom with measurements of each machined component. . . . .  | 61 |
| 2.9  | Arduino Code used to control the ring vortex phantom. Comments are in red on significant points. . . . .  | 63 |
| 2.10 | A flowchart of the setup of the ring vortex phantom for experiments. . . . .  | 64 |
| 2.11 | A schematic of the ring vortex phantom when being imaged by Laser PIV. The phantom, laser, laser plane and stereoscopic cameras are depicted. . . . .   | 65 |
| 2.12 | Example Laser-PIV dataset for the ring vortex phantom. (i) shows the raw velocity vector plot, (ii) the filled vorticity contours, (iii) the streamlines in the ring's reference frame. . . . .   | 65 |
| 2.13 | Diagram of the process of calculating instantaneous ring speed using PIV datasets. Axes are in millimetres and vectors in the stationary reference frame. . . . .   | 68 |
| 2.14 | The average ring vortex speeds at 8cm from the orifice for configurations listed in Table 2.1. The x axis lists both configuration number according to Table 2.1, and the corresponding generating conditions in the format [Orifice Diameter(mm)/Piston Speed(cm/s)]. Error bars represent 1 standard deviation, and each datapoint represents the average of ten ring vortices. . . . . | 69 |
| 2.15 | The average ring vortex speeds, relative to their starting speed, as the rings propagate over 8-22cm from the orifice. Datapoints represent the average of ten ring vortices. Errors are not shown for clarity but are cited in Figure 2.14, typically at 10%. . . . .  | 70 |
| 2.16 | A graph presenting the average ring vortex diameter at 8cm from the orifice for the configurations listed in Table 2.1. Error bars represent 1 standard deviation, and each datapoint represents the average of ten ring vortices. . . . .  | 71 |
| 2.17 | A graph presenting the evolution of ring diameter, relative to their values at 8cm from the orifice, across the PIV imaging domain. Error bars are not presented for clarity, but values typically vary by 5%, as listed in Figure 2.17. . . . .  | 72 |

|      |   |    |
|------|---|----|
| 2.18 | A graph presenting the average ring vortex core diameters at 8cm from the orifice. Error bars represent 1 standard deviation, and each datapoint represents the average of ten ring vortices. . . . .   | 73 |
| 2.19 | A graph presenting the evolution of core radius, relative to its starting value across the PIV imaging domain. Error bars are not presented for clarity but values typically vary by <15%, as listed in Figure 2.18 . . . . .   | 74 |
| 2.20 | Example PIV dataset with the circulation-measurement domain annotated. The dashed red line represents the closed path around which the line integral is performed. . . . .  | 75 |
| 2.21 | The average circulation values at 8cm from the orifice for configurations listed in Table 2.1. Error bars represent 1 standard deviation, and each datapoint represents the average of ten ring vortices. . . . .   | 75 |
| 2.22 | A graph presenting the evolution of circulation relative to its starting value, across the PIV imaging domain. . . . .  | 76 |
| 2.23 | Example ‘Length Tolerance Maps’ for configurations as listed in Table 2.1. Average vector plots are shown with a coloured contour plot superimposed. Local colour is encoded according to the colourbar and represents the coefficient of variability in vector length between the ten vortices in the relevant configuration. Areas of yellow highlight large variation in flow vector length. . . . . | 78 |
| 2.24 | Example ‘Angle Tolerance Maps’ for configurations as listed in Table 2.1. Average vector plots are shown, with a coloured contour plot superimposed. Local colour is encoded according to the colourbar, and represents the standard deviation in vector angle between the ten vortices in the relevant configuration. Areas of yellow highlight large variation in flow vector direction. . . . .      | 78 |
| 2.25 | The evolution of vector length reproducibility across the PIV imaging domain. Y-axis values represent the percentage of vectors which exhibit a coefficient of variation of less than 10% in vector length. . . . .   | 79 |
| 2.26 | The evolution of vector angle reproducibility across the PIV imaging domain. Y-axis values represent the percentage of vectors which exhibit a standard deviation of less than 5° in vector angle. . . . .  | 80 |
| 2.27 | Average values for CentVect measured at 8cm from the orifice for configurations listed in Table 2.1. Datapoints represent the average of ten vortices and error bars represent 1 standard deviation . . . . .   | 81 |
| 2.28 | A graph presenting the progression of CentVect, relative to the starting value across the PIV imaging domain. . . . .   | 82 |
| 2.29 | Photo of a configuration 1 ring vortex from the 10mm orifice using the O-ring piston. This image is captured at immediately post-formation and presents a <i>fast</i> ring. . . . .   | 85 |
| 2.30 | Photos of a configuration 3 ring vortex from the 15mm orifice using the O-ring piston. Images are captured at immediately post-formation and at 18cm from the orifice and present a <i>mid-speed</i> ring . . . . .   | 85 |

|      |   |     |
|------|---|-----|
| 2.31 | Photos of a configuration 7 ring vortex from the 25mm orifice using the O-ring piston. Images are captured at immediately post-formation and at 18cm from the orifice and present a <i>slow</i> ring . . . . .  | 85  |
| 3.1  | A MATLAB code snippet for collecting position measurements from the linear encoder at 100Hz. Data are transferred to double format and into a velocity matrix. . . . .  | 89  |
| 3.2  | Graphs presenting linear encoder data for the O-ring piston and non O-ring piston, moving at identical programmed speed of 1.3cm/s over 0.8mm in a top-hat motor pulse sequence. Graph (a) is the O-ring piston profile. Graph (b) is the non O-ring piston profile. . . . .  | 90  |
| 3.3  | The correlation between O-ring piston and non O-ring average ring vortex speeds over 5-15cm from the orifice. Datapoints are averaged values across ten ring vortices, and error bars represent 1SD. . . . .  | 91  |
| 3.4  | A schematic of the ring generation process in a piston/orifice setup with associated energy calculations using the slug model. . . . .  | 92  |
| 3.5  | Schematic of the idealised trapezoidal velocity profile for ring vortex generation. Acceleration, plateau and deceleration stages are annotated. . . .  | 94  |
| 3.6  | Graphs presenting the piston behaviour for long displacements over 2.4mm under a top-hat motor pulse sequence. Graphs (a),(b) present superimposed individual encoder-measured profiles, and (c),(d) the average of 5 profiles. Graphs (a),(b) record the piston behaviour for 2cm/s programmed speed, and (c),(d) for 1.33cm/s programmed speed. . . . .             | 95  |
| 3.7  | A schematic of the ring vortex phantom with the motor angling due to a flex in the PMMA base. . . . .   | 97  |
| 3.8  | Graphs presenting the piston behaviour for long displacements of 2.4mm under with the base reinforced with Perspex blocks. Graphs (a),(c) present superimposed individual encoder-measured profiles, and (b),(d) the average of 5 profiles. Graphs (a),(b) record the piston behaviour for 2cm/s programmed speed, and (c),(d) for 1.33cm/s programmed speed. . . . . | 98  |
| 3.9  | Graph presenting the proposed input code (black line) for the acceleration phase of the trapezoidal piston profile. The red plot shows the close-to-linear moving average. . . . .  | 100 |
| 3.10 | Graph presenting the proposed input code (black line) for the ring vortex phantom to generate a trapezoidal piston velocity profile. The red line shows the moving average of this profile. . . . .   | 101 |
| 3.11 | Schematic of the input code refined velocity profile for $PS=2\text{cm/s}$ . Annotations include steps to calculate 90% $PS$ and 100% $PS$ displacements . . .  | 102 |
| 3.12 | Experimental phantom profiles using the graded profiles. Graph (a) presents 5 profiles for a maximum programmed speed of 1.3cm/s and Graph (b) presents 5 profiles for a maximum programmed speed of 2cm/s. . . . .   | 103 |
| 3.13 | Graphs presenting average ring vortex speed over 5-20cm from the orifice in relation to stroke ratio. Graph (a) is for the 10mm orifice, Graph (b) for the 15mm orifice and Graph (c) for the 20mm orifice. . . . .   | 106 |

|      |   |     |
|------|---|-----|
| 3.14 | Graphs presenting the reproducibility of ring vortex starting speed (at 5cm from orifice) with varying stroke ratio, orifice diameter and maximum piston speed. Datapoints are colour-coded according to coefficient of variability and the in-figure key. (a) is Piston speed=2.5cm/s. (b) is Piston speed=2cm/s. (c) is Piston speed=1.33cm/s. . . . .        | 108 |
| 3.15 | Graphs presenting the ring vortex average speed between 5-20cm path-length with varying stroke ratio, orifice diameter and maximum piston speed. Datapoints are colour-coded according to coefficient of variability and the in-figure key. (a) is $PS=2.5\text{cm/s}$ . (b) is $PS=2\text{cm/s}$ . (c) is $PS=1.33\text{cm/s}$ . . . . .                       | 109 |
| 3.16 | Graphs presenting the ring vortex lifetime (defined as the distance travelled with stability of 70%) with varying stroke ratio, orifice diameter and maximum piston speed. Datapoints are colour-coded according to 70% Stability Lifetime and the in-figure key. (a) is Piston speed=2.5cm/s. (b) is Piston speed=2cm/s. (c) is Piston speed=1.33cm/s. . . . . | 110 |
| 3.17 | Ring vortex maps showing the stability, initial speed reproducibility and average speed reproducibility of ring vortices generated by the optimised ring vortex phantom. . . . .  | 111 |
| 4.1  | A qualitative graph presenting the QA procedure for device functionality in phantoms from the literature. ‘Averaged QA’ refers to pre-collected device characterisation, while ‘Real-Time QA’ refers to components being actively monitored during experiments. . . . .   | 117 |
| 4.2  | A qualitative graph presenting the QA procedure for flow behaviour in phantoms from the literature. ‘Averaged QA’ refers to pre-collected datasets whose averages are used as ground-truth, while ‘Real-Time QA’ refers to flow behaviour analysed directly during experiments. . . . .   | 118 |
| 4.3  | Photo of the laser-photodiode array, along with the circuit diagram used to power the photodiodes. . . . .  | 121 |
| 4.4  | A MATLAB code snippet for reading and processing laser data for the ring vortex phantom instrumentation pack. . . . .   | 122 |
| 4.5  | Flowchart presenting the steps in Doppler probe frequency analysis for performing real-time flow QA on the ring vortex phantom. CentVect values are inferred from the breakdown of frequency components within a Doppler signal. . . . .  | 124 |
| 4.6  | User interface displayed when the instrumentation pack is used with the ring vortex phantom. The encoder, laser, and probe raw data are displayed, along with basic derived parameters and colour-coded virtual LEDs indicating whether each parameter lies within experimental tolerances. . . . .   | 125 |
| 4.7  | The reproducibility of impulse measurements for configurations 1-6 listed in Table 2.1, with data collected using the linear encoder. Each datapoint is the average impulse generated by ten piston profiles for that particular configuration. Error bars represent 1SD. . . . .   | 127 |

|      |   |     |
|------|---|-----|
| 4.8  | The correlation between PIV-determined ring vortex speeds and laser-determined ring speeds. Each datapoint represents the average of ten rings and error bars represent 1SD. . . . .  | 128 |
| 4.9  | The correlation between PIV-determined and Doppler probe-calculated CentVect values. Each datapoint represents the average of ten rings and error bars represent 1SD. . . . .   | 129 |
| 5.1  | Schematic of the ring vortex on the cylindrical coordinate system. (a.) shows the 3D representation with axial,radial and azimuthal axes. (b.) shows the 2-D simplification, with axial and radial axes represented as $x$ and $y$ . . . . .  | 135 |
| 5.2  | Ring vortex streamlines from Laser PIV datasets. (a.) shows the ring vortex in the moving ring reference frame, with blue streamlines representing ambient fluid. (b.) shows the ring vortex in the stationary reference frame.   | 136 |
| 5.3  | Hill's Spherical Vortex visualised in MATLAB. (a) presents the velocity vector profile and streamlines in the moving RRF, (b) the filled vorticity contours and (c) the linear vorticity projection down the centre of the ring   | 137 |
| 5.4  | Lamb-Oseen Ring Vortex visualised in MATLAB. (a) presents the velocity vector profile and streamlines in the moving RRF, (b) the normalised vorticity profile and (c) the Gaussian vorticity projection down the centre of the ring . . . . .   | 140 |
| 5.5  | Kaplanski-Rudi Ring Vortex visualised in MATLAB. (a) presents the velocity vector profile and streamlines, (b) the normalised vorticity profile and (c) the Gaussian vorticity projection down the centre of the ring . . .   | 141 |
| 5.6  | Validation of Hill's Spherical Vortex formulations in MATLAB. (a) shows the streamlines from Shadden et al.[144] (b) shows the streamlines from Yattori et al [143] (c) presents the streamlines from this project. . . . .   | 145 |
| 5.7  | Validation of Lamb-Oseen formulations in MATLAB. (a) shows a single vortex with core radius 5. Circulation was measured to be 10 around the annotated contour (b) presents the vorticity across the centre of the core. (b) presents the full Lamb-Oseen ring vortex. . . . .   | 146 |
| 5.8  | Validation of Kaplanski-Rudi formulations in MATLAB. (a) shows the normalised vorticity contours for a vortex of $\Gamma_0 = 1, R_0 = 1, \theta = 4$ from [127]. (b) presents the Sheffield-produced validation contours with associated colourbar. (b) presents the full Kaplanski-Rudi ring vortex. . . . .   | 147 |
| 5.9  | Flowchart detailing the procedure for creating average length and angle maps for experimental ring vortices . . . . .   | 150 |
| 5.10 | Example similarity maps comparing experimental and analytical ring vortex vector plots with the average PIV vector plots overlaid. The colourbar is used for both length and angle maps. Length maps are coloured according to percentage difference between experimental and analytical vortex lengths. Angle maps are coloured according to absolute difference in degrees. | 151 |

|      |  |     |
|------|--|-----|
| 5.11 | Maps demonstrating where analytical vector lengths lie 'in bounds' when compared to an average experimental map. Yellow regions lie over the set threshold, and blue regions lie under the set threshold. Thresholds are varied between 5-20%. . . . .   | 152 |
| 5.12 | Maps demonstrating where analytical vector angles lie 'in bounds' when compared to an average experimental map. Yellow regions lie over the set threshold, and blue regions lie under the set threshold. Thresholds are varied between 5-20°. . . . .  | 153 |
| 5.13 | Example streamlines for ring vortex formulations. Experimental (Laser PIV), HSV, LO and KR formulations are included. An artefact in the PIV streamlines is apparent at the bottom left and is a result of PIV discretisation and the streamline seeding point. . . . .  | 154 |
| 5.14 | Flowchart for calculating spherical harmonics for ring vortex streamlines .  | 155 |
| 5.15 | Example streamline harmonics coefficients for different ring vortex formulations. . . . .  | 156 |
| 5.16 | Comparison between circulation values for post-formation ring vortices of different formulations for configurations listed in Table 2.1. Datapoints represent the average of ten vortices and error bars 1SD . . . . .   | 157 |
| 5.17 | Comparison between ring speed values for post-formation ring vortices of different formulations for configurations listed in Table 2.1. Datapoints represent the average of ten vortices and error bars 1SD . . . . .  | 158 |
| 5.18 | Comparison between CentVect values for post-formation ring vortices of different formulations for configurations listed in Table 2.1. Datapoints represent the average of ten vortices and error bars 1SD . . . . .  | 159 |
| 5.19 | Graph presenting the similarity in vector lengths between analytical and experimental ring vortices. Y axis values correspond to the percentage of sample ring velocity vectors whose lengths lie within 10% of the experimental average at that point. Datapoints represent the average of ten vortices and error bars 1SD. . . . .                     | 160 |
| 5.20 | Graph presenting the similarity in vector angles between analytical and experimental ring vortices. Y axis values correspond to the percentage of sample ring velocity vectors whose angles lie within 10° of the experimental average at that point. Datapoints represent the average of ten vortices and error bars 1SD. . . . .                       | 161 |
| 5.21 | Graph presenting the similarity in streamline Fourier coefficients between analytical and experimental ring vortices. Y axis values correspond to the percentage of Fourier components for the sample ring that lie within experimental bounds of the experimental average. Datapoints represent the average of ten vortices and error bars 1SD. . . . . | 162 |
| 5.22 | Example PIV dataset with superimposed streamlines in the moving ring reference frame. The open streamlines are visible, annotated by arrows. . .   | 166 |
| 6.1  | Photo of the 2023 Laser PIV experiment visualising the ring vortex phantom.  | 171 |

|      |  |     |
|------|--|-----|
| 6.2  | Photo of the calibration grid used for the 2023 Laser PIV experiment using the ring vortex phantom. The triangle on the grid correlates to the [0,0] origin in the PIV coordinate system. . . . .  | 172 |
| 6.3  | (a.) The evolution of circulation of reference ring vortices from $PIV_{23}$ data, relative to starting circulation at 7cm from the orifice. Datapoints represent the average of ten vortices. Error bars are not shown, but is typically $\sim 5\%$ as listed in (b.) . . . . .   | 173 |
| 6.4  | (a.) The evolution of ring radius of reference ring vortices from $PIV_{23}$ data, relative to starting values at 7cm from the orifice. Datapoints represent the average of ten vortices. Error bars are not shown, reproducibility is listed in (b.) as coefficient of variability. . . . .   | 174 |
| 6.5  | The evolution of core radius of reference ring vortices from $PIV_{23}$ data, relative to starting values at 7cm from the orifice. Datapoints represent the average of ten vortices. Error bars are not shown, reproducibility is listed in (b.) as coefficient of variability. . . . .  | 175 |
| 6.6  | Tolerance Maps for the reference datasets of the 2023 Laser PIV experiment for vector lengths. Regions are colour-coded according to the colourbar, with values representing the local coefficient of variation in vector length between ten vortices. . . . .   | 176 |
| 6.7  | Tolerance Maps for the reference datasets of the 2023 Laser PIV experiment for vector angles. Regions are colour-coded according to the colourbar, with values representing the local standard deviation in vector angle between ten vortices. . . . .   | 177 |
| 6.8  | (a.) The reproducibility of velocity vector lengths for reference ring vortex datasets, both at the start and throughout the journey. The y axis represents the % of vectors whose lengths vary by less than $\pm 10\%$ (1SD) across the ring and its immediate surroundings. (b.) The reproducibility of velocity vector angles for reference ring vortex datasets, both at the start and throughout the journey. The y axis represents the % of vectors whose angles vary by less than $\pm 5^\circ$ (1SD) across the ring and its immediate surroundings. . . . . | 178 |
| 6.9  | Correlation between experimental ring speeds and KR ring speeds calculated from 2023 PIV datasets. Error bars represent 1SD and are the variation between individual vortices. An outlier is annotated with the red arrow. . . . .   | 181 |
| 6.10 | Relative percentage error between PIV ring speed values and KR ring speed values for 2023 PIV datasets. Thresholds are set at 10% and 15% and an outlier is annotated with a red arrow. . . . .  | 181 |
| 6.11 | Correlation between experimental CentVect values and KR CentVect values, calculated from 2023 PIV datasets. Error bars represent 1SD and are the variation between individual vortices. An anomaly is annotated with the red arrow. . . . .  | 182 |
| 6.12 | Relative percentage error between KR CentVect values and PIV CentVect values for 2023 PIV datasets. Thresholds are set at 10% and 15%. . . . .   | 183 |

|      |   |     |
|------|---|-----|
| 6.13 | Agreement of KR and PIV velocity vector lengths for 2023 PIV datasets. Y axis values represent the percentage of KR vectors whose lengths lie within 20% of the corresponding PIV length. Error bars represent 1SD. . . . .                     | 184 |
| 6.14 | Agreement of KR and PIV velocity vector angles for 2023 PIV datasets. Y axis values represent the percentage of KR vectors whose angles lie within 10° of the corresponding PIV angle. Error bars represent 1SD. . . . .                        | 185 |
| 6.15 | Agreement of KR and PIV streamline coefficients for 2023 PIV datasets. Y axis values represent the percentage of KR coefficients who lie within pre-established bounds around the PIV coefficients. Error bars represent 1SD. . . . .           | 186 |
| 7.1  | Diagram of typical MRI safety zones as defined by the American College of Radiology. [147] . . . . .  | 193 |
| 7.2  | Classifications for devices when used in an clinical MRI-environment. [147]   | 194 |
| 7.3  | Example MRI-compatible flow phantoms which use hydraulic systems connecting the scanner bed to the adjoining control room [153][154]. . . . .   | 195 |
| 7.4  | Concept Design for the MRI-Compatible ring vortex phantom . . . . .   | 196 |
| 7.5  | Schematic of the Motor/Piston Input portion of the MRI phantom design.  | 198 |
| 7.6  | Schematic of the Plate/Tank Output component of the MRI ring vortex phantom . . . . .   | 199 |
| 7.7  | Schematic of the pipe couplers for the MRI-compatible ring vortex phantom. The couplers insert into each end of the pipe and attach to the plate cylinder and piston cylinder respectively. . . . .   | 200 |
| 7.8  | Photograph of the MRI-compatible phantom prototype in a laboratory environment. . . . .   | 201 |
| 7.9  | Flowchart explaining the post-processing methods used in tracking the plate in the MRI-Compatible Ring Vortex Phantom. . . . .  | 203 |
| 7.10 | Example piston velocity profiles for speeds of 2cm/s and 1.2cm/s for the MRI-Compatible ring vortex phantom. Each line represents an individual run. . . . .  | 205 |
| 7.11 | Graphs presenting the average piston accelerations for 2cm/s and 1.2cm/s piston speeds in the MRI-Compatible Phantom Prototype. Anomalies are annotated. Datapoints represent the average of ten impulses and error bars represent 1SD. . . . . | 206 |
| 7.12 | Graphs presenting the average piston displacements for 2cm/s and 1.2cm/s piston speeds in the MRI-phantom prototype. Datapoints represent the average of ten impulses and error bars represent 1SD. . . . .                                     | 207 |
| 7.13 | Graphs presenting the average piston velocities for 2cm/s and 1.2cm/s piston speeds in the MRI-phantom Prototype. Datapoints represent the average of ten impulses and error bars represent 1SD. . . . .  | 208 |
| 7.14 | Graphs presenting the average plate profiles for 2cm/s and 1.2cm/s piston speeds in the MRI-Compatible Phantom Prototype. Each line represents an individual run. . . . .   | 209 |

|      |  |     |
|------|--|-----|
| 7.15 | Maximum plate displacements for a range of programmed displacements for the MRI-phantom. Datapoints represent the average of ten impulses and error bars represent 1SD. Anomalies are annotated . . . . .  | 210 |
| 7.16 | Average Plate Speeds for a range of programmed displacements for the ring vortex phantom. Datapoints represent the average of ten impulses and error bars represent 1SD. . . . .   | 211 |
| 7.17 | Example piston and plate velocity profiles from the MRI-compatible ring vortex phantom. 'Fast' piston speed refers to 2cm/s programmed piston speed and 'slow' piston speed refers to 1.2cm/s programmed piston speed.   | 212 |
| 7.18 | Piston and Plate displacements for a range of programmed displacements. Datapoints represent the average of ten impulses and error bars represent 1SD. . . . .   | 212 |
| 7.19 | Plate displacements for slow piston speeds. Datapoints represent the average of ten impulses and error bars represent 1SD. Anomalies identified in Figure 7.18 have been removed. . . . .  | 213 |
| 7.20 | Average plate speed as a function of average piston speed on the MRI-compatible ring vortex phantom. Measurements from the fast piston speed (2cm/s programmed speed) and slow piston speed (1.2cm/s programmed speed) are presented. . . . .                                    | 214 |
| 7.21 | Plate displacement and average speed as a function of programmed piston displacement for the ring vortex phantom. Certain abnormal trends are identified through red and blue datapoints. Datapoints represent the average of ten impulses and error bars represent 1SD. . . . . | 215 |
| 7.22 | Schematic showing the boundaries in the plate cylinder beyond which the plate velocity profile will exhibit abnormal dynamics. . . . .   | 215 |
| 7.23 | 2-D map of MRI-ring vortex initial reproducibility. Stroke ratio, orifice diameter and piston speed are varied. Datapoints represent the CoV in each condition's initial speed, colour coded according to the in-figure key. . . . .   | 219 |
| 7.24 | 2-D map of MRI-ring vortex journey-long reproducibility. Stroke ratio, orifice diameter and piston speed are varied. Datapoints represent the CoV in each condition's average speed, colour coded according to the in-figure key. . . . .  | 220 |
| 7.25 | 2-D map of MRI-ring vortex stability. Stroke ratio, orifice diameter and piston speed are varied. Datapoints represent the 70% Stability lifetime for each condition, colour-coded according to the in-figure key. . . . .   | 221 |
| 7.26 | 2-D map of MRI-ring vortex phantom flow stability and reproducibility. Stroke ratio, orifice diameter and piston speed are varied. Datapoints represent the stability, initial reproducibility and average reproducibility of each conditions. . . . .                           | 222 |
| 8.1  | a. Example scan of the ring vortex using B-mode ultrasound with CDI to visualise the rings, saved as a cine loop. b. Example PW Doppler trace, measuring radial velocities across the centre of the top core. . . . .  | 231 |

# List of Tables

|     |  |     |
|-----|--|-----|
| 1.1 | List of medical flow imaging technologies with technical abilities, output format and angle dependence listed . . . . .  | 37  |
| 1.2 | A range of currently available 1D/2D flow phantoms. Authors, modality and basic geometry are listed. ‘Ground-Truth’ refers to the datasets used to characterise the reference flow of each phantom. ‘Dim’ refers to dimensionality, and ‘HF’ refers to high-frequency. . . . .   | 41  |
| 1.3 | A range of currently available 3-D flow phantoms. Authors, modality and technical specifications are listed. ‘SS’ refers to a steady-state flow and ‘Dim’ refers to flow dimensionality. . . . .   | 43  |
| 2.1 | Generating configurations historically used with the ring vortex phantom. .  | 66  |
| 2.2 | Table listing stability of speed for the Unit-0 ring vortex phantom. 14cm-Speed Stability = 100%-% of speed lost over 14cm path-length. . . . .  | 70  |
| 2.3 | Table listing stability of circulation for the Unit-0 ring vortex phantom. 14cm-Circulation Stability = 100%-% of speed lost over 14cm path-length. . . . .  | 77  |
| 2.4 | Classification of ring behaviour according to reproducibility and stability. A ✓ indicates that the ring property behaves according to stated tolerances. A × indicates failure to remain within stated tolerances. ‘R.Rad’ and ‘C.Rad’ represent ring radius and core radius respectively. Rows in bold identify configurations where all thresholds are met. . . . . | 83  |
| 3.1 | NOR piston profile measurements using the linear encoder for motion under the optimised, graded motor pulse sequences presented in Figure 3.11 . . .   | 102 |
| 3.2 | Experimental conditions used to generate ring vortices to measure stability and reproducibility for each configuration. . . . .  | 105 |
| 3.3 | List of suitable ring vortex configurations for phantom use. Ring vortices generated using these settings have reproducible speeds within ±5% and a 70% stability lifetime of over 15cm . . . . .  | 112 |
| 3.4 | List of suitable ring vortex configurations in terms of reproducibility only. Average speed over 5-20cm and starting speed at 5cm were considered. . .   | 113 |
| 5.1 | Tabulated summary of features relating to analytical ring vortex models . .  | 142 |
| 5.2 | Experimental Ring Vortex Properties Used for Comparison to Analytical Models . . . . .   | 143 |

|     |   |     |
|-----|---|-----|
| 5.3 | Table listing the results from comparing parameters of different ring vortex formulations. ✓ indicates that the analytical value lies within experimental tolerances, and × that they lie without . . . . .   | 163 |
| 5.4 | Table listing the agreement between ring vortex formulations for parameter comparison, velocity vector similarity and quantitative streamline similarity. Rows in bold present conditions where agreement is found with the Kaplanski-Rudi model across all methods. . . . .  | 165 |
| 6.1 | List of ‘reference’ datasets for the 2023 Laser-PIV experiment. Ten vortices of each configuration were visualised. * - low stability condition. . . . .  | 169 |
| 6.2 | List of all experimental conditions imaged in the 2023 Laser PIV experiment. † - Configurations 6 and 7 are identical, with these rings produced before and after the experiment to ensure phantom consistency. *** denotes a ‘reference’ dataset . . . . .   | 170 |
| 6.3 | Metrics of reference datasets for phantom flow requirements at the micro-scale. Abbreviations are used in the headings: ‘ <i>Circ</i> ’ is circulation, ‘ <i>R. Rad</i> ’ is ring radius, ‘ <i>C. Rad</i> ’ is core radius, ‘ <i>Ang</i> ’ is the vector angles with high reproducibility, ‘ <i>Len</i> ’ is the vector lengths with high reproducibility, ‘ <i>Reprod</i> ’ is the reproducibility, and ‘ <i>Stab</i> ’ the stability. . . . . | 179 |
| 6.4 | Agreement of 2023 PIV ring vortices with the Kaplanski-Rudi model for ring parameters, velocity vector dynamics and streamline coefficients. Lines in bold denote conditions where all conditions are met. Asterisks denote conditions where all thresholds are met except for CentVect similarity within 10%. . . . .  | 187 |
| 6.5 | List of ring vortex configurations and their adherence to the Kaplanski-Rudi analytical model according to declared tolerances. Their stroke ratios are also listed . . . . .   | 189 |
| 7.1 | Experimental errors in the measurement of plate displacement and plate average speed . . . . .  | 204 |
| 7.2 | Configurations tested using the MRI-Phantom for their accordance to the Kaplanski-Rudi model, along with results comparing the KR rings to PIV-imaged experimental rings. ‘Diff’ refers to the % difference between experimental and theoretical rings for that parameter. . . . .  | 224 |

# Terminology

## Stability

In this thesis, flow stability refers to the ability of a flow-field to retain its initial properties over an appreciable time duration or path-length.

## Reproducibility

In this thesis, flow reproducibility refers to the similarity of multiple flow-fields when generated under the same experimental conditions.

# Phantom Definitions

**Unit-0** - The ring vortex phantom in its status at the beginning of this project in 2019. This device was US-compatible with limited quantitative assessment. See Chapter 2 for a more in-depth description

**Unit-1** - The ring vortex phantom in its status at the end of this project in 2023, specifically with respect to its optimised functionality and flow profiles detailed in Chapter 3.

# Chapter 1

## Introduction

### 1.1 Background and Motivation

Cardiovascular diseases (CVDs) have significant impact on public health, affecting up to 7.6 million people in the UK alone [1]. Located in the heart and circulatory system, conditions such as heart attacks, strokes and embolisms result in an estimated 17.9 million annual deaths globally [2], and have significant effect on quality of life for survivors. 80% of these deaths have been deemed preventable by WHO [2], providing impetus for medical technology to focus on early diagnosis to improve patient outcomes.

With causes and consequences that are largely hidden, diagnosis of CVD is typically achieved through the medium of medical imaging, an ever-evolving field which unites medicine, physics and engineering disciplines. Imaging the cardiovascular system enables early detection of abnormalities, monitoring of disease progression and risk stratification. Traditionally medical imaging directly visualises anatomical structures whereas in recent years, the value of functional flow imaging where the haemodynamic behaviour is visualised has been recognised and implemented in a range of scenarios. The cardiovascular systems' innate relationship between tissue and fluid behaviour makes it a candidate for either imaging approach, with advantages for both. Anatomical imaging visualises the region over which blood is flowing (highlighting any abnormalities such as stenoses), whilst functional flow imaging visualises and assesses the behaviour within this region. Employing both imaging approaches therefore provides rich information of the 'full picture', with potential for understanding mechanisms and enabling more confident diagnoses and treatment decisions [3].

The medical imaging field has a long history, thus a plethora of flow imaging technologies are available, exploiting physical principles such as the Doppler Effect and Nuclear Magnetic Resonance. This range of options provides a host of approaches for optimal patient care, but there are disagreements in appointing a 'gold-standard', either for each modality or across the field. Quantitative factors such as resolution, accuracy and field-of-view size must be considered alongside practical considerations of cost, use of contrast agent, existing software and exposure to ionising radiation, complicating the matter. Angiography is currently regarded as the gold standard for anatomical cardiovascular imag-

ing [3],[4] however a functional flow-imaging counterpart is not clearly defined. A distinct transition is also underway in clinical medical imaging, with an active focus on shifting from qualitative to quantitative imaging in clinical practice [5], [6]. This coincides with recent technological advancements in the development of high-resolution 3D-vector flow visualisation methods. The combination of this transition and new technologies both advances the field and exacerbates the already complex discussion of appointing ‘gold-standard’ quantitative flow imaging technologies for modern clinical use.

To settle this debate, and determine the true abilities of new and conventional imaging technologies, rigorous Quality Assurance (QA) procedures are used. QA has an important role in modern clinical contexts, supporting regular calibration and functionality checks on imaging equipment. The increasing ability of state-of-the-art modalities and their quantitative focus should ideally be accompanied by a corresponding shift in QA procedure. Test objects (i.e. phantoms) are the foundation of QA testing, comparing ground-truth characteristics to scanner output, where suitable phantoms can challenge modern scanners and explore their limitations. There is also value in providing an unambiguous, direct comparison between modalities, both conventional and state-of-the-art. Current flow phantoms suffer from limited availability and potentially variable flows that often rely on a complexity which is beyond our understanding; there is room for a novel, more accessible flow standard here.

A previous project explored development of a novel flow phantom to fulfil such a need, with a US/CT compatible prototype already designed, manufactured, and tested in a laboratory environment. This thesis will present the continuation of this project by advancing the prototype to a complex flow phantom with multimodal capacity in its pre-commercial stage. An emphasis will be brought on the *characterisation*, *optimisation* and *expansion* of the existing device.

## 1.2 Thesis Aims

The development of this device has been historically challenging, and at the time of writing has spanned approximately 10 years of active research. The device timeline is clarified here to highlight the specific contributions of the author of this thesis. Previous to this project, a prototype device compatible with CT and ultrasound had been manufactured and the phantom flow (ring vortices) tested for its reproducibility at the macro (above 1cm) length-scale. Whilst considerable technical progress was made, detailed understanding of the phantom’s flow was lacking, both empirically and with reference to idealised analytical models. As the phantom was limited to ultrasound compatibility, a proof-of-concept MRI-compatible version was hypothesised with no quantitative assessment performed. Furthermore, the novel vortex behaviour was frequently (although unnecessarily as this work will demonstrate) under suspicion by external users.

Inspired by the previous findings, this thesis has four primary objectives:

- Gain a thorough understanding of the phantom’s ring vortices using experimental data. Understand their behaviour at a sub-mm (‘micro’) level, and determine whether the experimentally observed rings agree with idealised models.

- Optimise the current phantom device and its experimental protocol to ensure its effective use.
- Integrate a quality assurance tool with the phantom to confirm its functionality in real-time. This is anticipated to increase confidence in the phantom’s abilities.
- Redesign, manufacture and test an MRI-compatible version of the ring vortex phantom.

If achieved, these objectives will produce an accessible complex flow phantom which generates a known, well-characterised flow on demand. The phantom will promote confidence through rigorous in-built QA tests on its own functionality, and through multimodal expansion will be equally capable of being imaged in the ultrasound or MRI environments found in clinical settings. A multimodal, complex flow phantom.

### 1.3 Thesis Structure

The structure of this thesis follows these four objectives with each chapter representing either optimisation, expansion or characterisation for the device development.

**Chapter 1** introduces the thesis and performs a literature review on currently available flow imaging technologies. Their respective abilities are compared, assimilating available options in quantitative cardiovascular flow imaging. This is followed by a review of currently available flow phantoms. Their advantages and limitations are discussed and the current standard for flow imaging QA test objects is established.

**Chapter 2** introduces the ring vortex. Its history, notable properties and dynamics are discussed, introducing key concepts applied throughout the thesis. For context the ring vortex phantom (Unit-0 as passed on at the start of this project in 2019) is presented, covering the technical specifications, previous findings and status. An in-depth analysis reviewing previously collected visualisation data forms the central portion of this chapter, characterising the micro-behaviour of the phantom’s ring vortices and assessing them for their suitability for deployment in a phantom.

**Chapter 3** discusses optimisation of the phantom and ring vortices in response to the findings of Chapter 2. This chapter identifies under what experimental conditions the most suitable vortices are generated, and confirms the ring vortex ‘landscape’ that the phantom can generate using optimised protocols. Hardware and software upgrades are also performed in this chapter. The optimised device is known as Unit-1.

**Chapter 4** presents the design, development and validation of a real-time quality assurance tool for the phantom. This tool confirms phantom performance and ring vortex behaviour in real-time according to the tolerances found in Chapter 3.

**Chapter 5** determines whether vortices generated by the phantom act according to idealised analytical models at the micro-scale, to explore whether models could be used to enhance phantom characterisation. Theoretical models of increasing complexity are compared to high-resolution visualisation datasets. A range of semi-quantitative and quantitative methods are used to measure model adherence.

**Chapter 6** performs visualisation of the optimised ring vortices using Laser-PIV methods, imaging a broad range of vortices. Analysis confirms whether these vortices behave according to phantom flow requirements at the micro-scale. Their dynamics are also classified according to analytical models from Chapter 5, exploring the extent to which change in generating conditions affects model-like behaviour.

**Chapter 7** expands the phantom’s potential by considering its application to an MRI environment. A revised design is presented and manufactured, and experiments performed to characterise the device behaviour and its vortices at the macro-scale. A limited analysis is also performed at the micro-scale to confirm satisfactory flow behaviour.

**Chapter 8** completes the work by combining the findings from Chapters 1-7 and discussing their implications for the phantom as an in-development tool designed for commercial use. Recommendations for the future are discussed, from phantom design refinements to proposed imaging experiments. The take-home message summarises the contribution of this thesis and establishes the future direction of this device.

## 1.4 Medical Imaging Technology for Cardiovascular Flow - Angiography and Ultrasound

### 1.4.1 Introduction

A range of medical imaging technologies are available for visualising and quantifying haemodynamics within the cardiovascular system. These vary from ionising options such as angiography to non-ionising methods including ultrasound and MRI. Sections 1.4 and 1.5 will review these modalities, summarising their physical principles, practical considerations for clinical settings as well as advantages and limitations to each. Both clinical standard and state-of-the-art, in-development tools will be reviewed to form an appreciation of the current and next generation of flow medical imaging technologies. These modalities will then be compared with respect to their various attributes, with an emphasis on ‘quantitative ability’ - to what level the technology in question can measure and calculate advanced haemodynamic properties from standardised acquisition protocols.

### 1.4.2 Angiography

When considering the breadth of cardiovascular imaging technologies, angiography is a natural starting point. This modality has a long history and uses X-rays in conjunction with intravenous iodine contrast agents to generate high-contrast images delineating the blood vessels from surrounding soft tissue. Regular clinical practice sees this technique used for detecting stenoses, plaque deposits and aneurysms, among other anatomical abnormalities. Today it achieves a high spatio-temporal resolution of 0.1mm and 250Hz [7] and can be technically/technologically considered the gold-standard in cardiovascular imaging [4]. However, limitations exist, primarily invasiveness from catheter use, requirement for dye, radiation exposure and high cost. A more technical limitation is

its restriction to 2-D imaging, rather than 3-D volume visualisation. These drawbacks restrict its application in some cases and encourage alternatives to be sought [8]. Ionising radiation is a particular concern for repeat scans, as the dose accumulates with each additional scan.



Figure 1.1: Example angiography of the coronary artery. Image from [9]

A more modern technique which is often the preferred choice over standard angiography is CT angiography. This technique requires no catheter, as the dye is instead inserted through an IV port, however its clinical spatial resolution is 0.5mm at best, compared to traditional angiography's 0.1mm [7] and adequate temporal resolution is lacking.

Angiography achieves limited quantification of the vessel haemodynamics, calculating only peak and mean flow velocities at the macro-scale using time-of-flight techniques [10]. These results show good agreement with true values but more advanced haemodynamic parameters can't be found. Visualisation of the blood flow dynamics is also limited (Figure 1.1) with minimal in-vessel flow information visible. This limited quantification and visualisation limits its use in high-resolution haemodynamic assessment, so angiography is included here for completeness.

### 1.4.3 Doppler Ultrasound - Basic Principles

Perhaps the most widely-available medical flow imaging modality is ultrasound, a technique which exploits the reflection and absorption of longitudinal sound waves by biological tissue. For this modality, piezoelectric crystals generate mechanical waves which propagate into the sample and partially reflect at tissue boundaries of differing acoustic impedance. The reflected waves are detected and collated to generate a 2D greyscale image of the imaged anatomy [11]. Ultrasound imaging is often used as a first 'point-of-call' in diagnostics, due to its wide availability, low cost and high precision. Ultrasound imaging is advantageous for a number of practical reasons, particularly its low cost, fast acquisition time, lack of ionising radiation, portability, and lack of dye or contrast agent. In anatomical ultrasound imaging the flow field is not visualised, so a different method is used to analyse the flow behaviour.

The physical phenomenon employed for measuring blood flow through ultrasound is the Doppler Effect. This effect describes the observed frequency shift in a signal in the presence of a non-zero relative velocity between the signal source and observer. If the source travels towards the observer, the signal is compressed and the frequency increases, with frequency decreasing if the opposite is true. The ultrasound wave is scattered by red blood cells in motion, with the frequency shift ( $\delta f$ ) used to calculate local flow velocities. Equation 1.1 is the basis for these calculations.

$$\delta f = f_r - f_0 = \frac{2f_0 v \cos\theta}{c} \quad (1.1)$$

Where  $f_r$  is the received frequency (Hz)

$f_0$  the emitted frequency (Hz)

$v$  the scatterer velocity (m/s)

$\theta$  the angle between beam and velocity vector

$c$  the speed of ultrasound (m/s) [11]

The Doppler effect is advantageous for dependable blood velocity measurement, however the effect is only induced along one dimension, parallel to the beam. This limits Spectral Doppler measurements to one dimension unless more state-of-the-art factors are introduced. This effect is only reliable for velocities with a significant component parallel to the beam. If the beam is placed perpendicular to the vessel of interest, the  $\cos(\theta)$  factor in Equation 1.1 becomes zero, with no frequency shift or velocity information produced. As ultrasound imaging is directed by a trained clinician and a handheld probe, orienting the probe and correcting for Doppler angle on the B-mode image is a manual process.

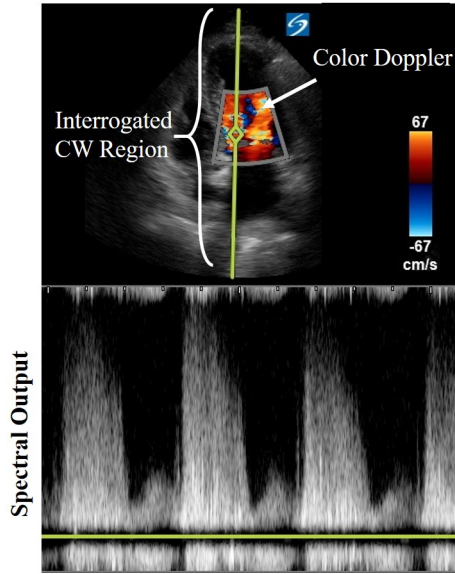
## 1.4.4 Doppler Imaging - Clinical Techniques

### Spectral Doppler

Spectral Doppler is the first genre of Doppler ultrasound imaging, with two types commonly used in clinical practice: continuous wave (CW) and pulsed wave (PW). These techniques generate spectral wave outputs: 2-D plots of time-resolved frequency information.

**CW Doppler** transducers continuously emit and receive signals, detecting velocities along a thin beam originating at the probe [12]. Scattering occurs from both static tissue and blood cells in motion, requiring signal filtering from non-zero phase shift frequency components. This method has demonstrated its ability to detect a large range of velocities, however it provides no depth information for any detected phase shifts [13]. The spectral output can be analysed using cross-correlation between the emitted and re-detected frequencies, with the distribution of Doppler shifts across the beam-line found. The spectral output is therefore broad and contains all velocity information for the beam line (Figure 1.2). CW Doppler is also limited by its limited area of interrogation, within its thin beam.

## CONTINUOUS WAVE DOPPLER



## PULSED WAVE DOPPLER

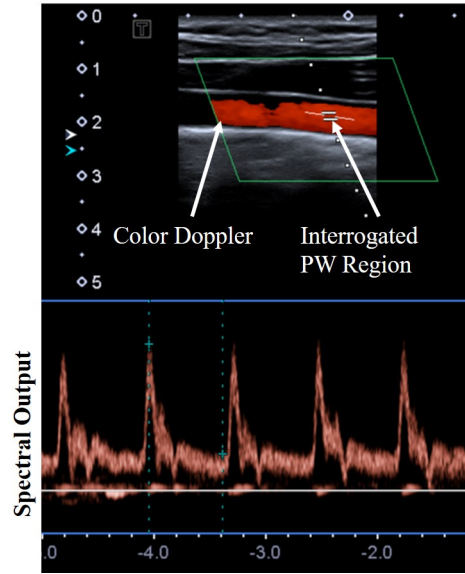


Figure 1.2: Examples of conventional CW and PW Doppler spectral outputs, supplemented with Colour Doppler. Images are annotated to show the types of Doppler imaging in use. Images from [14].

**PW Doppler** is a more refined genre of spectral Doppler, where beams are emitted consecutively rather than continuously. A beam pulse is transmitted into the tissue, with echoes detected as waves are scattered from boundaries between tissue structures. The time delay between transmission and echo detection is related to the scattering depth, with later echoes scattering from deeper structures. Specific echoes are analysed for their Doppler shift, dependent on the user's desired interrogation depth. A key parameter in PW Doppler is the frequency of pulse emission (PRF). As another pulse is transmitted into the tissue, no more echoes will be detected, thus the PRF sets a limit to the imaging depth.

With one pulse detected at a time, depth information on the scatterer is available. PW therefore interrogates a small domain at a user-defined depth, generating a spectral output with less noise (See Figure 1.2). This increases the usefulness of the data, as flow velocities can be attached to certain locations, but the pulsatility introduces a significant limitation to this method. The frequency of pulse emission (PRF) is determined by depth of the sample volume, as each pulse must return to the probe before the emission of the next, with deeper volumes requiring a lower PRF. This parameter, however, limits the velocities that can be detected as a result of the Nyquist principle. [15] The maximum detectable flow velocity (with high accuracy) is  $\frac{1}{2}\text{PRF}$  [16]. This limits quantification of deep vessel flow velocities as a compromise between maximum velocity (high PRF) and PRF travel time (low PRF) must be sought.

Both **CW** and **PW** offer different advantages, and the superior choice is determined on a case-by-case basis; taking into account vessel depth, maximum expected flow velocity, and required depth information. The two methods have the same quantitative

ability, with tools such as peak flow rate and mean flow rate calculation available. Both offer quantitative micro-flow velocities within their limited domains. More sophisticated measurement of how the flow varies throughout the vessel is possible but requires manual relocation of the region of interest and is time-consuming. Routine clinical practice often combines PW Doppler's spatially located velocity information with B-mode's tissue visualisation, allowing for accurate angle correction. CW Doppler is more commonly used where the interrogated flow is too deep to ensure adequate sampling.

## **Colour Doppler**

An extensively used modality underpinned by these principles is Colour Doppler (CDI), a technique which displays collected Doppler information as 2-D colour maps, in place of the traditional time-resolved spectrograms. CDI emits pulses across a local region, using the echoes' phase shifts to determine the region's velocity. This is repeated across a larger volume, with neighbouring small regions averaged to form a pixel. Each pixel is assigned a colour dependent on flow direction (red towards the transducer, blue away) and velocity magnitude. To obtain both flow and anatomical information, the emitted pulses for generating B-mode and Doppler information are interleaved [17] (Figure 1.2). Whilst the colours infer quantitative information in CDI output, the produced images are used qualitatively, as they present the component of velocity in the direction of the beam without angle correction, impacting the accuracy. Laminar CDI velocity values have exhibited values up to 50% from PIV measurements [18]. CDI's visualisation abilities offer valuable, informative data for locating abnormal flow and an understanding of global haemodynamics.

## **Conventional Doppler Ultrasound Angle Dependence**

The techniques described above are restricted by a significant limitation, namely their dependence on the beam angle with respect to flow velocity. Only velocity components parallel to the beam direction can be detected when using the Doppler effect, so choice of probe angle must ensure this component is significant. This poses problems as many major arteries run parallel to the surface. A flow-to-beam angle of  $20^\circ$  will introduce an error of 6% to the velocity value, with errors worsening with increasing angle [19] due to the dependence on the cosine function. Angle correction can be performed in Spectral Doppler, where the clinician will define the vessel angle on-screen. In the ideal scenario clinicians would image with an insonation angle of zero  $^\circ$ , however when this is not possible an angle of less than  $60^\circ$  would result in less error. The manual nature of this modality and its error variability can impede the quantitative usefulness and reliability of conventional Doppler imaging.

### **1.4.5 Doppler Imaging - State-of-the-Art**

An emerging technology which eliminates the angular restrictions of conventional Doppler methods is vector flow imaging (VFI). VFI is a significant technological advancement

from Spectral Doppler and CDI, with scanners generating high-precision quantitative velocity information over a sizeable region of interest. VFI achieves visualisation of global haemodynamic patterns through calculation of velocity vectors across the space in three dimensions. By imaging the entire field clinicians can more readily observe and understand complex 3-D flow structures in vessels.

This significant advancement in ultrasound imaging is achieved through a combination of methods, specifically speckle tracking, multi-directional beams and transverse oscillation [20]. Acoustic waves are scattered from red blood cells, as in traditional US imaging, with the resultant interference patterns used to calculate change in scatterer position and local concentration. These are used to calculate flow directionality and velocity magnitude. Multiple beams are directed over the domain from a range of angles to reduce the angle dependence, and transverse oscillation further reduces the dependence. By inducing a transverse oscillation in the waves, the Doppler effect can take place in 2 dimensions, generating 2-dimensional velocity information from one beam [21]. The combination of these methods results in 3-dimensional absolute quantitative velocity information over a 2-D region of interest.

Through this revolutionary technique, haemodynamic behaviours are presented in a more intuitive manner than the traditional colour map, instead employing quantified vector maps. The imaged region is plotted with arrow vectors which display the local velocity direction, absolute velocity and scatterer concentration through their colour, direction and length (See Figure 1.3) [21]. VFI achieves the large-area visualisation of CDI combined with the quantitative depth-specified velocity data of PW Doppler in a single acquisition.



Figure 1.3: Examples of VFI imaging dataset. Both the Colour Doppler and VFI vector flow field are presented to compare visualisation approaches. Arrow colours are encoded according to velocity magnitude. Image is from [22].

VFI was introduced in the 2010’s as a technique with the ability to estimate haemodynamic behaviour to a level previously achievable only by advanced MRI. A host of studies have since taken place to verify and validate the fledgling technology both *in vitro* and *in vivo*. *In vivo* work has proven its efficacy and high accuracy in imaging

the carotid artery, with strong correlation found with 2D PC-MRA results [23] and also with geometry-specific simulations [24],[25]. Its more recent introduction to some clinical scanners [26], [27] has further established its utility. The most significant factor of VFI’s technical abilities is the potential for revised assessment of cardiovascular dynamics. Its high-resolution quantitative imaging allows for parameters such as wall shear stress (WSS) to be calculated, with abnormal values reported widely to be associated with atherosclerosis and coronary plaque rupture[28]. WSS’s status as a routine metric for cardiovascular health is an active research topic currently under review but it is notable that VFI allows for advanced parameters to be calculated, an ability that was previously unachievable by ultrasound techniques. VFI’s accurate calculation of WSS in both healthy [29] and unhealthy [30] patients using the *Mindray Resonas7* technology is one example of its usefulness in this context.

Whilst the modality’s application in *in vivo* clinical studies is paramount for understanding its suitability for routine clinical practice, evaluating its technical and quantitative abilities is more suitably performed through *in vitro* techniques using phantoms. Phantom validation of VFI was limited until a recent advancement by Haniel et al in 2022 [31]. A spiral-shaped pulsatile flow phantom [32] was employed to assess the ability of VFI to accurately estimate blood flow velocity, pulse wave velocity and vector visualisation. CFD and limited experimental datasets were used as the ground-truth basis, and VFI was proven to accurately measure PWV and visualise the flow pattern. This work marks a significant advancement for VFI, as such systematic analyses of its abilities are a necessity for translation to clinical practice. Further assessment of its other abilities and variation between sites, users and machines is required.

### 1.4.6 Doppler Imaging Conclusion

Doppler ultrasound imaging has a firm standing in assessment of cardiovascular haemodynamics, with a range of modalities available. Traditionally a combination of B-mode, spectral Doppler and Colour Doppler are used to generate anatomical scans, semi-quantitative velocity maps and specified velocities in limited regions. These conventional techniques suffer from their dependence on angle and their user-reliant methods. These limitations provoked the development of the emerging technology known as VFI. VFI generates whole-region scans of quantitative velocity information to high-resolution, intuitively visualising the flow patterns through vector-arrow flow fields. This progress features an emerging hierarchy in quantitative measurement: from qualitative visualisation (CDI) to local flow velocities in a small volume or beam (spectral Doppler) to large-region quantification of haemodynamics (VFI), the available information from a single scan has increased significantly. This progress allows for vastly improved understanding of regional flow behaviour and calculation of advanced parameters which could improve and refine current clinical practice. Clinical trials are currently underway along with limited phantom experiments, signifying a wider acceptance of VFI. A direct comparison of the available Doppler US modalities is listed in Table 1.1.

## 1.5 Medical Imaging Technology for Cardiovascular Flow - Magnetic Resonance Imaging

### 1.5.1 Magnetic Resonance Imaging - Basic Principles

A second widely-used medical imaging technique for both anatomical and functional imaging is magnetic resonance imaging (MRI). This technology has been used since the 1980s and is long-standing in the clinical setting. It exploits the magnetic dipole moment generated by protons (hydrogen atom nuclei) with non-zero spin. A strong magnetic field applied to the patient causes protons to align according to its field-lines. The rate of relaxation of an excited sample within the boundaries of this field differs between biological tissues, so measuring local relaxation times (through monitoring of radiated EM radiation) generates images with contrast between differing tissues [33]. Anatomical visualisation is therefore achievable.

Different sequencing options exist for MRI, such as spin-echo where additional RF excitation pulses are used to realign the protons during relaxation, or gradient echo, where the initial RF pulse can induce a rotation of less than  $90^\circ$ , shortening the scan time and allowing for temporally-resolved ‘cine’ images. Importantly, this method’s reliance on magnetic properties allows for imaging without the need for ionising radiation or contrast. The physics of MRI are well-documented so won’t be discussed here, two particularly useful reviews on this topic are by Grover [34] and Seeger [35].

### 1.5.2 Magnetic Resonance Imaging- Clinical Techniques

A sub-genre of MR imaging exists known as magnetic resonance angiography (MRA), which aims to image and quantify blood flow behaviour *in vivo*. This is used regularly in clinic as a non-invasive alternative to angiography.

#### Non Contrast-Enhanced MRA

Two primary non contrast-enhanced methods exist for MRA: time-of-flight (TOF) and phase contrast (PC). Also known as bolus tracking, TOF saturates a thin band of nuclei and tracks its motion across an appreciable distance, calculating flow velocities from the bolus [36]. Offering higher spatial resolution ( $0.48 \times 0.75 \times 2.00$  mm) as standard [37] and lower acquisition times, TOF-MRA is often the foremost NCE-MRA imaging technique in clinics, however its quantitative abilities are low [38]. The resolutions of TOF-MRA are inferior to those of Doppler US, but superior to PC-MRA.

The second option is PC imaging. For this approach, a bipolar magnetic gradient field (two opposing field gradients of equal magnitude) are applied immediately after the excitation pulse. The first field will shift the phase of all captured protons, with the shift proportional to local field strength. The opposite-direction field will shift the phase back towards its starting point. If the proton is stationary, the opposing shifts will cancel, however moving protons will experience different field magnitudes and have a non-zero net phase shift. This net phase shift is proportional to both their velocity in the direction

of gradient, and the field strength [39]. This 'phase encoding' allows for visualisation of blood flow velocities (Figure 1.4).

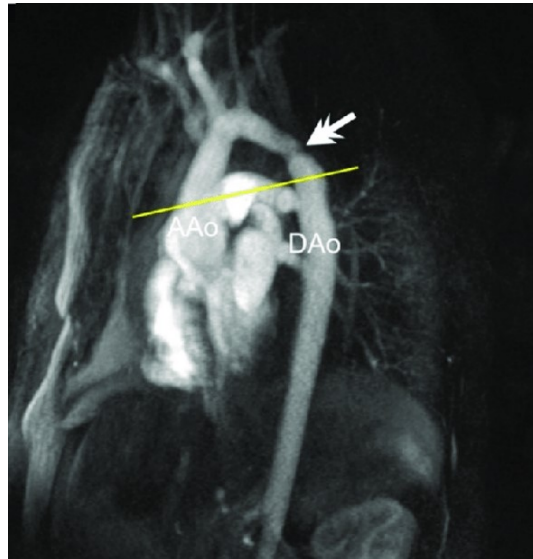


Figure 1.4: An example 2D PC-MRA image of the ascending and descending aorta. Image from [40]

Phase shift supports velocity encoding, but this limits the maximum detectable velocity. Phase shift can range from 0-360°, but angles (such as -270° and +90°) can interact with their opposite-direction counterparts and cause aliasing. A maximum detectable speed ( $V_{enc}$ ) is therefore selected and associated with the angular shift to mitigate against aliasing.  $V_{enc}$  values affect image quality - a value within 25% of the maximum expected velocity is ideal to ensure a high-amplitude signal with no aliasing.  $V_{enc}$  is user-selected, so the clinician must have an estimate of maximum expected flow velocity prior to imaging, often through conventional Doppler ultrasound techniques [35].

### Contrast-Enhanced MRA

MRA can use contrast to enhance its images, similar in principle to CT Angiography. A gadolinium-based (Gd) agent is injected intravenously into the patient, which propagates through the circulatory system. Images are taken before and after contrast injection, with subtraction leaving only the vessel information, generating clear visualisation of blood flow. Use of Gd contrast is controversial however, as it has proven dangerous for patients with renal dysfunction [41] although investigations are underway to quantify and improve the associated risks [42]. As imaging is only a precursor to treatment, associated risks and hazards to the patient should be kept to a minimum. The use of contrast is therefore a concern, and non-contrast methods are an alternative.

The final considerations in PC-MRA are user-dependence and practicality. Prior to scanning the clinician selects an imaging plane perpendicular to the vessel of interest. This user-performed method can introduce variability and error in plane orientation [43],

which is a fundamental concern of the qualitative-to-quantitative movement currently underway [5]. PC-MRA exhibits high quantitative abilities, able to calculate haemodynamic parameters such as flow volume, forward and reverse flow fraction and shear stress, along with peak and mean flow velocity, but subjective decisions can compromise quantitative accuracy. Finally, the longer scan times of MRA when compared to Doppler US, along with the requirement for gating over a number of cardiac cycles can impact its usefulness in regular use for clinical settings.

### 1.5.3 Magnetic Resonance Imaging - State-of-the-Art

In a similar manner to VFI in ultrasound imaging, technological progress has facilitated the invention of a quantitatively superior MRI modality known as 4D-MRI (Flow MRI). This technique achieves quantitative visualisation of global haemodynamic behaviour over a 3-D volume with velocity encoded in three dimensions. The ability to quantify flow over a volumetric space rather than a plane as in 2D PC-MRA is significant, allowing for complex flow structures such as helices or vortices to be truly visualised and understood (See Figure 1.5).

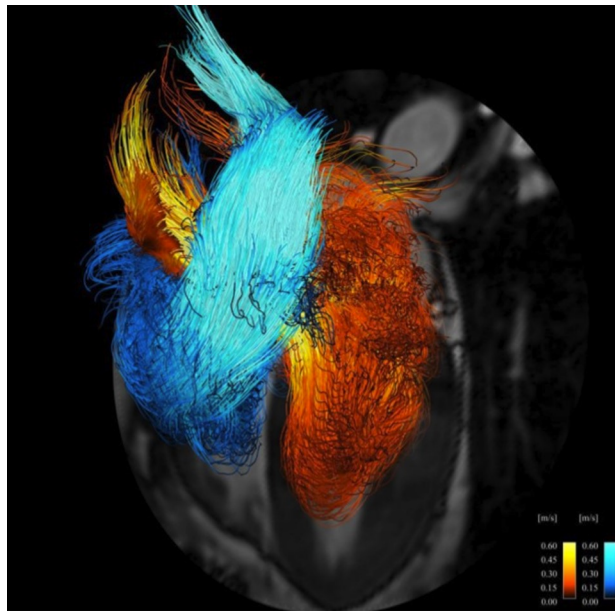


Figure 1.5: A 4D-MRI scan of the heart, visualising the intracardiac flow. Streamlines are visible, with colours encoded according to velocity direction and magnitude. Image from [44].

To generate these scans, bipolar gradient fields are applied in three orthogonal directions, with phase encoding applied along each direction, allowing for 3-dimensional velocity vectors. A particular advantage over PC-MRA is retrospective analysis plane selection - rather than the clinician imaging a specific pre-selected plane, a volume is imaged and planes are selected during post-processing. This generates a full quantitative

volume where values can be determined at any arbitrary location across the domain and removes user-dependence during acquisition. This modality relies on extended acquisition times, resulting from the higher volume of interest.

Similar to VFI, visualisation of the haemodynamics is achieved through intuitive arrow-vector fields. These high-resolution data are reflected in 4D-MRI's superior quantitative abilities, with parameters such as WSS, turbulent kinetic energy, pressure differentials and pulse wave velocities [45] derivable from the velocity output. These parameters have exhibited high reproducibility [46].

Validation of 4D-MRI is currently underway, with values found to agree well with 2D PC-MRA [47],[48] and phantom measurements [49]. Scan-rescan tests have been performed and have shown good repeatability across different sites for basic quantitative flow measurements [50] but varying results between scanner vendors [49]. This is promising but confirms that rigorous validation is a necessity prior to widespread clinical use.

Limitations are inherent in any novel technology, and those of 4D-MRI are largely practical concerns. An often-quoted issue is the long scan times, with a typical duration of 5-20 minutes [40] followed by 30 minutes of post-processing [51]. Reduction of scan time is an active research topic to improve clinical viability.

Overall, 4D-MRI is viewed as a new champion for blood flow visualisation, however its applicability for clinical settings remains limited, largely due to scan times. A consensus in 2015 highlighted the need for a structured workflow across sites and research groups to ensure uniformity, as well as established commercial and efficient data processing techniques once in use [45]. These concerns have been reiterated in a recent 2021 review by Zhang et al. [50], with limitations including non-uniform and limited literature, the time-consuming and non-uniform post-processing procedures and inconsistency in reporting. These limitations are common in new and novel technologies, but by no means limit the intrinsic capabilities of this technology. These advantages and limitations are clarified in Table 1.1.

#### **1.5.4 Discussion - Gold-Standard Quantitative Flow Imaging**

This review of flow imaging technologies has highlighted the range of options available for quantitative imaging of cardiovascular flow. Each method has unique limitations and advantages, so comparing attributes across the group is valuable to gauge the status of current and next-generation medical flow imaging. This is performed through the table below.

| <b>Modality</b> | <b>Output</b>                 | <b>Spatial Resolution</b>                 | <b>Temporal Resolution</b>    | <b>Parameters</b>                             | <b>Angle Dep?</b> |
|-----------------|-------------------------------|---|-------------------------------|---|-------------------|
| Angiography     | 2D Greyscale                  | 0.1mm                                     | 250Hz                         | Flow Velocity                                 | Yes               |
| CW Doppler      | 1D Flow-time                  | ~ 2mm<br>beam width [52]                  | N/A - device<br>speed limited | Peak Flow<br>Mean Flow Vel<br>P Gradient      | Yes               |
| PW Doppler      | 1D Flow-time                  | 0.12mm min.<br>domain size                | 1-20kHz                       | Peak Flow<br>Mean Flow Vel<br>P Gradient      | Yes               |
| Colour Doppler  | 2D Colour                     | 0.2mm<br>[53]                             | 24Hz<br>[54]                  | N/A   | Yes               |
| VFI             | 3D with<br>coloured<br>arrows | 0.40mm(axial)<br>1.3-2.3mm<br>(lat.1)[56] | 400-1200Hz<br>[55]            | Local velocity<br>PFV, MFV<br>WSS, Turbulence | No                |
| 2D PCA-MRA      | Greyscale<br>Image            | (1.8×2.3×6)mm                             | 20Hz<br>[57]                  | Flow dir<br>Regurg. fraction<br>PFV, MFV      | No                |
| 4D Flow MRI     | 3D with<br>coloured<br>arrows | 0.8 – 3mm <sup>3</sup><br>[58]            | 12-25Hz<br>[58]               | Local Velocity<br>PFV, MFV,<br>TKE, WSS, PWV  | No                |

Table 1.1: List of medical flow imaging technologies with technical abilities, output format and angle dependence listed

Table 1.1 presents the key specifications of each technology relevant to this review, focusing on quantitative abilities. Quantitative abilities is defined in this work as the extent to which imaging data can be used to determine certain parameters, for example angiography is limited to flow velocity, whereas 4D-MRI can be used to calculate a range of more advanced haemodynamic parameters.

Firstly, conventional Doppler ultrasound is well-established in the clinical settings and is a safe, inexpensive option which can be performed bedside. The combination of B-mode, CDI and PW Doppler offers anatomical assessment, flow visualisation and dimensionality. The PW Doppler is limited to velocities in a limited domain - if a more comprehensive velocity map is required, an alternative method would be required. Doppler US's quantitative abilities are limited to peak flow, mean flow and pressure gradients, limited when compared to more advanced systems in scope. Arguably, however, the primary limitation of Doppler US is its potential uncertainty and variability from user reliance and angle dependence.

Conventional MRA techniques offer a different skillset, with their ability to determine 3-D velocity magnitude and direction across a selected plane, rather than the limitation of a 1mm area or thin beam used in Spectral Doppler. MRA is also non-invasive, and its planar visualisation can be used to calculate parameters such as regurgitation fraction. Beyond this its quantitative abilities remain limited by its 2D imaging domain. A notable consideration for considering these traditional techniques is practicality, as MRA is limited by its requirement of large, non-portable and costly equipment and lengthy scan times. Both Doppler US and MRA are well-trusted and often used to calculate benchmark values for new techniques and phantom devices (as discussed in Section 1.6).

Such conventional tools are useful and have performed well for many years in clinic, and will continue to do so. There is, however, a distinct evolution occurring in the medical imaging field, with a transfer from qualitative information which is clinician-led to quantitative imaging with technology capable of higher levels of quantification [6].

The Radiological Society of North America (RSNA) defines quantitative imaging as *'the extraction of quantifiable features from medical images for the assessment of normal or the severity, degree of change, or status of a disease, injury, or chronic condition relative to normal. Quantitative imaging includes the development, standardization, and optimization of anatomical, functional, and molecular imaging acquisition protocols, data analyses, display methods, and reporting structures. These features permit the validation of accurately and precisely obtained image-derived metrics with anatomically and physiologically relevant parameters, including treatment response and outcome, and the use of such metrics in research and patient care.'* [5]

This identifies a subset of imaging that can perform at a higher level than qualitative alone, with flow imaging fitting into the 'functional imaging' category. Transitioning to quantitative imaging will mitigate intra- and inter- user variability (both in data acquisition and post-processing) and extract the maximum information from the patient data through automated systems rather than relying on clinical staff with high workloads. The challenge of moving from qualitative to quantitative methods in research and clinical en-

vironments boils down to ensuring quantitative uniformity and comparability between sites, machines and users [59].

This transition is intrinsically related to technological developments, as it is only possible to aim for quantitative imaging thanks to modalities such as 4D-MRI and VFI. Both techniques generate high-resolution velocity vectors encoded in 3 dimensions, ensuring the full flow profile is accounted for. Increased information allows for elevated quantitative abilities, and more derivable metrics rather than the limited options and assumptions implicit to conventional techniques. The primary limitations of these modalities are practical: high cost for both, high scan time for 4D-MRI, limited literature for both and lack of uniform protocols for their use. These practical restrictions sit alongside the core difficulty of the qualitative-to-quantitative shift, which is ensuring the quantitative consistency and comparability between sites, machines and users [59]. A universal concern for new technology and imaging approach is the level of trust and uniformity, which can only be rectified through effective QA, using flow phantoms which operate at the same level of capability as these high-specification modalities. A refined ring vortex phantom is a possible candidate and its position in the context of imaging phantoms is discussed below.

## 1.6 Flow Phantoms for Medical Imaging Assessment

### 1.6.1 Phantom Introduction

Imaging phantoms are test objects designed to quantify imaging system performance during development and ensure its satisfactory function in regular use [60]. Often this is achieved through the mimicking of a physiological or physical characteristic where the ground-truth is known, enabling comparison between imaging scanner output and the true value. Phantoms can mimic soft tissue, with modality-specific characteristics tested (T1, T2, proton density for MRI, attenuation coefficient for X-ray and US [61]), however a sub-genre of phantoms generate a specific flow-field as their reference characteristic. These are known as ‘flow phantoms’ and assess technologies capable of imaging blood flow.

Flow phantoms typically constitute five components: pump, pump controller, tubing, reservoir, and flow section [61]. Fluid is pumped through the system into the flow section where the pump conditions and geometry impose a certain flow-field (reference flow) and is then imaged. This geometry can be arbitrary but anthropomorphic geometry is often chosen, replicating certain cardiovascular structures such as bifurcations or stenoses. Tissue-mimicking material (TMM), vessel-mimicking material (VMM) and blood-mimicking fluid (BMF) may be employed to ensure similarity to physiological conditions, with values according to IEC 61685 standard 1999 [62]. Wall-less phantoms are also an option, with the VMM omitted and the flow directly in contact with the TMM (silicone or agar) [63], [64]. These phantom design components summarise the conventional approach to flow phantoms. A noted disadvantage in conventional anthropomorphic phantoms is the inability to truly mimic cardiovascular dynamics due to their simplic-

ity [61], and mathematically describing the complex flow fields in vascular structures is no trivial task. A quantitative, in-depth understanding of the phantom reference flow is paramount for effective assessment of imaging technology.

A second genre of flow phantoms therefore exists with a ‘flow-centric’ design process, where the primary objective is characterising the flow to high confidence. A well-characterised, reproducible, controllable and trusted flow profile is selected (such as 2-D rotation or fully-developed laminar flow) and a basic geometry constructed to generate it. A consequence of the requirement for confident characterisation is that these flows are typically simple - velocity components are either 1-D or 2-D.

### 1.6.2 Other Phantom Applications

The primary application of flow phantoms is for the assessment and characterisation of medical imaging technologies, however some phantoms are designed for other purposes. This can be to further understanding of physiological flow conditions for certain pathologies. Phantoms are designed based off of specific geometries, with conditions varied, allowing for exploration of the effects of haemodynamics. This is evident in the literature [65],[66]. Alternatively, phantoms can be manufactured to increase understanding of the flow itself. This is evident in the Taylor-Couette flow phenomenon, generated when fluid is trapped between two rotating cylinders. Devices which generate these flows have been manufactured and imaged using PIV and other visualisation methods [67]. Notably in this context, an MRI-compatible Taylor-Couette phantom was manufactured and imaged using novel MRI techniques [68]. Whilst these phantoms hold great value for the understanding of flows, whether physiological or otherwise, their objective is not focussed on performing QA on imaging technologies, thus they are not included in this review.

This review will establish the abilities of flow phantoms designed for the QA of imaging technologies. The flows, dimensionality, geometry and suitability for state-of-the-art imaging technology will be reviewed. Phantoms are nominally separated by flow-dimensionality (1-D and 2-D, then 3-D).

### 1.6.3 1-D and 2-D Phantoms

The simplest phantom genre is those which provide flow profiles with one or two non-zero orthogonal velocity components. 1-D flows are laminar along a straight line, and 2-D is largely concerned with rotating flows in a x-y plane, with a zero z component. An important facet of phantom design introduced in this review is the choice of ground-truth datasets. These are used to quantitatively characterise the reference flow, often visualising the whole flow-field, and can be achieved through analytical, numerical or experimental means.

| Author           | Date | Dim | Geometry          | Condition            | Modality   | Ground-Truth |
|------------------|------|-----|-------------------|----------------------|------------|--------------|
| Zhou [69]        | 2017 | 1-D | Straight tube     | pulsatile laminar    | US Doppler | Manual       |
| Kenwright [63]   | 2016 | 1-D | Straight tube     | SS parabolic laminar | HF US      | Analytical   |
| Sun Nuclear [70] | 2023 | 1-D | Straight tube     | SS parabolic laminar | US Doppler | Unknown      |
| Grice [71]       | 2016 | 1-D | Straight channel  | SS laminar           | US Doppler | Manual       |
| Nordell [72]     | 1988 | 2-D | Rotating disk     | SS rotation          | PC-MRI     | Analytical   |
| Vali [73]        | 2020 | 2-D | Rotating disk     | SS rotation          | PC MRI     | Analytical   |
| Yiu [32]         | 2017 | 2-D | Concentric spiral | SS laminar           | VFI        | CFD, PW      |

Table 1.2: A range of currently available 1D/2D flow phantoms. Authors, modality and basic geometry are listed. ‘Ground-Truth’ refers to the datasets used to characterise the reference flow of each phantom. ‘Dim’ refers to dimensionality, and ‘HF’ refers to high-frequency.

The range of phantoms listed in this table can largely be grouped into two families: 1-D straight-tube phantoms and 2-D rotation-disk phantoms. Those in the former group propel fluid (BMF) through straight channels embedded in TMM. Such examples are suitable for use with US Doppler [69],[63],[70] and are regularly encountered, along with string phantoms, in regular UK clinical QA procedures. A pump propels the fluid through the phantom at a known rate, either as a steady-state parabolic [63],[70] (Figure 1.6a) or pulsatile waveform [69]. Fully-developed parabolic flow is stable over a range of Re and forms a simple velocity profile which can be characterised with analytical expressions (e.g.  $V_{max} = 2V_{mean}$ ). Use of these idealised expressions enables calculation of flow velocity at any arbitrary location within the flow field. Pulsatile flow better approximates the pulsatile nature of physiological flow, characterised analytically as a Womersley flow or requiring numerical or experimental ground-truth datasets. Notably, *increasing* the flow complexity *reduces* the quantitative characterisation. Overall, 1-D straight tube phantoms are reliable, well-trusted, compact and closed-loop, however the geometry and flow profile bear little resemblance to physiological flow conditions. Their limited dimensionality is also restrictive for assessing multi-directional scanners in a single acquisition.

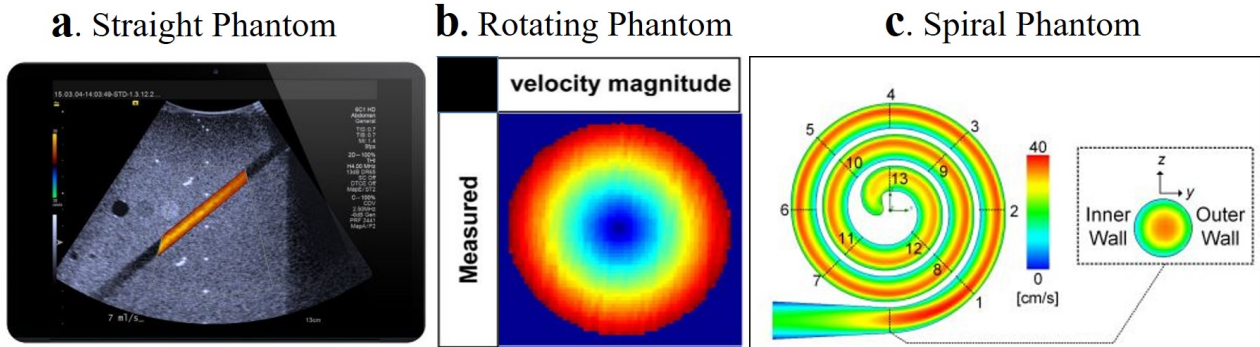


Figure 1.6: Examples of 1D and 2D phantom flow profiles. (a.) presents the flow of Sun Nuclear 1430 Doppler phantom [70], a straight tube phantom example used often in regular clinical QA and research. (b.) presents the flow of Vali [73], an example of a rotating gel phantom. (c.) presents the flow of Yiu [32], a novel spiral phantom

The second group in this table is the 2-D rotational phantoms which counteracts this limited dimensionality. These test objects employ rotating plates of gel (typically agarose) [72],[73] to generate a 2-D flow profile in the plane of the plate (Figure 1.6b). Rotational flow is easily characterised by measuring angular velocity and calculating components across the disk using analytical expressions. These phantoms are also quite common, with publication dates ranging from the 1980’s [72] to the 2020’s [73]. Similar to 1-D phantoms, these devices are reliable, well-trusted and compact, and do offer a 2-D flow which is highly characterised. Their flow profile, however, is not representative of any aspect of cardiovascular haemodynamics, limiting their physiological relevance.

A notable outlier in this review is the spiral flow phantom by Yiu et al [32]. In this device, BMF is pumped through a flat concentric spiralling structure, generating a laminar flow field with bent streamlines (See Figure 1.6c). This profile is more complex than the straight channels or rotating gels, particularly given that an eccentric parabolic flow is induced by centrifugal force [32]. The flow is beyond analytical characterisation, so CFD and PW Doppler are used as the ground-truth visualisation. This phantom is interesting, as it arguably avoids the pitfalls of the 1D straight-phantoms and 2D rotating phantoms with a novel, more challenging flow. It remains limited by its 2-D flow, and its lack of similarity to haemodynamic flow behaviour. The spiral phantom is specifically designed for VFI assessment rather than traditional non-quantitative modalities by employing the more complex profile, and thus represents the only 1-D/2-D phantom specifically designed for the next-generation imaging modalities.

In summary, these 1D/2D phantoms constitute a significant portion of available phantoms, are largely well-trusted and are associated with tried and tested QA protocols. Analytical representations are the primary source of ground-truth datasets, providing quantitative characterisation of the entire flow-field with high confidence. More complex flows rely on numerical or experimental representations but this is limited. These phantoms generate flows which are stable, controllable, reproducible and well-characterised, with the only limitation being their lack of complexity, dimensionality and marginal relevance

when compared to haemodynamics.

### 1.6.4 3-D Flow Phantoms

Phantoms with more complex flow profiles have been manufactured and imaged for years, typically aiming to replicate certain vascular structures. These flows have 3-dimensional, multi-directional flow with the potential to facilitate assessment of modalities in 3D-imaging, but their designs can lead to challenging complications. Table 1.2 lists a variety of phantoms with 3D reference flows.

| Author       | Date | Dim. | Modality   | Geometry              | Condition      | Ground-Truth       |
|--------------|------|------|------------|-----------------------|----------------|--------------------|
| Meagher [74] | 2007 | 3-D  | Doppler US | ID bifurcation        | pulsatile      | PIV on 2nd phantom |
| Kohler [75]  | 2001 | 3-D  | MRI        | bifurcation, stenosis | Steady state   | CFD                |
| Summers [76] | 2005 | 3-D  | PC MRI     | U-bend, stenosis      | SS & pulsatile | MRI, pump          |
| Chee [77]    | 2016 | 3-D  | Doppler US | bifurcation           | pulsatile      | previous PIV       |
| Smith [78]   | 1999 | 3-D  |            | Bifurcation           | pulsatile      | Angiogram          |
| Lai [79]     | 2013 | 3-D  | US Doppler | Rotating disk         | Steady state   | Analytical         |
| Vali [73]    | 2020 | 3-D  | PC MRI     | bifurcation, stenosis | pulsatile      | Qualitative        |
| Chee [80]    | 2021 | 3-D  | VFI        | Helical toroid        | Steady state   | CFD, PW Doppler    |

Table 1.3: A range of currently available 3-D flow phantoms. Authors, modality and technical specifications are listed. ‘SS’ refers to a steady-state flow and ‘Dim’ refers to flow dimensionality.

The vast majority of 3D flow phantoms in the literature employ a vessel bifurcation as their flow field/imaging domain (Figure 1.7a). These are manufactured either through CAD models developed from patient data [74],[80] or average/idealised models [75],[78],[79]. Utilising this structure generates a physiologically relevant flow, particularly given the predilection of bifurcations to the growth of atherosclerotic plaque. The phantoms generate 3-D reference flows, which often contain complex flow structures such as eddies and flow separation. These features are frequently a focal point of cardiovascular flow analysis, thus their inclusion in QA protocol would be beneficial.

## a. Bifurcation Phantom      b. Helical Toroid Phantom

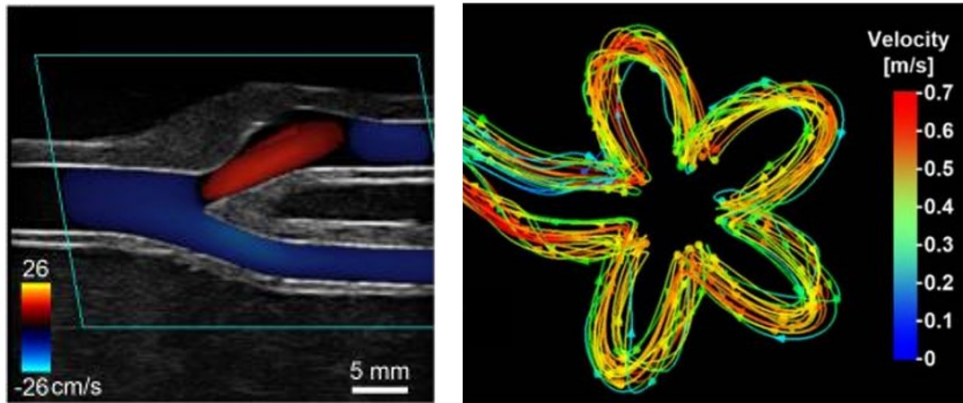


Figure 1.7: Examples of 3D flow phantoms. (a.) presents the stenosed bifurcation phantom of Chee et al. [77]. (b.) presents the helical toroid phantom, also from Chee et al [80]

A certain limitation inherent to the complex geometry is loss of accurate characterisation in the reference flows. These phantoms are often manufactured to study TMM, VMM, or BMF, or factors such as vessel distension [74],[79]. This shift in focus away from flow behaviour results in inferior characterisation of the flow when compared to the rigorously characterised 1-D/2-D phantoms. Rather than computing the entire flow field, bulk parameters such as volume flow rate [76], peak flow velocity [80] and qualitative assessment [79] are used to characterise the phantom flow fields. Relying solely on these variables could lead to ambiguity of the true flow dynamics, as there is an unknown relationship between the bulk parameters and the micro-flow field.

A central cause of this lack of characterisation is the flow complexity. Upgrading from parabolic laminar or rotational flows to pulsatile profiles distorted by bifurcation, corners or stenoses (See Figure 1.7) is beyond current analytical characterisation. Validation is therefore sought through methods such as CFD, angiograms, MRI scans or by monitoring motor behaviour, each of which is accompanied by their own inherent inaccuracies. High-resolution flow visualisation techniques such as particle imaging velocimetry (PIV) are used sparingly [74][80]. Despite its ability to provide quantitative visualisation of the entire flow field at sub-mm level, PIV is a demanding technique to deploy well, and is complicated when combined with medical imaging technologies. Pre-collected experimental data also lack the flexibility of theoretical characterisations whose conditions can be varied (such as analytical or numerical representations).

The helical toroid phantom by Chee et al [80] is an interesting device with a unique design. Specifically designed to assess modern 3-D imaging systems such as 4D MRI and VFI, this phantom offers a 3-D flow as fluid is pumped through a toroid with a looped helical structure around its circumference (Figure 1.7b). This device produces laminar flow with bent streamlines and is characterised through CFD and PW Doppler. It represents an improvement on the complexity of flow compared to the previous section but it is still very limited. Only laminar and steady state flow is available and no recirculation, eddies

or extreme streamline angles are exhibited.

On the whole, these 3-D flow phantoms all offer 3-D flow velocities allowing for simultaneous assessment along different axes for multi-directional scanners, overcoming a primary limitation of the 1-D/2-D phantoms. They also improve flow complexity and physiological relevance, however this advancement compromises the flow characterisation, with analytical methods no longer applicable and alternatives subject to inaccuracies. This can lead to lower confidence in the true nature of the flow-field. With phantoms regarded as the ground-truth when compared to scanner output, it is paramount that the exhibited flows are quantitatively characterised to high confidence. Generally factors such as reproducibility, predictability and stability of these complex flows are not declared in these works.

### 1.6.5 Phantom Findings

The range of flow phantoms described here have varying levels of use - some have evidence of regular application in clinical QA (e.g. Sun Nuclear [70]), whilst some phantoms' published works are limited to their design and manufacturing specifications. A variety of these phantoms, however, have been used to determine accuracy of imaging modalities. A number of examples are listed below:

- The wall-less phantom (Kenwright et al.) demonstrated the change in velocity accuracy from **PW Doppler** when the Doppler angle is increased, increasing from 15-95% error as the angle was varied from 43-79°[63].
- The wall-less phantom (Meagher et al.) was used to establish the high accuracy of **PW Doppler**, with high agreement found between manual measurements and scanner output [74].
- The vortex flow phantom (Bock et al.) was used to compare accuracy of volume flow in two 4D-MRI scanner models, finding variation between the two and between measurements from different days [49]
- The pulsatile tube phantom (Ebel et al.) also investigated 4D-MRI, exploring their accuracy in velocity measurements from two sequences. High correlations ( $R > 0.98$ ) between scanner and ground-truth was found for flow volumes and velocities. This investigation also found that 2D-MRI underestimates these quantities when the imaging plane is misaligned [81].
- The spiral phantom (Yiu et al.) explored VFI accuracy, with high correlations found between scanner output and PW measurements for lateral and axial velocity measurements.

This list presents the range of application for flow phantoms, and the range of modalities that are assessed using their reference flows, from the more simple techniques to state-of-the-art scanners and sequences. These phantoms continually find limitations of modern scanners, and are invaluable for ensuring their readiness for clinical application.

## 1.7 Discussion - Phantom Design for Next-Generation Flow Imaging

The literature review performed in this chapter has revealed the status of quantitative flow imaging technologies and the status of currently available test objects.

Two main messages are apparent: Firstly, there is a new breed of flow imaging technologies capable of visualising and quantifying cardiovascular haemodynamics at the micro-scale. These technologies inherently require complex phantom flows, relying on QA protocols to ensure their assessment of physiological flows is performed correctly. Secondly, the range of currently available flow phantoms is not able to fulfil this need. Current designs cover a range of flows, with simple 1-D/2-D flow phantoms offering reliable, well-characterised flow profiles in a well-trusted geometry but fail to provide a suitable challenge for scanners. More sophisticated phantoms offer 3-D flows, but the increase in complexity is compromised by an inability to confidently characterise the flows at a micro-scale, relying on CFD models which may be inaccurate or bulk metrics which will not characterise eddies or recirculation. The review of these phantoms has identified some central focal points for designing a phantom for modern imaging technologies.

Firstly, flow complexity is key. A compromise must be sought between overly-simple flows with no complex features (such as eddies, recirculation zones) which can be confidently characterised, and too-complex flows which exhibit the desired complexities but whose characterisation and prediction is restricted. Two phantoms in particular (2-D spiral phantom and 3-D helical toroid phantom) strike a balance with laminar-esque flows with bent streamlines and eccentricity, and are designed specifically for the next-generation flow imaging technologies.

The choice of ground-truth datasets to characterise the flow is also significant to ensure confidence and an accurate basis for interpreting scanner output. Options such as analytical representation (with proven accuracy) and experimental visualisation (with high accuracy and precision) are the gold-standard, as they lack the inaccuracies that CFD, MRI and Doppler techniques can harbour. In-depth characterisation of a fully visualised flow field at the micro-scale is useful to confidently understand the flow behaviour.

In order to produce a reliable, trustworthy flow phantom with a complex yet well-characterised 3-D flow, a suitable reference flow should be sought, along with an accurate and reliable ground-truth benchmark. The flow ought to bridge the gap between simple flows which are stable and well-characterised, and complex flows which are challenging yet uncharacterised and unreliable. An ideal phantom would generate a flow which was complex, characterised at the micro-scale and 3-D, whilst fulfilling basic phantom requirements of high reproducibility, predictability and controllability.

## 1.8 Conclusion

This thesis proffers a new technology to bridge the gap in the field found in this review, aiming to facilitate the translation of novel imaging techniques from research to clinical environments. It is intended to be multimodal, safe, cost-effective and easy to manu-

facture. It pursues a reference flow that fulfils a number of requirements: reproducible, controllable, predictable, robust, stable, quantitatively characterised to high-resolution, with a complexity which is sufficiently challenging for micro-scale imaging technologies. Its flow should have laminar-like characteristics to ensure reproducibility, but flow structures like eddies and recirculating fluid should be incorporated to challenge imaging techniques. The ring vortex is hypothesised as a suitable flow, offering complex characteristics and the opportunity for thorough characterisation. This reference flow candidate will be discussed in Chapter 2, both in the context of literature and in a phantom device.

# Chapter 2

## The US-Compatible Ring Vortex Phantom: Unit-O

### 2.1 Introduction

The preceding review of medical imaging modalities and available flow phantoms has emphasised the key requirements of a candidate reference flow and the need for a novel approach for flow imaging QA. The proposed solution in this research is the ring vortex, a well-established vortical flow phenomenon. The ring vortex will be explored in this chapter with a summary of literature on its dynamics and a brief description of its history in Section 2.2. Section 2.3 will present the in-development prototype phantom around which this project is based, along with principal findings from previous work. Finally, previously collected datasets will be analysed in detail for Section 2.4 to a level not previously accomplished on this device. The suitability of the phantom and its reference flows will be discussed in 2.5, establishing a baseline for future experiments. This chapter represents the transition between previous work and this project, with Section 2.4 and thereafter constituting original work by the author.

### 2.2 The Ring Vortex

The ring vortex is a historically significant and widely-studied fluid phenomenon which was first reported as smoke rings when smoking tobacco, as far back as the 17th century. Its unique nature and enticing visuals have made it an attractive and intriguing topic for scientists in the centuries since, being studied by some of the most well-known and highly-regarded names in physics and mathematics. The field of vortices, and vorticity in general, was established by H. Helmholtz, when he deviated from his speciality in anatomy to lay strong theoretical foundations for vortex dynamics. The field advanced further with W. Thomson (later Lord Kelvin) proposing the ring vortex as an atomic model in the late 19th Century [82]. Despite support from Hicks and JJ Thomson, the theory was disproved [83]. This high-impact and exciting start to vortex study caught the attention of those in the fluid dynamics field, and generations of scientists have since studied the

formation, behaviour and decay of vortices, and specifically ring vortices. In more modern times, aerospace engineers have taken a particular interest in the ring vortex, studying its unique mass transfer with minimal energy loss for application in jet engines. In nature, the ring vortex can be observed in marine biology (dolphins playing with ring vortices is common [84]), aerodynamics (present in the flow field of helicopter blades [85]) and defence physics (the atomic mushroom [86]), along with a number of other examples.

The field of fluid mechanics has been accelerated by rapid development of high-accuracy, high-precision visualisation methods, and this has been reflected in ring vortex research. Quantitative, high-resolution visualisation has allowed researchers to study vortex dynamics at the micro-scale. At the time of writing Google Scholar finds 385,000 results for ‘Vortex Rings’, compared to 11,700 in 2012 [83], demonstrating a significant uptake in academic interest.

### 2.2.1 Basics of the Ring Vortex and Characteristics

The ring vortex has a unique structure with notable simplicity, allowing for straightforward characterisation. Two components comprise the structure: the central ring and vortex atmosphere. The central ring is an axisymmetric toroidal construct comprised of layers of circulating fluid which propagates along its central axis through an ambient fluid volume. This is surrounded by the vortex atmosphere; a fluid ‘bubble’ which separates the central ring from surrounding fluid in a flattened ellipsoid shape and propagates with the central toroid [87]. Mechanically, the ring vortex is a fascinating flow feature, as it exhibits low energy loss with efficient fluid transport, challenging engineers in its application, whilst its vortical nature challenges mathematicians in creating accurate models for its temporal evolution and breakdown. Superficially, it seems to subvert intuitive laws of fluid dynamics and poses significant challenges as outlined by Saffman in 1981 [88]:

*‘One particular motion exemplifies the whole range of problems of vortex motion and is also a commonly known phenomenon, namely, the vortex ring . . . Their formation is a problem of vortex sheet dynamics, the steady state is a problem of existence, their duration is a problem of stability, and if there are several we have a problem of vortex interactions.’*

By virtue of its simple structure, quantitatively summarising the ring vortex is possible, with the primary characteristics annotated on Figure 2.1. The torus has a major radius  $R$  (‘Ring Radius’), defining the distance between core centres, and a minor radius  $a$  (‘Core Radius’), whose definition varies in the literature. Core radius is defined as either half the distance between maximum and minimal tangential velocities [89], or half the distance between points of 10% maximum vorticity [90] when measured across the core centre. Vorticity is defined here as the curl of the local velocity, and describes the tendency of fluid to rotate [91]. The ring propagates at a speed  $V_{trans}$  along its central axis, and is enveloped in a vortex atmosphere of volume  $V_a$  (with the central torus holding a volume of  $V_r$ ). Vortex strength is defined by circulation ( $\Gamma$ ), calculated as either the line integral of velocity components along a closed loop, or the surface integral of vorticity components across the area enclosed by this same loop (resulting in SI units of  $m^2s^{-1}$ ).

These definitions are equal by Stoke’s theorem: ‘The circulation about any closed loop is equal to the integral of the normal component of vorticity over the area enclosed by the contour’. Circulation is linked to the dimensionless Reynolds number by  $Re = \frac{\Gamma}{\nu}$  where  $\Gamma$  and  $\nu$  are circulation and dynamic viscosity respectively. The ring vortex is usefully described using a cylindrical coordinate system, with axial  $z$ , radial  $r$  and azimuthal  $\theta$  axes, as seen in Figure 2.1.

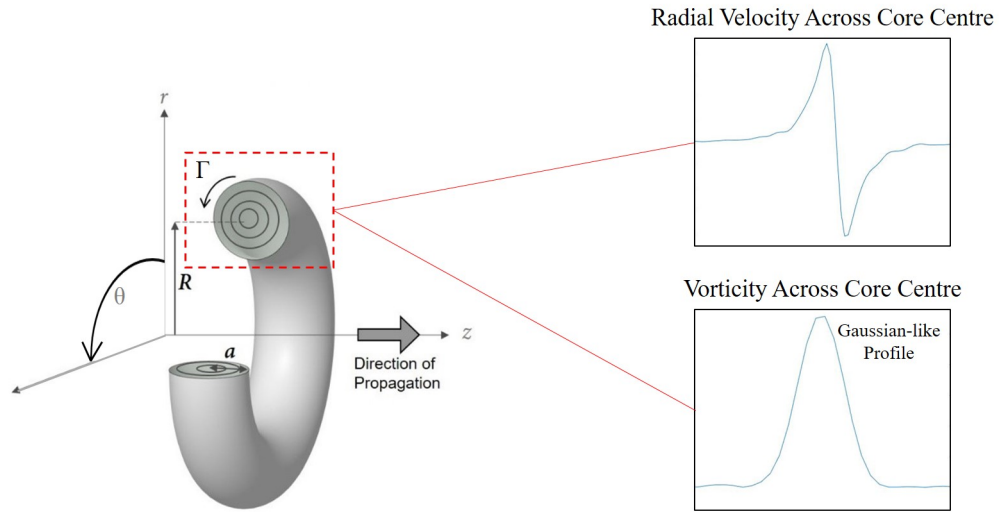


Figure 2.1: Schematic of the ring vortex using the cylindrical coordinate system. Ring radius ( $R$ ), core radius ( $a$ ), circulation ( $\Gamma$ ) and direction of propagation are annotated. The radial velocity and vorticity distribution across the core centre are also presented, demonstrating the Gaussian-like properties.

The circulation summarises the total vorticity within the ring, however the spatial vorticity distribution is also a significant property of the ring vortex. The majority of vorticity is contained in the central torus, reaching a maximum at the core centre and reducing rapidly, forming a Gaussian-esque distribution in both axial and radial directions (Figure 2.1). This vorticity then tends towards zero through the vortex atmosphere. Asymmetry in the cores has been observed, with its axial diameter larger than radial, giving a ‘squashed’ look, believed to result from the ring’s axial propagation [92].

## 2.2.2 Formation

The ring vortex’ common presence in nature implies a simple and robust formation process, resistant to natural perturbations. This has been confirmed through thorough investigation, and has been the subject of a number of papers, with an increased interest in the period of 1970-2005.

The typical formation mechanism of a ring vortex is the propulsion of a jet of fluid through a circular orifice into a larger volume of ambient fluid. As the slug is propelled,

peripheral fluid layers are decelerated by contact-friction with the wall, and bend outwards at the orifice exit plane (Figure 2.2c). As the propulsion continues, these layers bend further around on themselves, forming an axisymmetric spiral around the orifice edge (Figure 2.2d). Ambient fluid is entrained by convection as the spiralling core accumulates. At a later time, the ring will detach from the orifice exit plane by virtue of its circulation, the vortex atmosphere will fully enclose the toroidal flow and it will propagate along the axis of the original jet propulsion (Figure 2.2e). The dynamics of this resulting ring are directly controlled by the conditions by which it was generated.

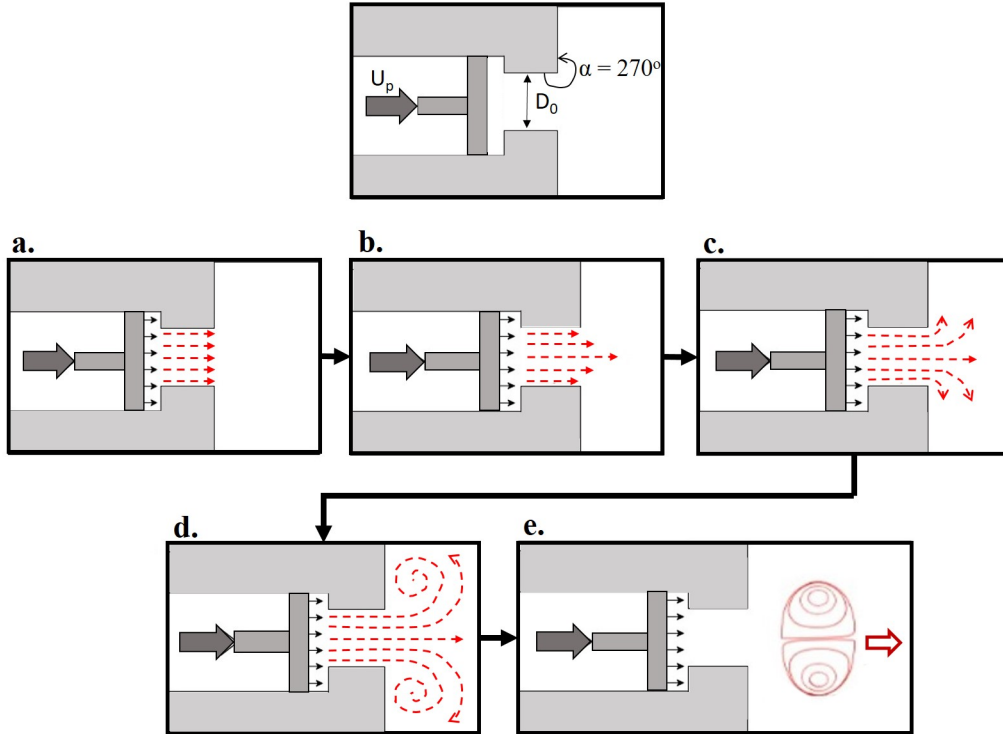


Figure 2.2: A schematic of ring vortex formation using the piston/orifice experimental setup. The first pane defines key parameters for ring vortex generation. Panes (a)-(b) presents the propulsion of a slug of fluid through a circular orifice, forming a jet. Pane (c) demonstrates the bending of peripheral fluid layers due to friction, causing the accumulation of a vortical core in pane (d). Pane (e) then presents the formed ring vortex propagating away from the orifice. All panes represent a ‘slice’ across a circular orifice and piston, axisymmetric around the horizontal central axis.

Assuming a piston/orifice setup as presented in Figure 2.2, the primary generating conditions are orifice diameter  $D_o$ , piston displacement  $D_p$ , piston velocity profile (characterised often by the running mean  $U_p = \frac{1}{t} \int_0^t U_p dt$ ) and turning angle  $\alpha$  (set as  $270^\circ$  in Figure 2.2). Further parameters can be derived from these, including jet length  $L$ , initial circulation  $\Gamma_0$ , stroke length  $L/D$ , and Reynolds Number  $Re = \frac{U_p D_o}{\nu}$ . A thorough understanding of these parameters and sensitive tuning of experimental equipment allows the

user to control the ring vortex, dictating properties to a significant degree.

Two partial analytical models are acknowledged for vortex ring formation: ‘Slug Model’ and ‘Self-similar Roll-up’. The former is based on the assumption that the velocity profile across the orifice exit plane is constant and equal to the piston velocity [93]. This model is used to approximate initial ring circulation and, despite being proven to underestimate final circulation values [94], is applied as a simple base mechanism for models, as its relative circulation values are correct, if not absolute. The self-similar roll-up model was proposed by Pullin [95], expanding the results of Saffman [96] who modelled an axisymmetric system from an impulsive jet. Pullin applied this to tube and orifice geometries as presented above, leading to core size and circulation expressions. More recent work in modelling formation uses this as their basis [97],[98]. The challenges of generation mechanics are widely recognised and significant, contrasting with the comparatively straightforward stable ring propagation, which is discussed in the next section and the primary focus of this thesis. Direct consideration of generation mechanics is limited in this thesis, however the slug model is employed for preliminary energetics calculations.

### 2.2.3 Evolution

Once formed, the ring vortex enters the post-formation stage which dominates most of its lifetime. Throughout this stage, the ring evolves, giving rise to a number of mechanisms which impact its dynamics. There are two groups of ring vortex - those which are turbulent from their formation and those which start laminar and later become turbulent, quantified by Reynold’s Number and stroke ratio. This section will concentrate on the evolution of the latter type (although a brief description of the former is included in Section 2.2.4). Initially laminar post-formation vortices undergo three stages: *laminar*, *transition* and *turbulent*.

#### Laminar Stage

Immediately post-generation, the ring enters its laminar stage, where the forming cores have settled into a coherent, Gaussian-like vortical structure with an elliptical meridional cross section and fully enclosed vortex atmosphere. This ring is readily characterised by the parameters discussed in Section 2.2.1 (circulation, ring radius, core radius, ring speed and volume), with an axisymmetric central torus. The ring is propelled by self-induced velocity borne of the core’s circulation. An important mechanism present throughout the ring journey is diffusive entrainment - the constant entrainment of ambient fluid into the circulatory ring system as it travels. First investigated by Maxworthy in 1972, this mechanism was postulated to be a result of vorticity exceeding the boundary set by the bubble streamline. Ambient fluid is contaminated by this vorticity and either entrained into the vortex atmosphere, or convected past the ring to form a gently vortical wake [99]. This mechanism underpins observations long made about ring vortices - they get progressively larger and slower as they evolve, a result of sharing momentum with an increasingly larger mass of fluid [100].

Maxworthy also proposed a number of scaling power laws to describe the rings' spatiotemporal evolution ( $\Gamma \sim t^{-\frac{2}{3}}$ ,  $V_{trans} \sim t^{-1}$ ) [101], which was the first of a number of papers investigating the entrainment mechanism. This mechanism has been confirmed, with an approximate [1:3] ratio of [entrained:jet] fluid identified [102]. Maxworthy's scaling laws have been disputed although further analysis has proved their validity [92]. It was predicted here that thicker core rings (large ratio between core and ring radius) would entrain fluid faster, due to a larger 'contamination zone' outside of the bubble. This was later confirmed by Archer et al. in 2008 using computational simulations [103].

The ring evolves constantly throughout its journey, yet the slow diffusive entrainment allows for bulk ring vortex properties to remain relatively stable over an appreciable path-length. Core and ring radii have been observed to remain constant within 10% for a simulated ring [103], with clear, concentric and quasi-elliptical streamlines observed over the simulation time. Some varied stability has been observed experimentally also [104], further highlighting the efficient mass-transfer and therefore the ring's inherent stability and reproducibility under certain conditions. This reported stability is a central motivation for the ring vortex' proposal as an imaging phantom flow.

### **Transitional Stage**

The laminar regime could theoretically continue until the ring collides with a wall or has insufficient energy to propel its augmented volume. However, an underlying mechanism disrupts the motion as the ring propagates. A number of small standing waves form around the circumference of the ring, arising from elliptical instability. These are well-observed in the literature, often described as 'azimuthal waves at 45° to the ring propagation' [93],[86]. These are linear, however as they grow they interact non-linearly, forming constructive superpositions and enlarging. This is characterised by an alternating 'flex' on the core, where a 'flower-like' shape can be observed head-on (See Figure 2.3).

Simultaneously the outer core arc distorts in the opposite direction, rolling up to form a secondary, looping vortical structure around the central core. This structure pierces the bubble surface and sheds small hairpin vortices into the ring wake. By definition the transitional period represents the entire stage from standing waves becoming larger (visible to the naked eye) to intermittent hairpin vortex shedding [103],[86]. A schematic of the stages is presented in Figure 2.3.

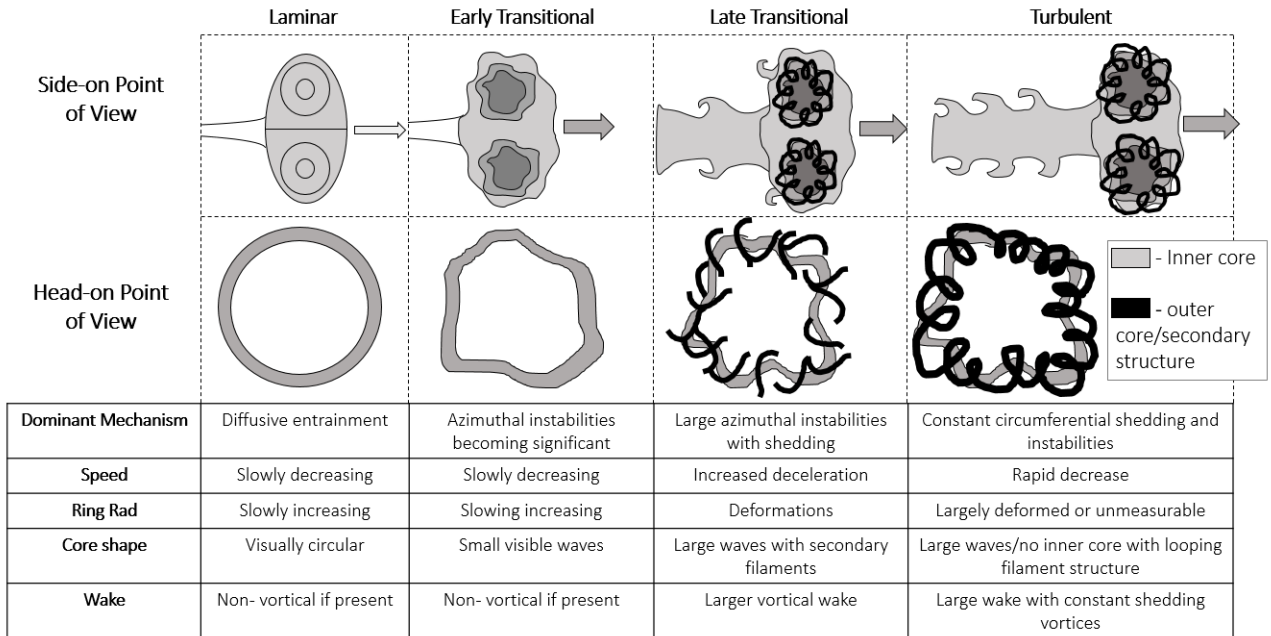


Figure 2.3: A schematic presenting the stages of initially-laminar ring vortices, with laminar, transitional and turbulent stages listed. Key properties of the ring in each regime is included.

### Turbulent Stage

The transition stage eventually develops into the final, turbulent stage when hairpin vortices are being shed from the entire ring core circumference [103]. The ring here loses energy rapidly and in unpredictable amounts, localized turbulence is observed at the core centre, and the ring is no longer characterised by the straightforward parameters of the laminar ring vortex. Interestingly, thin vortex rings retain their inner core. Although deformed, it is present and weaves between the secondary filament structures. Thick core vortices lose their inner core and are comprised fully of the looping, unpredictable secondary structure [93].

### 2.2.4 Turbulent Rings

A second genre of rings are those which are turbulent from their conception due to their generating conditions. This occurs when too much circulation accumulates during formation for it to be contained relative to the ring size. This requires a stroke ratio of  $L/D > \approx 4$  known as ‘formation time’ [105], which has been confirmed through further experimental and theoretical studies [106],[107]. Evidence for this relation include a trailing jet of vortical fluid for larger vortex rings ( $L/D > 4$ ) whereas smaller stroke ratio rings showed all jet fluid being entrained into the forming ring with minimal wake [105]. The high stroke ratio rings shed vortical structures (Figure 2.4), attempting to reach an optimal circulation-to-ring size balance.

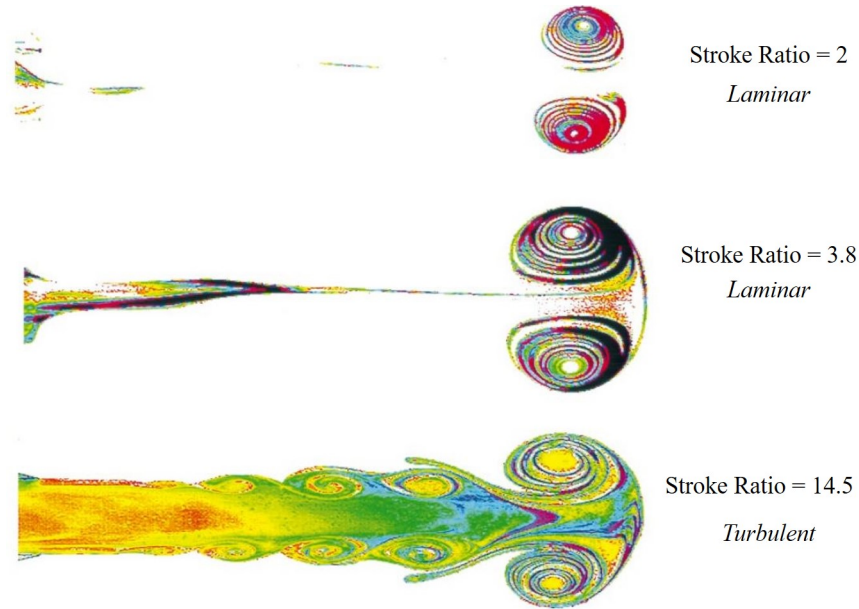


Figure 2.4: Digital Particle Imaging Velocimetry visualisations of the ring vortex at stroke ratios of 2, 3.8, and 14.5 respectively. Laminar and turbulent ring vortex behaviour is visible. Image from [105]

Vortex shedding and turbulence are fundamentally unpredictable flow characteristics over which a user generating the flow has little control. The use of turbulent vortices as a phantom flow is therefore not recommended, as they lack the stability, controllability, predictability and reproducibility required for a phantom. The description of these vortices is included for completeness.

### 2.2.5 Intracardiac Vortices

As discussed, the ring vortex is present in a plethora of natural environments, and this includes cardiovascular flow. Ring vortices are generated in intracardiac flow as blood is expelled through the mitral valve from the left atrium to left ventricle (Figure 2.5) and are commonly known as transmitral vortices (TM vortices). This is a long-observed physiological feature, with *in-vitro* valve models generating vortices in the 1980s [108],[109] followed by *in-vivo* imaging using Doppler echocardiography in 1994 [110].

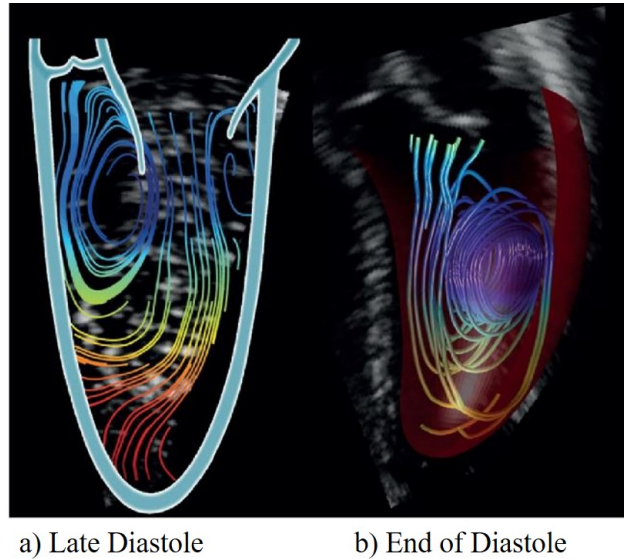


Figure 2.5: Ultrasound Echo-PIV images of the intracardiac ring vortex, in late diastole and onset systole. Image from [111]

The TM vortex has been observed to be asymmetric [112], likely a result of the asymmetric valve. The anterior cusp is larger than the posterior, causing an imbalanced accumulation of circulation during the formation process. Falahatpisheh et al. demonstrated that the anterior leaflet improves axisymmetry [113] however its form is still complex from interactions with intra-ventricular structures and its constrained nature.

The vortex' presence in the ventricle is more than just a notable haemodynamic structure, with potential application in diagnostic and monitory processes in the clinical environment. The vortex' strong reliance on its formation infers that a minor change to generating condition (e.g. valve size, input flow rate) will significantly impact the resulting vortex. As a result, a number of studies have explored connection between TM vortex dynamics and cardiac health. Notably, Töger et al were the first to quantitatively assess TM vortex volume, comparing healthy participants to those with dilated ischaemic cardiomyopathy [114]. It was found that 'healthy' TM vortices contained 50% of the ventricular fluid volume, whilst 'abnormal' vortices contained only 21%. Healthy vortices were close to the internal ventricular wall whilst pathological vortices were clearly separate [114]. This work was extended in 2016 to a proposal that cardiac size and form is tuned to optimal vortex function. Healthy vortices exhibit a consistent wall-vortex boundary distance, whilst abnormal vortices are variable [115].

The role and usefulness of the TM vortex is yet to be fully explored, but is under review in clinical fields and promotes interest in diagnostic imaging. Properties which commend the ring vortex as a candidate for an imaging phantom (i.e. reliable generation, unambiguous characterisation, clear visualisation) make it a useful point of interest for characterising the complexities of cardiac flow. Analysis of its dynamics has been useful for investigating post procedural complications for TM valve replacement [116] and the effect of diastolic dysfunction [117], both a result of subtly altered generating

conditions causing a clear effect on the vortex. This sub-field reflects the importance of flow imaging over traditional anatomical imaging: imaging and quantifying myocardial tissue is complex, yet characterising the ring vortex could be more straightforward, detecting pathological abnormalities and influencing patient management through flow analysis.

### 2.2.6 Discussion - The Ring Vortex as a Phantom Reference Flow

The ring vortex is clearly a unique phenomenon with a multitude of characteristics not necessarily found in other flows. There are a number of behaviours which specifically indicate its potential as a reference flow for quantitative flow imaging techniques:

- **Distinct Characterisation** - The ring vortex has a clear structure, with dimensions (ring and core radii), circulation, atmosphere size, intra-ring velocities and ring speed which can be readily measured. The flow field can be characterised using these micro- and macro- properties.
- **Simple Generation Mechanism** - With the only requirement for its formation being a propelled slug of fluid through a circular orifice, the ring vortex can be generated in a laboratory environment in a safe and cost-effective manner.
- **Evolution** - When in the laminar regime, the ring vortex retains similar ring radius, core radius and circulation to within tight bounds over an appreciable path length, allowing for repeated imaging of the same flow.
- **Complexity** - Recirculating fluid, finite vortices and even eddies are present in this flow, mimicking aspects of cardiovascular flow.
- **Physiological Relevance** - This is a flow that has physiological relevance and can change as a result of pathology. As a reference flow it has characteristics that are encountered by quantitative flow imaging techniques.

Despite these qualities, there are complications. For example, at the transitional stage the rings have an increasingly deformed central torus (reducing confident characterisation) and shed vortices at an increasing frequency. This mechanism is unpredictable and non-reproducible, given the errant nature of vortex shedding. The energy/circulation loss is also accelerated here, thus the ring will become increasingly unstable with uncertain evolution. This comment is valid also for turbulent rings, therefore only rings in their laminar stages are suitable for phantom flow - here the axisymmetric assumption is correct and minimal energy loss is present, along with characterisation through the primary parameters.

Within this laminar stage, the exact stabilities and reproducibilities of the ring vortices isn't well-defined in the literature, and requires investigation. The level of stability and reproducibility that the ring vortex can attain will influence its suitability and declared dynamics for any commercial ring vortex imaging phantom. These declarations will be explored throughout this project.

## 2.3 The Ring Vortex Phantom - Historical Context

With the ring vortex identified as a suitable candidate [118] for a complex flow phantom, a prototype device was built (designated **Unit-0**). Designed, manufactured and tested in a project between 2015-2019 in a collaboration between University of Sheffield and Leeds Test Objects, the Unit-0 ring vortex phantom generates ring vortices in a cost-effective, portable and simple setup, suitable for laboratory or clinical environments. Previous project outcomes will be detailed in this section, before continuing to the original work of this thesis in Section 2.4.

### 2.3.1 Technical Specification

The phantom prototype is a relatively simple device, generating ring vortices in an ultrasound- and CT-compatible setup. It is comprised of Perspex infrastructure (Water tank, cylinder, piston and base), a motor, attached electronics and is controlled by a laptop. (See Figure 2.6) The specifications of each component will be described in this section.

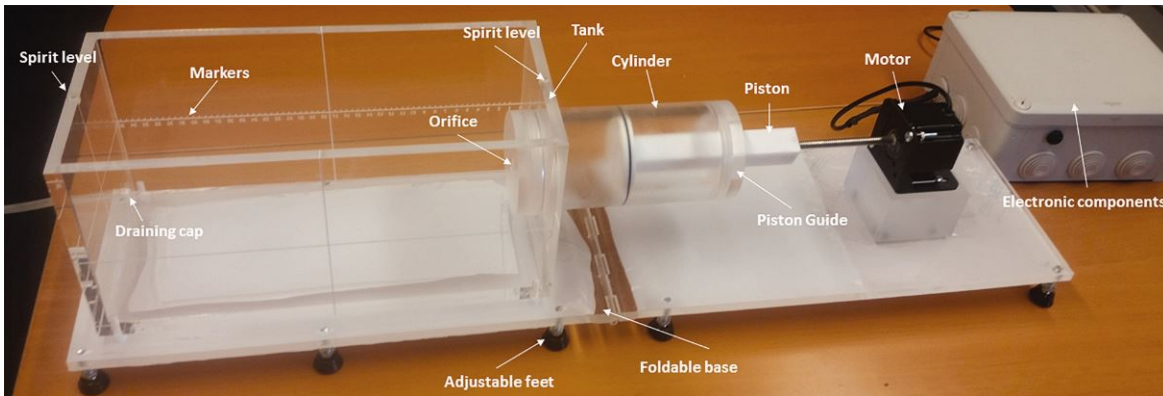


Figure 2.6: Photograph of the assembled Unit-0 ring vortex phantom in 2019 with components annotated for clarity. Image is from [119]

### Motor

The first, and arguably most important, phantom component is the motor. A NEMA-23 bipolar linear stepper motor is adopted in this device, with an attached lead screw of 150mm(L)x8mm(D) threaded along its length (TR8X8 threads). Stepper motors are used regularly for high-precision work such as robotics and 3D printing, due to their ability to power on/off quickly and provide accurate motion over small displacements. A toothed electromagnet rotates in the centre of the motor, surrounded by a stator magnet and coils of alternating phase. The phantom motor is specifically a ‘bipolar’ stepper motor which alternates the coil phases, so is able to use every coil when turning. The lead screw is used in tandem with a threaded nut, which when held at one orientation (for example by a piston), will convert the screw’s rotation to linear propulsion. The piston is threaded

onto the lead screw and is thus translated by the lead screw’s rotation. The motor is 3A and 36V (i.e.  $\sim 100\text{W}$ ), and propels the piston upon command to generate the vortices.

A linear stepper motor moves in discrete ‘steps’ - programmed to rotate its lead screw over a user-determined number of steps with a set time delay between each. For this motor, each step rotates the lead screw over  $1.8^\circ$ , and a full rotation (200 steps) will result in a forward propagation of 8mm of the threaded nut, thus each step will move the piston over 0.04mm. This forward motion is a function of the threading pitch. As detailed in Figure 2.7, the specified time delay will influence the average piston speed, thus allowing control of the piston displacement (through number of steps ‘SetDisplacement’) and speed (through delay time - ‘SetSpeed’). A standard displacement of 0.8mm (40 steps) has been historically used for ring vortex generation in this phantom. Implementing an inter-step time delay of 500ms results in an average programmed speed of 2cm/s.

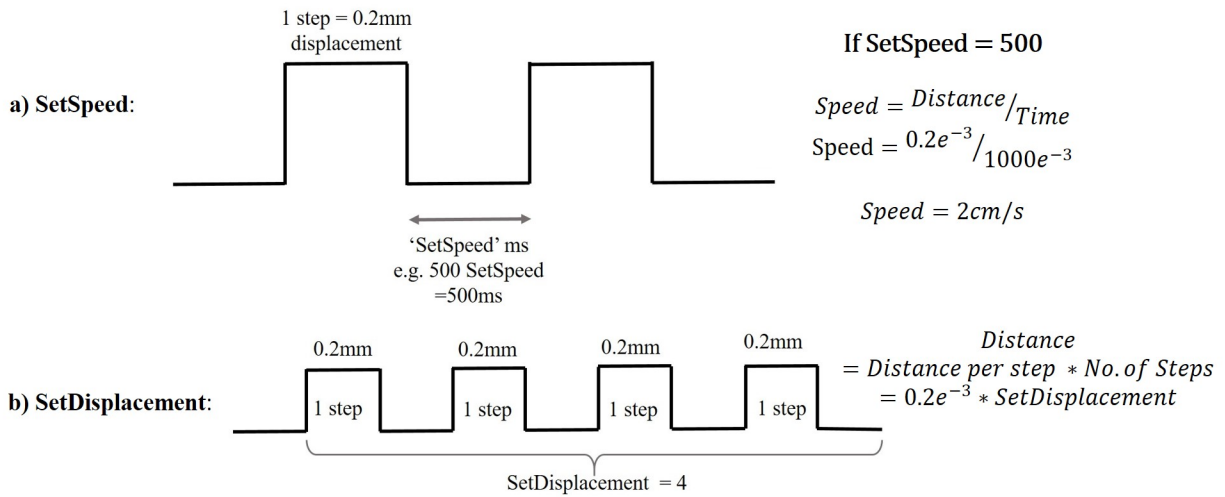


Figure 2.7: A schematic presenting the square wave mode of bipolar linear motor motion. The *SetDisplacement* and *SetSpeed* variables are annotated, with the calculations used to determine average piston speed and displacement.

The motor is controlled by a DM542 stepper driver, which restricts the current supplied to the actuator. The driver is set to limit the current supply to 2.69A to avoid overheating and can be configured to introduce ‘half-stepping’ or ‘quarter-stepping’, where only fractions of steps will take place rather than full. Throughout this project full stepping was, as it allows for faster propulsion.

## Electronic Setup

The driver and motor are controlled by an Arduino Uno board, a component which permits the receiving and conveying of instructions and data. The ATmega382P controller in the Uno board generates a digital square wave of amplitude 5V, which is sent to the driver and subsequently converted into the required square wave pulse for the motor. Four digital pins connect the Uno board to the driver: 9,10,11 and 12, which enable, disable, control

direction and move the motor respectively. A power supply is used to power the driver (specs of 150W, 36V, 4.17A). All electrical components are housed in a closed box and located more than 30cm from the water tank to minimise risk of water contact. The power supply is connected to 230V, 50Hz mains via a standard UK three-pin plug and a residual-current device (RCD). The RCD is a widely used component which will break the circuit if any current loss is detected. This component was recommended for use in routine testing due to the proximity of the open water tank to the electronics.

### **Perspex Infrastructure**

The physical structure of the phantom is CNC-machined Perspex, comprising a base, water tank, hollow piston cylinder, piston, piston guide and orifice plates (See Figures 2.1, 2.8). The phantom sits on a PMMA base mounted on adjustable threaded feet, ensuring that it can be levelled flat on any surface. This base is hinged at its centre to enable space-efficient packaging, with the hinge reinforced with a Perspex plate when in use to eliminate bending under stress of motor operation. The feet elevate the base to 20mm above the table/surface, with the base at a thickness of 20mm. The motor is attached via screws at one end onto a solid Perspex block permanently attached to the base. An open-topped water tank is also present, comprising the majority of the device body. The tank measures 175(H)x170(W)x370(L)mm externally with 10mm thick walls, allowing for an appreciable path-length for the ring vortex and large enough to avoid boundary effects from the walls and floor. The tank is open-topped to enable easy filling and for imaging probes to be inserted into the fluid. Perspex was selected as the primary material for its robustness, wide availability, X-ray attenuation similar to soft tissue and transparency, allowing for optical measurements through the walls or base. These measurements are visualised in Figure 2.8.

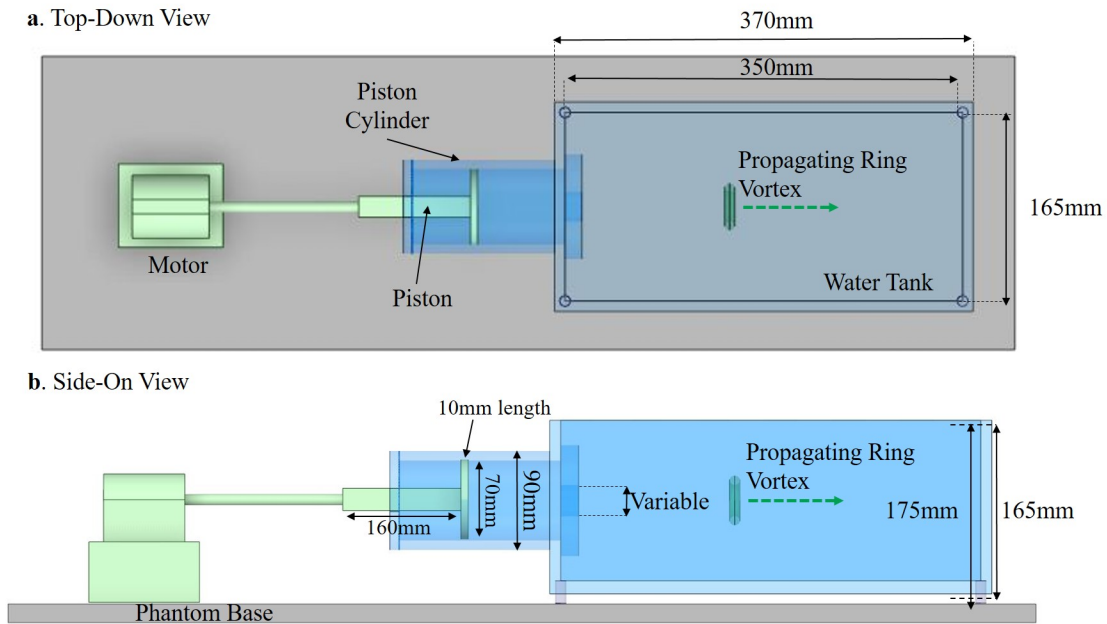


Figure 2.8: A schematic of the ring vortex phantom with measurements of each machined component.

A threaded 70mm-diameter hole is cut into the tank on one end, into which the piston cylinder is inserted. This piston cylinder is 145mm long with an external diameter of 90mm and 10mm thick walls. Both ends are threaded, with the tank-end long enough to extrude 1cm into the tank when attached. A plate of diameter 90mm is screwed onto this extrusion until flush with the tank wall. Four orifice plates were manufactured, with a cut-out hole with diameters of 10mm, 15mm, 20mm and 25mm respectively, accurate to within  $\pm 0.25$ mm. Orifice sizes were selected for analogy to physiological vessel size (the ascending aorta has a diameter of approximately 2.1cm). It is through the orifice plate that the ring vortex is generated.

A piston is inserted into the piston cylinder, with the stem threaded onto the motor lead screw via an embedded threaded nut and the piston head facing the tank. The 10mm-long piston head is flush with the cylinder's interior wall, and a nitrile O-ring is embedded in its circumference to eliminate water leakage past the piston. A threaded plate on the cylinder rear-end has a square cut-out around the piston stem with 1mm spacing, designed to avoid piston rotation. Once assembled, the phantom takes up a space of 900x200mm on a table or scanner bed. This size ensures any standard table or scanner bed can be used to support the phantom. A custom-made case is supplied for the components, which can be easily transported via inbuilt wheels, improving the prototype accessibility.

## Control Code

The phantom is controlled by an Arduino IDE algorithm, written in C++. This is a simple program which sends a set number of pulses ('steps') to the motor to push the piston. As discussed above, the number of pulses corresponds to the piston displacement, and the time between pulses relates to the average piston speed. Thus, the user can control the variables via code, changing the number of rings generated, the time delay between them, the piston displacement and its average speed. 'Top-hat' velocity profiles are used, with only one speed requested from the motor per profile. The control code is presented below.

```

int pulPin = 9; int dirPin = 10; int enbIPin = 11; int buttonPin = 7;
int revolution = 0;
int buttonState = 0;
int StepDisplacement = 30;
int HowManyRings = 10;
int SetSpeed = 500;
void setup() {
  pinMode(pulPin, OUTPUT); pinMode(dirPin, OUTPUT);pinMode(enbIPin, OUTPUT); pinMode(buttonPin, INPUT); digitalWrite(enbIPin, LOW);
  delayMicroseconds(6); digitalWrite(dirPin, HIGH); delayMicroseconds(6);
  digitalWrite(pulPin, LOW); delay(1000); digitalWrite(enbIPin, HIGH);}
void loop() {buttonState = digitalRead(buttonPin); if (buttonState == HIGH){
  delay(10); while (revolution < HowManyRings) {
    digitalWrite(enbIPin, HIGH);
    delay (20000);
    digitalWrite(enbIPin, LOW);
    delayMicroseconds(6);
    digitalWrite(dirPin, LOW);
    delayMicroseconds(6);
    digitalWrite(pulPin, LOW);
    delay (2000);
    for (int i = 0; i <= StepDisplacement; i++) {
      digitalWrite(pulPin, HIGH);
      delayMicroseconds (SetSpeed);
      digitalWrite(pulPin, LOW);
      delayMicroseconds(SetSpeed);}
    revolution++;}
  digitalWrite(enbIPin, HIGH); }

```

Identify Pins

Piston Displacement per impulse

How many rings to generate

Piston Speed

Initialise – requirements from driver datasheet

Detect button push

20 second delay between rings

Generate square wave as seen in Figure 2.7.

Figure 2.9: Arduino Code used to control the ring vortex phantom. Comments are in red on significant points.

### 2.3.2 Phantom Workflow and Vortices

Performing an experiment using the phantom involves a particular protocol. Setup of the phantom requires its assembly as presented in Figure 2.8, then the water tank is filled with water (distilled or tap water), and air removed from the piston cylinder via syringe. A neutrally buoyant liquid colourant is injected into the piston cylinder using a syringe to generate visible coloured rings. The code is then verified and uploaded to the motor on the attached laptop. A push button is pressed and the code initialised, starting the 25

second countdown to the first ring. Once the first ring is generated the timer resets, and the remaining rings are generated at set intervals. The rings propagate across the tank at a steady speed and are visible by virtue of the liquid colourant in the piston chamber. The overall process is summarised in Figure 2.10, including the set up and use of a camera to record the rings and analyse their behaviour (an optional step).

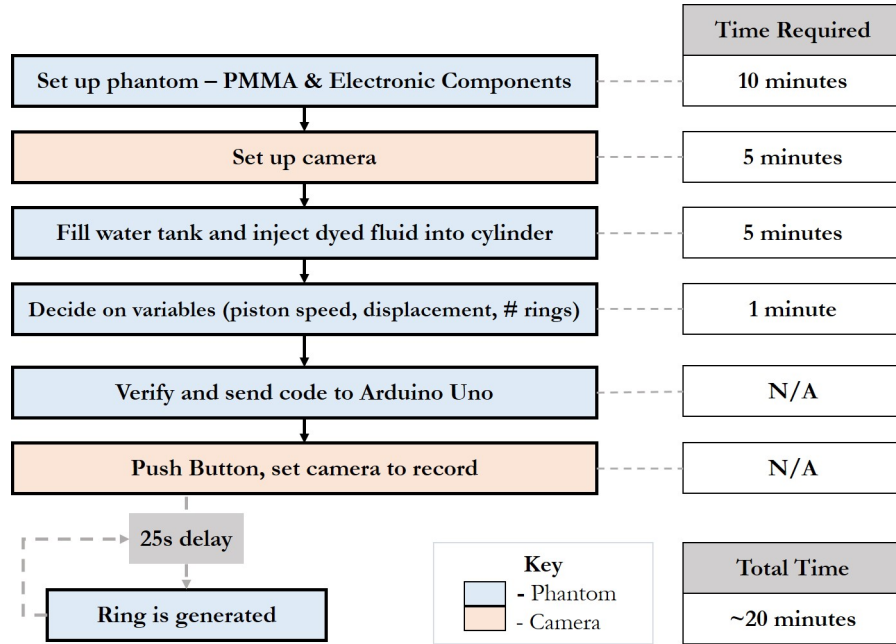


Figure 2.10: A flowchart of the setup of the ring vortex phantom for experiments.

### 2.3.3 Flow-Field Visualisation

A key validation experiment which took place during previous work was a Laser Particle Imaging Velocimetry (Laser-PIV) exercise. This was performed to enable visualisation of the rings' behaviour at sub-mm scale. With ring dimensions approximately 1cm(W)x2cm(H) this permits understanding of how the rings work beyond the naked eye. An Nd:YAG double-pulse laser was placed below the tank, projecting a vertical laser sheet aligned to the central axis along which the ring travels (Figure 2.11). Nylon particles of diameter 10-20microns were seeded into the piston cylinder and water tank, scattering the laser beam for camera detection. As the ring propagated through the tank, the laser was pulsed twice and the particles were tracked between the two pulses using stereoscopic cameras to calculate velocity in 3-dimensions. Appropriate post-processing computed velocity vectors from the recorded scatterer motion. This created a 2-D vector flow field of the cross section of the ring which could be used for analysis of streamlines, vorticity and velocity components and from which basic ring properties could be measured. (Figure 2.12). This was repeated a number of times at 14Hz as the rings travelled across the tank.

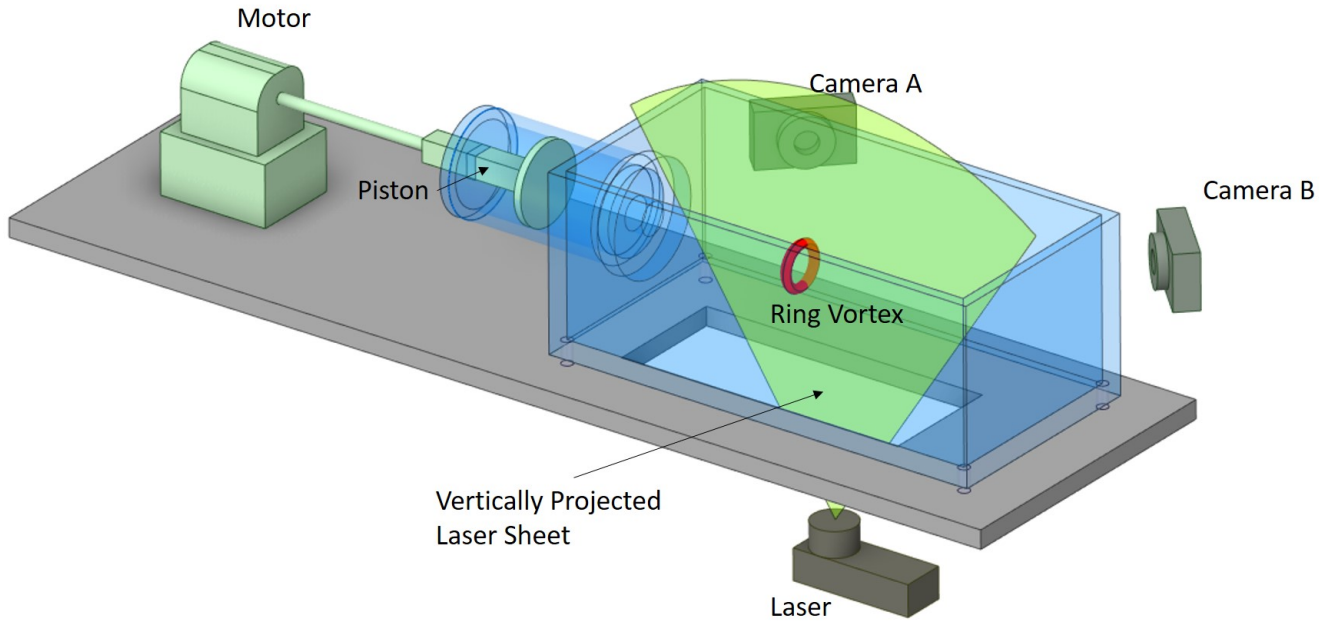


Figure 2.11: A schematic of the ring vortex phantom when being imaged by Laser PIV. The phantom, laser, laser plane and stereoscopic cameras are depicted.

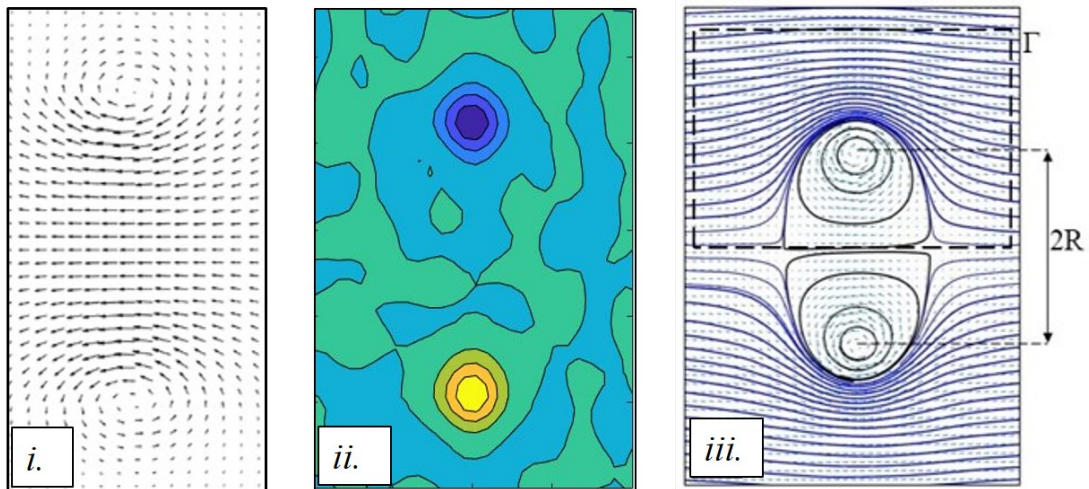


Figure 2.12: Example Laser-PIV dataset for the ring vortex phantom. (i) shows the raw velocity vector plot, (ii) the filled vorticity contours, (iii) the streamlines in the ring's reference frame.

Table 2.1 illustrates a number of configurations selected for this experiment, designed to image rings over a range of speeds. These generating configurations were chosen specif-

ically to lie within the motor’s ability (both in piston displacement and speed).

| Config | Orifice Diameter | Programmed Piston Speed | Piston Displacement | Stroke Ratio |
|--------|------------------|-------------------------|---------------------|--------------|
| 1      | 10mm             | 2cm/s                   | 0.8mm               | 3.92         |
| 2      | 10mm             | 1.33cm/s                | 0.8mm               | 3.92         |
| 3      | 15mm             | 2cm/s                   | 0.8mm               | 1.16         |
| 4      | 15mm             | 1.33cm/s                | 0.8mm               | 1.16         |
| 5      | 20mm             | 2cm/s                   | 0.8mm               | 0.49         |
| 6      | 20mm             | 1.33cm/s                | 0.8mm               | 0.49         |
| 7      | 25mm             | 2cm/s                   | 0.8mm               | 0.25         |

Table 2.1: Generating configurations historically used with the ring vortex phantom.

### 2.3.4 Project Outcomes

The primary outcomes of the previous project were the design and manufacture of the phantom (Unit-0 version) which has been outlined in this section. A number of experiments took place, with the Laser-PIV experiment producing extensive data. Limited analysis was performed on the Laser-PIV datasets due to time constraints, with a focus on the reproducibility of bulk parameters. To this end, the following quantitative conclusions were obtained regarding flow behaviour.

1. Configurations 1-5 varied by less than +/-10% in speed at 5cm from the orifice, showing high initial reproducibility. Configurations 6,7 varied by a higher proportion.
2. The reproducibility of the rings’ entire lifetime was assessed. For a particular position with respect to time, the maximum variability for Configurations 1-7 was recorded as +/-10%.
3. The device robustness was proven, with a repeat experiment conducted before and after an intensive 8-hour experiment generating over 100 rings. Comparison of the two datasets demonstrated a maximum deviation of 5%.

Overall this exercise demonstrated the potential of this proof-of-concept device, with Configurations 1-6 identified as rings with satisfactory dynamics at the macro-level and reproducible speeds. Stability was not explicitly measured and Laser-PIV analysis was restricted to macro measurements of the vortex translational velocity. Further experiments took place to explore the validity of the phantom, with the main outcomes listed below.

- An MRI-compatible proof-of-concept prototype was manufactured, and was observed to generate a ring vortex. Visually this ring was distorted and non-reproducible, and no quantitative measurements were taken

- Quality of phantom performance was explored and instrumentation was tested for their ability to read basic ring properties in real-time.

Overall, the previous work achieved significant advances in designing and manufacturing the ring vortex phantom. Its well-considered design and construction has held up to intensive use over four further years with little evidence of wear-and-tear. This project continues the work through further device development, with a greater focus on the ring vortex flow behaviour. Specifically, characterisation of the phantom, optimisation of its use and expansion of its abilities will be described

## 2.4 Ring Vortex Phantom Unit-0 Micro-Analysis (Present Day)

At the commencement of this project, the phantom was working according to design specifications and generating rings consistent with the configurations defined in Table 2.1. The phantom's correct functionality, along with preliminary results from the Laser PIV experiments demonstrated that the phantom prototype as described has potential as an imaging phantom intended for clinical and research use. However, certain refinements were foreseen to consolidate its performance and expand its capabilities. This thesis strives to fulfil these refinements.

A key requirement for broader application is a thorough understanding of the ring vortex at a micro-scale. Comprehension of the micro-flow will (a) characterise the rings' internal dynamics, (b) clarify the reproducibility/stability tolerances of the phantom reference flow, (c) increase confidence for new users. Previous work limited analysis of the ring vortex to its bulk behaviour, viewing the ring vortex as a bulk translating object, whilst this work will remove ambiguity of the ring micro-behaviour for each imaged configuration. Analysis is performed in this section on the PIV datasets from the 2019 experiment. The objective was to determine the stability and reproducibility that this device/vortex flow could achieve, and to de-mystify ring mechanics. Reproducibility and stability of each property were the primary assessment criteria. In this context:

- **Reproducibility** refers to the capacity of the ring vortex phantom to consistently generate the same flow behaviour under a given set of generating conditions. It also refers to the capacity of each ring to follow an identical journey.
- **Stability** refers to the time period or propagation length over which a ring exhibits unchanging behaviour to within tolerances.

High reproducibility is desirable for a phantom reference flow to ensure uniformity between experiments and individual rings. High stability will enable repeat visualisation of the rings throughout their evolution with minimal variation in the flow. This chapter will explore the level to which the ring vortices can achieve these metrics. The reproducibility and stability will be calculated for key ring vortex properties: speed, ring radius, core radius, circulation and the full flow-field, before reviewing the results together.

### 2.4.1 Ring Speed

The ring vortex' translational speed is a key bulk characteristic which is impacted by ring energy and size thus is a useful immediate indicator of abnormal behaviour. For the rings to act as appropriate reference flows, their speeds must be reproducible and stable to within known tolerances. To calculate speed, the ring's axial position was manually located within each individual PIV frame. Displacement between subsequent frames was combined with the inter-frame time interval of  $1/14$ s to calculate the instantaneous speeds throughout the journey (Figure 2.13).

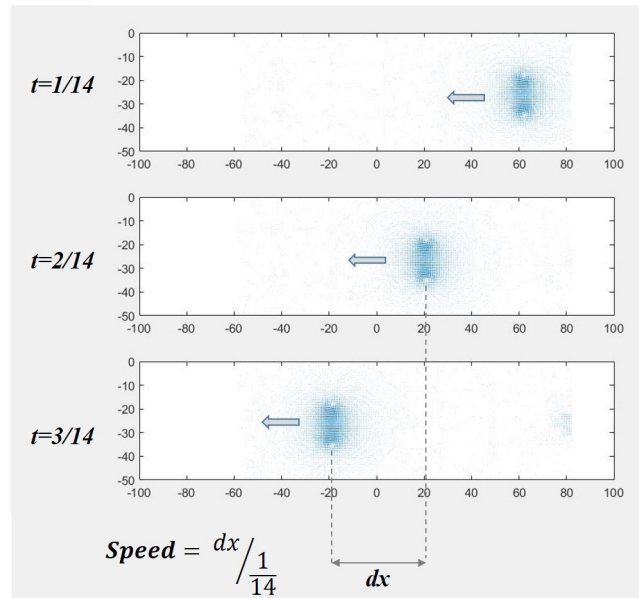


Figure 2.13: Diagram of the process of calculating instantaneous ring speed using PIV datasets. Axes are in millimetres and vectors in the stationary reference frame.

This was performed for each ring vortex across the seven configurations, with results plotted below.

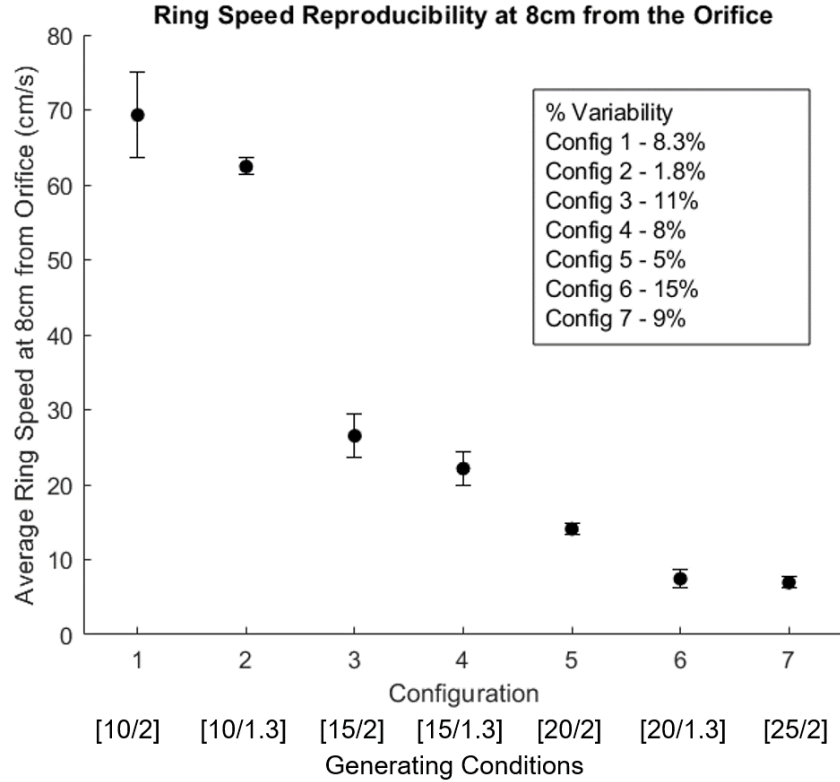


Figure 2.14: The average ring vortex speeds at 8cm from the orifice for configurations listed in Table 2.1. The x axis lists both configuration number according to Table 2.1, and the corresponding generating conditions in the format [Orifice Diameter(mm)/Piston Speed(cm/s)]. Error bars represent 1 standard deviation, and each datapoint represents the average of ten ring vortices.

Figure 2.14 presents the average speeds for the configurations at approximately 8cm from the orifice. Reproducibility is presented in the error bars and the annotated in-figure text, which lists the coefficient of variability ( $\frac{standard.dev}{mean} \times 100$ ) for each configuration. In this analysis, configurations 1,2,4,5,7 demonstrated variability under 10%. Error from discretisation is apparent here, as the values will be discretised according to the 0.72mm and 14Hz spatiotemporal resolutions achieved by the experiment.

Stability can also be measured from ring speed. As discussed in Chapter 1, rings decelerate throughout their journey due to their incrementally increasing volume and any vortical shedding. Stability was quantified here as the proportion of speed lost (relative to initial speed at 8cm from the orifice) over a given path-length. The progressive relative decrease in speed is plotted in Figure 2.15.

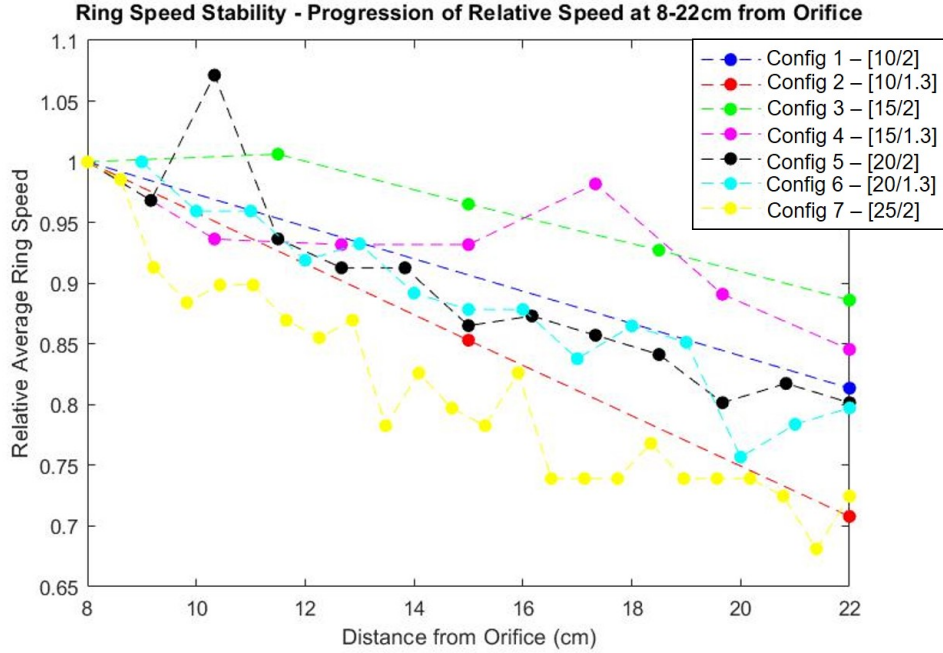


Figure 2.15: The average ring vortex speeds, relative to their starting speed, as the rings propagate over 8-22cm from the orifice. Datapoints represent the average of ten ring vortices. Errors are not shown for clarity but are cited in Figure 2.14, typically at 10%.

Figure 2.15 presents the evolution of ring speed for each configuration across the 8-22cm imaging domain with the origin at the orifice. Clearly complete stability (i.e. unchanging speed) is unrealistic with viscous effects, so even the most stable rings will lose some speed. Figure 2.15 demonstrates that configurations 2,7 decelerated the most, and configurations 3,4 were the most stable. To quantify stability, a metric was devised - *the percentage of speed retained over a path-length of 14cm, relative to its starting speed at 8cm from the orifice*, known as ‘14cm Stability’ hereafter. This allowed direct comparison between configurations. Following this definition, the 14cm-Stability values are listed below:

| Config | % of Speed lost over 14cm | 14cm-Speed Stability |
|--------|---------------------------|----------------------|
| 1      | $18.7 \pm 4.6\%$          | $81.3\% \pm 4.6\%$   |
| 2      | $29.3 \pm 8.8\%$          | $70.7\% \pm 8.8\%$   |
| 3      | $11.4 \pm 5.9\%$          | $88.6\% \pm 5.9\%$   |
| 4      | $15.5 \pm 4.6\%$          | $84.5\% \pm 4.6\%$   |
| 5      | $19.8 \pm 6.2\%$          | $80.2\% \pm 6.2\%$   |
| 6      | $20.3 \pm 10.0\%$         | $79.7\% \pm 10.0\%$  |
| 7      | $27.5 \pm 9.2\%$          | $72.5\% \pm 9.2\%$   |

Table 2.2: Table listing stability of speed for the Unit-0 ring vortex phantom. 14cm-Speed Stability = 100%-% of speed lost over 14cm path-length.

This analysis demonstrated the relatively high stability of the PIV-imaged ring vortices with respect to their speeds. A maximum loss of 30% over 14cm is observed, with most rings losing  $\sim 20\%$  over the distance. It is noteworthy that configurations 2,7 were the least stable.

### 2.4.2 Ring Diameter

Ring diameter was the second analysed characteristic, a property largely determined by the generating orifice size. This property was measured from 2019 PIV datasets as the distance between core centres, defined as locations of maximum absolute vorticity. The ring diameter was calculated for each imaged vortex, with the average values and variability plotted below.

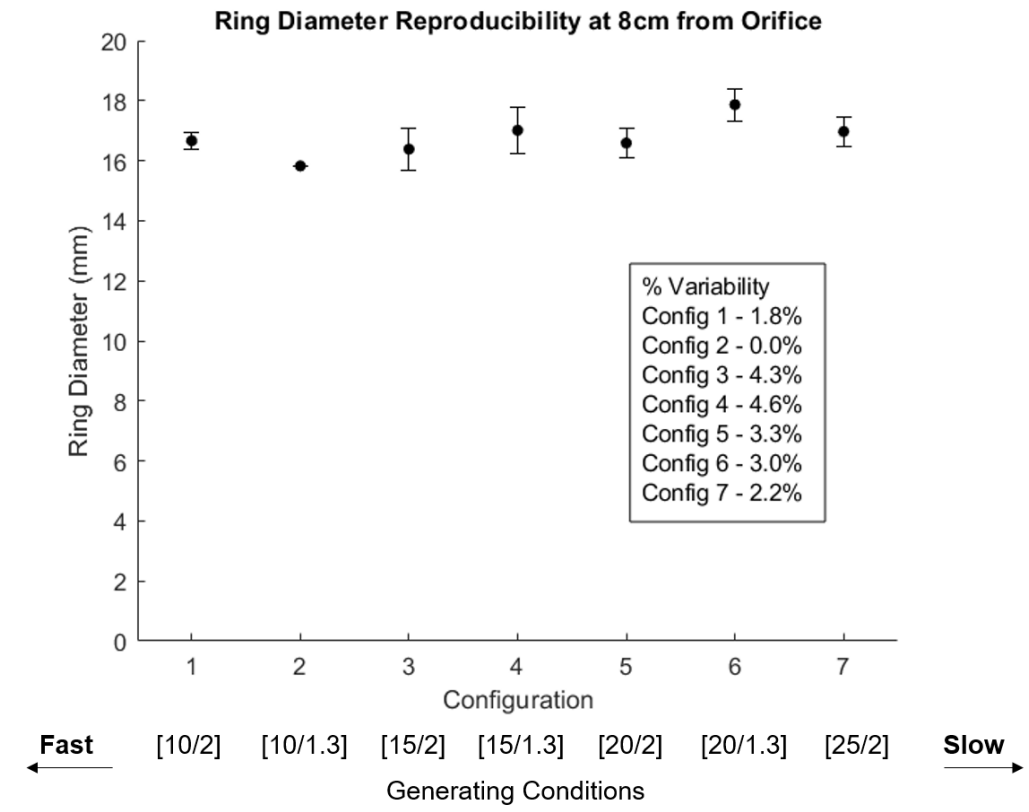


Figure 2.16: A graph presenting the average ring vortex diameter at 8cm from the orifice for the configurations listed in Table 2.1. Error bars represent 1 standard deviation, and each datapoint represents the average of ten ring vortices.

Figure 2.16 presents the reproducibility of ring diameter at 8cm from the orifice, plotted as the error bars and in the in-figure text. Each datapoint represents the mean of 10 vortices with error bars indicating 1SD. Reproducibility is high, with all configurations demonstrating variability of less than 5%. Measurement error of up to 5% is introduced in this analysis, due to PIV discretisation of 0.72mm.

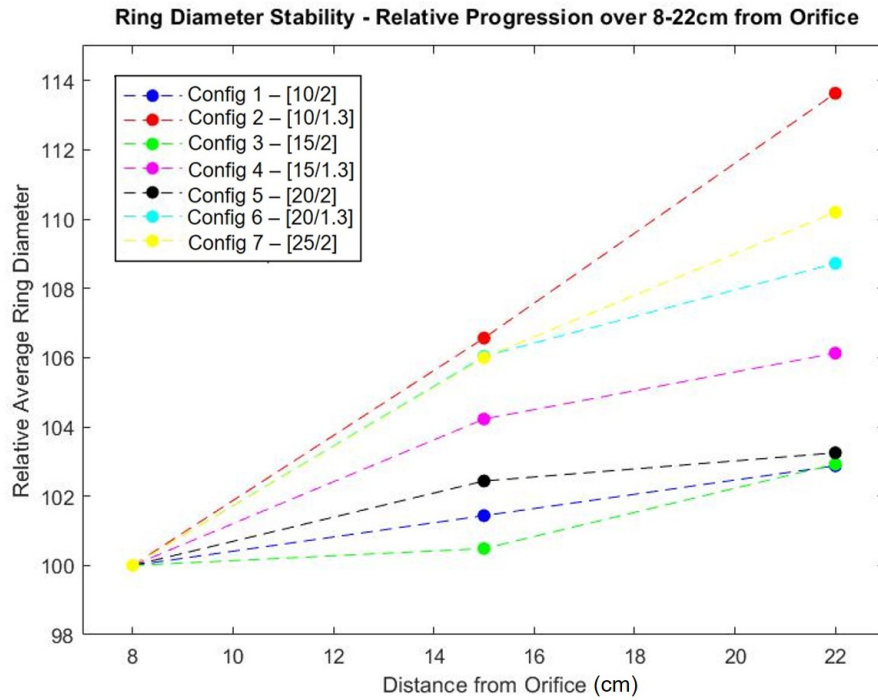


Figure 2.17: A graph presenting the evolution of ring diameter, relative to their values at 8cm from the orifice, across the PIV imaging domain. Error bars are not presented for clarity, but values typically vary by 5%, as listed in Figure 2.17.

Figure 2.17 presents the evolution of relative ring diameter over 8-22cm from the orifice, visualising the stability. Diameter increases over the journey for all configurations, which was expected from entrainment and historical observations [99]. Configurations 2,7 have the lowest stabilities, with values increasing by over 10%.

### 2.4.3 Core Diameter

Core diameter was also measured, defined as the distance between the maximum and minimal tangential velocities when measured across the core centre. Axial and radial measurements were averaged. Values are plotted below.

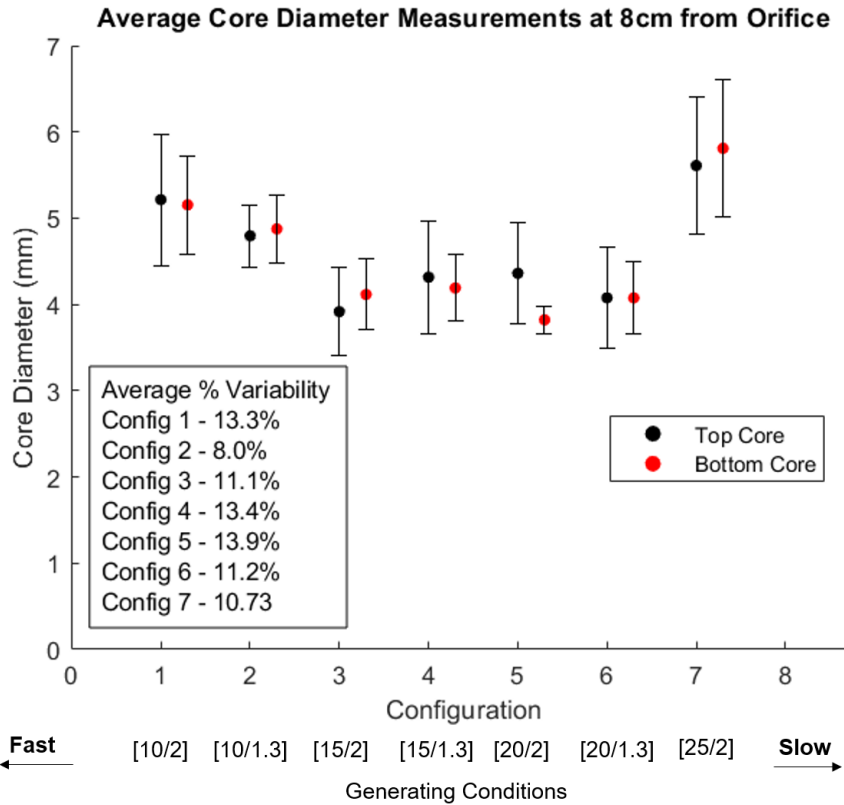


Figure 2.18: A graph presenting the average ring vortex core diameters at 8cm from the orifice. Error bars represent 1 standard deviation, and each datapoint represents the average of ten ring vortices.

Figure 2.18 presents the average core diameters for the configurations at 8cm from the orifice and their reproducibilities through the error bars and in-figure text. The values were seen to match between the two cores for configurations 1-4,7. Notably configuration 5 has a mismatch, with the bottom core exhibiting a smaller value and much higher reproducibility than the top core. This is a clear anomaly in the data. Reproducibility ranges from 8-14% CoV, notably higher than the 0-4.5% variation of ring diameter. A likely contributing factor is the PIV discretisation of 0.719mm, which is significant when working at the core length-scale, introducing an error of up to 20% from the true value.

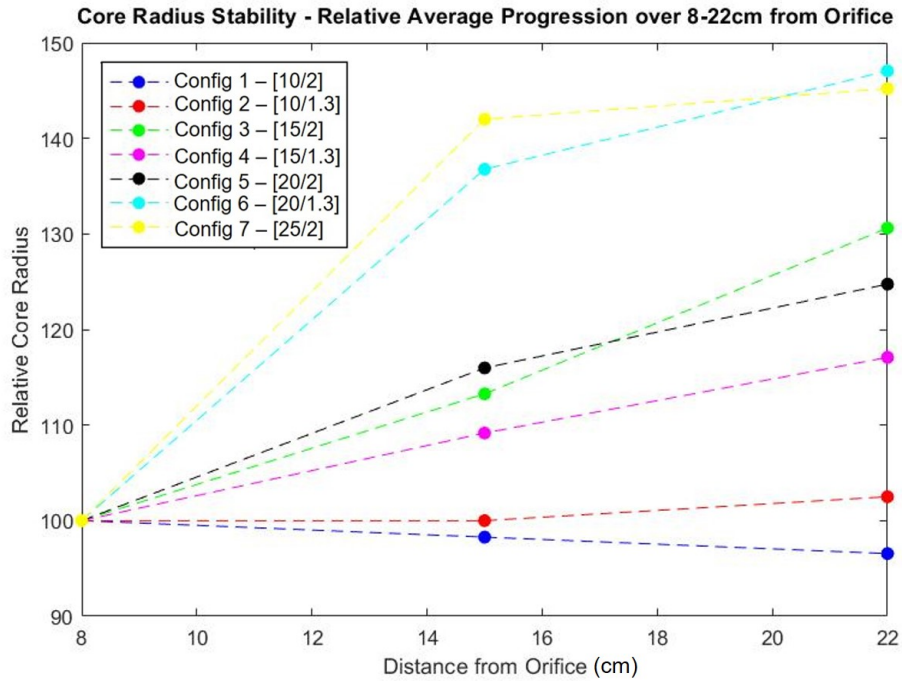


Figure 2.19: A graph presenting the evolution of core radius, relative to its starting value across the PIV imaging domain. Error bars are not presented for clarity but values typically vary by <15%, as listed in Figure 2.18

Figure 2.19 displays the relative evolution of average core diameter values, visualising this parameter’s stability. Similar to the ring diameter, most values increase as the rings propagate. A higher relative increase is evident, ranging from 5-48%, and configurations 6,7 are the least stable.

### 2.4.4 Circulation

The next property was circulation, a parameter used often to quantify vortex strength and defined as the line integral of velocity components around a closed loop. A domain of 18mm(H) x 22mm(W) was set for each ring, projecting radially from the central axis, and a line integral was performed around the perimeter (See Figure 2.20). This domain was chosen for its distance from the ring edge. Ring size varies slightly between configurations, but the large domain allows this path to be constant between rings without affecting the result. A variation of <1% was observed in the circulation value when slightly differing domains were tested between configurations.

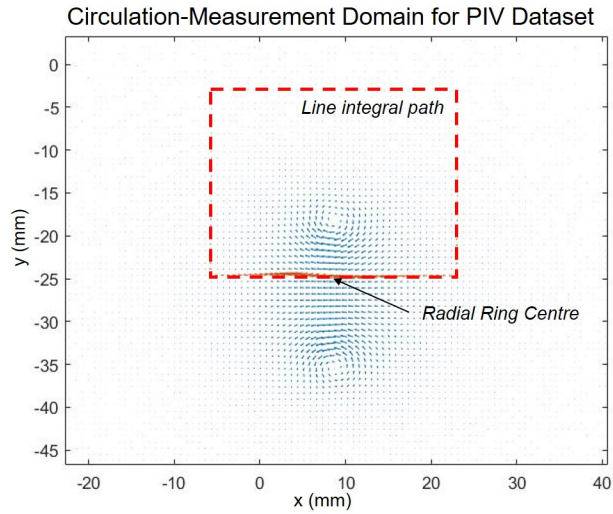


Figure 2.20: Example PIV dataset with the circulation-measurement domain annotated. The dashed red line represents the closed path around which the line integral is performed.

Values at 8-22cm from the orifice were calculated, with initial averaged circulation values plotted below.

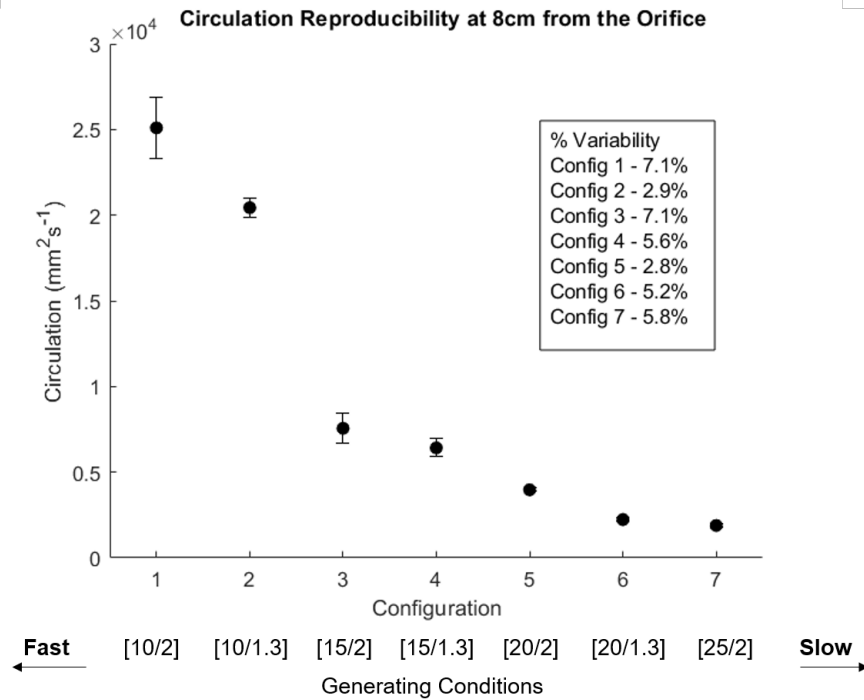


Figure 2.21: The average circulation values at 8cm from the orifice for configurations listed in Table 2.1. Error bars represent 1 standard deviation, and each datapoint represents the average of ten ring vortices.

Figure 2.21 displays the average circulation values at 8cm from the orifice. Reproducibility is plotted as the error bars (1SD) and in the in-figure text (CoV). High reproducibility is observed for all conditions, with variability of less than 10%.

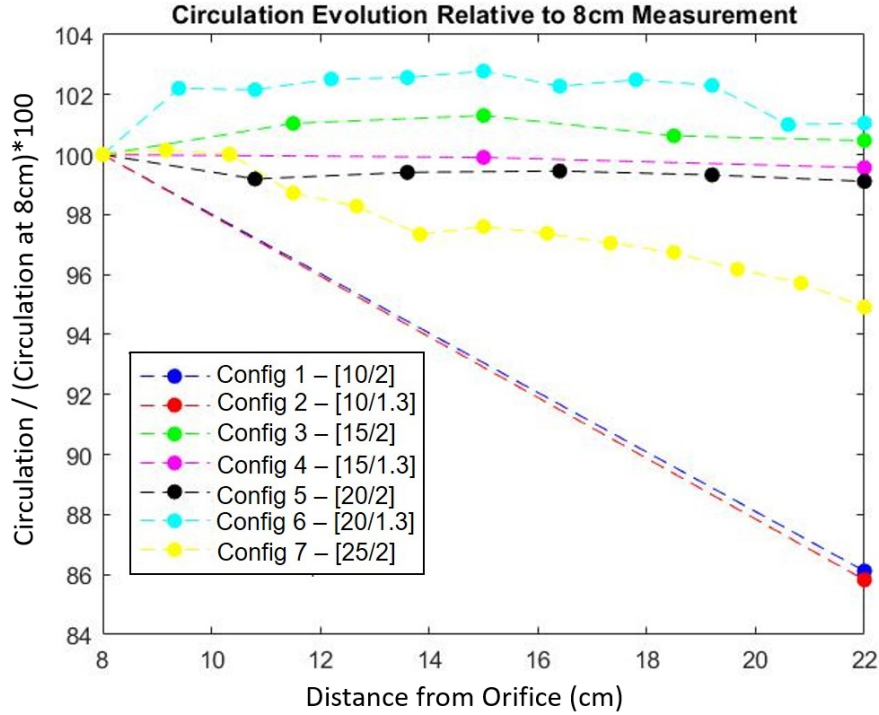


Figure 2.22: A graph presenting the evolution of circulation relative to its starting value, across the PIV imaging domain.

Figure 2.22 displays the evolution of relative circulation as the rings propagate across the tank, visualising stability. Circulation is directly related to energy (and ring speed) so is expected to decrease from viscous effects as the rings propagate. Configurations 3-7 exhibit high stability to within 5%, and interestingly some configurations gain a small amount of circulation before a subsequent reduction but this is less than 3% so not a concern. Configurations 1 and 2 exhibit higher loss in circulation than the slower rings of configurations 3-7. All rings exhibit 14cm-Stability over 80%, with configurations 3-7 demonstrating a 14cm-Stability over 90% (See table below).

| Config | % of Circulation lost over 14cm | 14cm-Circulation Stability |
|--------|---------------------------------|----------------------------|
| 1      | 13.3%                           | 86.7% $\pm$ 8.5            |
| 2      | 14.2%                           | 85.8% $\pm$ 7.7            |
| 3      | -0.1%                           | 100.1% $\pm$ 2.9           |
| 4      | 0.4%                            | 99.6% $\pm$ 8.7            |
| 5      | 0.9%                            | 99.1% $\pm$ 4.2            |
| 6      | -1.2%                           | 101.2% $\pm$ 9.9           |
| 7      | 5.1%                            | 94.9% $\pm$ 5.1            |

Table 2.3: Table listing stability of circulation for the Unit-0 ring vortex phantom. 14cm-Circulation Stability = 100%-% of speed lost over 14cm path-length.

### 2.4.5 Vector Reproducibility

The final assessment of the 2019 PIV vortices assessed the entire flow field of the ring vortices. This was performed to ensure that analysis of isolated parameters derived from the PIV data wouldn't overlook characterisation of the vortex' overall micro-flow behaviour. To achieve this, a domain of 20mm(W)x30mm(H) was established, centred around the ring vortex centre-point. Axial and radial velocity components were collected for all imaged rings at the start (8cm from the orifice) and end (22cm from the orifice) of the PIV imaging domain. Vector length and angle were calculated for each vector at every coordinate position using the equations below.

$$VectorLength = \sqrt{(U_{x,y}^2 + V_{x,y}^2)}$$

$$VectorAngle = atan^{-1}(V_{x,y}, U_{x,y})$$

Where  $U$  is axial velocity,

$V$  is radial velocity,

(x,y) are the axial and radial coordinate position

Length values were averaged at each point for all rings of the same configuration, with the average value and coefficient of variability found for each coordinate. Plotting the CoV across the domain produced a 'tolerance map' for the configuration, displaying which locations within the ring exhibited high reproducibility and where was more variable. This was computed for all seven configurations throughout the rings' journeys. These tolerance maps are presented below for the vector length (Figure 2.23). This was repeated to determine the variability in vector angle. The average value and standard deviation was calculated at each location. CoV is an inappropriate measure of angle variability, as absolute values range from 0-180°, distorting percentage values. The absolute variation was used for the angle tolerance maps, using the standard deviation. These are presented below in Figure 2.24.

### Length Tolerance Maps – Percentage Variation

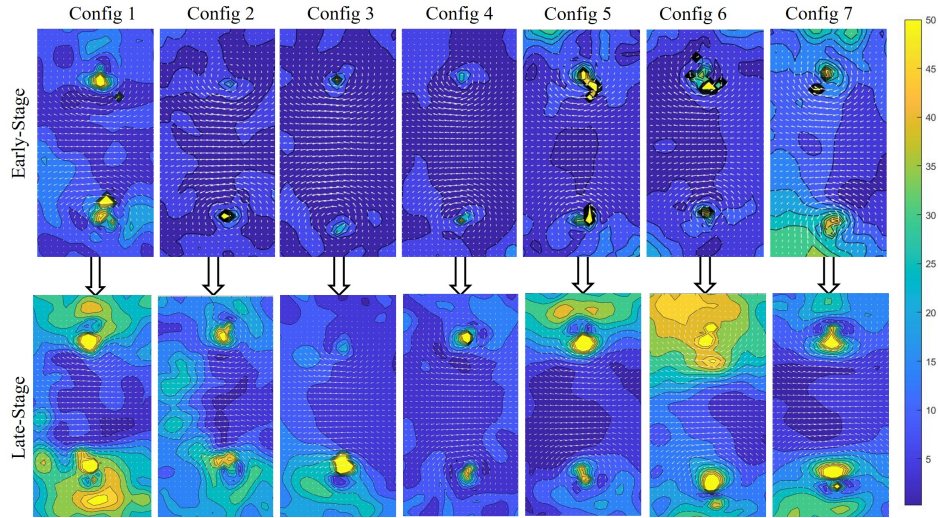


Figure 2.23: Example ‘Length Tolerance Maps’ for configurations as listed in Table 2.1. Average vector plots are shown with a coloured contour plot superimposed. Local colour is encoded according to the colourbar and represents the coefficient of variability in vector length between the ten vortices in the relevant configuration. Areas of yellow highlight large variation in flow vector length.

### Angle Tolerance Maps – Absolute Variation

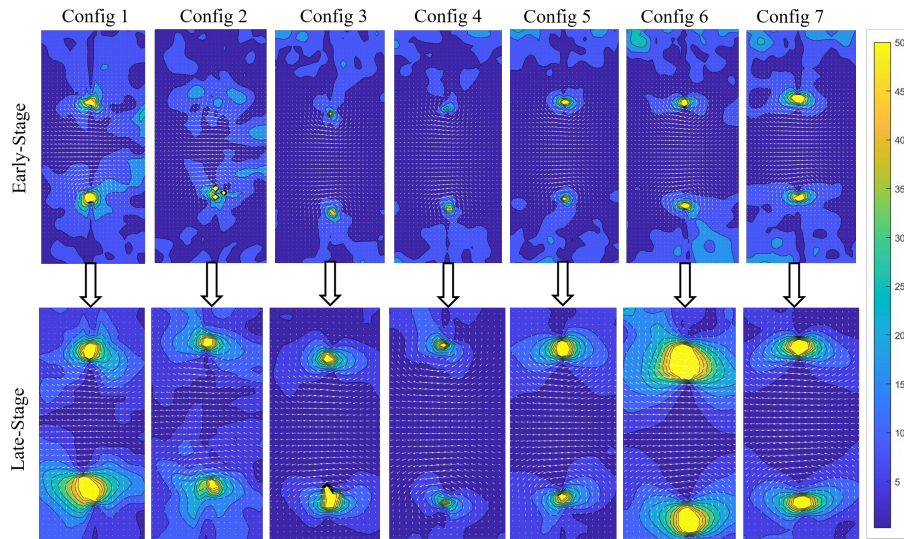


Figure 2.24: Example ‘Angle Tolerance Maps’ for configurations as listed in Table 2.1. Average vector plots are shown, with a coloured contour plot superimposed. Local colour is encoded according to the colourbar, and represents the standard deviation in vector angle between the ten vortices in the relevant configuration. Areas of yellow highlight large variation in flow vector direction.

These maps demonstrate how the reproducibility of each condition varies over time. Both angle and length show an increase in CoV (decrease in reproducibility) over their journeys, which is expected due to individual rings being affected differently by entrainment or other mechanisms. It is visually evident that configurations 3,4,5 are more reproducible, particularly in angle, as the majority of angles vary by less than  $5^\circ$  in the late-stage maps. Increased variability is present in the core centres and the surrounding region.

This analysis resulted in 1176 values for length and angle respectively for each individual frame, and benefited from a single metric to simply quantify these visual observations. A thresholding method was selected for quantifying agreement, representing the proportion of the ring which acts in a similar fashion (low variability) for each individual run. Thresholds of 10% and  $5^\circ$  were chosen for vector length and vector angle respectively. The metrics are therefore as follows:

- **Vector Length Reproducibility** - The percentage of vectors which exhibit a CoV of  $<10\%$  in length over ten ring vortices.
- **Vector Angle Reproducibility** - The percentage of vectors which exhibit a STD of  $<5^\circ$  in angle over ten ring vortices.

These metrics were calculated for the configurations, and are plotted below.

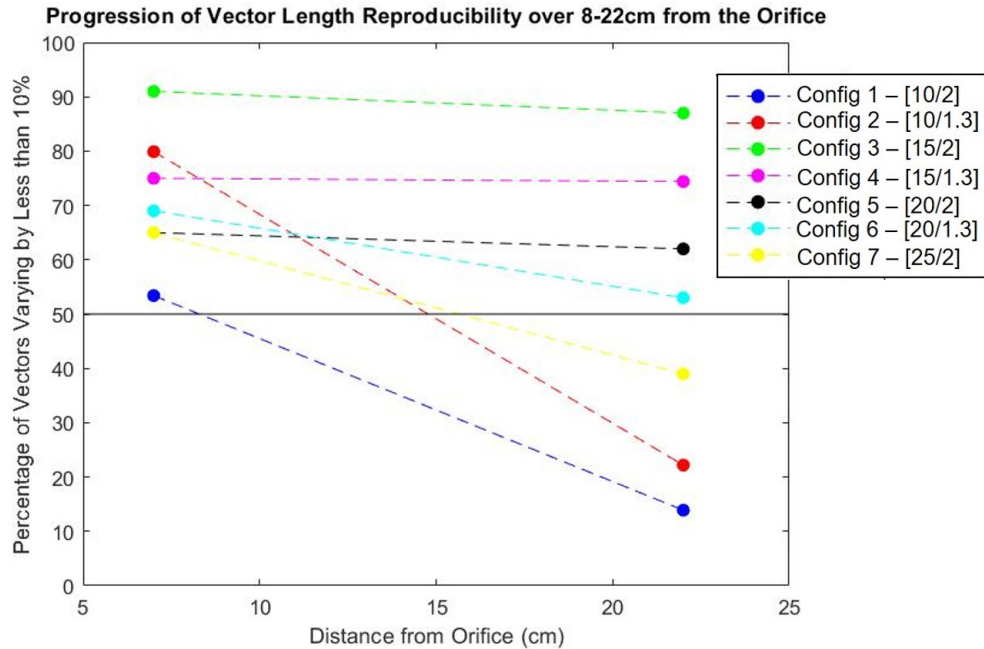


Figure 2.25: The evolution of vector length reproducibility across the PIV imaging domain. Y-axis values represent the percentage of vectors which exhibit a coefficient of variation of less than 10% in vector length.

Figure 2.25 presents the vector length reproducibility at the start and end of the imaging domain. This graph presents both the reproducibility of the rings and the stability, by

how much the metric changes over the rings' journeys. Establishing an arbitrary threshold of 50% agreement clarifies the results, where configurations 3,4,5 stay above the threshold across their journeys. Configurations 2,6,7 start above 50% then fall during propagation, and configuration 1 is below the threshold throughout its journey. Lines represent the overall change over the journey through the imaging domain, they do not represent a linear progression.

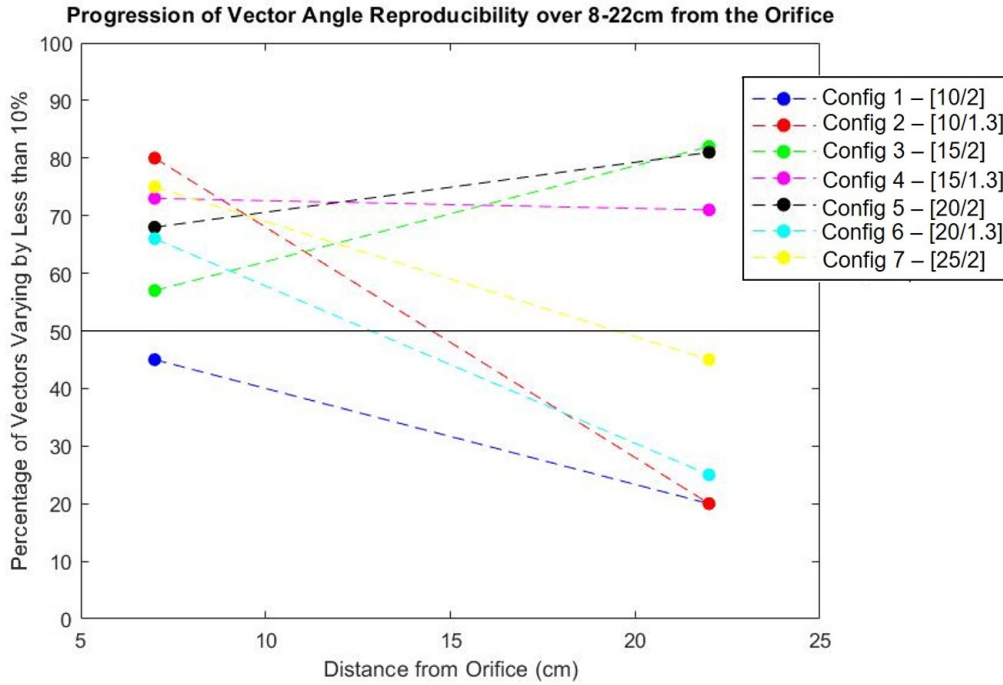


Figure 2.26: The evolution of vector angle reproducibility across the PIV imaging domain. Y-axis values represent the percentage of vectors which exhibit a standard deviation of less than  $5^\circ$  in vector angle.

Figure 2.26 plots the vector angle reproducibility across the rings' journeys. Varied reproducibility was evident across the configurations. Assuming an arbitrary threshold of 50%, configurations 3,4,5 stay above the threshold across their journey and actually increase in reproducibility, which is unexpected. Configurations 1,2,6,7 fall below it throughout their journeys, and configuration 1 is again always below the threshold. These findings notably reflect those of the vector length. Lines represent the change over the journey through the imaging domain, they do not represent a linear progression.

### Local Flow Velocity Measurement

Visualising the rings in this manner (Figures 2.23 and 2.24) aids in observation of where the rings are most reproducible. Throughout this thesis it is useful to measure micro-flow through the entire flow field, however this is time consuming and not always possible. A specific micro-velocity would be useful for characterising the ring vortex. The axial and

radial centre of the vortex (midpoint of the central axis) is notably reproducible in the length and angle maps, varying by less than 10% across all configurations, and often less than 5%. This high reproducibility lends this position’s velocity vector to being a reliable point of reference. This was therefore named ‘CentVect’. The velocity magnitude along the ring’s centre-line is affected by ring diameter, core diameter and energy/circulation, so this was deemed a useful property to characterise the micro-flow when more in-depth methods are not suitable.

### 2.4.6 CentVect

With CentVect proffered as a low-tolerance micro measurement, its reproducibility and stability deserve to be analysed in a similar fashion to the other measurements. The axial velocity component was measured for each ring across the configurations at the centre of the ring vortex. CentVect is a useful parameter as it is less susceptible to variation in measurement position in the PIV datasets (due to automated calculation) and yet is representative of the broader flow fields quantified in the analysis above.

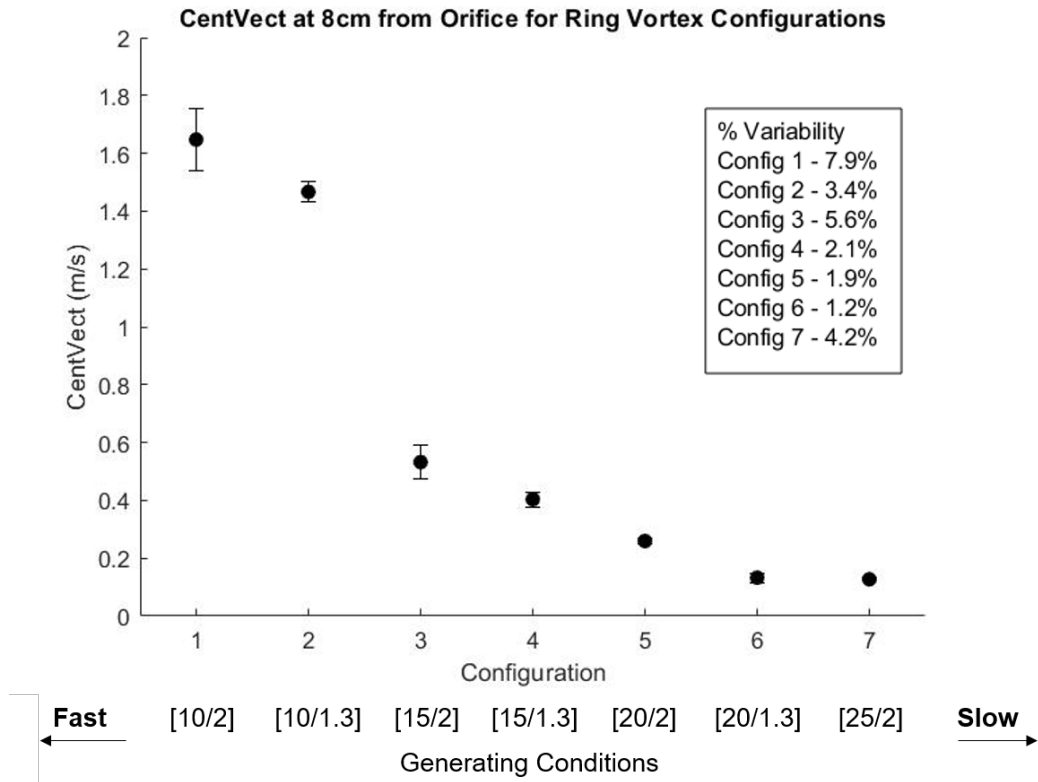


Figure 2.27: Average values for CentVect measured at 8cm from the orifice for configurations listed in Table 2.1. Datapoints represent the average of ten vortices and error bars represent 1 standard deviation

Figure 2.27 displays the reproducibility of CentVect when measured at 8cm from the

orifice through the error bars and in-figure text. High reproducibility was observed, with all configurations exhibiting reproducibility of <10%. Configuration 1 has the highest variability.

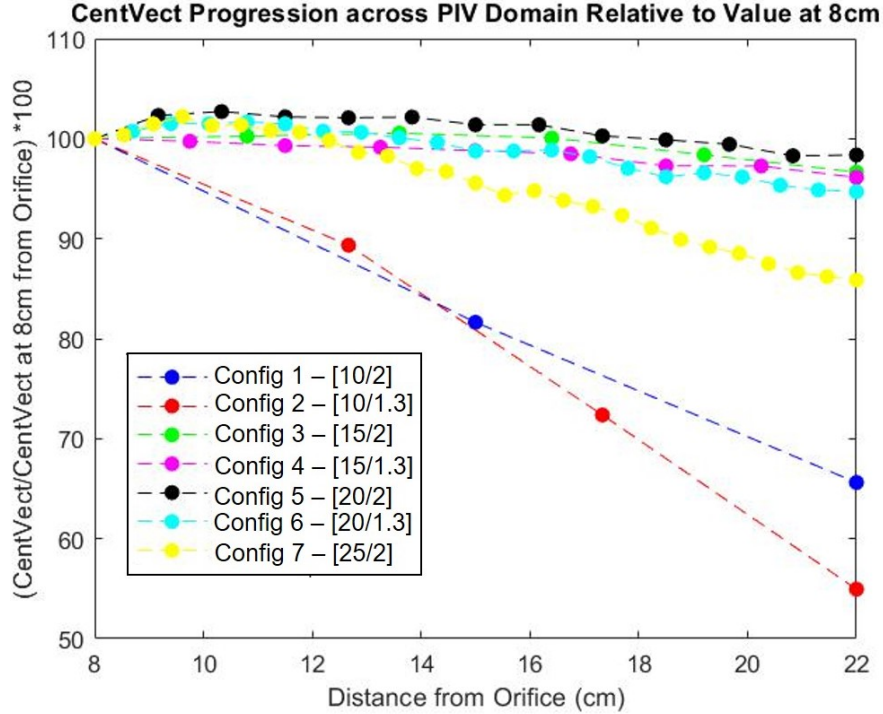


Figure 2.28: A graph presenting the progression of CentVect, relative to the starting value across the PIV imaging domain.

Figure 2.28 presents the relative evolution of CentVect as the ring propagates across the PIV imaging domain, depicting its stability. Varied stability is observed, with configurations 1 and 2 losing between 40-50% of the starting CentVect value and other configurations remaining above 80%. This notably reflects the high loss of circulation from configurations 1,2. The reproducibility and stability findings of each parameter will be collated and reviewed in the next section.

## 2.5 Discussion - Suitability of Ring Vortex Configurations as Reference Flows

### 2.5.1 Phantom Flow Analysis

This chapter has presented the ring vortex as a potential reference flow and identified key attributes that lends it well to this task. Innate features such as its physiological-level complexity and straightforward generation are significant, however its advantageous levels of reproducibility and stability in the phantom are foremost for this research. The

reproducibility and stability have been analysed in isolation across a variety of ring properties, with reasonable thresholds of behaviour identified throughout. Table 2.4 below lists whether each individual parameter reaches these thresholds for reproducibility and stability.

Considering the trends in the data across the parameters, the following requirements were set:

- **Reproducibility** - Parameters have a reproducibility of  $<\pm 12\%$ . Core radius has a reproducibility of  $\pm 15\%$  due to discretization.
- **Stability** - Parameters are stable within  $<\pm 10\%$  over 14cm. Core radius has a stability of  $<\pm 15\%$ .
- **Tolerance Maps** - An initial value of 60% is reached, where  $>60\%$  of locations have variability of less than 10% or  $5^\circ$  for vector angle and length respectively. A late-stage value of 50% is reached.

These thresholds were selected to clarify the reproducibility and stability that the vortices demonstrate when generated by this phantom, and allow comparison between configurations. Each configuration is listed in the table below, with a  $\checkmark$  if they reach the relevant threshold, and a  $\times$  if they do not.

| Config               | Speed        |              | R. Rad       |              | C. Rad       |              | Circ/n       |              | CentVect     |              | Vector Len   |              | Vector An    |              |
|----------------------|--------------|--------------|--------------|--------------|--------------|--------------|--------------|--------------|--------------|--------------|--------------|--------------|--------------|--------------|
|                      | R            | S            | R            | S            | R            | S            | R            | S            | R            | S            | Start        | End          | Start        | End          |
| 1 - [10/2]<br>(fast) | $\checkmark$ | $\times$     | $\checkmark$ | $\times$     | $\times$     | $\times$     |
| 2 - [10/1.3]         | $\checkmark$ | $\times$     | $\checkmark$ | $\times$     | $\checkmark$ | $\checkmark$ | $\checkmark$ | $\checkmark$ | $\checkmark$ | $\times$     | $\checkmark$ | $\times$     | $\checkmark$ | $\times$     |
| <b>3 - [15/2]</b>    | $\checkmark$ |
| <b>4 - [15/1.3]</b>  | $\checkmark$ |
| <b>5 - [20/2]</b>    | $\checkmark$ |
| 6 - [20/1.3]         | $\times$     | $\checkmark$ | $\checkmark$ | $\checkmark$ | $\checkmark$ | $\times$     | $\checkmark$ | $\times$     |
| 7 - [25/2]<br>(slow) | $\checkmark$ | $\times$     | $\checkmark$ | $\times$     | $\checkmark$ | $\times$     | $\checkmark$ | $\checkmark$ | $\checkmark$ | $\checkmark$ | $\checkmark$ | $\times$     | $\checkmark$ | $\times$     |

Table 2.4: Classification of ring behaviour according to reproducibility and stability. A  $\checkmark$  indicates that the ring property behaves according to stated tolerances. A  $\times$  indicates failure to remain within stated tolerances. ‘R.Rad’ and ‘C.Rad’ represent ring radius and core radius respectively. Rows in bold identify configurations where all thresholds are met.

Summarising this analysis’ important features:

- Configurations 3,4,5 reached the threshold on all parameters These configurations demonstrated the **highest stability and reproducibility**.

- Configurations 1,2 (the fastest rings) exhibited lower stability than the slower rings. For both settings the vector lengths and angles were highly variable at the journey end, showing that each individual ring behaved differently over the established thresholds. Interestingly CentVect, speed and circulation showed poorer stability for these configurations, indicating that these rings are losing energy faster than other rings. These configurations show **lower stability and reproducibility**
- Configs 6,7 (the slowest rings) showed similar instability to configs 1,2 with configuration 7 in particular having unstable speed and ring radii. These configurations therefore show **lower stability and reproducibility**.

Analysing the results in this manner has highlighted the variability in ring vortex behaviour under different generating conditions. The thresholds were selected to highlight the most stable configurations, and what level of stability and reproducibility they were able to achieve. These are therefore proposed as the reproducibility/stability declarations for using this phantom under these conditions. It was noted that three configurations (3,4,5) are able to reach the thresholds on all metrics. A more systematic analysis is required to determine what other configurations the phantom generates, and whether these proposed thresholds are reached by other experimental conditions. This analysis has provided insight into the variability of vortex type and what the phantom is capable of. These thresholds set a high bar for phantom performance so there is certainly potential for the phantom/ring vortices to provide effective QA for imaging technologies.

## 2.5.2 Ring Behaviour and Stability

It has been consistently observed throughout this analysis that the most stable and reproducible rings are the mid-speed rings (between 15-27 cm/s), while the more extreme slow and fast rings are less stable. The concept of ring ‘stages’ (laminar, transitional and turbulent) was also introduced during this chapter, and there are connections that can be hypothesised between them. Section 2.2 discussed conditions under which rings become disturbed through azimuthal instabilities and subsequently turbulent rings where they shed vortices into their wake. Initially-turbulent rings were also discussed, with stroke ratios of over 4. Both mechanisms will accelerate loss of circulation/speed and act unpredictably due to the unstable nature of vortical shedding, reducing both reproducibility and stability if present. To determine the nature of fast rings (configs 1,2) and slow rings (configs 6,7) were visible through camera data rather than PIV, camera recordings were analysed visually. Three examples are presented below.

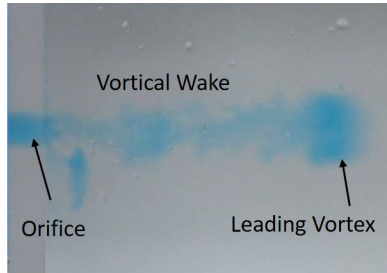


Figure 2.29: Photo of a configuration 1 ring vortex from the 10mm orifice using the O-ring piston. This image is captured at immediately post-formation and presents a *fast* ring.

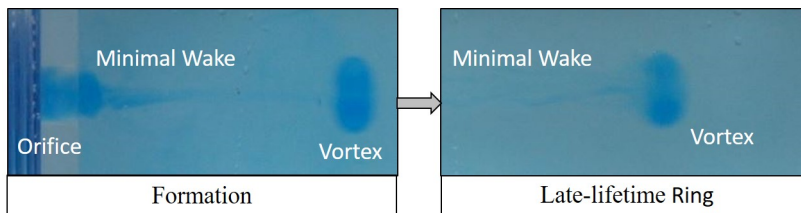


Figure 2.30: Photos of a configuration 3 ring vortex from the 15mm orifice using the O-ring piston. Images are captured at immediately post-formation and at 18cm from the orifice and present a *mid-speed* ring

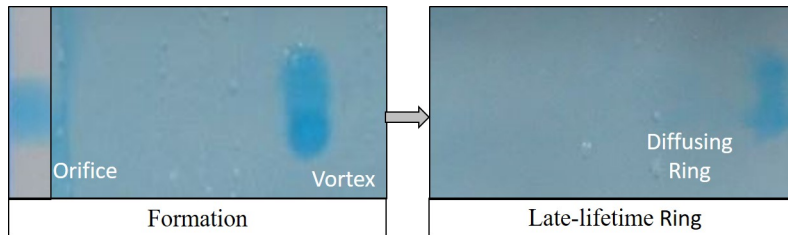


Figure 2.31: Photos of a configuration 7 ring vortex from the 25mm orifice using the O-ring piston. Images are captured at immediately post-formation and at 18cm from the orifice and present a *slow* ring

These photos confirm clear behaviours across the spectrum, comparing configurations 1, 3 and 7. Configuration 1 demonstrates a significant vortical wake - this will accelerate the loss of circulation/energy and de-stabilise the ring. Configuration 3 shows an elliptical meridional cross section across its journey with minimal wake. This configuration was noted as highly reproducible and stable at the micro-level. Finally, configuration 7 starts elliptical but loses this structure as it propagates and the ring starts to breakdown, visibly leaking dye. There is a clearly a connection between the macro/visible behaviour of a ring vortex and its stability/reproducibility at the micro-scale. The high-stability, high-reproducibility configurations exhibited elliptical cross sections and minimal visible wake or diffusion across its propagation.

The visible differences between these configurations clearly arise from their generating conditions. A parameter which differs between them is the stroke ratio. For each configuration the piston moves by 0.8mm, which results in a different stroke ratio for each orifice, since stroke ratio is defined as the ratio of jet length to orifice diameter. Configurations 1,3,7 have stroke ratios of 3.92, 1.16 and 0.25 respectively, which is a wide range. The literature reports that stroke ratios over 4 generate turbulent vortices. Configuration 1 is close to this boundary, so the vortical, disturbed behaviour it exhibits indicates that it is close to the ‘turbulent’ boundary, and the rings are likely disturbed from the start. The most stable rings imaged in this experiment (configurations 3,4,5) had stroke ratios of 1.16, 1.16 and 1.49 respectively, which is a useful starting point for establishing more rings of this stability/reproducibility. More extreme stroke ratios should be avoided to ensure stable and reproducible rings.

## 2.6 Conclusions

This chapter has explored a candidate for a novel complex flow suitable for assessing state-of-the-art quantitative flow imaging technologies. This candidate is the ring vortex, a toroidal vortex comprised of layers of recirculating fluid. The ring vortex’ straightforward generation, high complexity yet unambiguous characterisation are well-documented and ideal for integration into a flow phantom. The ring vortex phantom Unit-0 prototype has been described, along with its current workflow and a previously conducted Laser PIV experiment, where test ring vortices were imaged over a 14cm path-length. This has been complimented by an in-depth analysis conducted on ring speed, dimensions, circulation and local velocity variability, with a new metric ‘CentVect’ identified as a suitable parameter for characterising ring vortex behaviour. Three configurations exhibited higher stability and reproducibility, achieving reproducibility of  $<\pm 10\%$  and stability of  $<\pm 10\%$  across all parameters except for core radius, which is susceptible to PIV discretisation. These rings propagate at 27cm/s, 22cm/s and 15cm/s respectively. This exercise demonstrated the stability and reproducibility that the phantom device and its generated flows can attain.

This exercise confirms that the phantom is able to generate reproducible rings which are stable in certain settings. A visual relationship was found between generating conditions and stability, where high stroke ratio rings shed vortices from generation (causing instability) and low stroke ratio rings started to breakdown during their journey (also causing instability). It was observed that in these conditions, the mid-range stroke ratio of 1.1-1.5 generated rings which are more stable and reproducible. The phantom is currently limited by generating rings of specific speeds, and ought to be used to its full potential. This will be investigated further in the next chapter.

# Chapter 3

## Optimising the US-Compatible Ring Vortex Phantom: Unit-1

### 3.1 Introduction

Chapter 2 introduced the ring vortex phantom (Unit-0) as it was at the commencement of this project. This device was capable of generating ring vortices over a range of speeds and sizes and was proposed as the basis for an imaging phantom, but was not assessed in detail. Analysis of Laser-PIV in Chapter 2 datasets examined the suitability of a subset of vortices in terms of stability and reproducibility of both bulk- and micro-scale parameters. It was found that the vortices were able to achieve reproducibility to  $\pm 10\%$  and stability to  $\pm 10\%$  in a range of parameters over a path-length of 14cm. Three configurations reached these values on all metrics, confirming the potential of the device and its vortices. Further study into the ring vortex landscape is warranted to establish whether other vortices are as stable, and under what conditions. A diverse range of stable and reproducible vortices will provide added confidence for the adaptability of the phantom.

This chapter therefore has one primary objective, namely optimisation of the device, which will be undertaken at two levels: *device* optimisation, by development of revised protocols for its use, and *flow* optimisation and characterisation, by further clarifying suitable vortices for use as a phantom reference flow. Through the flow optimisation experiments a broader understanding of the ring vortex ‘landscape’ will be obtained, to understand under what conditions the vortices are stable and reproducible. Flow assessment will be performed at the macro-level in this chapter, using video recordings. Micro-analysis will follow later in the thesis, in Chapter 6.

### 3.2 Device Optimisation I - Piston Re-Design

#### 3.2.1 Introduction

A design change was proposed towards the end of the previous project to improve phantom functionality. It was observed that during use the piston would ‘jump’ forward, often with

enough force to move the phantom. During long experiments it was also noticeable that rings became less reproducible as the piston would sometimes stick in the cylinder, despite use of lubricant. This was hypothesised to result from the nitrile O-ring around the piston head sticking to the piston cylinder interior wall, with a high nitrile-to-Perspex coefficient of friction. Poorer reproducibility and likely strain on the motor inspired a design change for the component. Consequently a new piston was designed and manufactured, omitting the O-ring and lengthening the piston head to 5cm to ensure correct alignment. This piston was manufactured along with a new piston cylinder, reamed for optimal fit between the two components. The new piston was tested in the previous project and observed to react well to motor propulsion but no quantitative testing was completed (Note: the Laser-PIV experiment used the O-ring piston). This chapter will investigate the effect of this new component on the phantom functionality and its vortices, with the resulting version of the device (and vortices) defined as Unit-1.

For this thesis, the following terminology will be used: ‘*OR*’ piston is the old, O-ring piston. ‘*NOR*’ piston is the new, non O-ring piston introduced here.

### 3.2.2 Effect on Piston Velocity Profile

Generation of a ring vortex is straightforward, with the sole dynamic component the piston as described by its velocity profile. A strong relationship exists between velocity profile shape and ring dynamics [98], as the velocity profile represents the accumulation of circulation around the orifice, forming the vortex core. The first task the NOR piston replacing the piston was establishing how it reacted to the motor pulse sequences and whether this response differed from that of the OR piston. A discrepancy between the two would lead to different vortices being generated.

#### Linear Encoder

The piston motion was tracked by introducing the RLS LM10 linear encoder, a commercial device designed to track its own uniaxial motion to high spatio-temporal resolution. To track the piston motion, a 10cm-long magnetic strip was embedded into the piston stem. The encoder was then mounted onto a plate on the piston guide, at  $\sim 1$ mm above the magnetic strip. The encoder remains stationary, thus as the motor propels the piston (and magnetic strip) forward its relative motion can be tracked. The device was purchased with custom MATLAB functions for its use, allowing simple commands such as power on/off and reading the encoder position. The device is powered and controlled through a USB3.0 connection from a laptop. The encoder is bidirectional with a digital output, with a quoted resolution of  $625 \mu\text{m}$  to  $5 \mu\text{m}$  [120].

The encoder position can be read iteratively in a number of ways, with varying resolution. Repeated measurements using a for-loop produced a sampling frequency of 40Hz, which is insufficient for this use as for some conditions the piston is only in motion for 40ms. To ensure sufficient sampling frequency, continuous sampling was required. By commanding the encoder to constantly read its position for 1 second, sampling frequency was limited only by the encoder transmission speed. This method resulted in a sampling

frequency of 100Hz ( $\pm 3Hz$ ), providing a suitable number of readings over a profile of 40ms or longer. Spatial and temporal resolution were now 0.2mm and 0.01s respectively. The resolution of 100Hz was still below the quoted 1MHz encoder threshold, restricted by the USB baudrate, but this was sufficient for this application.

```

%Open port and turn on encoder
E2019Q_ID = E2019Q.Open_COM_Port('COM3');
Power_Supply = E2019Q.EncSupply_ON(E2019Q_ID); % turn on
%read continuous data for 1 second
tic;
OneOutput=E2019Q.One (E2019Q_ID);
pause(1)
    E2019Q.Zero (E2019Q_ID);
LoopTimeOne=toc;
%turn off encoder and close port
Power_Supply = E2019Q.EncSupply_OFF(E2019Q_ID); % turn encoder off
E2019Q.Close_COM_Port(E2019Q_ID); % Close Port
%create double file format from Loops #1,#2 char position readouts
PositionOne=splitlines (OneOutput);
PositionsDBLOne=str2double (PositionOne);
dT=LoopTimeOne/size (PositionsDBLOne,1);
PosChangeOne=[];
%generate velocity profile from Position Data
for i=2:size (PositionsDBLOne,1)
    P=abs ((PositionsDBLOne (i)-PositionsDBLOne (i-1))/dT)*1e-4;
    PosChangeOne=[PosChangeOne;P];
end
Matrix(1:size (PosChangeOne,1),a)=PosChangeOne;

```

Figure 3.1: A MATLAB code snippet for collecting position measurements from the linear encoder at 100Hz. Data are transferred to double format and into a velocity matrix.

### Piston Velocity Profiles

The encoder was used to compare the velocity profiles achieved by the OR and NOR pistons when propelled by the same motor pulse sequence. The motor was programmed to travel over 0.8mm at 1.3m/s using a top-hat function. Both pistons were tracked over multiple instances, with their velocity profiles presented below.

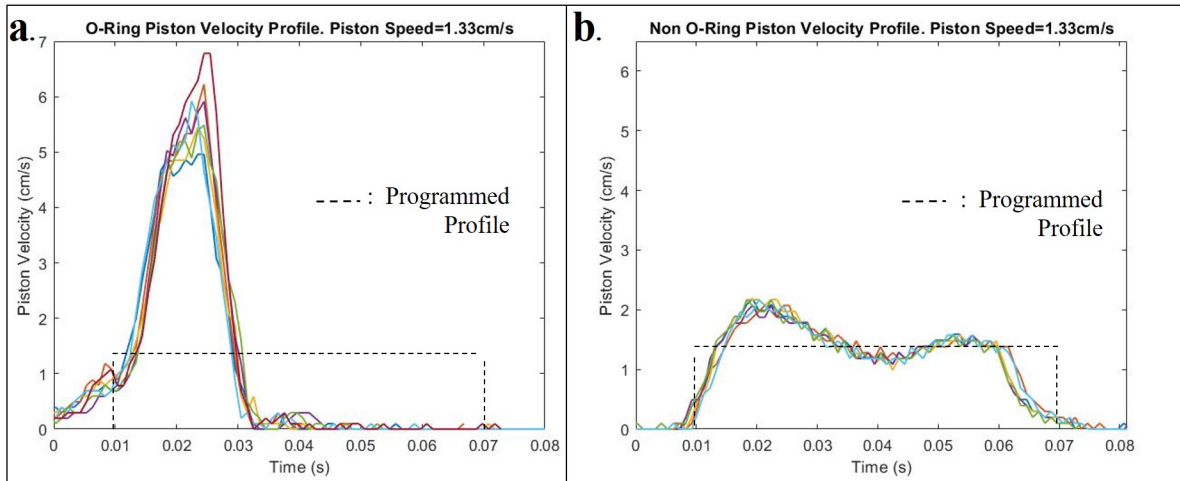


Figure 3.2: Graphs presenting linear encoder data for the O-ring piston and non O-ring piston, moving at identical programmed speed of 1.3cm/s over 0.8mm in a top-hat motor pulse sequence. Graph (a) is the O-ring piston profile. Graph (b) is the non O-ring piston profile.

Figure 3.2 reveals a significant difference between the pistons' velocity profiles when propelled by the same motor pulse sequence. The OR piston reached a maximum speed of 5-7cm/s and travelled for approximately 0.02s, whilst the NOR piston propagated for  $\sim 0.05$ s reaching a maximum speed of approximately 2cm/s. Neither profile followed the programmed top-hat profile exactly, however the NOR piston visually followed a better approximation, with its average speed at  $\sim 1.4$ cm/s over its impulse. This finding was significant as it implied the small design change had a remarkable effect on the phantom functionality, which would undoubtedly affect the generated ring vortices. In addition, the NOR piston profiles were satisfyingly reproducible, following a specific pattern within tight bounds, whereas the OR piston speed varied by up to 2cm/s at its peak speed. Overall, it is desirable to have the piston following what the motor demands as this improves the controllability of the phantom.

### 3.2.3 Effect on Vortex Flow - Ring Speed

The drastic change in velocity profile was hypothesised to affect the generated vortices. The most straightforward method to confirm this was to measure the rings' speeds. An experiment was therefore performed to compare speeds of the OR piston vortices and NOR piston vortices. Ten rings of configurations 2,4,6,8 from Table 2.1 were generated using identical actuation for each piston. The rings were recorded at 100fps using a tripod-mounted SONY RX10 positioned at approximately 3m from the phantom to reduce parallax. Rings were generated at 25 second intervals to minimise inter-ring disturbance, and their propagation was recorded for the entire journey. Post-processing was performed in MATLAB using a custom algorithm where the user defined the tank length (35cm) on-screen, then located the ring in individual video frames as it propagated across the

tank. The instantaneous speed between frames was then calculated using this information. This analysis was performed on every recorded ring, with the speed over 5-20cm from the orifice measured. These results are presented below.

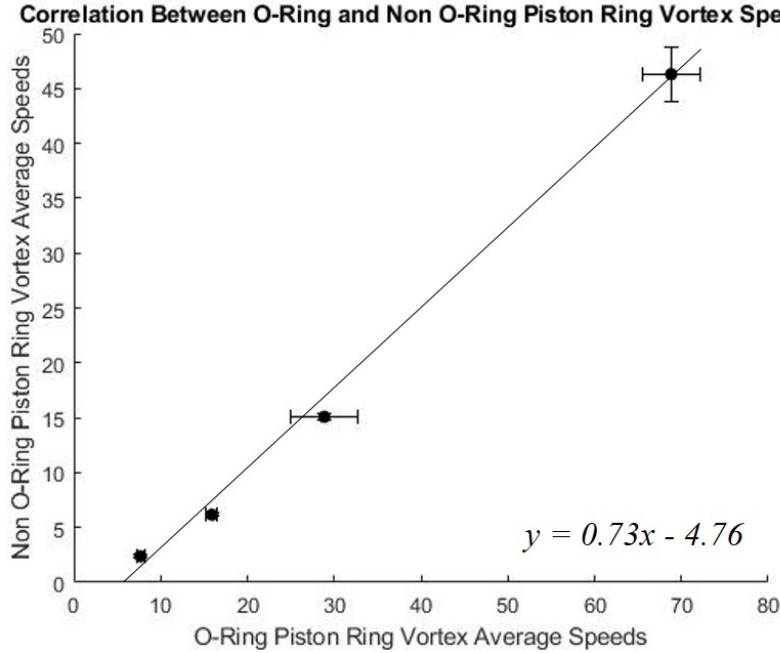


Figure 3.3: The correlation between O-ring piston and non O-ring average ring vortex speeds over 5-15cm from the orifice. Datapoints are averaged values across ten ring vortices, and error bars represent 1SD.

This analysis of vortex speeds confirmed the expected change in ring behaviour from replacing the pistons, as the NOR piston rings were observed to propagate at significantly slower speeds (approx. 75%) than the OR piston-generated vortices. Another interesting observation was that the OR-piston rings were more variable in speed, likely from the varying piston velocity profiles discussed above. This analysis confirmed that any rings generated by the NOR piston were **not** the same as any studied vortices from the previous work using the OR piston.

### 3.2.4 Effect on Vortex Flow - Energetics

Previously, the information available on ring generation was limited, as it was assumed that the piston was following a profile which mirrored that of the motor input code. That assumption has been disproved by Figure 3.2, and the addition of the encoder has provided rich information on piston motion and ring generation. Using simple calculations it is informative to quantify the change in piston profile in terms of energy, a more universally useful parameter.

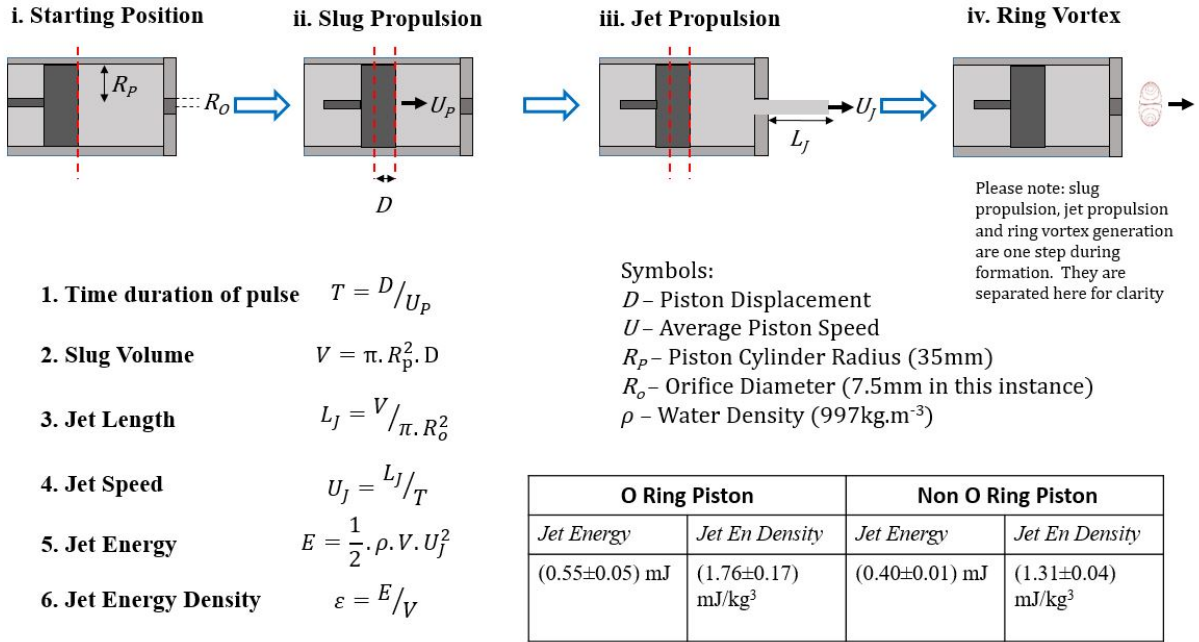


Figure 3.4: A schematic of the ring generation process in a piston/orifice setup with associated energy calculations using the slug model.

The process detailed in Figure 3.4 clarifies the steps to approximate energy in the jet when propelled through a 15mm diameter orifice. This method applies the slug model (uniform velocity across the slug/jet cross section that matches the (volume-corrected) piston speed) and that energy is conserved from the piston to slug, and then to jet. The images define the language used here, where the piston propels a *slug* of fluid through the 35mm-diameter piston cylinder (Fig 3.4i). This slug is then propelled through the smaller, 15mm-diameter orifice as a *jet* of fluid (Fig 3.4ii). As the orifice is smaller in diameter than the piston cylinder, the jet is longer and faster than the slug, to ensure the same volume is displaced. The smaller the orifice, the longer and faster the jet is, resulting in a jet of higher energy. This is a simplified description of why ring vortices from smaller orifices are faster, because the jet that generates them has higher energy and is travelling faster.

This method was used to estimate jet energy from the two pistons for comparison. Using the profiles presented in Figure 3.2, the energy and energy density was calculated for ten profiles for each piston. This resulted in the values listed in the table in Figure 3.4. Interestingly, the NOR jet energy is 73% of the OR jet energy. This mirrors the 0.74 gradient found between the OR and NOR piston ring speeds. The primary finding here is that the NOR piston moves slower than the OR piston and more closely follows the programmed motor profile. The NOR piston rings are approximately 25% slower, and the energy of the NOR jets are approximately 25% lower also. Vortices generated by the NOR piston under the same conditions will have lower energy than the previous configurations.

### 3.2.5 Conclusion - Piston Re-Design

Section 3.2. has compared the old OR piston and the new NOR piston for their functionalities. The NOR piston more closely followed the motor programmed profile, improving controllability of the device, and a more reproducible profile was achieved. Extended use of the OR piston could lead to component degradation and potential damage, whereas the newer design was more responsive to motor propulsion. Due to higher reproducibility and controllability, the NOR piston was adopted within the phantom design and used for all experiments from this point on. By making this design change it's important to note that the ring dynamics change - the energy and ring vortex speed decrease due to the slower piston. The implications for ring vortex behaviour was further investigated, discussed in Section 3.5.

## 3.3 Device Optimisation II - Piston Response to Motor Sequence

Tracking the piston profile through addition of the linear encoder allowed the piston motion to be visualised for the first time. Unexpected behaviour was seen on the NOR piston motion and presented in Figure 3.2b where a 'double-peak' motion is visible. The piston reaches a peak speed of 2.5-3cm/s, with the velocity falling, and peaking again at around 2-2.2cm/s. The motor operates at a constant speed, thus this double peak feature is not expected, and is certainly an abnormality that warrants investigation. The literature broadly discusses ring vortices generated by trapezoidal piston profiles. To generate reliable vortices that can be compared to published results, a trapezoidal profile is desirable.

### 3.3.1 Ideal Piston Profile

The desired piston velocity profile for ring vortex generation is a trapezoidal profile, comprised of three components: the acceleration phase (A), the plateau phase (B) and the deceleration phase (C) (Figure 3.5). Phases A and C follow a consistent acceleration, and Phase B should keep close to its central value, within tolerances. There is a clear non-trapezoidal profile followed by the NOR piston (Figure 3.2) particularly in the plateau phase as it varies by close to 40%. Refinement of the motor pulse sequence and device will enforce a consistently trapezoidal profile.

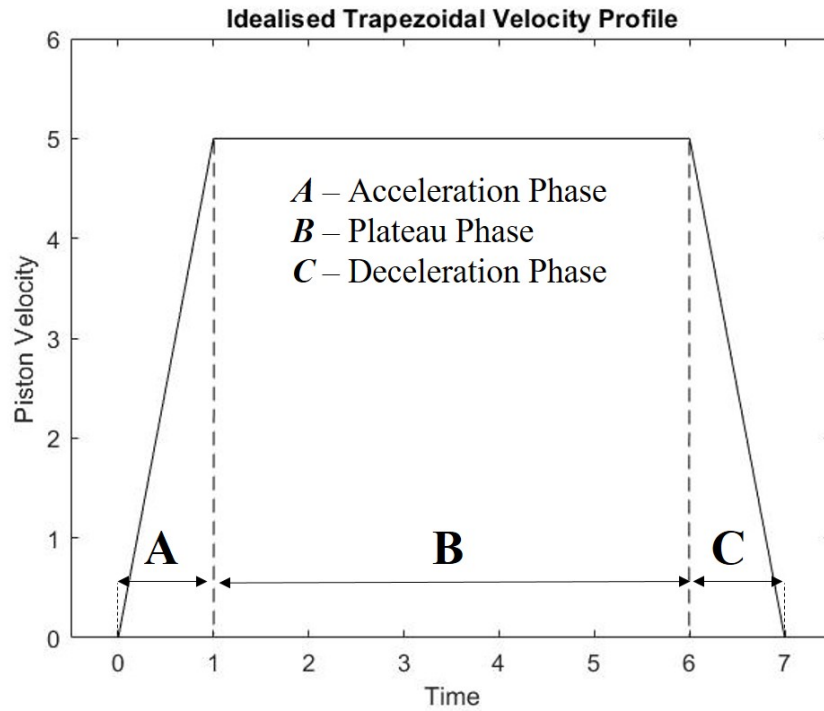


Figure 3.5: Schematic of the idealised trapezoidal velocity profile for ring vortex generation. Acceleration, plateau and deceleration stages are annotated.

### 3.3.2 Piston Oscillation and Cause

Investigating the double-peak phenomenon in Figure 3.2b is limited through the profile's short time duration. Longer displacement (thus longer time duration) profiles were therefore generated to fully visualise the dynamics. Using the NOR piston, and a top-hat function motor pulse sequence of speeds=2cm/s and 1.33cm/s over a displacement of 2.4mm, five impulses were generated for each speed. These profiles last for 120-180ms thus allowed easier visualisation and are plotted below.

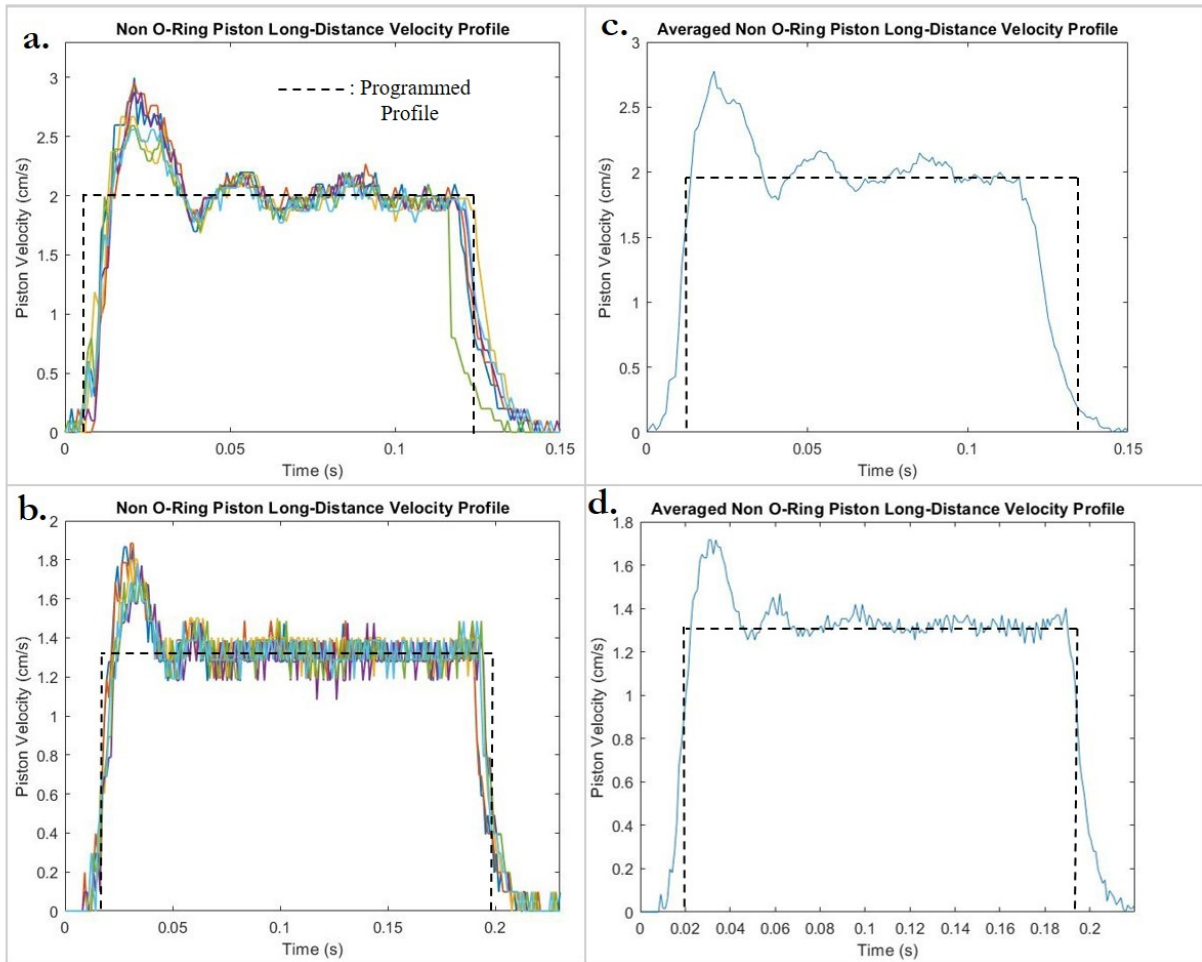


Figure 3.6: Graphs presenting the piston behaviour for long displacements over 2.4mm under a top-hat motor pulse sequence. Graphs (a),(b) present superimposed individual encoder-measured profiles, and (c),(d) the average of 5 profiles. Graphs (a),(b) record the piston behaviour for 2cm/s programmed speed, and (c),(d) for 1.33cm/s programmed speed.

These profiles present a clear deviation from the input square wave function. The longer displacement revealed that an oscillation-like motion was present, where the piston speed oscillates above and below the programmed speed in the plateau stage (this is particularly visible on the faster speed profiles in Graphs (a),(c)). For both speeds, the piston speed initially overshoot to a value above its programmed speed (PS) (140%PS for 2cm/s, 130%PS for 1.33cm/s), before decelerating to a value below the PS. The speed then oscillated back above the PS then continued to oscillate until settling around the PS at equilibrium. It was notable that the slower speed (Graphs (b),(d)) reached an equilibrium (100%PS) after only one to two cycles, whereas the faster 2cm/s profile exhibited oscillatory motion until the end of its profile. The oscillation reproducibility was fairly reproducible, suggesting a systematic mechanical oscillation in the device, rather than a varying factor in each propulsion.

These profiles are visually similar to the velocity response for a damped simple harmonic oscillator. In damped harmonic oscillation, an oscillatory object is subject to an external force, inducing an oscillation. An opposing force then resists this oscillation and progressively reduces the amplitude until the object rests at equilibrium. A classic example is a weight hanging on a spring, where it is pulled down (external force) and released, starting an oscillation around the equilibrium position. The spring tension (damping force) will gradually reduce its amplitude until the weight ceases motion and rests at its equilibrium position with zero net force.

In the phantom, it was hypothesised that the piston was acting as a damped oscillator in its velocity dynamics due to an oscillatory device component. The oscillation was causing speeds up to 40% different from the programmed speed in the plateau stage, and was the root of the ‘double-peak’ phenomenon which may result in abnormal vortices. It should therefore be eliminated to ensure reliable vortex generation.

The cause of this oscillation must be from the relevant device component(s): the motor/base/piston/leadscrew combination must have some looseness in it to allow an oscillation.

### 3.3.3 Phantom Base Reinforcement

Firstly, the phantom mechanics were assessed. The piston head is 5cm long and forced into alignment through the tight-fit piston cylinder with no discernible looseness, so significant lateral piston head oscillation can’t occur. The piston cylinder was tightly adhered to the tank and bound to the table. No visible water disturbance was observed during experiments, so it was very unlikely that the tank/cylinder/piston were the root of this oscillation.

The remaining components in contention were the motor, base, and lead-screw. It was observed that with minimal force, a user could manually angle the lead-screw up and down, with less force than the motor would exert during propulsion. The skewed leadscrew during propulsion would cause the piston and cylinder to minutely angle and subsequently oscillate. It was also observed that as the lead-screw was angled, the motor angled as well. The motor is affixed to a solid block of Perspex with no visible give. This block is mounted on the phantom base, a 10mm thick PMMA block supported only by feet around its periphery. The centre is therefore unsupported, with empty space between its underside and the table. Manually angling the lead-screw produced a visible ‘flex’ in the base as the motor mount angled, depressing the weaker base (See Figure 3.7). With this observation, it was concluded that when the motor applied force for propulsion, and as the force accumulated due to static friction, the base was flexing and lead-screw angling, resulting in this oscillation when the piston moved. A 1mm-tolerance between the piston stem and guide cut-out allowed space for the piston to oscillate slightly with the lead-screw.

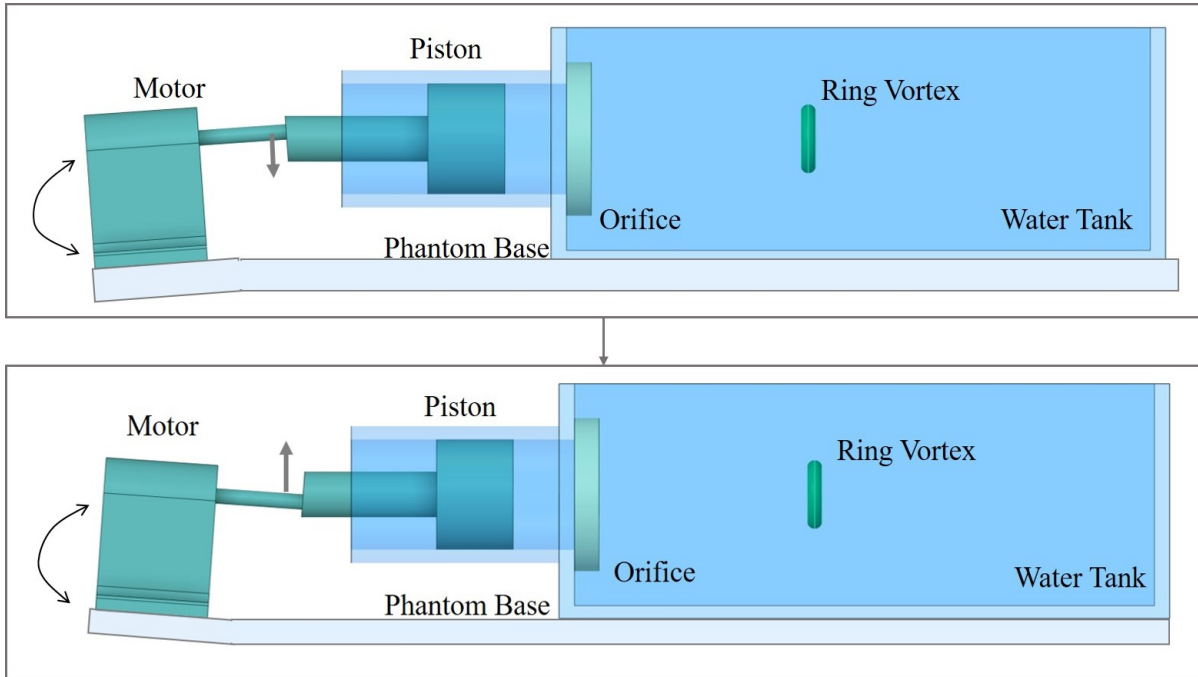


Figure 3.7: A schematic of the ring vortex phantom with the motor angling due to a flex in the PMMA base.

To test this hypothesis and to reduce this effect, solid Perspex blocks were inserted beneath the base under the motor base. By reinforcing the base at the point of force, this was hypothesised to reduce the oscillation motion. This was tested with ten impulses generated for programmed speeds of 2cm/s and 1.3cm/s respectively, with a piston displacement of 2.4mm. These results are plotted below.

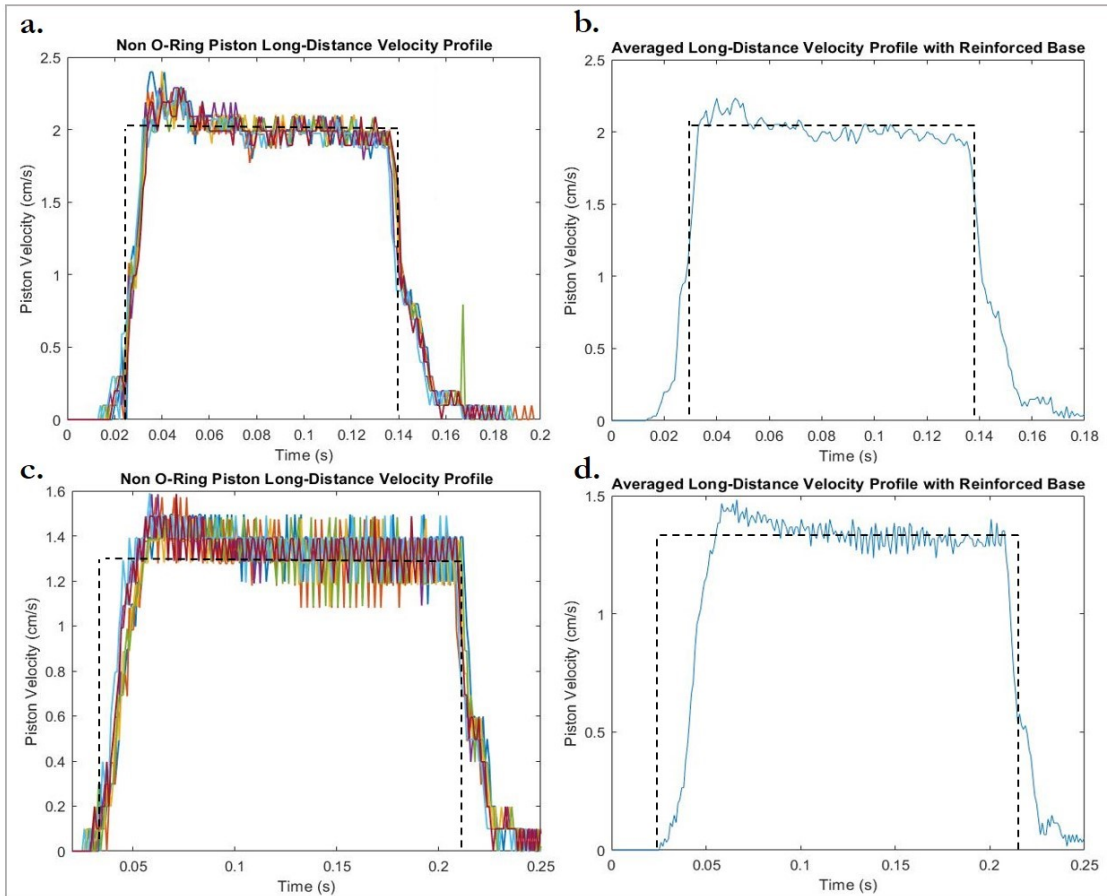


Figure 3.8: Graphs presenting the piston behaviour for long displacements of 2.4mm under with the base reinforced with Perspex blocks. Graphs (a),(c) present superimposed individual encoder-measured profiles, and (b),(d) the average of 5 profiles. Graphs (a),(b) record the piston behaviour for 2cm/s programmed speed, and (c),(d) for 1.33cm/s programmed speed.

A clear difference results from this reinforcement in both fast 2cm/s (Graphs a,b) and slow 1.33cm/s (Graphs c,d) profiles. The 'fast' profile overshoot to 2.5-3cm/s for unreinforced profiles, but reached only 2-2.5cm/s with reinforcement. Meanwhile, the slow profile overshoot improved from 1.6-1.8cm/s (unreinforced) to 1.4-1.6cm/s (reinforced). The reduction in initial overshoot indicated that the flexing base was a significant factor in abnormal piston motion. There was still an overshoot which should be further reduced, however it was clear that reinforcing the base under the motor was a simple design change that improved piston/motor motion. It is expected that reinforcing the base and improving the profiles minimises oscillatory piston motion and reduces the chance of abnormal vortex generation.

## 3.4 Device Optimisation III - Refined Motor Pulse Sequence

This chapter has clarified how adaptation of the design has ensured efficient use and suitable piston velocity profiles for ring vortex generation. This has employed a simple Arduino code where a top-hat function is used as the pulse sequence, striving to generate a trapezoidal profile. This top-hat function is idealised with infinite acceleration and deceleration, and drives the motor to go from zero to 100% of the requested speed instantly. Such discontinuity is not ideal for use, and may be straining the motor or exacerbating the oscillation issue. Stepper motor resources recommend a ‘graded’ profile where an acceleration is incorporated into the code to minimise strain on the motor and give the piston a chance to start moving before propelling it at maximum speed. Furthermore this may improve variability, as the piston behaviour will rely on the code rather than the minutiae of its setup - whether there is sufficient lubrication, water temperature etc. This section explores the most effective use of the motor in this device to ensure safety, reproducibility and longevity of the dynamic components.

### 3.4.1 Refined Pulse Sequence for Trapezoidal Piston Response

Here we consider optimised motor pulse sequences to generate trapezoidal profiles where the piston motion is a function of the **motor** input rather than phantom mechanics. This will be achieved by computing optimised pulse sequences for the acceleration, plateau and deceleration phases.

#### Acceleration

Acceleration is straightforward to programme for the Arduino Uno through an array of incrementally increasing speeds. An array of speeds from 0 – 2 cm/s was produced where the programmed speed increased linearly in a controlled manner (See Figure 3.9). Piston acceleration was measured at  $198 \pm 5\%cm/s^2$  when controlled by the top-hat function, demonstrating the maximum acceleration achieved by the piston in this environment. The programmed acceleration must be below the ‘threshold’ acceleration of  $198 \pm 5\%cm/s^2$  when under load to avoid strain on the motor.

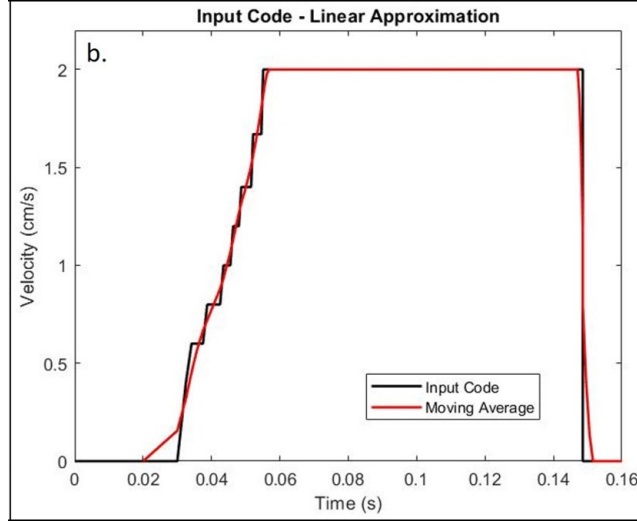


Figure 3.9: Graph presenting the proposed input code (black line) for the acceleration phase of the trapezoidal piston profile. The red plot shows the close-to-linear moving average.

Figure 3.9 presents the input code for the acceleration phase, where an acceleration of  $66.7\text{cm}/\text{s}^2$  is requested from the motor. A higher acceleration was achievable, but required less steps at each speed and resulted in skipping on occasion. This input code was tested with the phantom when the piston was under load through a full water tank. The piston achieved  $62\text{cm}/\text{s}^2 \pm 9\%$  over ten impulses. A slight discrepancy was expected due to friction and inertial effects, so this difference is not a concern. Its close proximity to the motor-commanded acceleration value and high reproducibility confirmed this acceleration method as viable for use with the phantom.

## Plateau

In an ideal environment, once the piston reaches its maximum programmed speed ( $PS$ ) it will remain at that speed until the deceleration phase. Any deviation from this top speed could impact the accumulation of circulation into the vortex core so ought to be minimised and a steady plateau achieved. An initial overshoot in speed was observed after implementing the acceleration phase for the piston profiles. This overshoot was effectively counteracted by time spent at  $90\%PS$ , where  $PS$  is the maximum programmed speed. The oscillation frequency was  $55\text{Hz} \pm 7\%$ , correlating to  $34\text{steps} \pm 7\%$  when at  $100\%PS$ . Therefore, the  $90\%PS$  stage lasts for 35 steps, before requesting  $100\%PS$  for the remainder of the plateau stage (See Figure 3.10). A number of input codes were investigated, and this regime was found to generate the best profiles with speeds within  $10\%$  of  $PS$  across the plateau phase. The oscillation amplitude after the first cycle was sufficiently small to not require further countermeasures.

## Deceleration

To complete the optimised input code profiles, a deceleration array was used to ensure reproducibility and minimal strain on the motor. Under a top-hat function the deceleration is slower than acceleration, as acceleration must overcome the static friction, producing a small ‘jump’ as the piston starts moving from stationary. The piston’s deceleration does not experience this, thus will be lower. The threshold piston deceleration for a top-hat input function was measured as  $101.82\text{cm/s}^2 \pm 7\%$ . The array used for acceleration was therefore reversed and implemented for deceleration for symmetry, with a steeper gradient to ensure maximum time at  $PS$  in the plateau stage. This deceleration array is presented below.

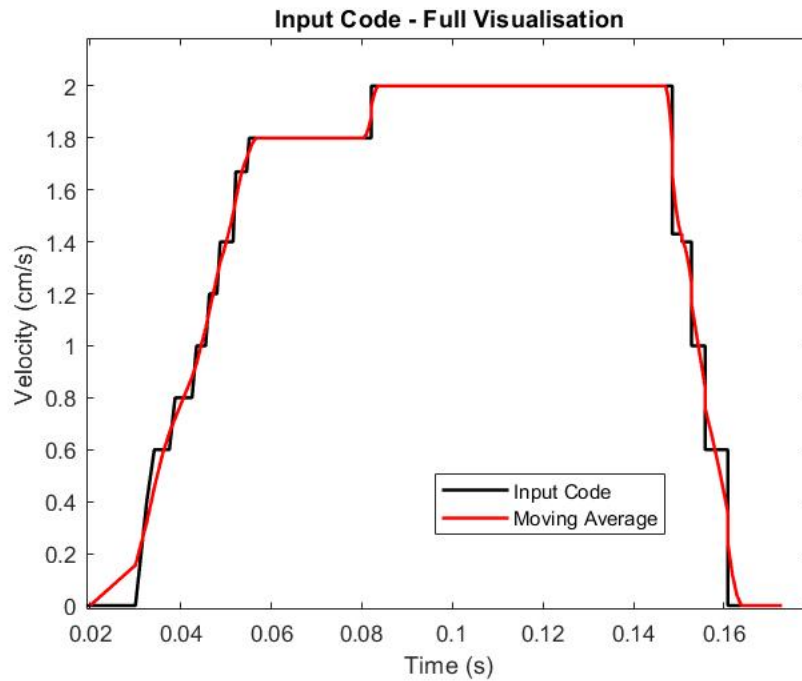


Figure 3.10: Graph presenting the proposed input code (black line) for the ring vortex phantom to generate a trapezoidal piston velocity profile. The red line shows the moving average of this profile.

The requested deceleration for the input code was approximately  $80\text{cm/s}^2$ . Once implemented on the piston, deceleration was measured at  $55.15\text{cm/s}^2 \pm 8\%$ . This was lower than the programmed deceleration, but its high reproducibility and proximity to the acceleration value ( $\sim 62\text{cm/s}^2$ ) commended this method for phantom use.

### 3.4.2 Full Input Profile Pulse Sequence

These code components were combined into a full template for piston impulses as presented in Figure 3.11.

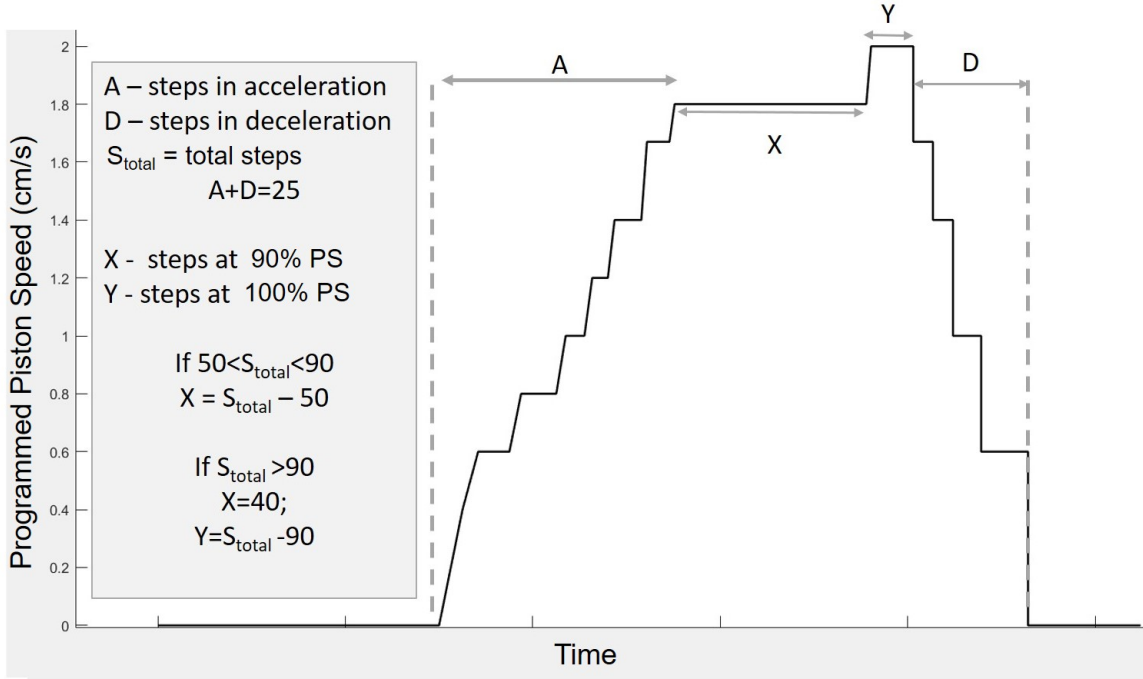


Figure 3.11: Schematic of the input code refined velocity profile for  $PS=2\text{cm/s}$ . Annotations include steps to calculate 90% $PS$  and 100% $PS$  displacements

To use this template for phantom experiments,  $A$  and  $D$  are fixed values, defined by the acceleration and deceleration array lengths.  $X$  and  $Y$  vary based on the overall displacement the user requests, as  $A+D+X+Y=Total\ Displacement$ . This template was tested for a range of conditions, varying the total displacement from 0.8mm to 2.4mm. Ten impulses were generated for each configuration with the piston under load and the encoder tracking each impulse. Analysis calculated the maximum speeds, acceleration, deceleration and average displacement for each condition. These results are presented below.

| Prog.Disp | Max Speed ( $cm/s$ ) | Accel. ( $cm^2s^{-1}$ ) | Decel. ( $cm^2s^{-1}$ ) | Displacement ( $mm$ ) |
|-----------|----------------------|-------------------------|-------------------------|-----------------------|
| 0.8mm     | $2.33 \pm 2.4\%$     | $63.7 \pm 10\%$         | $56.2 \pm 9.6\%$        | $0.81 \pm 1.51\%$     |
| 1.2mm     | $2.17 \pm 2.8\%$     | $63.4 \pm 6.9\%$        | $51.7 \pm 9.7\%$        | $1.13 \pm 1.2\%$      |
| 1.6mm     | $2.20 \pm 1.8\%$     | $59.5 \pm 8.9\%$        | $55.3 \pm 2.8\%$        | $1.6 \pm 0.52\%$      |
| 2.0mm     | $2.33 \pm 5.7\%$     | $64.6 \pm 9.3\%$        | $54.6 \pm 7.7\%$        | $1.9 \pm 0.9\%$       |
| 2.4mm     | $2.22 \pm 3.5\%$     | $62.7 \pm 9.8\%$        | $51.4 \pm 9.4\%$        | $2.4 \pm 0.86\%$      |

Table 3.1: NOR piston profile measurements using the linear encoder for motion under the optimised, graded motor pulse sequences presented in Figure 3.11

The values in this table, specifically the associated errors (listed as coefficient of variation throughout) indicate the reproducibility produced by using the optimised profiles

in place of top-hat functions. Across all conditions reproducibility was high, with variability less than 10% for maximum piston speed, acceleration, deceleration and overall displacement for displacements higher than 1.2mm. Acceleration was close to the expected  $66\text{cm/s}^2$  for all conditions, and deceleration was within 10% of the expected  $55\text{cm/s}^2$  with high reproducibility. These values indicated that the piston acceleration was now dependent on the motor pulse sequence rather than the mechanics of the setup. Measured displacement was also close to the programmed displacement for all profiles, ensuring the predictability of piston motion in response to the input code.

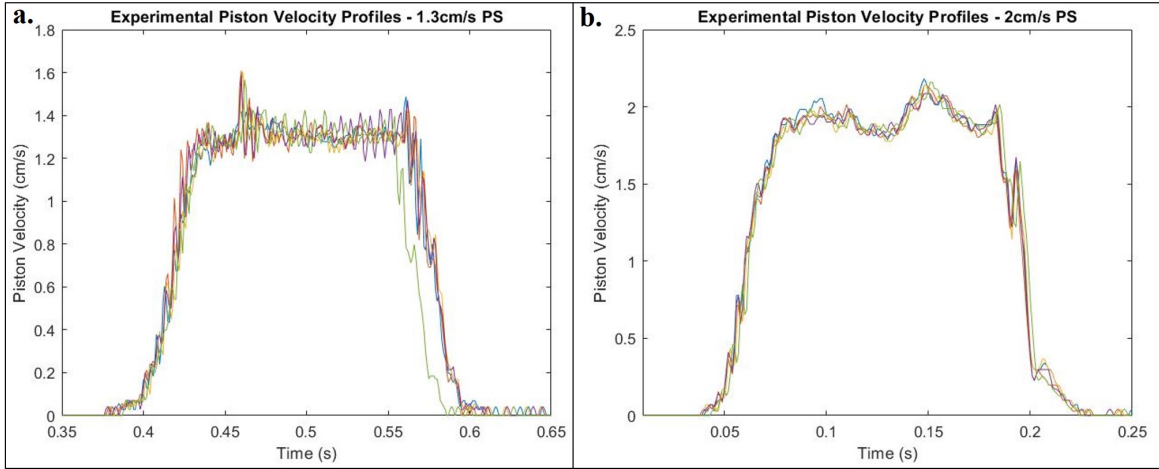


Figure 3.12: Experimental phantom profiles using the graded profiles. Graph (a) presents 5 profiles for a maximum programmed speed of 1.3cm/s and Graph (b) presents 5 profiles for a maximum programmed speed of 2cm/s.

In response to the optimised input code, the velocity profiles were considerably more trapezoidal and follow a reproducible shape. This is visualised in Figure 3.12, demonstrating the smooth acceleration and steadier plateau of two example profiles, with high reproducibility between runs. This template profile was deemed suitable for use in future experiments. By optimising the piston response profiles, the controllability of the phantom was much improved, and the phantom behaviour also now more closely reflects that found in the literature in similar devices.

## 3.5 Flow Optimisation

### 3.5.1 Introduction

This chapter has described the optimisation of the phantom, both through hardware improvements and refined motor pulse sequences. This has resulted in highly reproducible and controllable piston velocity profiles over a range of displacements and speeds. These alterations will have a significant impact on the phantom's vortices, particularly given the change of energy from the new, slower piston. The last stage in this phantom development

is to characterise these new flows, and to determine their **controllability**, **stability** and **reproducibility**. It is unknown whether the modified ring vortex energy will result in vortices with inferior reproducibilities and stabilities, so the ring vortex landscape will be investigated over a range of generating conditions and results compared to those from Chapter 2. Boundaries of this landscape are defined by the motor limitations, which is discussed in Appendix A.

### 3.5.2 Method - Ring Vortex Landscape

The experiments which are presented place in this sub-chapter had two objectives:

- Clarify the relationships between ‘input’ parameters (orifice diameter, stroke ratio etc.) and ‘output’ parameters (ring speed, stability, reproducibility) to ensure a full understanding of the ring vortex landscape and ensure controllability.
- Identify the most suitable vortices for use as reference flows using this phantom, with high stability and reproducibility. Determine whether these are as stable as previous vortices.

To achieve these objectives, a wide range of generating conditions were tested and their vortices analysed at the macro-scale using video recordings. Piston speed, piston displacement and orifice size were varied. The 10mm, 15mm and 20mm orifices were employed, with piston speeds of 2.5cm/s, 2cm/s and 1.3cm/s chosen. Stroke ratio was then varied through piston displacement to systematically generate vortices across the range that this phantom can generate.

To complete this experiment, the phantom was set up as described in Chapter 2, with the additional reinforcement under the motor stand. Motor pulse sequences were produced according to the templates listed in Section 3.4.2, with all tested configurations listed in the table below. It is worth noting that the 10mm orifice has no  $PS = 2.5\text{cm/s}$  configurations, as the displacement to achieve sufficient stroke ratio is shorter than the required acceleration and deceleration arrays combined.

## Tested Configurations

| Orifice | Max Programmed Speed (PS) | Stroke Ratios                          |
|---------|---------------------------|--|
| 10mm    | 1.33cm/s                  | /                                      |
| 10mm    | 2cm/s                     | 2.4, 2.7, 3.0, 3.3                     |
| 10mm    | 2.5cm/s                   | 2.4, 2.7, 3.0, 3.3                     |
| 15mm    | 1.33cm/s                  | 1.2, 1.5, 1.8, 2.1, 2.4, 2.7, 3.0, 3.3 |
| 15mm    | 2cm/s                     | 1.2, 1.5, 1.8, 2.1, 2.4, 2.7, 3.0, 3.3 |
| 15mm    | 2.5cm/s                   | 1.2, 1.5, 1.8, 2.1, 2.4, 2.7, 3.0, 3.3 |
| 20mm    | 1.33cm/s                  | 1.2, 1.5, 1.8, 2.1, 2.4, 2.7, 3.0, 3.3 |
| 20mm    | 2cm/s                     | 1.2, 1.5, 1.8, 2.1, 2.4, 2.7, 3.0, 3.3 |
| 20mm    | 2.5cm/s                   | 1.2, 1.5, 1.8, 2.1, 2.4, 2.7, 3.0, 3.3 |

Table 3.2: Experimental conditions used to generate ring vortices to measure stability and reproducibility for each configuration.

Fifteen rings of each configuration listed in Table 3.2 were generated, with an inter-ring time delay of 25 seconds. The rings were recorded at 100fps using the SONY RX10 camera mounted on a tripod at approximately 3m from the phantom wall. The camera was focussed onto the centre plane of the phantom tank, ensuring that the entire ring vortex path was captured. The linear encoder was used to ensure that the piston acted as expected within tolerances.

This experiment was performed without Laser-PIV equipment. Quantifying the dynamics of these vortices was therefore limited to macro-analysis using video capture. Properties such as circulation, energy and ring/core diameters can be inferred or estimated, however this analysis was limited to the direct measurement of ring velocity at any location. Post-processing calculated the initial speed (at 5cm from orifice), average journey speed (5-20cm from orifice) and the stability of each configuration. Desirable attributes for suitable phantom vortices mirror those discussed in Chapter 2, mainly speed reproducibility both at the start of the journey and overall journey, and high stability in speed. The data were plotted in two approaches: as absolute speed values with respect to generating conditions to establish **controllability**, then plotted as a function of **stability and reproducibility**.

### 3.5.3 Results I - Ring Vortex Landscape (Controllability)

Firstly the controllability of the ring vortices was evaluated. In this context controllability is how the user can ‘choose’ the ring vortex they’re generating by varying input conditions i.e. whether changing conditions has a distinct effect on the generated ring vortex. The vortices listed in Table 3.4 were analysed for their average speeds and plotted against stroke ratio (jet length/orifice diameter) for each orifice and piston speed.

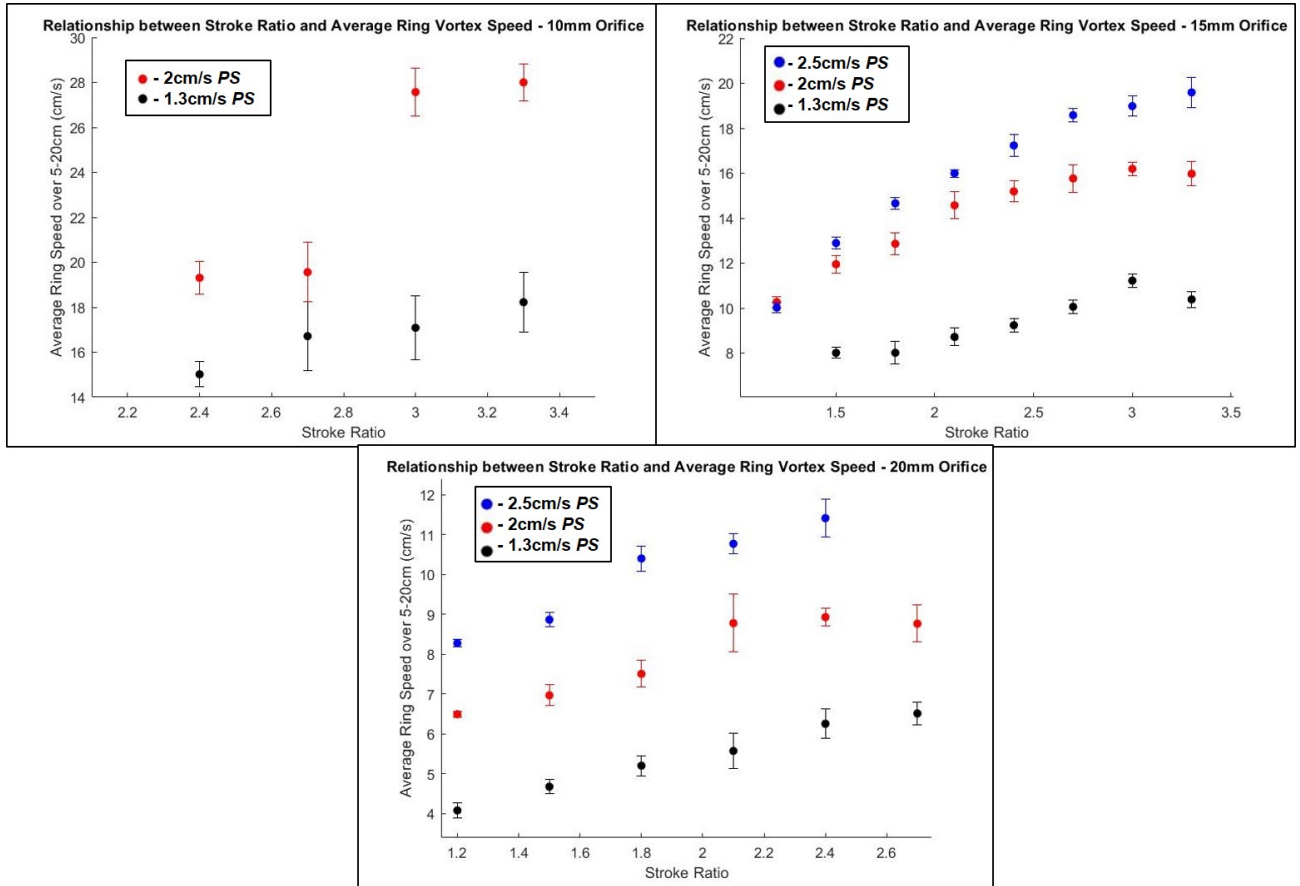


Figure 3.13: Graphs presenting average ring vortex speed over 5-20cm from the orifice in relation to stroke ratio. Graph (a) is for the 10mm orifice, Graph (b) for the 15mm orifice and Graph (c) for the 20mm orifice.

These graphs display a fundamental relationship for both the 15mm orifice (Graph B) and the 20mm orifice (Graph C) - as the stroke ratio was increased, the ring speed increased. This was evident in all piston speeds for these orifices, and was fairly consistent with few anomalies. The relationship was not fitted to a model as the quantitative relationship is not required; it is sufficient that the qualitative positive relationship exhibits controllability. If the user requires a faster ring, they can increase the piston displacement and the speed will increase. By comparing the y axes it was clear that decreasing the orifice size would increase the ring speed also, as expected. Interestingly the fast (red data-points) 10mm rings do not follow a smooth increase in speed. These datapoints represent vortices with a higher Reynold's number, so may indicate a transitional effect, but further investigation would be required to confirm this. These graphs can be used as reference to select the desired ring speed and read the corresponding input parameters to generate it.

The speed increase due to stroke ratio can be connected to ring vortex theory and formation mechanics, as the higher stroke ratio is achieved through a larger piston displacement. The piston propelling more fluid will accumulate more circulation (or energy)

into the jet, resulting in a higher speed of ring vortex. The literature [105] cites  $\frac{L}{D} = 4$  as the stroke ratio above which the ring vortex stops accumulating circulation from the jet. The maximum stroke ratio analysed here is 3.4, hence the increasing speed across the graphs so this threshold is not reached. Beyond that point the ring speed would stop increasing as the extra circulation is shed. Higher stroke ratios were not investigated as they produced visually disturbed, shedding vortices and unsuitable for a phantom flow. Some disturbance was observed in the fastest rings (red datapoints on Figure 3.13a) but other rings were visually laminar.

### 3.5.4 Results II - Ring Vortex Landscape (Stability, Reproducibility)

#### Initial Speed Reproducibility

With the controllability of the vortices confirmed, each individual configuration was assessed for its stability and reproducibility, relative to the stability and reproducibility achieved by configurations in Chapter 2. Dynamics achieved by the Chapter 2 OR piston vortices were as follows:

- **Reproducibility** - Parameters have a reproducibility of <12%.
- **Stability** - Parameters are stable within <10% over 14cm.

These were used for the basis of analysing the vortices in this experiment. Firstly, reproducibility of the ring speed at the start of its journey was analysed. The instantaneous speed of each vortex was calculated for 5cm from the orifice, along with the variability for each condition. This is plotted in the graphs below. Each graph represents the results from a different piston speed. Axes on the graphs are orifice diameter and stroke ratio respectively. Each datapoint represents the average of fifteen vortices and the coefficient of variability for the initial ring speeds, therefore representing the reproducibility of each condition. ‘Green’ datapoints exhibit the reproducibility previously seen on this phantom.

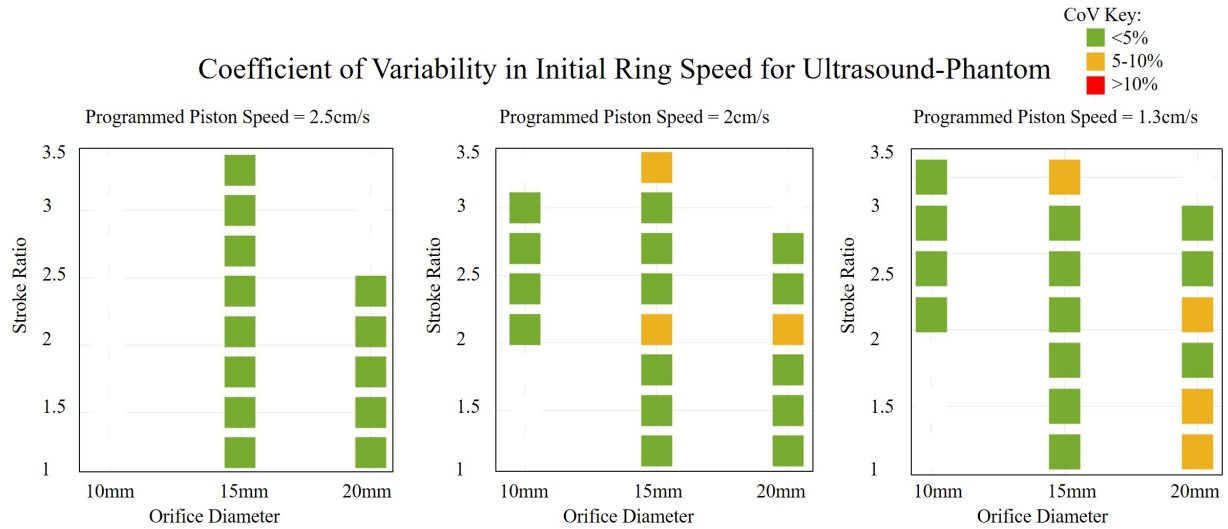


Figure 3.14: Graphs presenting the reproducibility of ring vortex starting speed (at 5cm from orifice) with varying stroke ratio, orifice diameter and maximum piston speed. Datapoints are colour-coded according to coefficient of variability and the in-figure key. (a) is Piston speed=2.5cm/s. (b) is Piston speed=2cm/s. (c) is Piston speed=1.33cm/s.

The reproducibility of the vortices varied over the conditions, however notably no ‘red’ datapoints are present, indicating that all vortices were reproducible to within  $\pm 10\%$  when at 5cm from the orifice. This value was taken at 5cm from the orifice to confirm reproducibility of the *generation*, as the ring has just formed and will not have undergone destabilising mechanisms such as diffusion or wake shedding at this point. A few datapoints indicate reproducibility over 5%, however these are scattered throughout the dataset.

### Average Journey Speed Reproducibility

The rings were also analysed for the reproducibility of their speeds over the journey. Unlike the first measurement which assessed the formation reproducibility, this indicated whether the rings’ *propagation* was reproducible, i.e. whether the ten assessed vortices in a configuration propagated in a similar manner. These results were plotted below in the same format as Figure 3.14, with each datapoint representing a coefficient of variation for each condition. ‘Green’ datapoints exhibit the reproducibility previously seen on this phantom.

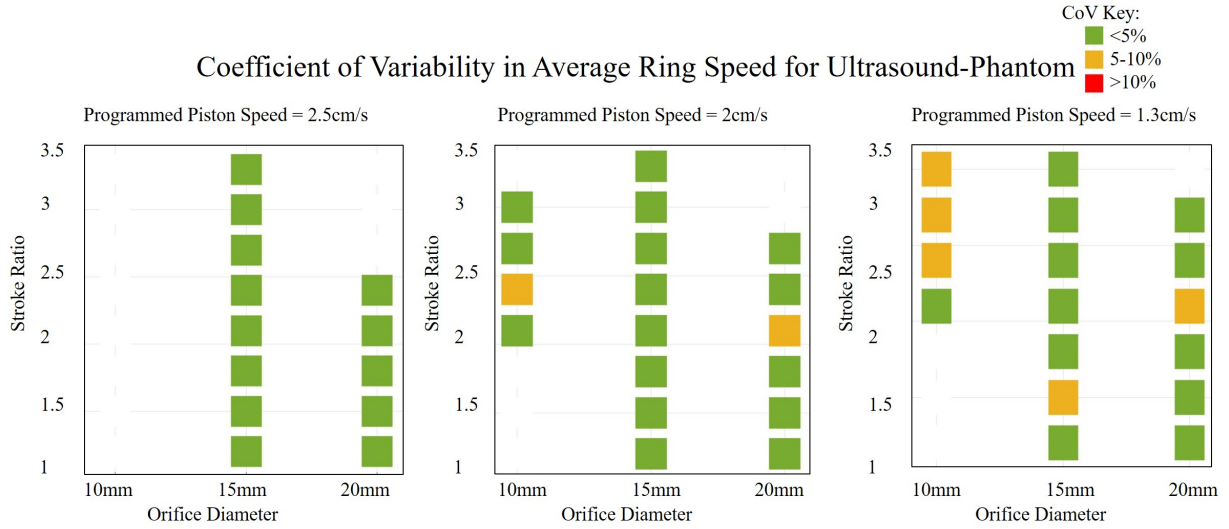


Figure 3.15: Graphs presenting the ring vortex average speed between 5-20cm path-length with varying stroke ratio, orifice diameter and maximum piston speed. Data-points are colour-coded according to coefficient of variability and the in-figure key. (a) is  $PS=2.5\text{cm/s}$ . (b) is  $PS=2\text{cm/s}$ . (c) is  $PS=1.33\text{cm/s}$

The results are largely positive, with a range of conditions exhibiting high reproducibility (<5%) over their journeys. Unlike the previous scattered ‘yellow’ datapoints, there is a localised yellow region in these results (Graph C), where the 10mm orifice had slightly elevated reproducibility between 5-10% across 3 of its 4 conditions. Values within this yellow region do not follow any trend, and range between 6.2-9.3%. This could be indicative of a mechanism becoming significant enough to hamper the vortex reproducibility, for example shedding. Shedding would decrease the reproducibility, as its unpredictable nature would affect each ring differently. This higher variation will be taken into account when selecting vortices, as it is important for phantom flows to behave the same (within tolerances) each time they are generated.

## Stability

The final parameter to be analysed was the stability of the ring vortices - how much they decelerated over a given path-length. In chapter 2 this was quantified by the ‘14cm-stability lifetime’, defined as how much the rings decelerated over the 14cm Laser PIV imaging domain. In this analysis the camera recorded the rings across the full tank, so more information was available. It was observed in Chapter 2 that the Unit-0 rings (measured in 2019) decelerated between 6-29% over the 8-22cm domain relative to the orifice. More stable rings were  $\sim 85\%$  of their starting speed at the end of the domain. The rings here are analysed from 5-25cm from the orifice. The closer-to-orifice and larger domain requires a new metric, so ‘70% Stability Lifetime’ was established, defined as the path-length over which the ring travels before decelerating by 30% of its initial speed. This metric indicates over how long each condition can be imaged and the ring remains

the same within these tolerances, with longer path-lengths indicating a more stable ring. A 70% Stability lifetime of 15cm and above would demonstrate similar stability to the most stable configurations in Chapter 2. The rings' progressive speeds were calculated with the results plotted below. Please note, each datapoint is the 70% stability lifetime, **not** the coefficient of variation for this figure.

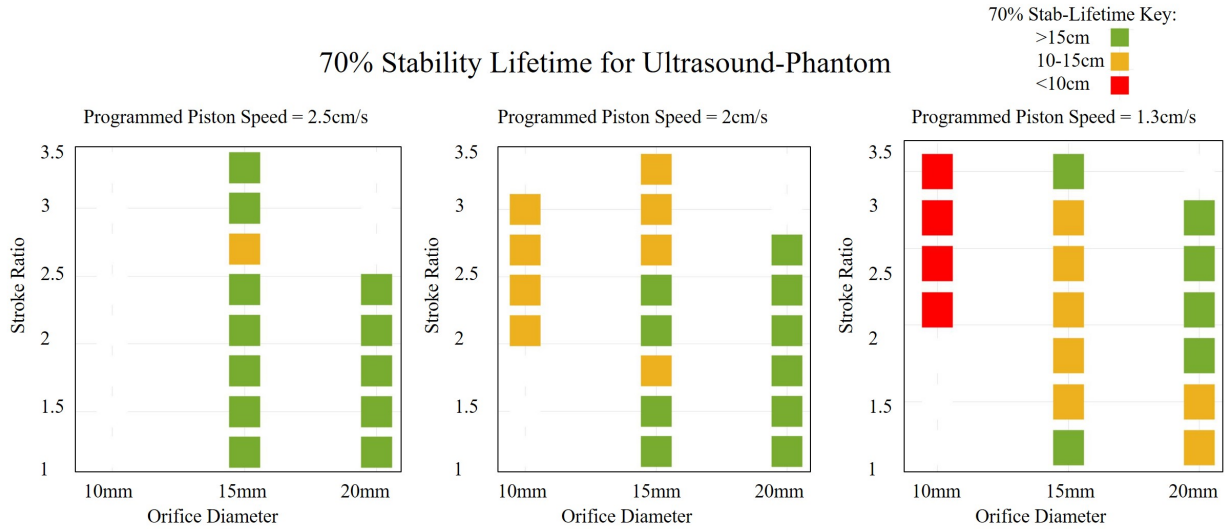


Figure 3.16: Graphs presenting the ring vortex lifetime (defined as the distance travelled with stability of 70%) with varying stroke ratio, orifice diameter and maximum piston speed. Datapoints are colour-coded according to 70% Stability Lifetime and the in-figure key. (a) is Piston speed=2.5cm/s. (b) is Piston speed=2cm/s. (c) is Piston speed=1.33cm/s.

A range of stabilities is evident in these graphs for the conditions assessed. Most notably, no 10mm orifice rings exhibited a lifetime of over 15cm, with the Graph C datapoints exhibiting a lifetime less than 10cm. Twenty seven conditions exhibited 70% stability lifetimes of over 15cm, reflecting values similar to those found in Chapter 2 for the OR piston vortices. Lifetimes between 10-15cm can be observed for the larger orifices also, particularly in the slower piston speeds.

## 3.6 Discussion

### 3.6.1 Suitability of Optimised Ring Vortices for Phantom Flow Use

The rings have been assessed at the macro-scale for their suitability on three different metrics: initial speed reproducibility, average speed reproducibility and stability. Visualising these datasets in one plot is helpful for determining the suitability of each generating condition for phantom flow use. This is visualised in Figure 3.17.

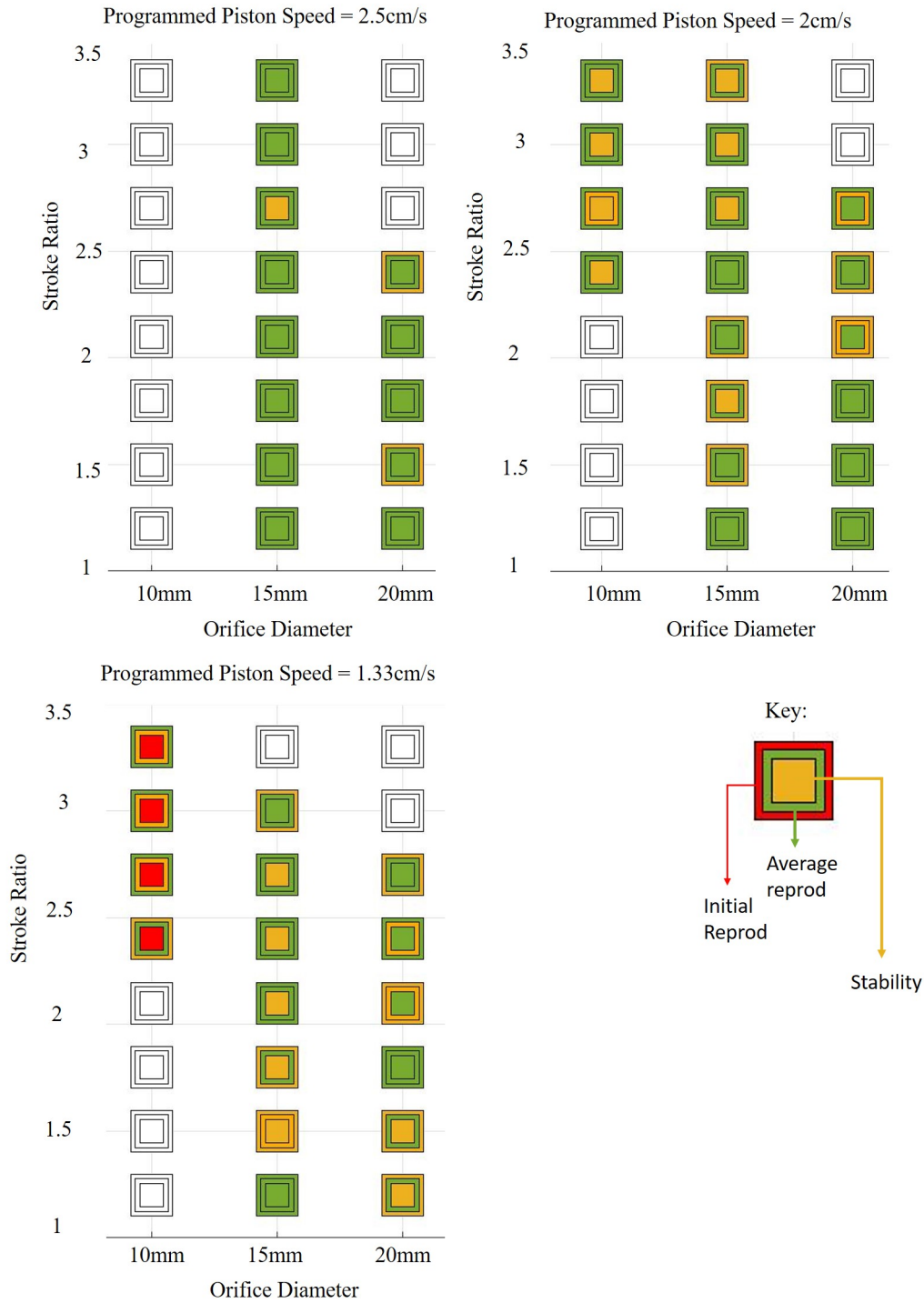


Figure 3.17: Ring vortex maps showing the stability, initial speed reproducibility and average speed reproducibility of ring vortices generated by the optimised ring vortex phantom.

Vortices who hold green datapoints on all three metrics exhibited the same stability

and reproducibility (at least) as previously imaged vortices from Chapter 2. Using the stated thresholds as requirements for a suitable phantom reference flow using this device, there are 20 valid configurations which fulfil the requirements. These configurations are listed in the table below.

| Orifice | Max Speed | Stroke Ratio                      |
|---------|-----------|-----------------------------------|
| 15mm    | 2.5cm/s   | 1.2, 1.5, 1.8, 2.1, 2.4, 3.0, 3.3 |
| 15mm    | 2cm/s     | 1.2, 1.5, 2.4                     |
| 15mm    | 1.33cm/s  | 1.2                               |
| 20mm    | 2.5cm/s   | 1.2, 1.8, 2.1, 2.4, 2.7           |
| 20mm    | 2cm/s     | 1.2, 1.5, 1.8                     |
| 20mm    | 1.33cm/s  | 1.8                               |

Table 3.3: List of suitable ring vortex configurations for phantom use. Ring vortices generated using these settings have reproducible speeds within  $\pm 5\%$  and a 70% stability lifetime of over 15cm

This is a substantial number of high-stability, high-reproducibility ring vortices that can be generated by the optimised ring vortex phantom. These rings range from 9cm/s to 23cm/s and are generated by two orifices, thus are grouped into two groups with similar ring radius. Each has a unique vector flow profile, circulation, energy, and core radius, thus will give a variety of assessment parameters for QA procedures on scanning equipment. However, there is similarity in neighbouring conditions: for example, when the orifice diameter = 20mm, piston speed = 2cm/s and stroke ratio = 1.5 and 1.8 respectively the generated rings' speeds differ by only 0.6cm/s. This calls into question the diversity of these selected configurations and whether their application would rigorously challenge imaging modalities and reveal limitations. A more diverse range of vortices in both speed and size would be beneficial for effective testing.

This limitation can inspire an interesting debate regarding the requirements for state-of-the-art imaging technologies' QA protocols. The ring vortex phantom is designed for use on all quantitative flow imaging technologies, ranging from basic US techniques to modern modalities capable of generating high-res vector flow maps. Suitable ring vortices may therefore vary depending on which modality is being tested and its scanning procedure. For example, a Doppler probe for a 2D B-mode scan would visualise and measure the ring over a limited path-length ( $\sim 5\text{cm}$  - typical probe length) if the probe is aligned along the ring travel-path. Factors such as stability are not important here, as the probe can be placed at any point on the vortex path. For example, if it were positioned to image the domain at 5-10cm from the orifice, the stability up to 10cm from the orifice would be relevant, but not beyond. The key vortex attributes here would be high ring reproducibility and stability over 5cm-10cm so rings with a lifetime of 5cm would be sufficient. Rings would be selected based on their speed to ensure a good number of frames capture the flow, which will depend on the selected US parameters (e.g. depth, frame rate, frequency).

On the other hand, state-of-the-art scanners such as 4D-MRI or VFI are designed to image and quantify larger volumes over time. 4D-MRI can capture the heart in one scan (approx. 12cmx8.5cmx6cm [58]), thus depending on orientation, could image an individual ring multiple times as it travels over the imaging domain. Up to 12cm of stability would therefore be required from the vortex as the vortex is visualised throughout its propagation. Stability is important here to ensure that the ring at end-of-domain is identical to the ring at start-of-domain, within tolerances. This will fulfil the requirement of a consistent flow. Phantom requirements therefore vary based on imaging technology specifications.

Pertaining to this argument, Table 3.4 show an additional 23 configurations which are suitable in terms of reproducibility alone. These rings range from 10cm/s to 33cm/s at 5cm from the orifice, which gives a larger range in available speeds and cover all three orifices in question. If a particular scanner or user required a high-speed ring, they would be able to use these, however a recommendation would be given to image it over a shorter path-length, e.g. 10cm. This results in 43 viable ring vortex configurations available for use, with particular caveats for use given the scanner requirements.

| Orifice | Max Speed | Stroke Ratio                      |
|---------|-----------|-----------------------------------|
| 10mm    | 2cm/s     | 2.1, 2.4, 2.7, 3.0                |
|         | 1.33cm/s  | 2.1, 2.4, 2.7, 3.0                |
| 15mm    | 2cm/s     | 2.1, 2.7, 3.0, 3.3                |
|         | 1.33cm/s  | 1.5, 1.8, 2.1, 2.4, 2.7, 3.0, 3.3 |
| 20mm    | 2cm/s     | 2.4, 2.7                          |
|         | 1.33cm/s  | 2.4, 2.7                          |

Table 3.4: List of suitable ring vortex configurations in terms of reproducibility only. Average speed over 5-20cm and starting speed at 5cm were considered.

The phantom is limited mechanically by what it can generate, but is able to generate a range of vortices over a spectrum of conditions for assessment of imaging modalities.

### 3.7 Conclusions

This chapter has assessed the effectiveness of the ring vortex phantom in its status at the commencement of this project (Unit-0) and identified optimisations which improved and characterised its application as a test object, resulting in the **Unit-1** version of this phantom. A piston re-design, combined with high-resolution tracking, highlighted the variability and ‘jolting’ motion of the original piston, prompting a move to the new, non O-ring piston. The new piston generates jets (and therefore rings) with significantly less energy than previous work. The piston profiles were then refined through tailor-made input code profiles, which resulted in a non-oscillatory trapezoidal velocity profile more closely related to those in the literature. These profiles consistently exhibit accelerations and decelerations of  $\pm 65\text{cm}/\text{s}^2$  and  $\pm 55\text{cm}/\text{s}^2$  respectively within tight tolerances, and a plateau stage with minimal variation.

The new piston and refined profiles were then exercised to investigate the vortices that the phantom can generate, and determine whether they attained similar stability and reproducibility to previous vortices. Their stability, initial reproducibility and journey-long reproducibility was analysed at the macro-level using ring speed. 20 configurations were found to exhibit high stability and reproducibility similar to those from the OR piston, with a further 23 demonstrating suitable reproducibility. The relative importance of these two genres of ring were discussed in relation to imaging modality assessment. It can be confirmed that the modified Ultrasound-Phantom Unit-1 is able to generate stable and reproducible ring vortices with high confidence in the piston motion and vortex macro-behaviour. Characterisation of the micro-field is not achieved in this exercise.

# Chapter 4

## Quality Assuring the Ring Vortex Phantom in Real-Time

### 4.1 Introduction

The ring vortex phantom has been optimised and characterised with respect to device and flow behaviour. It has proven its high reproducibility and stability for a range of ring vortices at the macro-scale. The phantom is therefore technically ready for more widespread testing and validation using clinical imaging techniques. A barrier to its application here, however, is the low confidence exhibited by new users. Both the device's novel flow profile and the ring vortex' relative obscurity result in users questioning the reliability and robustness of the flow and device during use. The phantom currently uses pre-collected experimental data to characterise phantom functionality, where sub-mm PIV (OR piston) or macro-scale camera (NOR piston) is available for each experimental condition. It has been argued however that these benchmarks don't account for unintended variability in the phantom at the point of experimental application.

Currently if a user wishes to have information regarding individual vortices, analysis relies on video capture, a time-consuming technique which requires 3m of laboratory space, an expensive camera, and is sensitive to human error through manual analysis. Analysing rings in this manner proves that the rings are propagating at the expected speed, and reassures users. However, it is limited by the various inefficiencies, as no real-time feedback is given and rings are assessed after the end of the experiment. Unless a clear malfunction occurs, users may be unaware of abnormal dynamics until after the fact, potentially invalidating any collected data. Real-time information regarding the phantom behaviour would be beneficial and allow for adjustments as needed. A transition between user-performed analyses to automated processes is also desirable to ensure consistency.

This chapter will therefore present the design, manufacture and testing of a novel tool which performs quality assurance on the device in real-time, ensuring that both its components and the flow are behaving within tolerances, and highlighting any abnormal behaviour. A review of other phantoms will be conducted to establish different levels of QA on phantom devices. The ring vortex phantom's QA tool will be described in

Section 4.3., followed by the user interface and combination code. Section 4.4. will compare experimental results to both video capture and PIV datasets to validate its use. Finally, Section 4.5. will discuss its potential for clinical translation and future device improvement. This QA tool was manufactured in collaboration with an electrical engineer.

## 4.2 Background - Phantom Quality Assurance in the Literature

Chapter 1 presented a wide range of phantoms available both commercially and as one-off research objects, and briefly discussed their ‘ground-truth’ datasets - whether flow profiles were characterised by values derived from analytical, numerical or experimental methods. These datasets provide a benchmark representation of the flow field, increasing trust in the device and its flow. This confidence can be furthered through quality assurance on the phantom during use. A range of phantoms will therefore be reviewed here to determine to what level, if at all, phantoms are being quality assured during their use, or if their correct functionality is being assumed.

Dynamic flow phantoms use commercial (e.g. stepper motor) or custom-built components (e.g. piston) to generate the desired flow profile. Commercial components are validated by the manufacturer, often accompanied by a data-sheet of their tolerances in certain environments. However, once the component is integrated into a custom-built phantom environment, it should be re-characterised to ensure no abnormal behaviour. An example of this is the unexpected motor/piston motion discovered in Chapter 3. Arguably this validation at point of manufacture should continue and QA should be performed regularly on the phantom to detect abnormalities from one-off malfunctions or component wear. This discussion investigates two forms of QA: ‘*device QA*’, to determine whether dynamic components are functioning to specification, and ‘*flow QA*’, to ensure the flow profile is within tolerances.

### 4.2.1 Device QA

Device QA is a straightforward task, with dynamic components (motors, pumps, pistons) often tracked or sensed, either through in-built tools or additional devices such as encoders in the literature. Different levels of device QA exist, with varying confidence in the associated device behaviour. The most basic level is characterising the component motion (typically piston velocity profile or input waveform) before commencing data collection and assuming that the behaviour remains unchanged during use. This is seen often in the literature [80],[72],[32],[74],[49] and is useful, but will not detect any malfunctions/abnormal behaviour during data collection. This is also currently used by the ring vortex phantom. The next level of device QA is tracking component motion in real-time during data collection to detect any abnormal motion [81],[73],[63],[121],[122]. This inspires more trust as it gives individualised information for each flow profile and allows the discounting of flow profiles if any malfunctions occur. For example, if a piston sticks,

or a motor skips steps during a specific run, this will be immediately detected and the resulting flow discounted. Overall, device QA is a well-established practice in phantom development, whether in pre-collected average functionality or real-time individualised measurements.

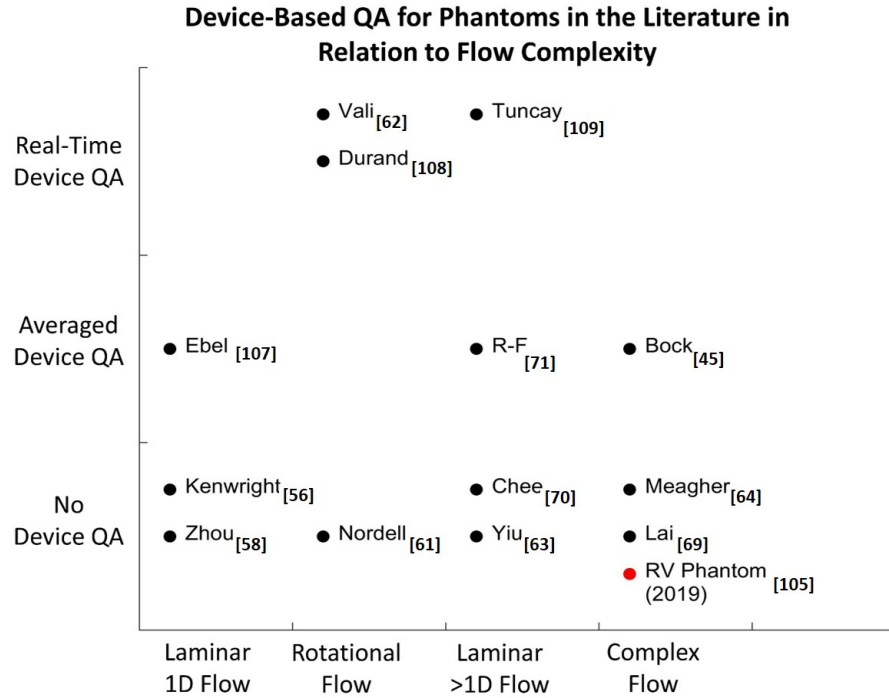


Figure 4.1: A qualitative graph presenting the QA procedure for device functionality in phantoms from the literature. ‘Averaged QA’ refers to pre-collected device characterisation, while ‘Real-Time QA’ refers to components being actively monitored during experiments.

Figure 4.1 presents a range of phantoms in the literature and their associated device QA. They are classified according to flow complexity and their level of device QA. Most devices perform a level of QA on their components. Simple phantoms generating laminar 1D flows and rotational flows primarily perform real-time QA through tracking the motor motion or light-gates. A notable finding is that no phantoms which generate complex flows perform real-time device QA. Instead they rely on averaged functionality.

### 4.2.2 Flow QA

Flow QA is a less straightforward task in phantom development, particularly when considering complex flows. Flow QA levels exist, similar to those for device QA. These are related to the form of ground-truth datasets that characterise the flow dynamics. The most basic flow QA collects ground-truth datasets (through analytical, experimental or numerical means) in a single collection session and assumes they describe the flow behaviour in further experiments. This is the current flow QA level achieved by the ring

vortex phantom, by collecting Laser PIV data and assuming its validity, or the macro-scale data collected in Chapter 3. To surpass this, the next level requires real-time flow visualisation.

If analytical or numerical formulations are used to describe the flow, then this will involve taking real-time device QA measurements (e.g. how fast the motor propels fluid for a certain run) and using these values as the basis for the analytical or numerical formulation. If the theoretical representation of the flow is accurate, this is an effective form of flow QA. Another form of real-time flow QA is through direct measurements of the flow in real-time. This can be achieved through imaging (e.g. PW Doppler) or select measurements (e.g. flow rate) which are used to characterise the flow field.

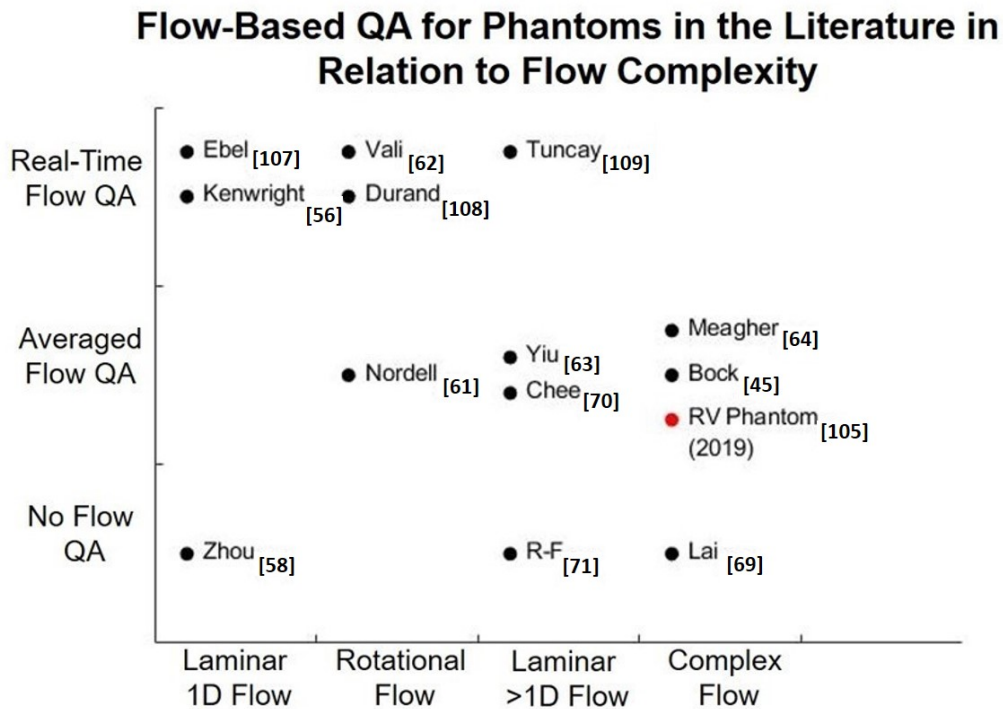


Figure 4.2: A qualitative graph presenting the QA procedure for flow behaviour in phantoms from the literature. ‘Averaged QA’ refers to pre-collected datasets whose averages are used as ground-truth, while ‘Real-Time QA’ refers to flow behaviour analysed directly during experiments.

Levels of flow QA were reviewed across phantoms in the literature with a range of QA methods observed. More complex phantoms (spiral phantom from Yiu [32], helical toroid form Chee [80]) typically rely on averaged flow QA through CFD or PIV. Real-time flow QA is present but largely limited to the simpler flows, where analytical ground-truth datasets are used, refined using real-time device QA. Direct measurements of flow behaviour is evident, but seemingly not implemented in regular use. It is notable that for more complex flows where analytical models are not available, flow QA is reduced to

relying on averaged, experimental visualisations.

### 4.2.3 Phantom QA and Flow Complexity

A trend is clear in this review, where the more complex a phantom's reference flow, the less real-time QA is performed, particularly flow QA. This is linked to the ground-truth datasets used for flow characterisation. Increased flow complexity can lead to decreased trust in its flow reproducibility/stability and reduced availability of analytical or numerical solutions. Transitioning to non-laminar, 3-dimensional flow in complex geometries such as bifurcations or stenoses introduces uncertainty around the intricacies of the flow profile, and experimental ground-truth datasets are required. Using PIV or LDV to visualise the flow every time is unrealistic, either through lack of space, high cost, or environmental restrictions such as MRI magnetic fields. More complex phantoms therefore rely on one-time visualisations which are averaged and used as the ground-truth for the long term. This gives accurate and precise visualisations of the flow with theoretical assumptions removed but risks becoming invalid since complex behaviour is rarely predictable, and components can vary over time, with an unknown effect on the flow.

The 'gold-standard' quality assurance for a dynamic, complex flow phantom would therefore integrate real-time device and real-time flow QA, so both the dynamic components and flow behaviour are monitored in real-time to ensure their correct dynamics. Flow QA is difficult to perform on complex flows, so would require either an accurate analytical representation or a flow profile where taking bulk measurements could be reliably mapped to a flow field at the micro-scale.

### 4.2.4 Ring Vortex Phantom QA Procedures

The ring vortex phantom has to this point used averaged device QA, taking encoder readings and assuming the piston moves as such in all experiments. Flow QA was performed through a one-time PIV experiment and one-time macro-scale experiment where the vortices were averaged for each condition and all future rings assumed to lie within these tolerances. These methods were useful but limited for further experiments as there was no guarantee that the rings and device still behaved accordingly. The ideal ring vortex phantom would incorporate real-time device QA through tracking the piston on every impulse, and taking measurements from the flow to characterise each vortex. The ring vortex is a unique structure with consistent behaviour and well-established properties. Any abnormality in function is immediately apparent through a visually different speed ring, or a ring which breaks down before it should. If this happens, the vortex in question can be discounted. The ring vortex phantom, is therefore in a position to achieve real-time device QA and flow QA through a series of simple measurements. If successful, this will surpass other available phantoms and increase confidence in the device and its vortices for external users.

## 4.3 Methods - Instrumentation Pack

A QA tool for the ring vortex phantom is therefore proposed, comprised of individual components which combine to form an ‘instrumentation pack’. The quality assurance tool is comprised of three components: a linear encoder (as introduced in Chapter 3), a laser-photodiode array, and a Doppler probe. These devices each measure a key property of either the phantom or ring vortex behaviour, to ensure it is working correctly and the reference flow is acting within tolerances. This will implement flow and device QA, both in real-time.

### 4.3.1 Linear Encoder- Device QA

To achieve device QA, the LM10 linear encoder is used, which has been described in detail in Chapter 3. To recap, this digital device is attached to a plate adjacent to a magnetic strip embedded in the piston stem at a ride height of 1mm. As the piston is propelled, the encoder tracks its changing relative position at 100Hz and transmit the data to MATLAB, where its velocity profile is calculated. Tracking the piston profile is key to ensure the phantom is working correctly, as it is the only dynamic component and has a proven effect on ring vortex behaviour (Chapter 3). Consistent tracking of the piston motion will ensure no oscillation is occurring and the correct trapezoidal velocity profile is achieved. The combined cost of the encoder, interface and 10cm long magnetic strip is £420 at the time of writing, significantly increasing the cost of the phantom. This component measures the average speed and displacement of each piston profile.

### 4.3.2 Laser-Photodiode Array - Flow QA

The second component performs QA on the ring vortex itself, by measuring its translational speed. This is a significant bulk property for the ring vortex and is often the first indicator of anomalous behaviour, given its close relationship to circulation/energy and ring size. For this component, two Class 3B 500nm wavelength pencil lasers were mounted on the tank wall and projected across the fluid volume crossing the ring vortex path. Their beams were positioned at 8cm and 18cm from the orifice exit plane, incident on a photodiode circuit located outside the opposing tank wall, generating a current. Each photodiode (model BPW34) was connected to a 14-pin transimpedance amplifier with a  $10\text{M}\Omega$  resistor and 1pF capacitor in parallel, ensuring circuit stability and sufficient current amplitude. The diodes were connected in photovoltaic mode, with cathode to negative input and anode to ground (See Figure 4.3). This circuit in turn was powered and controlled by an Arduino Mega 2560 Rev3 board. Components were selected for their number of input pins, as given the transient nature of the device, more circuitry may need to be added at a later date. Using a 4 op-amp amplifier and a larger Arduino Mega board will facilitate any upgrades.

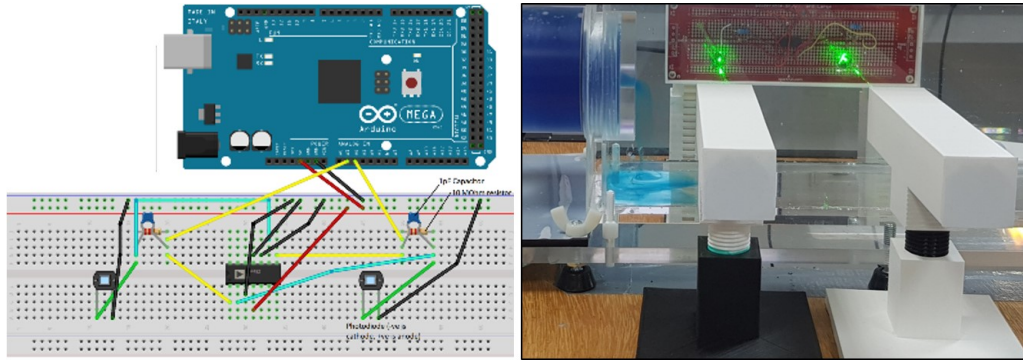


Figure 4.3: Photo of the laser-photodiode array, along with the circuit diagram used to power the photodiodes.

The lasers generate a current as their illumination falls incident on the photodiodes. By seeding the ring vortices with neutrally buoyant dye and  $10\mu\text{m}$ -diameter polyamide particles, the laser beam will be partially scattered as the ring travels through the beam. This causes a momentary fluctuation in the diode current, regaining its original magnitude once the ring has passed. Combining the time delay between current ‘dips’ and the known inter-diode distance of 10cm, the ring’s average speed can be easily calculated.

To ensure repeatability and reproducibility between measurements, the lasers and photodiode circuit must be securely mounted onto the phantom. This was achieved through rapid-prototype 3D printing, with structures designed and printed for both the lasers and the circuit/Arduino board. Both the laser and circuit holders are height adjustable. A cover was printed for the circuit also, to ensure no water from the open tank splashed onto the circuit, according to health and safety regulations. These structures are lightweight and cheap to manufacture however are not robust and can be easily broken if manhandled. They are designed for laboratory use only in the current phantom development stage, and must be upgraded for any extensive/commercial use in the future.

Laser data collection is straightforward using Arduino libraries supported by MATLAB. A program was written to detect and analyse diode readings, and calculate ring speeds. Photodiode readings are collected through a for loop (using readVoltage function) and are saved to an array. The loop time duration is recorded and used to calculate sampling frequency. Alerts sound before and after the loop so the user is confident that the timing is correct and the photodiodes were transmitting data as the ring passed. The minimum value from each voltage array is then found, corresponding to each current ‘dip’ as the ring crosses the beam, and the time delay between dips found. The inter-diode distance (10cm) is divided by this time difference to calculate the ring’s average speed. This process is repeated for the number of generated rings (the user defines this value at the start of the code), with a rateControl function ensuring the ring-loop takes 22.2 seconds to complete for a 20 second inter-ring delay so each ring is captured. A code snippet is displayed below for photodiode data collection and analysis.

```

pause(3); %Initial delay for ring #1
r=rateControl(1/5); %Fixes loop rate - denominator = phantom delay +
2.2s
mega=arduino(); %Starts connection with arduino

reset(r);
for a=1:NumberofRings

tic %starts timer
for p=1:looplength
    voltage1(p)=readVoltage(mega, 'A1'); %Collect voltage readings
from A1 pin
    voltage2(p)=readVoltage(mega, 'A2'); %collect voltage readings
from A2 pin
end

timelasers=toc %stops timer, calculates loop duration
timevectorlaser=linspace(0,timelasers,looplength);%create time
vector

%plot voltage values collected
plot(timevectorlaser,voltage1);hold on;
plot(timevectorlaser,voltage2);

[Min1laser,Ind1laser]=min(voltage1); %find minimum voltage value
[Min2laser,Ind2laser]=min(voltage2); %find minimum voltage value
ringspeed=10/(timevectorlaser(Ind2laser)-
timevectorlaser(Ind1laser)); %calculates ring speed

waitfor(r); %waits for the loop time to end
end

```

Figure 4.4: A MATLAB code snippet for reading and processing laser data for the ring vortex phantom instrumentation pack.

### 4.3.3 Doppler Probe - Flow QA

The third component for the instrumentation pack is the Doppler probe, which assesses the ring vortex micro-flow. The entire flow-field of the ring can't be measured in 2-D in real-time, however specific values can be inferred through effective instrumentation. Measuring micro-flow in addition to ring speed will increase confidence in the flow and ensure the ring is correctly formed. This can be achieved using the Doppler effect. Doppler probes are widely used in medicine to detect micro-flow velocities by measuring frequency shift from scattered waves. By scattering ultrasound waves from scattering particles within the ring, its behaviour can be characterised. The probe used here was 1-D, continuous wave with a 5MHz frequency and had a focal length of 4-8cm and beam width of approximately 5cm. It was mounted at the end of the tank with the beam axis directed along the ring path, aligned to the orifice centre, with coupling gel used to reduce attenuation between the probe and tank wall. Polyamide particles seeded within the rings ensured sufficient scattering and signal amplitude.

Data collection from the probe through MATLAB was facilitated by a 2-band 3.5mm aux cord and an audio interface (a requirement due to combined headphone/microphone jack on the laptop). The probe was turned on before the experiment starts, with MATLAB

recording its output ('AudioRecord' function) from 1.5s before the motor is propelled. The ring generation and propagation was recorded for 3 seconds, generating a signal which detected the motor motion, piston propulsion and ring propagation.

The beam has a 5cm height, encompassing the entire 2cm tall ring and some surrounding ambient fluid, thus a multitude of micro-velocities are detected in the probe signal. It would be impossible, given the probe's continuous wave and lack of depth information to fully dissect the signal frequencies. It was found, however, that the parameter of CentVect is detectable within a frequency signal, with an amplitude higher than surrounding components.

To detect this frequency, the 'ring signal' (portion of the audio which corresponds to the ring propagating towards the probe) is detected through increased moving average above background noise (Panel (a) on Fig 4.5). This array is segmented into 0.1s sections, with a fast Fourier transform (FFT) applied to each section (Panels (c,d) on Fig 4.5). This generates a complex output, so the absolute is found, and the second, mirrored, portion of the FFT removed, leaving a spectrum of varying amplitudes. This is converted into frequency space and into the corresponding speed components using the Doppler equation.

The output encodes the relative amplitudes of speed components within the signal. The frequencies were grouped into 10Hz bins to ease analysis, and plotted in a histogram (Panel (d) on Fig 4.5). The moving mean was found along this histogram, and the percentage difference found between each bin and its corresponding moving mean, to detect any anomalous frequency amplitudes (Panels (e,f) on Fig 4.5). If the bin mean was more than the moving mean this flagged, as CentVect has a higher-than-surrounding mean. These percentage differences were saved to an array. Frequencies within a range of 600Hz centred at the 'expected' CentVect (CentVect based on configuration speed average) were assessed, to eliminate low-speed frequencies (Panel (g) on Fig 4.5). The two most dominant frequencies were found within this range, defined by those with the largest % difference between their amplitudes as the local moving average. This was repeated across all 0.1s segments of the signal. The anomalies were filtered for those within 10% of CentVect, with those within the range deemed to be CentVect. CentVect should be detected consistently throughout the signal, whereas noise or fluid fluctuations will not, thus the output was the number of 'CentVect' readings detected throughout the signal. For example, if the signal is 1s long, and there are 8 dominant readings which lie with the CentVect tolerance, this will be a reliable reading of CentVect, whereas only 1-3 detections will not, and the ring should be analysed further. Similar to the previous algorithms, this was repeated across all generated rings and the 'Number of CentVects' and average 'CentVect' readings saved for future assessment. This method is visualised in a flowchart in Figure 4.5, and semi-quantitatively confirms expected ring behaviours, highlighting anomalous ring flows that deviate from this.

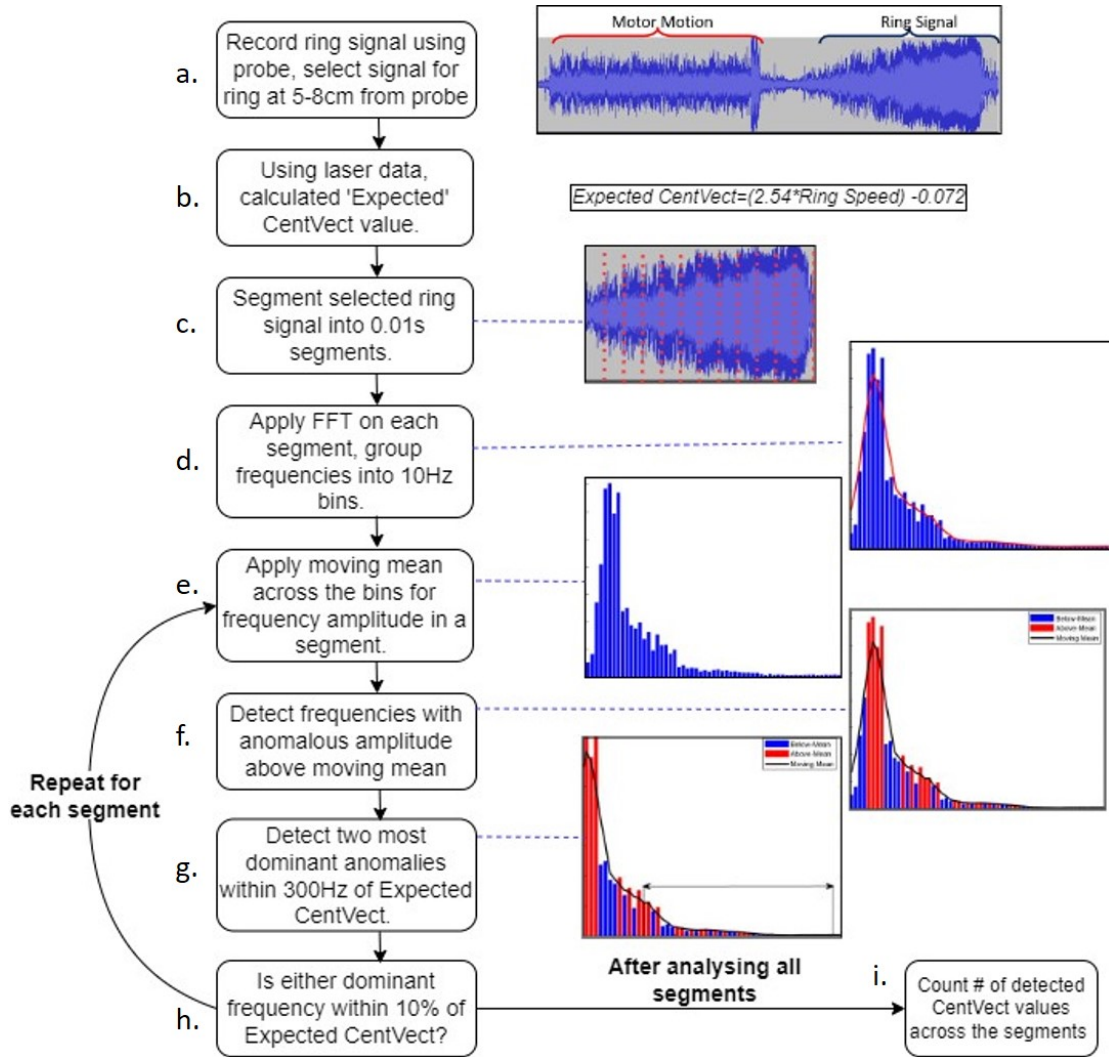


Figure 4.5: Flowchart presenting the steps in Doppler probe frequency analysis for performing real-time flow QA on the ring vortex phantom. CentVect values are inferred from the breakdown of frequency components within a Doppler signal.

This analysis assumes that the frequencies with dominant amplitudes within the expected region of CentVect are in fact CentVect. This can't be validated without a 2-D or 3-D measurement, thus it can't be described as a direct measurement. It instead *infers* the magnitude of CentVect from observed frequency patterns and highlights the speed-to-CentVect relationship.

#### 4.3.4 User Interface and Combined Code

These separate components each perform either device or flow QA. However, a combined and efficient tool would benefit the phantom by integrating these measurements into one central algorithm with an attached user interface. This was achieved by combining the separate functionalities in MATLAB 'App Designer' application. A simple user interface

was designed to display collected data and for the user to select the phantom parameters (Figure 4.6). The user selects the number of rings to analyse, the orifice size and piston speed being used. This is echoed in the Arduino code for the phantom (on a separate laptop), press ‘Start’ and the phantom button simultaneously, and the 20 second countdown will begin for the first ring.

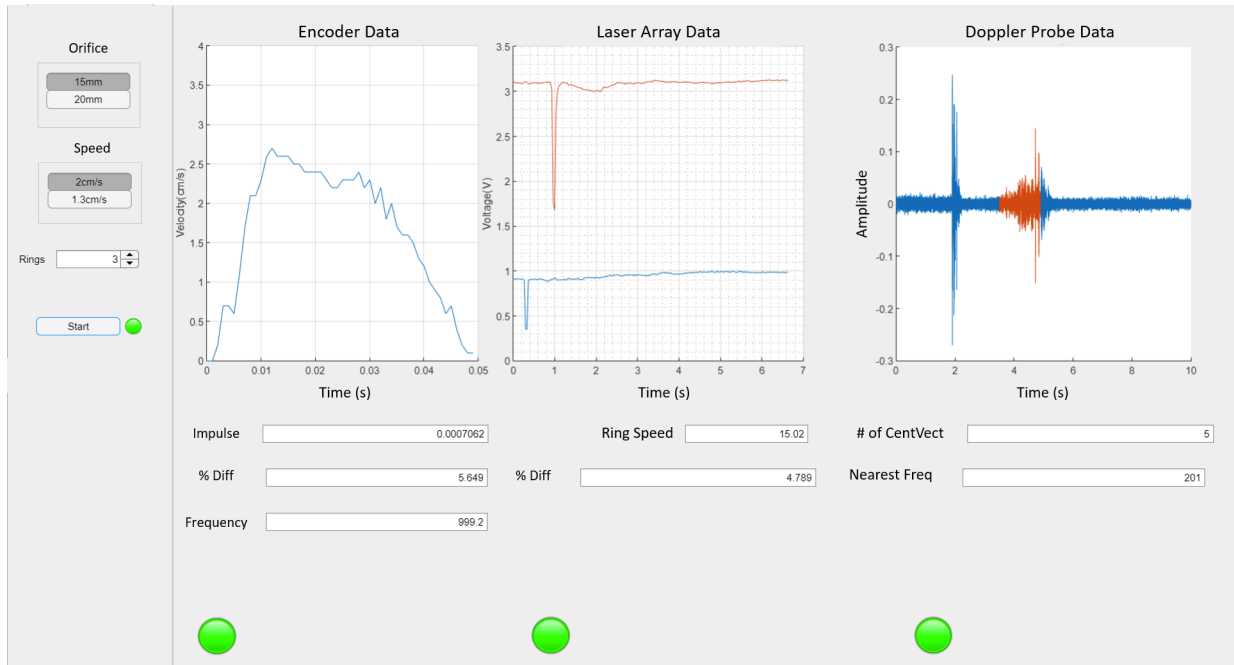


Figure 4.6: User interface displayed when the instrumentation pack is used with the ring vortex phantom. The encoder, laser, and probe raw data are displayed, along with basic derived parameters and colour-coded virtual LEDs indicating whether each parameter lies within experimental tolerances.

In the MATLAB code, the required arrays are initialised and parameters defined for each device. Once the countdown is at zero, synchronous measurements were achieved through the ‘parfor’ function, a parallelised version of a for loop, where each iteration occurs simultaneously. At its commencement, the probe records audio, the diodes transmit their voltages to the workspace, and the encoder tracks the piston motion. All raw data are then saved to the workspace. The encoder data are analysed, with the profile detected (through values above a 0.1cm/s threshold), and the average speed calculated. The laser data are analysed as discussed above, with the voltage drops detected and ring speed calculated. Finally the Doppler probe frequency analysis is performed on the ring signal (detected through specific times based on average configuration speeds). Resulting variables are: piston average speed (encoder), ring speed (laser), number of CentVect readings and average CentVect value (probe). These values are compared to pre-collected average data for each configuration, with the percentage difference found between average and measured parameters for each. This will immediately flag up whether any parameter is more than 10% away from its expected, averaged value. Coloured indicators are on the

user interface for each device and will turn green and red if the value is inside/outside of bounds respectively. Raw data are also plotted on the interface to allow the user to see if any insufficient data (e.g. noisy probe signal, mistiming in diodes) has occurred, and to discount the metric outputs. This process takes approximately 5 seconds after the ring is generated, allowing the user to quickly see (a) exactly how fast the ring is and (b) if any abnormal behaviour is evident, e.g. air bubble, power surge, stuck piston etc.

### 4.3.5 Validation Experiment

This instrumentation pack required testing before regular use with the phantom through comparison to ground-truth datasets. Real-time camera recordings and the 2019 PIV datasets were used as the benchmark for macro- and micro- measurements respectively. Experimental values of CentVect were needed to validate the Doppler probe's measurement, therefore the OR piston and PIV configurations (i.e. the Unit-0 phantom) were used for this experiment instead of the optimised vortices established in Chapter 3. This assessed the instrumentation pack's functionality over a wide range of vortices. If found to be accurate, it can then be used for the optimised NOR piston rings.

Therefore, ten vortices each of configurations 1-6 listed in Table 2.1 were generated and tracked using the instrumentation pack. The rings were recorded using the SONY RX10 camera at 100fps (positioned at 3m from the tank wall) and analysed using the manual frame-by-frame MATLAB code described in Chapter 3. Comparison between instrumentation pack results and those from PIV data and real-time camera data assessed the instrumentation pack's accuracy and reliability. These comparisons are presented below.

## 4.4 Results - Instrumentation Pack

### 4.4.1 Linear Encoder

For the linear encoder, its functionality relied on accurately measuring the piston velocity profile in a reproducible manner.

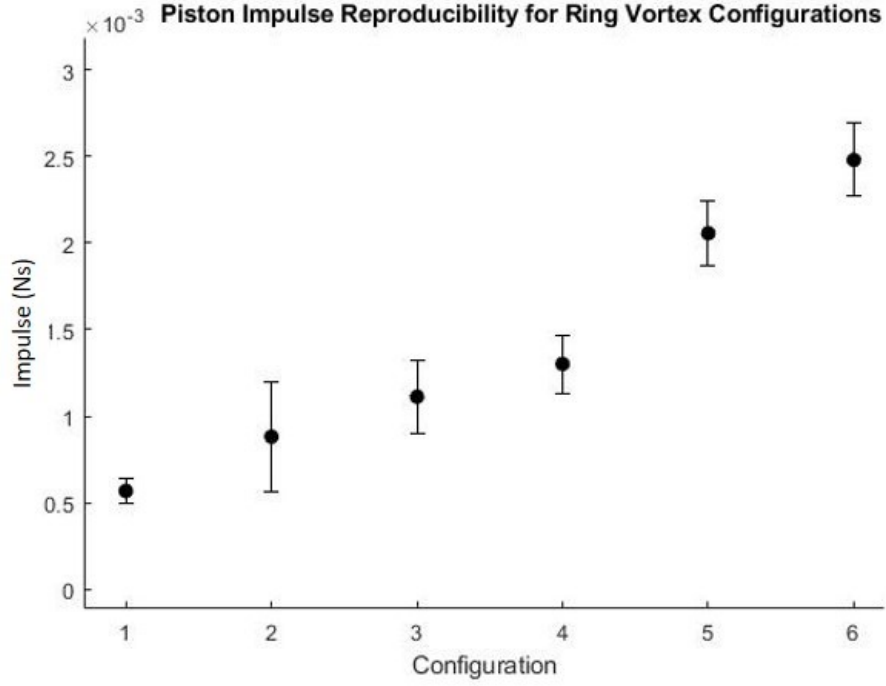


Figure 4.7: The reproducibility of impulse measurements for configurations 1-6 listed in Table 2.1, with data collected using the linear encoder. Each datapoint is the average impulse generated by ten piston profiles for that particular configuration. Error bars represent 1SD.

Figure 4.7 presents the reproducibility of the piston impulses for each configuration through its error bars. Datapoints represent the average of ten impulses with error bars covering +/-1SD. Average impulse was used for this analysis for its relation to the integral of the velocity profile, ensuring both profile shape and magnitude are quantified. Impulse is defined as the total energy expended over time and was derived from encoder measurements using the equations below.

$$\text{Fluid Slug Volume} = V = \pi R_0^2 L$$

$$\text{Jet Length} = L_s = \frac{V}{\pi r^2} = \frac{R_0^2 L}{r^2}$$

$$\text{Jet Speed} = S = L_s / T = (R_0^2 L) / (r^2 T)$$

$$\text{Jet Energy} = E = \frac{1}{2} m v^2 = \frac{1}{2} \rho V S^2 = \frac{1}{2} \frac{R_0^6 L^3 \rho \pi}{r^4 T^2}$$

$$\text{Force of Jet} = \frac{\text{Energy}}{\text{Distance}} = E / L_s = \frac{1}{2} \frac{R_0^6 L^3 \rho \pi r^2}{r^4 T^2 R_0^2 L}$$

$$\text{Jet Impulse} = \text{Force} \cdot \text{Time} = \frac{1}{2} \frac{R_0^4 L^2 \rho \pi r^2}{r^2 T}$$

$T$  – Piston Pulse Time Duration  
 $R_o$  – Piston Radius  
 $L$  – Piston Displacement  
 $r$  – Orifice Radius  
 $\rho$  – Density of water

#### 4.4.2 Laser-Photodiode Array

The laser-photodiode array measures the average ring speed between 8cm and 18cm from the orifice. This was compared to PIV averaged datasets, to ensure that the detection and calculation is working correctly.

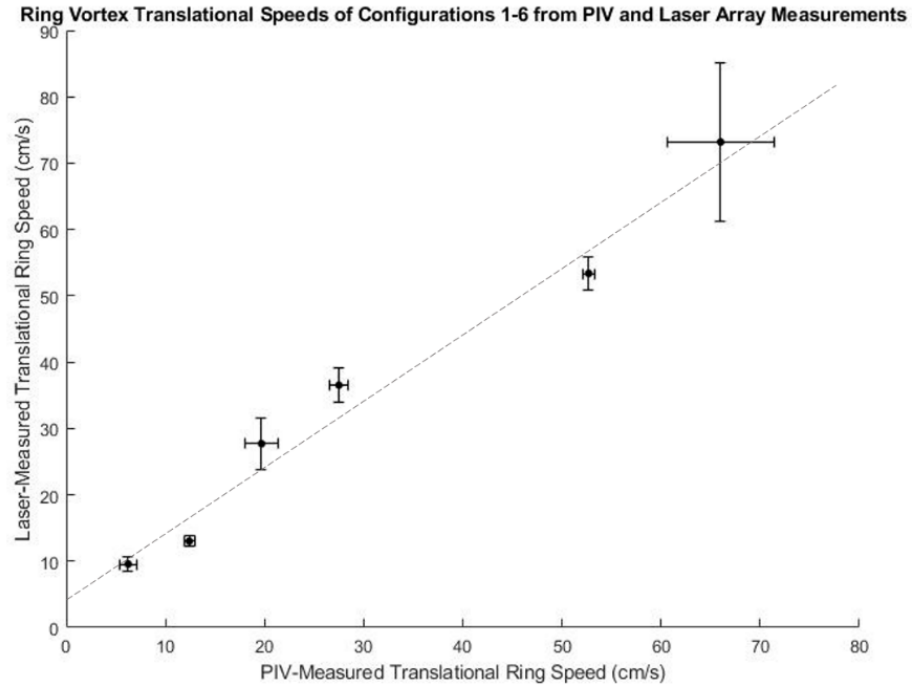


Figure 4.8: The correlation between PIV-determined ring vortex speeds and laser-determined ring speeds. Each datapoint represents the average of ten rings and error bars represent 1SD.

This correlation has a  $R^2$  value of 0.977 and p-value of 0.0206, showing strong linearity between the two methods. When fitted to a linear model, the gradient is 1.02 and the intercept 4.16. A gradient of 1 would indicate perfect agreement between the two methods, thus the close-to-unity gradient offers confidence that the laser measurement accurately reports ring speed. Worth noting here is that the PIV and laser-diode datasets were collected in different measurement sessions, with a camera also used for validation.

### 4.4.3 Doppler Probe

To assess the probe's ability to infer CentVect values from the ring vortices, the correlation between probe-calculated CentVect values and PIV-calculated CentVect values was found.

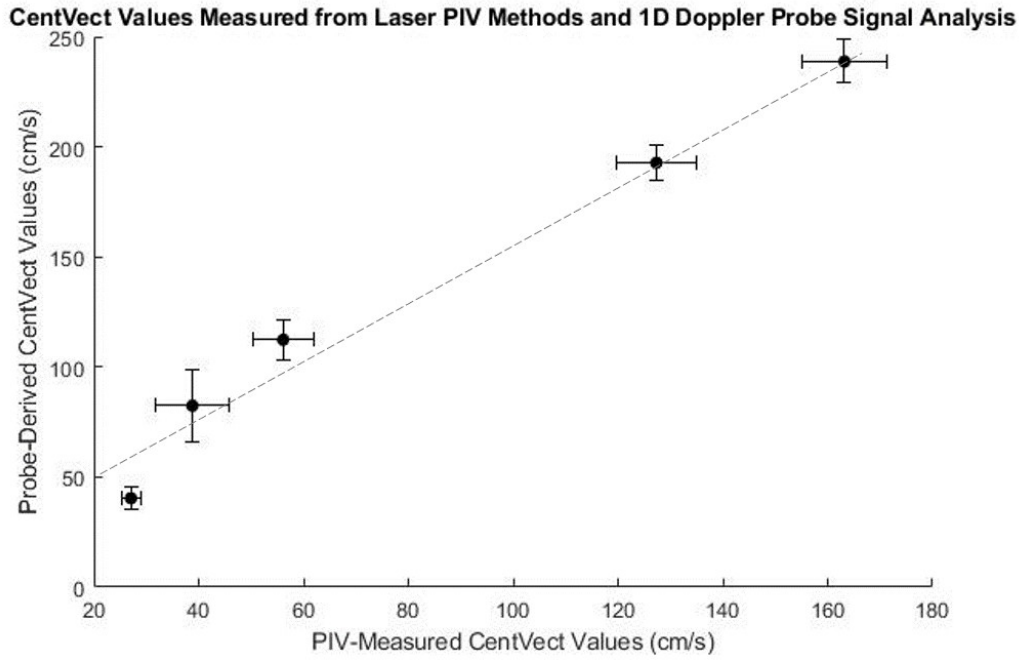


Figure 4.9: The correlation between PIV-determined and Doppler probe-calculated CentVect values. Each datapoint represents the average of ten rings and error bars represent 1SD.

When fitted to a linear model, the correlation gradient and intercept are 1.3 and 51cm/s respectively. A  $R^2$  value of 0.98 indicates strong linearity. The discrepancy between these results and the ideal relationship (gradient=1, intercept=0) is discussed below.

## 4.5 Discussion - Instrumentation Pack

### 4.5.1 Results Assessment

The results from each component has been presented. The linear encoder demonstrated a reproducible impulse for the piston propulsions, which was desirable. There was variability of <10% across all configurations. Similar reproducibility across different orifice sizes indicates that any varying resistance between orifice has no significant effect on the piston motion.

There was a strong correlation between laser-calculated ring speeds and PIV-calculated ring speeds, indicating that the laser-photodiode array method is valid and accurate within tolerances. The gradient of 1.02 is within 2% of the ideal correlation. There were concerns

that the vortical wake observed in configurations 1,2 would distort the data but this was not evident in the collected photodiode readings. Error bars were slightly larger for the laser-calculation, however not significantly, and they remain less than 10% of the average, maintaining high reproducibility.

Finally, the probe results were promising. The direct probe-to-PIV correlation ( $R^2 = 0.98$ ) indicates a strong linear relationship but the ideal correlation (gradient=1, intercept=0) was not achieved. This was due to the probe beam's width beyond ring boundaries and the involved frequency analysis. The primary metric of in this analysis was a linear relationship between the PIV and probe readings, and significant difference between configurations, i.e. that the probe can detect different configurations through CentVect readings. These behaviours are evident in the data, with a strong linear relationship between the two methods. The gradient of 1.3 is close to ideal, but clarifies that probe-derived CentVect values are 30% higher than PIV-measured values. This can be used as the basis for calibration, with 30% subtracted from the final measured frequency. The probe predicting higher velocities than the PIV measurements indicates that higher velocity components are being detected within the rings, likely from the inner-core areas which neighbour the CentVect region.

Overall, all three components demonstrate their ability to accurately and reliably measure device and flow QA in real-time when compared to gold-standard datasets. The combined algorithm and user interface worked correctly throughout the experiments, with values appearing approximately 5 seconds after each ring is generated. If an abnormal vortex were generated, for example through the piston getting stuck, the UI would immediately highlight this through an incorrect piston impulse, ring speed and micro-flow reading.

#### 4.5.2 Instrumentation Requirements for End-Users

The phantom has an eventual goal of becoming a commercial product, suitable for use in clinical and research environments. The instrumentation pack is a useful addition which would greatly benefit the phantom when in widespread use. The two primary objectives of the QA tool are (a) to provide confidence to the user that this novel technology and flow are acting as expected and (b) to provide real-time individual information regarding the device and flow behaviour. Arguably it is not clear what level of QA is needed for different uses once commercialised. The level to which the phantom needs to be assessed in regular use would depend on its user.

For example, a researcher wishing to use the ring vortex phantom in an academic/industrial setting will likely require an in-depth quality assurance for real-time ring vortex visualisation with minimal assumptions. They would therefore benefit from the 'full' instrumentation pack with all three components. Potential applications of the phantom here would be testing a new scanner/imaging algorithm, testing a new visualisation technique, or assessing the ring vortex for its dynamics. Here the user would require high levels of information regarding the ring vortex/phantom functionality to reduce assumptions.

A second group of users, perhaps the most common, is a hospital-based user (i.e. medical physicist) performing regular quality assurance checks. In this scenario, the phantom

would come with well-defined tolerances for each configuration, along with strict protocol regarding its setup and operating environment. Whilst researchers may deliberately alter the phantom setup or vary an environmental factor for analysis, the hospital environment would operate according to well-defined protocols, relying on pre-determined tolerances that remain valid. The ring vortex is predictable in numerous configurations and this is closely related to the input profile, so in regular QA sessions only the encoder would be required. The piston velocity profile would be tracked to ensure it operates within tolerances, and using pre-collected data, the user would know the average ring vortex that this configuration generates, along with associated tolerances. Without direct ring vortex analysis, however, this would be reliant on averages. Any abnormality/malfunction would be immediately evident, for example if the clinician has not levelled the phantom and the piston alignment is off, or if there is an air bubble in the piston cylinder, as the piston cylinder would act abnormally. Only having the encoder would reduce the device cost and aid with health and safety requirements, as the laser-photodiode array would no longer be directly next to the open water tank. This may aid in clinical translation, as health and safety regulations are strict and must be adhered to. The hospital environment could benefit from a regular calibration service, where the full instrumentation pack is brought onto site and used to ensure correct functionality.

### 4.5.3 Commercialisation

For commercial translation, certain technical upgrades would also be required. The phantom itself, and certainly the instrumentation pack, is designed for use in the laboratory, with only university-standard PAT tests and regulations to follow. As a result, the infrastructure and circuitry is temporary and unrefined for commercial use or regular transportation. It is recommended for more permanent use that the lasers are upgraded to laser diodes, powered through the diode circuit. This would reduce their intensity and conform to laser health and safety regulations in the clinical/research environment. It would also improve the diode lifetime, as despite filtering the diodes occasionally burnout and need replacing. The circuitry would need rehousing in a more permanent structure. Permanent instrumentation pack structures would require CNC-milling or robust 3D-printing manufacturing to ensure longevity and portability. Finally, embedding components in the device itself would aid in setup and portability. The laser diodes and detectors could be easily embedded into the wall exterior during manufacture which would improve attenuation, with permanent wiring running alongside the motor cable. A well-characterised Doppler probe would be required, with as thin a beam as possible to ensure that minimal surrounding-frequencies are picked up, as the frequency analysis processing is largely removing noise to detect CentVect.

Finally, integration of phantom use and instrumentation pack use would be beneficial. To run the phantom and pack, the user must currently use two laptops (one of which needs high processing power to run the encoder), one with Arduino software to use the phantom, and the other with MATLAB to use the instrumentation pack. Variables are inputted into each and both buttons are pressed to start the process. This method is adequate for development in the laboratory but for clinical use no laptop would be

best, with the Arduino controlled by a touch-screen module. This would be difficult to achieve with the instrumentation pack, so either custom components could be built which interface with Arduino, or a single laptop could run the full device. Interfacing between MATLAB and Arduino is non-trivial, particularly given timing as MATLAB can perform delays of a minimum 0.5 seconds, whilst the Arduino code can integrate delays down to the microsecond. A high-spec laptop would be paramount for this, as the use of probe, phantom, lasers, photodiodes and high-resolution encoder would be computationally expensive. The cost of different options would have to be considered here, as a high-spec laptop for regular QA sessions in the clinic is likely not viable. Finally, reliance on MATLAB is difficult as it is a paid service, and not one regularly funded by the NHS and other medical bodies. Transfer to an open-access platform such as Python is recommended, or perhaps LabVIEW as it is an instrumentation-focussed platform and has been used during development of the MATLAB code for this project.

## 4.6 Conclusions

This chapter has introduced a new factor to the ring vortex phantom - quality assurance. It is relatively uncommon for phantom manufacturers to focus on quality assuring their devices in regular use beyond the manufacturing stage, however its integration can significantly increase the trust in a novel device, and will give immediate feedback in the event of a malfunction. A review was performed on other available flow phantoms in the literature, assessing their level of device- and flow- QA procedures, and it was found that no phantoms with complex 3-D flows implemented offer real-time flow and device QA. A particular difficulty is characterisation of the complex flow profiles, as complex devices often rely on pre-collected experimental datasets. The ring vortex' unique structure allows for real-time measurements which relate to its micro-flow. A Doppler probe, linear encoder and laser-photodiode array measure the CentVect, piston impulse and ring speed respectively, displaying the information and tolerance adherence on a MATLAB user interface. All three methods demonstrated strong linear correlation to gold-standard methods and reproducibility within experimental tolerances of 10%. The ring vortex phantom is therefore able to perform real-time QA of its device and flow functionality in real-time. Integration of real-time measurements increases the validity and confidence in pre-collected experimental ground-truth datasets. The findings detailed in this chapter have also been disseminated in a publication [123], published in 2023.

# Chapter 5

## Analytical Classification of the Ring Vortex

### 5.1 Motivation

The review of Chapter 1 introduced the role of theoretical modelling of reference flow profiles in flow phantom development. Experimental, numerical and analytical representations are the most commonly used forms of ground-truth reference datasets used to characterise reference flow behaviour, with Chapter 4 demonstrating that more complex, 3-D flows employ experimental visualisation (LDV, PIV) in the absence of accurate analytical models. The ring vortex phantom has thus far used this method, visualising the vortices experimentally using Laser PIV and using them as ground-truth benchmarks enhanced with real-time QA measurements.

It can be argued that accurate theoretical representations offer more value than experimental visualisations, as they are cost-free, require no specialist equipment and their resolution and domain size can be varied to suit the user. These theoretical representations can be formulated through numerical simulations (CFD) or analytical representations using established models. Previous work attempted to simulate the phantom flows using CFD methods, and whilst ring vortices were generated consistently, they deviated from experimental behaviour at both macro- and micro-scales. It was therefore decided that analytical solutions would be investigated for their accuracy when compared to the experimental PIV datasets. If successful, the combination of analytical and experimental visualisations would complement the phantom, particularly in combination with the real-time QA readings, as these readings could be incorporated into the theoretical vortex formulation. With that in mind, this chapter aims to establish whether the experimental vortices act according to any established analytical models, and within what tolerances.

There is a long history to ring vortex analytical modelling, originating with Helmholtz' groundbreaking work in the 19th century [124] where vorticity was first defined and basic vortex dynamics established. Subsequent models used this theory as their foundation, deriving idealised expressions for the ring vortex in terms of vorticity, velocity, stream-function and other formats. A wide range of models are available, and this chapter will

focus on the most influential and relevant in the field.

Section 5.2. will introduce the well-established, idealised models evident in the literature, along with the basic foundations of analytically modelling ring vortices. This will be followed by a comparison between relevant models and the experimental phantom ring vortices, with methods described in Section 5.3 and results in Section 5.4 Finally, Section 5.5 will discuss to what extent the experimental vortices can be described by the idealised formulations. 2019 PIV datasets from the Unit-0 phantom will be used as the experimental ground-truth datasets for this work, as they contain the required micro-flow information to assess model accuracy.

## 5.2 Analytical Rings in the Literature

### 5.2.1 The Basis of Analytical Models

Whilst the ring vortex' well-defined internal structure and unambiguous dynamics make it a candidate for analytical formulations, the three-dimensional, dual-vortex system is difficult to summarise analytically. This is exacerbated by formation mechanics and dissipation/breakdown. This work will only study the post-formation ring vortex once it is fully formed and propagating along its central axis, thus removing the complication of formation modelling. This simplification is pertinent to the phantom as only post-formation rings are imaged and analysed.

The complexity of ring vortex modelling is eased through axi-symmetry, and combines fluid transport equations with vorticity, viscous effects and potential flow. A brief summary of model foundations is beneficial before describing specific models. Key concepts include the coordinate system, streamfunction and assumptions made by the model.

#### *Co-ordinate System and Geometry*

Cylindrical coordinates are the most intuitive choice for toroidal systems, using the system in Figure 5.1. The ring propagates along the  $z$  axis, with its meridional cross section in the [axial,radial]=[ $r,z$ ] plane. Axial symmetry around the  $z$  axis is assumed, as is zero swirl (zero velocity in the azimuthal direction along the torus circumference), reducing the ring vortex problem to two dimensions. For the purposes of this chapter, the  $r, z$  plane is visualised as the  $x, y$  plane (Figure 5.1b), mimicking Cartesian axes, as the angular  $\theta$  axis can be ignored and the rings' cross section visualised in 2-D.

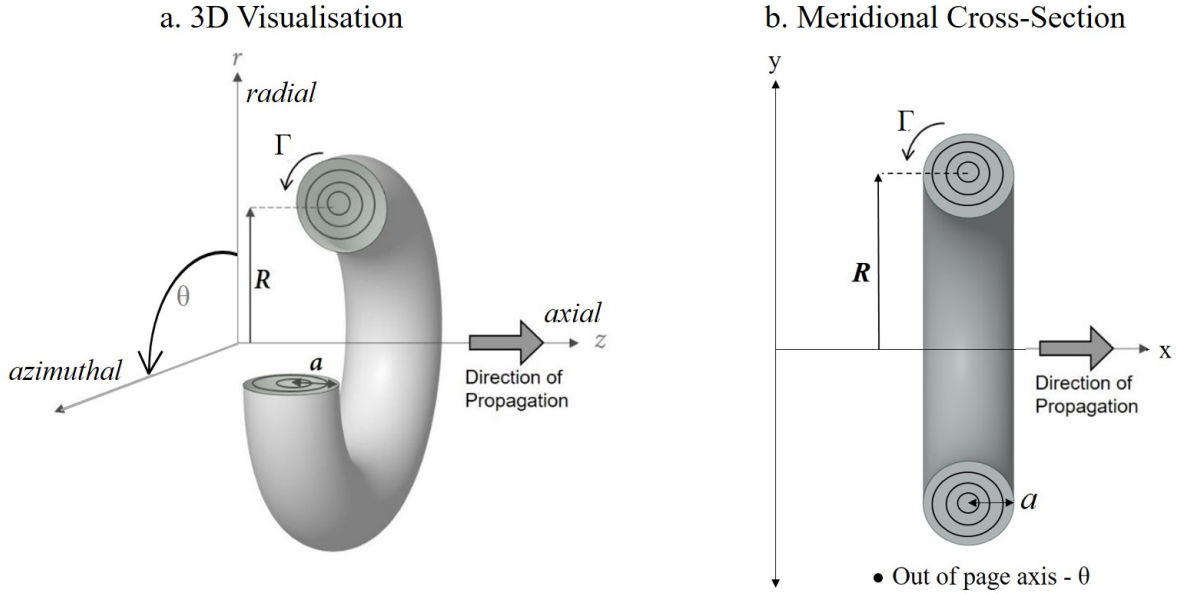


Figure 5.1: Schematic of the ring vortex on the cylindrical coordinate system. (a.) shows the 3D representation with axial, radial and azimuthal axes. (b.) shows the 2-D simplification, with axial and radial axes represented as  $x$  and  $y$ .

### ***Stokes Streamfunction***

The models discussed in this thesis describe the vortical flows through use of streamfunctions, a commonly seen method of analytically representing flow fields. A streamfunction is a scalar field, defined as the curl of the vector velocity potential field and can be employed to calculate velocity components, vorticity, and pressure gradients of a certain flow field. Key properties of the streamfunction include that gradients that run perpendicular to the local velocity field at all locations, and it is constant along the direction of the flow. The latter properties allows fluid dynamicists to employ streamlines - path-lines throughout the field along which the streamfunction value is constant, and runs parallel to the local velocity vector [125]. See Appendix B for a derivation of the streamfunction from the continuity equation for the mathematical background.

For describing the ring vortex, a simplified class of streamfunction is used, known as the *Stokes Streamfunction*. This class describes incompressible flows which are axisymmetric around a central axis in a cylindrical coordinate system thus are functions of the radial and axial directions only. The ring vortex' axisymmetry around its central axis lends itself to Stokes streamfunctions for analytical description. The Stokes streamfunction can be used to infer velocity components through Equations 5.1 and 5.2. Please note, in these equations 'x' and 'y' represent the axial and radial axes as seen in Figure 5.1b, not a Cartesian coordinate system. The mathematical reasoning for these expressions is also covered in Appendix B.

$$v_y = \frac{1}{y} \frac{\partial \psi}{\partial x} \quad (5.1)$$

$$v_x = -\frac{1}{y} \frac{\partial \psi}{\partial y} \quad (5.2)$$

Where  $\psi$  is the local streamfunction value [96],[126]

Each analytical model expresses ring vortex behaviour in terms of the Stokes streamfunction. This chapter will use the velocity component conversion above to generate analytical velocities across a 2-D coordinate grid pertaining to each model.

### ***Ring Vortex Model Assumptions and Formation***

Analytical ring vortex models are created using a set of assumptions, which are combined to form a corresponding streamfunction. These assumptions are as follows:

- **Fluid Viscosity:** Models will either assume inviscid or viscous fluid. The latter is time-dependent as viscous losses modify the flow over time.
- **Core model:** Established vortex models are used to describe the ring vortex core. Choices include Rankel vortex, Oseen vortex, Bessel-spiral function, or a point vortex.
- **Vorticity function:** What relation the local vorticity has to the distance from the radial axis. This can be linear, Gaussian-esque, or other. This is related to the core model choice.
- **Reference frame:** Lab reference frame (ring moving past at  $U$  m/s) or ring reference frame (ambient fluid translating at  $-U$  m/s). Conversion between the two occurs by superimposing a constant field of axial flow travelling at  $U$  m/s. Rings are visualised in the ring reference frame in this thesis, as this gives a more intuitive understanding of ring flow, with easily observed boundary streamlines and external potential flow (see Figure 5.2)

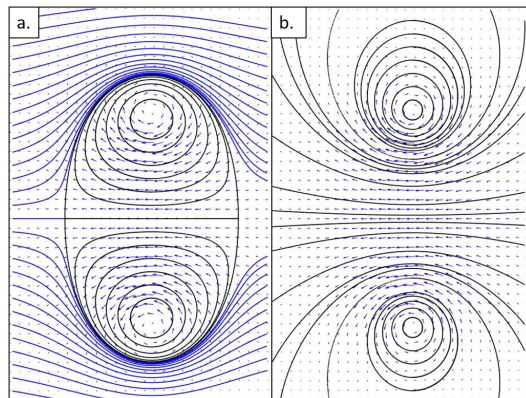


Figure 5.2: Ring vortex streamlines from Laser PIV datasets. (a.) shows the ring vortex in the moving ring reference frame, with blue streamlines representing ambient fluid. (b.) shows the ring vortex in the stationary reference frame.

These assumptions are combined into a single streamfunction model. A range of models are introduced below.

## 5.2.2 Steady State Inviscid Models

Early theoretical models considered inviscid flows, following time-independent equations. The absence of viscous effects results in steady-state solutions which can be viewed as an instantaneous ‘snapshot’ of ring dynamics.

### Circular Vortex Filament Model (CVF)

The first of two exact solutions to the inviscid ring vortex problem is the circular vortex filament (CVF). This assumes a ring radius  $R$  and core radius  $0$ , with a vorticity distribution of a Dirac delta function at the core centre [126], [127]. This model is non-physical, with micro-velocities, translational velocity and energy becoming infinite due to the zero-size core. It is included here for completeness, demonstrating its relevance in subsequent models. This description is generally viewed as an interesting exercise of ring vortex visualisation at its limit rather than a practical model, due to its infinitely small core radius assumption [127].

### Hill’s Spherical Vortex (HSV)

The second solution to the inviscid ring vortex problem [128] is Hill’s Spherical Vortex (HSV), presented by M.J.M. Hill in 1894 [129]. HSV models the ring vortex as a self-contained sphere propagating through inviscid fluid at rest at infinity. The core edge is defined as the position where the tangential velocities are at a maximum (Figure 5.3). In the HSV model, the core edge coincides with the vortex atmosphere boundary. For this model, the vorticity distribution is linear, increasing linearly with increasing distance from the axis (Figure 5.3c) [129]. These equations are presented in the  $(r, \theta)$  system and will be re-defined to  $(x,y)$  coordinates in Section 5.3.

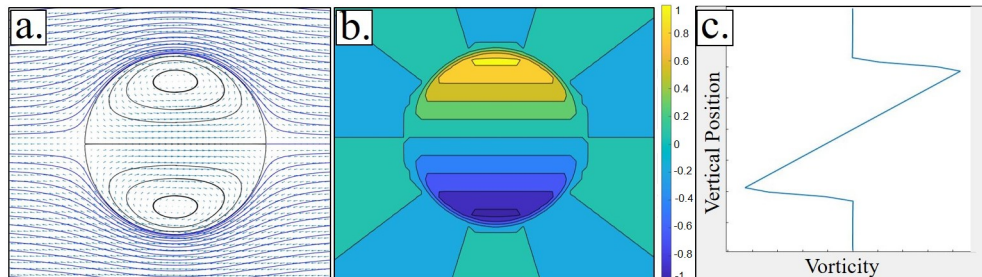


Figure 5.3: Hill’s Spherical Vortex visualised in MATLAB. (a) presents the velocity vector profile and streamlines in the moving RRF, (b) the filled vorticity contours and (c) the linear vorticity projection down the centre of the ring

The ambient fluid is modelled as flow past a solid moving sphere, and the stream-function is presented below. Unlike other, more sophisticated models, two regimes are required, for inside and outside of the spherical bubble respectively. The Stokes stream-functions for the HSV model in the ring reference frame are listed below.

$$\psi = -\frac{3U}{4}\left(1 - \frac{r^2}{a^2}\right)r^2 \sin^2\theta \quad \text{for } r \leq a \quad (5.3)$$

$$\psi = \frac{U}{2}\left(1 - \frac{a^3}{r^3}\right)r^2 \sin^2\theta \quad \text{for } r \geq a \quad (5.4)$$

Here  $U$  is ring speed

$a$  is the radius of the vortical sphere.

These equations are in the spherical polar coordinate system.

The HSV is, by default, in the ring reference frame so must be converted to the laboratory reference frame. Whilst the HSV model largely solves the inviscid axisymmetric Navier-Stokes equation (it remains unsolved only at the boundary) and presents a closed-form solution to the problem, its assumptions impact its validity. By assuming that the torus is spherical and that its core encompasses the entire bubble, the HSV is known to be useful for evaluating bulk motion rather than fine structure [130].

### Norbury-Fraenkel (N-F)

A well-known venture to formulate a more refined inviscid ring vortex formulation is the Norbury-Fraenkel model (N-F). Its conception originated with Fraenkel extending the CVF solution to a small finite thickness in 1970 [131], postulating a ring of small cross-section. Norbury independently extended the HSV model to just below HSV, where the core cross-section was very large [132]. Norbury subsequently combined the results into a single family of vortex rings, with geometries ranging from close-to-CSV (small core) to close-to-HSV (large core) [133]. These rings are defined by a single geometric parameter, are axisymmetric and move unchanged through unbounded inviscid ideal fluid at rest at infinity. A linear vorticity distribution was imposed, where local vorticity is linearly dependent on distance from the axis of symmetry, as in HSV.

To form the model, the dimensionless, defining parameter is defined:

$$\alpha = \frac{\sqrt{\Omega_c^{2d}/\pi}}{R_c}$$

Here  $\Omega_c^{2d}$  is the vortex core boundary area

$R_c$  the ring radius

$\alpha$  therefore represents the dimensionless core radius.

In dimensionless form, the following equation is derived:

$$k(\alpha) = \frac{1}{2}W(\alpha)r^2 + \frac{1}{2\pi\alpha^2} \int \int_A G(r, z) dr dz$$

Where  
 $W$  = ring speed,  
 $k$  = a given constant,  
 $\partial A$  = vortex core radius.

To solve this solution,  $\partial A$  (core radius) must be found to satisfy the other variables. This unknown, finite parameter requires the equation to be solved numerically, with  $\partial A$  approximations found through Fourier series analysis [133].

The N-F model is used widely in ring vortex research [134],[135],[107] most often for comparison to numerical and experimental rings. Notably, the model gives reasonably accurate ring speeds and energy for low stroke ratio post-formation rings [134]. Further comparison using the velocity components is not useful, as the linear vorticity distribution correlates poorly to the Gaussian-esque vorticity distribution in experimental vortices [135].

### 5.2.3 Viscous Ring Vortex Models

Whilst inviscid models are plentiful and useful, they ignore the significant viscous effects on the ring vortex, particularly dissipation. Viscous models will therefore be the central focus for this work, as they offer flexibility in comparison to experimental vortices, rather than a constrained 'snapshot'. Time-dependent models are inevitably more complex, however two prominent ring vortex models are noted in the literature: Lamb-Oseen and Kaplanski-Rudi.

#### Lamb-Oseen Ring Vortex

Posed by Lamb [126], the Lamb-Oseen vortex ring model has a different approach to forming the ring vortex. It is built from a single Oseen vortex, rather than a ring vortex expression from the beginning. Its formulation therefore generates a vortex centred at the coordinate origin for the correct dimensions then is radially translated and mirrored across the symmetry axis to form the ring cross-section. The Oseen vortex is a 2-D line vortex (with appropriate symmetry) with an impulse circulation at the centre, and concentric circles of fluid circulating around it. It is quantitatively defined by its circumferential velocity, expressed by Equation 5.5 [130].

$$u_{\theta} = \frac{\Gamma}{2\pi r} (1 - \exp(-\frac{r^2}{4\nu t})) \quad (5.5)$$

Here  $\Gamma$  is the circulation,  $r$  the distance from core centre, and  $\nu$  the fluid viscosity. This vortex' application improves on the inviscid models, as its vorticity function is a Gaussian with its maximum at the vortex centre, visually similar to experimental ring vortices. Its velocity profile, meanwhile, reaches a maximum at a distance  $a$  from the vortex centre, defining the edge of the core. This is consistent with experimental ring vortices, thus the LO vortex model is a suitable candidate for plausible ring vortex modelling. Unlike the HSV model, the core edge does *not* coincide with the vortex atmosphere edge, therefore representing a step-up in terms of micro-velocity accuracy.

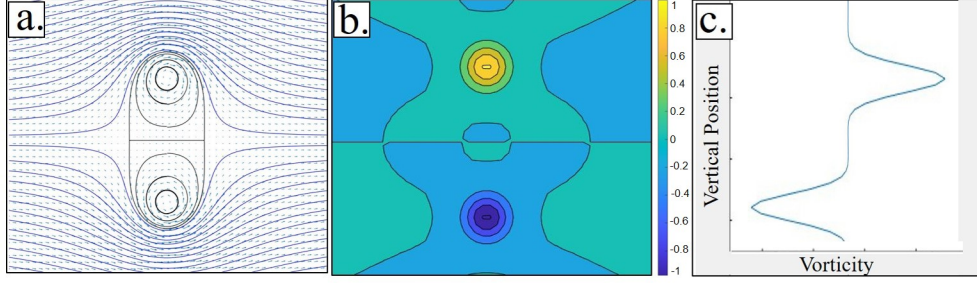


Figure 5.4: Lamb-Oseen Ring Vortex visualised in MATLAB. (a) presents the velocity vector profile and streamlines in the moving RRF, (b) the normalised vorticity profile and (c) the Gaussian vorticity projection down the centre of the ring

Preliminary investigation with the LO model is present in the literature. Yehoshua et al. applied the LO model in their work on ring vortices interacting with a wall. Streamlines were qualitatively compared between experimental and LO vortices, with the LO vortices found to be more circular than the deformed experimental cores [136]. The application of LO is limited in other work, but it is often the basis for numerical ring vortex simulations.

### Kaplanski-Rudi Model

The most recent significant model is the viscous ring vortex model first published by Kaplanski and Rudi (KR) in 1999 [137] and since refined [138]. This model assumes a viscous fluid and is built upon the linear time-dependent Stokes equation. Central to this model is the imposed notion that the ring core expands due to dissipation as the ring travels [137],[139]. The rings in this formulation have constant ring radius  $R$  and a core radius  $L$  which evolves in time. Similar to  $\alpha$  in the N-F model, a dimensionless parameter,  $\theta = \frac{R}{L}$ , is defined to characterise ring dimensions. The model derives a dimensionless streamfunction expression:

$$\Psi = \Gamma_o R_o \frac{\sigma}{4} \int_{\infty} F(\eta, \mu) J_1(\theta\mu) J_1(\sigma\mu) d\mu \quad (5.6)$$

Where

$$F(\eta, \mu) = \exp(\eta\mu) \operatorname{erfc}\left(\frac{\eta + \mu}{\sqrt{2}}\right) + \exp(-\eta\mu) \operatorname{erfc}\left(\frac{\mu - \eta}{\sqrt{2}}\right) \quad (5.7)$$

And  $\operatorname{erfc}(x) = 1 - \operatorname{erf}(x)$ , where  $\operatorname{erf}$  denotes the error function.

The published work converts this streamfunction into its velocity component format:

$$u = \frac{\Gamma_o \theta^2}{4R_o} \int_0^{\infty} F(\eta, \mu) J_1(\theta\mu) J_0(\sigma\mu) \mu d\mu \quad (5.8)$$

$$v = -\frac{\Gamma_o \theta^2}{4R_o} \int_0^{\infty} G(\eta, \mu) J_1(\theta\mu) J_1(\sigma\mu) \mu d\mu \quad (5.9)$$

Where

$$G(\eta, \mu) = \exp(\eta\mu) \operatorname{erfc}\left(\frac{\eta + \mu}{\sqrt{2}}\right) - \exp(-\eta\mu) \operatorname{erfc}\left(\frac{\mu - \eta}{\sqrt{2}}\right) \quad (5.10)$$

Here  $\Gamma_0$  is initial circulation,  
 $R_0$  the ring radius,  
 $\eta$  the dimensionless axial coordinate,  
 $\mu$  the dimensionless radial coordinate,  
 $J_1$  and  $J_0$  denote Bessel functions

This model has associated boundary conditions where the streamfunction tends to 0 at infinity and on the axis of symmetry. Similar to the LO model, this formulation creates Gaussian-esque vorticity distributions (See Figure 5.5) within the vortex core by using Bessel functions as the core model.

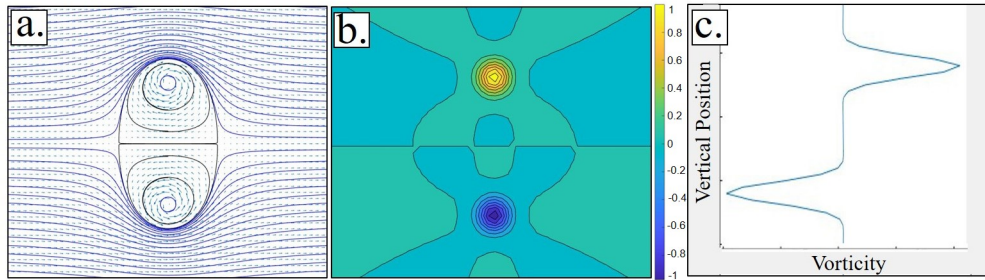


Figure 5.5: Kaplanski-Rudi Ring Vortex visualised in MATLAB. (a) presents the velocity vector profile and streamlines, (b) the normalised vorticity profile and (c) the Gaussian vorticity projection down the centre of the ring

With this model's more recent development, it is a feature of active research examining its similarity with numerical (CFD) and experimental data. Numerically, three major comparisons have taken place:

- Stanaway et al used numerical rings in the formation stage of  $Re_\Gamma = \frac{\Gamma_0}{\nu} = 0.1, 100, 200$ . These numerical rings were compared to KR in terms of ring speed, with best agreement found at  $Re=0.1$  [140].
- Danaila et al. [135] generated numerically simulated rings, with  $\frac{L}{D} = 4$ ,  $Re_D = \frac{U_0 D}{\nu} = 1400$  and compared it to the KR model at dimensionless time  $t^* = \frac{t U_0}{D} = 30$ , corresponding to the post-formation stage. These numerical rings were compared to KR and NF through normalised vorticity and streamfunction comparisons. KR was a better fit than NF, but failed to mimic the numerical rings' asymmetrical cores.
- Kaplanski compared high-speed rings of  $Re_D = 17000$  to numerical counterparts, noting that the models compared 'very well' despite the high  $Re$  [127].

Less explicit comparison is evidenced for experimental rings, with findings limited to:

- Weigand [141] generated rings of  $Re_D = 830 - 1650$  and compared them at  $t^* = 10^{-4} - 10^{-1}$ . Acceptable agreement was found, with ring speed compared.

- Kaplanski [127] compared KR rings to 2004 experimental data from Cater et al. [142] at  $Re_D = 2000$  and  $t^* = 0.04$  at  $x/D = 2$ . Radial and axial core vorticity distributions were compared, with the radial core agreeing at  $t^* = 0.0313$  and the axial core agreeing at  $t^* = 0.0556$ . As the core increases as it travels, this exhibits the oblate asymmetry observed by Daniele et al [135].

These findings highlight certain patterns in comparisons between KR and numerical/experimental rings. These methods involve a range of Re and stroke ratios. Comparison to ring vortices is frequently superficial, often relying on qualitative streamline comparison, and quantitative methods only comparing basic parameters (ring speed, energy) and occasionally vorticity. This is recent work however, so a thorough comparison between KR and experimental vortices considering local velocities, ring streamlines and integral properties is yet to take place. The work in this chapter represents the most in-depth comparison of the Kaplanski-Rudi model at the time of writing.

## 5.2.4 Conclusion

A range of published analytical ring vortex models have been introduced, with the Kaplanski-Rudi viscous ring vortex (KR) deemed the most developed model available, with favourable published qualitative results when compared to numerical ring vortices. It is, therefore, the primary comparative model in this study. The attributes of each model are listed in the table below.

| Model | Viscosity | Defining Parameters                        | Vorticity Distribution | General Notes         |
|-------|-----------|--|------------------------|-----------------------|
| HSV   | Inviscid  | $V_{trans}$ , radius                       | Linear                 | Spherical Vortex      |
| NF    | Inviscid  | $\alpha = \frac{\sqrt{\Omega_c/\pi}}{R_c}$ | Linear within core     | Numerically Optimised |
| LO    | Viscous   | Core radius, Ring Radius                   | Gaussian               | Thin Cores            |
| KR    | Viscous   | $\theta = \frac{R}{L}, \omega$             | Gaussian               |                       |

Table 5.1: Tabulated summary of features relating to analytical ring vortex models

The following work aims to determine whether the vortices of the ring vortex phantom can be quantitatively described, within defined tolerances, using the KR model. Absence of consistent experimental-to-analytical comparison methods means that novel methods will be proposed and applied in this thesis. To ensure method sensitivity and appropriate application, HSV and LO will also be included for comparison. Both HSV and LO formulations are clearly qualitatively different to the phantom vortices, with LO considered accurate in small-core vortices ( $\frac{L}{R} \rightarrow 0$ ) and HSV a spherical, inviscid vortex. If these inaccuracies are reflected quantitatively, this will demonstrate the sensitivity and validity of our proposed methods. These analytical are selected as the most prominent closed-form

models available. The absence of the popular N-F model is worth noting. It is out of contention for this exercise due to its linear vorticity distribution and requirement for a numerical solver.

The following work will investigate the similarity between the experimental vortices generated by the phantom and the Kaplanski-Rudi viscous model. A range of Reynolds numbers will be analysed to reveal any relationships between ring dynamics and model-like behaviour.

## 5.3 Methods I - Formation of Analytical Vector Fields

To enable comparison with the experimental phantom vortices, theoretical ring vortex representations were formed to mimic the experimental datasets. These datasets are from the 2019 Laser PIV experiment, so are in the form of high-resolution velocity vector plots of the ring vortex cross section, which the theoretical representations will reproduce. For each individual ring, properties were measured from the PIV data and a corresponding HSV, LO and KR vector field was formed using MATLAB. This section describes the formation of these vector fields from the model-derived mathematical expressions.

### 5.3.1 Experimental Ring Sampling

For collection of experimental ring properties, the PIV datasets were analysed when the ring was at 15cm from the orifice exit ( $\pm 5\text{cm}$  due to discretization). A range of experimental vortices were selected for a diverse assessment of the KR model, with the relevant parameters listed in the table below.

| Config | Reynold's No.     | Stroke Ratio | Dimensionless Distance | Ring Speed |
|--------|-------------------|--------------|------------------------|------------|
| 1      | $13028 \pm 6.2\%$ | 3.92         | 1.5                    | 69.6cm/s   |
| 2      | $11166 \pm 4.5\%$ | 3.92         | 1.5                    | 53.4cm/s   |
| 3      | $8674 \pm 1.85\%$ | 1.16         | 1                      | 28.3cm/s   |
| 4      | $7434 \pm 8.4\%$  | 1.16         | 1                      | 19.9cm/s   |
| 5      | $6514 \pm 1.0\%$  | 0.49         | 0.75                   | 12.2cm/s   |
| 6      | $5583 \pm 10.3\%$ | 0.49         | 0.75                   | 5.9cm/s    |
| 7      | $1888 \pm 6.1\%$  | 0.25         | 0.6                    | 5.0cm/s    |

Table 5.2: Experimental Ring Vortex Properties Used for Comparison to Analytical Models

Each model has a different method of forming velocity vector flow fields, derived from the provided expressions, but these can be directly compared with the experimental PIV data.

### 5.3.2 Hill's Spherical Vortex Formulation

The HSV model vortex requires ring speed ( $U$ ) and vortex atmosphere height ( $2a$ ) only to describe this spherical vortex, both of which were measured from experimental datasets. To generate the velocity vector plot of the ring cross section, the velocity expressions were converted from a spherical coordinate system ( $r, \theta, \phi$ ) to a cylindrical polar system ( $z, r, \theta$ ), further reducing to  $x, y$  (See Figure 5.1). The spherical streamfunctions were converted to cylindrical coordinates then into the velocity expressions, according to the following process.

For  $r \geq a$

$$\Psi = -\frac{1}{2}Vr^2\sin^2\theta\left(1 - \frac{a^3}{r^3}\right) \implies \Psi = \frac{1}{2}Vy^2\left(1 - \frac{a^3}{(y^2 + x^2)^{\frac{3}{2}}}\right)$$

For  $r \leq a$

$$\Psi = -\frac{3U}{4}\left(1 - \frac{r^2}{a^2}\right)\sin^2\theta \implies \Psi = -\frac{3Uy^2}{4a^2}(a^2 - x^2 - y^2)$$

The streamfunctions can now be converted to velocity components by way of differentiation using the expressions below.

$$v_y = \frac{1}{y} \frac{\partial \Psi}{\partial x}, v_x = -\frac{1}{y} \frac{\partial \Psi}{\partial y}$$

Hence the cylindrical velocity components become:

$$v_y = \frac{3Uyx}{2a^2} \quad \text{for } r \leq a \quad (5.11)$$

$$v_x = \frac{-3U}{2a^2}(2y^2 + x^2 - a^2) \quad \text{for } r \leq a \quad (5.12)$$

$$v_y = \frac{3Ua^3yx}{2(x^2 + y^2)^{\frac{5}{2}}} \quad \text{for } r \geq a \quad (5.13)$$

$$v_x = -U\left(1 - \frac{a^3}{(x^2 + y^2)^{\frac{3}{2}}} - \frac{3Ua^3y^2}{2(y^2 + x^2)^{\frac{5}{2}}}\right) \quad \text{for } r \geq a \quad (5.14)$$

An [X,Y] coordinate grid was generated over X=0:50mm,Y=0:20mm, with coordinates spaced at 0.7193mm apart (as seen in PIV datasets). Equations 5.11,5.12 were employed to calculate velocity components within the ring, and Equations 5.13,5.14 for coordinates external to the ring bubble. This vector field was then mirrored across the z axis, resulting in the ring vortex meridional cross-section in the ring reference frame (See Figure 5.6c). To validate this formulation, the derived velocity component expressions were compared to published work using HSV [129],[143] and found to be correct. The vorticity distribution

is linear as reported [143],[144], [145], and the streamline shape matches those presented in published works also, presented in the figure below.

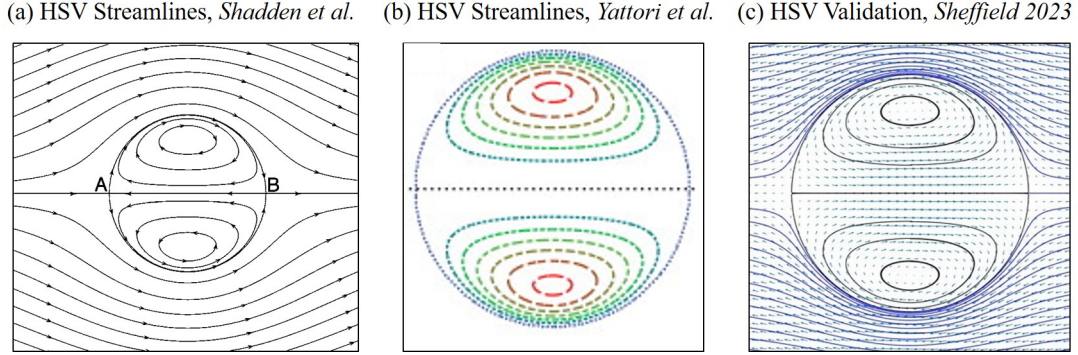


Figure 5.6: Validation of Hill's Spherical Vortex formulations in MATLAB. (a) shows the streamlines from Shadden et al.[144] (b) shows the streamlines from Yattori et al [143] (c) presents the streamlines from this project.

### 5.3.3 Lamb-Oseen Ring Vortex Formulation

As briefly discussed, formation of LO vector fields is different to HSV and KR, as its model is based on a singular vortex rather than a ring vortex. To generate the LO ring vortex, the core radius, ring radius and circulation was measured from each experimental vortex. An LO vortex vector field was then formed using these values, translated above the radial axis and mirrored. With the stipulation of zero radial velocity ( $v_r = 0$ ), the L-O vortex is defined by Equation 5.15 in polar coordinates. Core radius, circulation and ring radius are required from experimental datasets and used as inputs. To map this vortex onto a 2-D orthogonal plane, it is converted to Cartesian  $(x, y)$  components, where x and y are axial and radial coordinates.

$$v_\theta = \frac{\Gamma}{2\pi r} (1 - e^{-\frac{r^2}{a^2}}) \quad (5.15)$$

Using  $x = r\cos(\theta)$  and  $y = r\sin(\theta)$  where  $\theta$  is a parameteric function of t

$$\frac{dx}{dt} = \frac{d}{dt}(r\cos(\theta(t))) = \frac{dr}{dt}\cos(\theta(t)) - r\frac{d\theta}{dt}\sin(\theta(t))$$

$$\frac{dy}{dt} = \frac{d}{dt}(r\sin(\theta(t))) = \frac{dr}{dt}\sin(\theta(t)) + r\frac{d\theta}{dt}\cos(\theta(t))$$

As  $v_r = \frac{dr}{dt} = 0$ ,

$$\frac{dx}{dt} = v_x = -v_\theta\sin(\theta) \quad (5.16)$$

$$\frac{dy}{dt} = v_y = v_\theta\cos(\theta) \quad (5.17)$$

Applying these equations to Equation 5.15 gives the following expressions for the orthogonal velocity components:

$$v_x = -\frac{\Gamma y}{2\pi(x^2 + y^2)}\left(1 - e^{-\frac{x^2 + y^2}{a^2}}\right) \quad (5.18)$$

$$v_y = -\frac{\Gamma x}{2\pi(x^2 + y^2)}\left(1 - e^{-\frac{x^2 + y^2}{a^2}}\right) \quad (5.19)$$

A domain of  $[X,Y]=[-30:30\text{mm},-30:30\text{mm}]$  was generated and discretized to 0.7193mm. Using Equations 5.16 and 5.17, an LO vortex of radius  $a$  was produced, centred at  $(0,0)$ . This vortex was then translated to  $R\text{mm}$  above the  $x$  axis and mirrored, creating two opposite-facing vortices of equal and opposite vorticity. Both vortical fields are superimposed, resulting in a ring with the same  $R$ ,  $a$  and  $\Gamma$  as its corresponding experimental ring. No published plots were available for this model, so validation was performed by generating a vortex of circulation 10 and core radius 5. The vorticity distribution across the core was Gaussian as expected, and the circulation was calculated at 10, thus was plotted correctly (presented in the figure below).

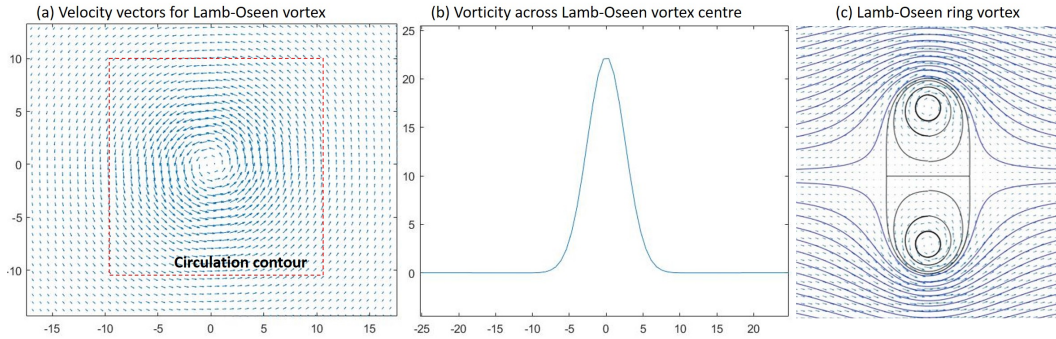


Figure 5.7: Validation of Lamb-Oseen formulations in MATLAB. (a) shows a single vortex with core radius 5. Circulation was measured to be 10 around the annotated contour (b) presents the vorticity across the centre of the core. (b) presents the full Lamb-Oseen ring vortex.

### 5.3.4 Kaplanski-Rudi Formulation

The KR vector description is straightforward to produce, as its velocity components are provided in Cartesian form. These were presented in dimensionless coordinates, normalised by the core radius  $L$ .

$$v_x = \frac{\sqrt{\pi}}{2\sqrt{2}} \int_0^\infty \mu F(\mu, \eta) J_1(\tau\mu) J_0(\sigma\mu) d\mu \quad (5.20)$$

$$v_y = -\frac{\sqrt{\pi}}{2\sqrt{2}} \int_0^\infty \mu [-G(\mu, -\eta) + G(\mu, \eta)] J_1(\tau\mu) J_1(\sigma\mu) d\mu \quad (5.21)$$

Where

$$F(\mu, \eta) = G(\mu, \eta) + G(\mu, -\eta), G(\mu, \eta) = \text{expt}(\eta\mu)(1 - \text{erf}(\frac{\mu + \eta}{\sqrt{2}}))$$

$$\sigma = \frac{r}{L}, \eta = \frac{x - x_0}{L}, \tau = \frac{R}{L}$$

$$\zeta = \frac{M}{(2\pi L^2)^{\frac{3}{2}} R}$$

$$\text{Where } M = \frac{\Gamma}{R^2}$$

The required experimental inputs are circulation, core radius and ring radius, all of which were measured from experimental vortices. A coordinate grid of  $[X, Y] = [-30:30\text{mm}, -20:20\text{mm}]$  was generated and discretized to 0.7193mm. The integrals above (Equations 5.20 and 5.21) were computed numerically with limits of 0-100 to ensure finite values. The dimensionless vectors were then configured for absolute values by multiplying by  $L$ , the normalisation constant and  $\zeta$ , the vorticity constant. Validation of this method was performed by reproducing an example contour plot of a ring vortex with  $\Gamma_0 = 1, R_0 = 1, \theta = 4$  as seen in [127]. The vorticity field was calculated and normalised against the maximum value, with the isocontours compared. The comparison is presented below, with the two formulations found to be equal.

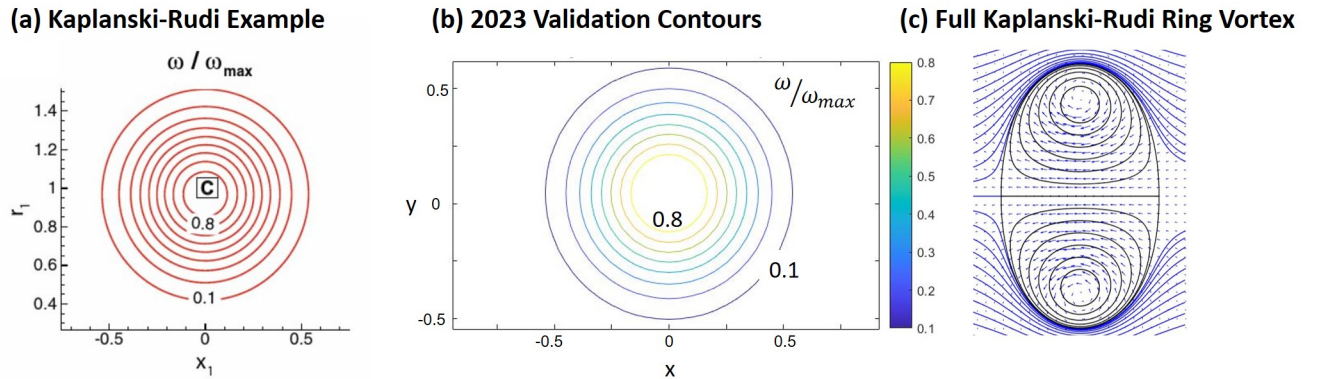


Figure 5.8: Validation of Kaplanski-Rudi formulations in MATLAB. (a) shows the normalised vorticity contours for a vortex of  $\Gamma_0 = 1, R_0 = 1, \theta = 4$  from [127]. (b) presents the Sheffield-produced validation contours with associated colourbar. (b) presents the full Kaplanski-Rudi ring vortex.

### 5.3.5 Conclusion

The methods presented here describe the process of replicating the experimental vortices within the confines of each analytical model. This represents a 'fitting' method, where parameters such as ring diameter and speed were measured from experimental datasets and used as inputs to generate corresponding analytical vortices. The inputs for HSV are

ring speed and ring height, whilst both LO and KR require circulation, ring diameter and core radius.

This method deviates from the numerical simulation alternative, where input parameters are used to establish an entire flow field. In this approach, typical inputs would include domain size and shape, boundary conditions (e.g. zero velocity at the tank walls) and the generating boundary condition (here being the velocity profile of the piston). Characteristics such as fluid viscosity, density and mesh size would also be incorporated. The methods fundamentally vary, where this analytical approach replicates a 'snapshot' of the post-laminar vortex, whereas a numerical approach would simulate the entire time-resolved process of generation, propagation and breakdown. Previous work employed numerical methods using CFD, however the resultant ring vortices were not consistent with experimental measurements.

For this analysis, a KR, HSV and LO vector field was produced for every individual experimental vortex from the 2019 PIV dataset, using the relevant experimentally-derived properties. This enabled comparison between experimental and theoretical ring vortices to identify the accuracy of the KR model in the context of this phantom. The following section describes the methods employed to compare these formulations.

## 5.4 Methods II - Comparison between Experimental and Analytical Ring Vortex Formulations

Comparison between theoretical (analytical/numerical) and experimental ring vortices in the literature employs a variety of methods with little consensus between research groups, and are often qualitative or superficial. For this work, a quantitative comparison is required, which will be achieved through three methods: similarity of ring properties (e.g. ring speed, size, energy), comparison of velocity vector flow fields, and quantitative comparison of streamlines from each model. Together, these methods can be used to characterise the phantom vortices in the context of the theoretical models. The aim of these methods is to ascertain to what level the experimental vortices agree with the Kaplanski-Rudi theoretical vortices.

### 5.4.1 Method A: Ring Vortex Properties

The first, and most straightforward method of comparison was comparing significant ring properties between experimental and analytical vortices. This is a common method for model validation in the literature [141],[135], as it can quickly ascertain accuracy at the macro-scale. The properties compared here were: ring translational speed, circulation and CentVect (the central axial velocity along the axis-introduced in Chapter 3). These properties effectively summarise the ring vortex dynamics, and were calculated using the following methods:

- **Ring Speed** is calculated for experimental rings through ring displacement between subsequent PIV frames. Analytical ring speed is calculated through derived

equations provided by the authors.

- **Circulation** is calculated by performing a line integral of the velocity components across a domain 20mm high and 30mm wide from the centre of the ring. This is valid for both analytical and experimental formulations.
- **CentVect** is extracted from the velocity flow fields. For both experimental and theoretical rings it is the axial velocity present in the centre of the ring vortex.

Applying the above gave an early indication of any large disagreements between experimental and theoretical rings, with results presented in Section 5.5. Its reliance on equations relating to bulk properties, however, provided limited information on differences in the micro-level of vector fields. The remaining two methods therefore interrogate the flow at a more detailed level.

### 5.4.2 Method B: Local Velocity Vector Agreement

The second method compared velocity vector fields between formulations. This was deemed a ‘semi-quantitative’ method as it relied on user-performed alignment between individual vortices. This method calculated the similarity of individual ring vortex vectors (either KR, LO, HSV or PIV) to averaged experimental (PIV) datasets for a certain configuration. Velocity vector lengths (magnitude) and angles were analysed separately across the ring vortex domain. The angles and lengths of each vector across the domain were calculated for each PIV ring. They were aligned through the point of maximum vorticity (the centre of the top core) and the average value for angle and length was found at each coordinate for each configuration. This produced a set of 7 ‘Average Maps’, one for each configuration, where each location had a recorded average experimental reading. See Figure 5.9 for this process.

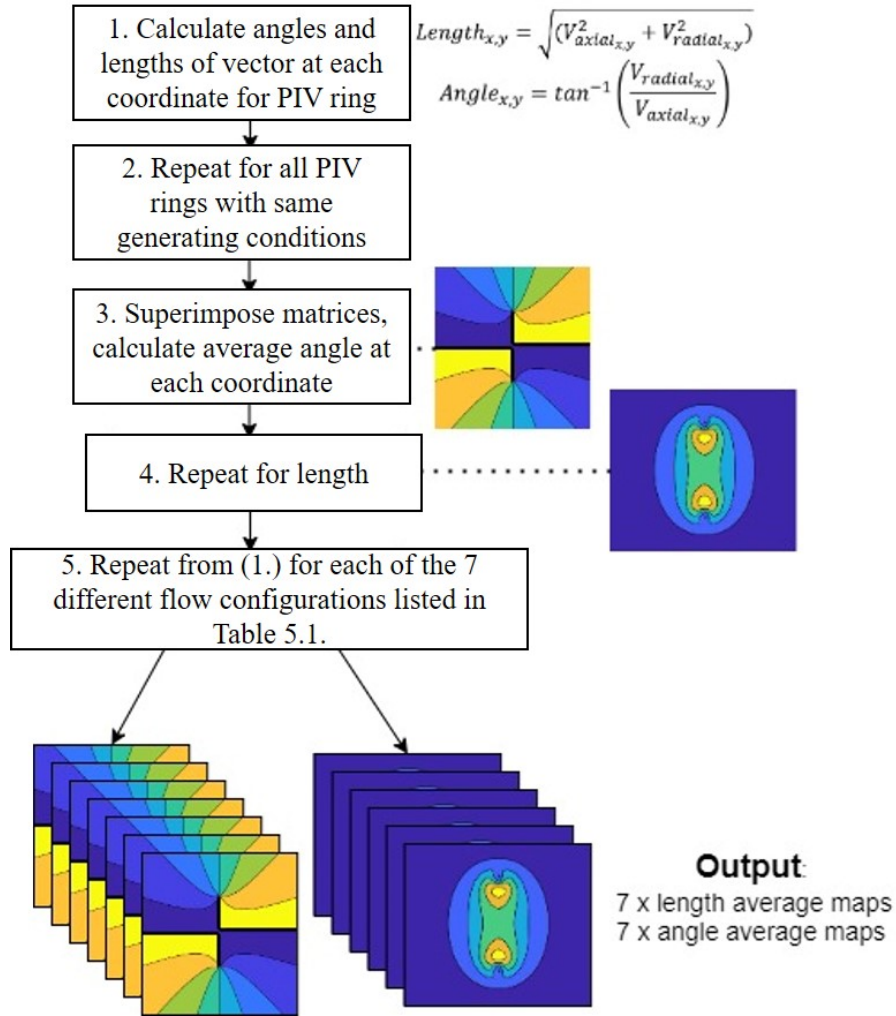
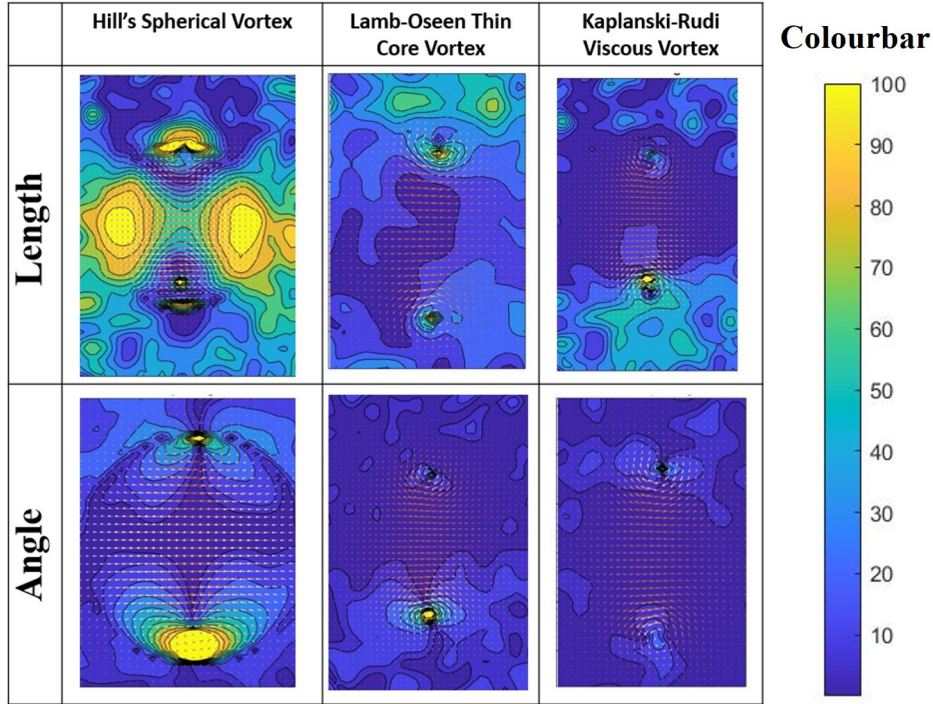


Figure 5.9: Flowchart detailing the procedure for creating average length and angle maps for experimental ring vortices

Following this, a sample theoretical ring was selected (HSV, LO or KR) and its vector angles and lengths calculated. It was then compared to the average map for that condition, aligned using the points of maximum vorticity. The absolute difference between average angle and sample vector angle was calculated at each point. This was repeated for the vector length data, with the percentage difference calculated. This produces a difference map which immediately highlights discrepancies between theory and experiment. An example map for each is presented below, using configuration 3 rings for both angle and length similarity at each coordinate.



Colourbar values correspond to **percentage difference** for vector lengths, and **absolute difference** for vector angle, between the experimental and analytical formulations.

Figure 5.10: Example similarity maps comparing experimental and analytical ring vortex vector plots with the average PIV vector plots overlaid. The colourbar is used for both length and angle maps. Length maps are coloured according to percentage difference between experimental and analytical vortex lengths. Angle maps are coloured according to absolute difference in degrees.

There are clear differences between formulations visualised in these maps. The HSV-PIV comparison (column 1) shows large differences in both angle and length. For velocity vector lengths, there is a band of agreement (dark blue on the colourmap) around the cores, but there are differences up to and above 100% across the domain. The angles are correct in the vortex centre and around the boundary edge, but differ across the rest of the domain. Interestingly, both LO and KR have high agreement in vector angle, with differences of less than 5-10% across a large portion of the ring. This is expected as they both assume a Gaussian core, accurately mimicking the experimental vortices. In terms of vector length, however, LO deviates from the PIV for much of the domain with differences over 30%, whilst KR more closely follows the PIV data with large sections under 10%.

These observations were quantified through a thresholding process. For vector length, each vector is classified as 'in bounds' (where the sample ring vector was <10% different from the corresponding vector on the average map) or 'out of bounds' (where the sample length was >10% from the average length at that point), and the % of vectors lying in bounds was calculated. For example, a 100% 'in bounds' analysis would indicate that all vector lengths lie within 10% of the averaged vectors lengths for that configuration.

This was repeated for the vector angles, where ‘in bounds’ vectors lie within 10° of the average. This threshold used absolute degrees instead of percentage. The percentage of vector angles lying within bounds was calculated. Maps of different thresholds for each formulation are presented below in Figures 5.11, 5.12.

Exploiting symmetry, only the top half (positive y values) are shown. This ensures that the core, CentVect location and ambient fluid behaviour were compared without results being skewed from experimental fluctuations. Quantitative results are listed in the Results section.

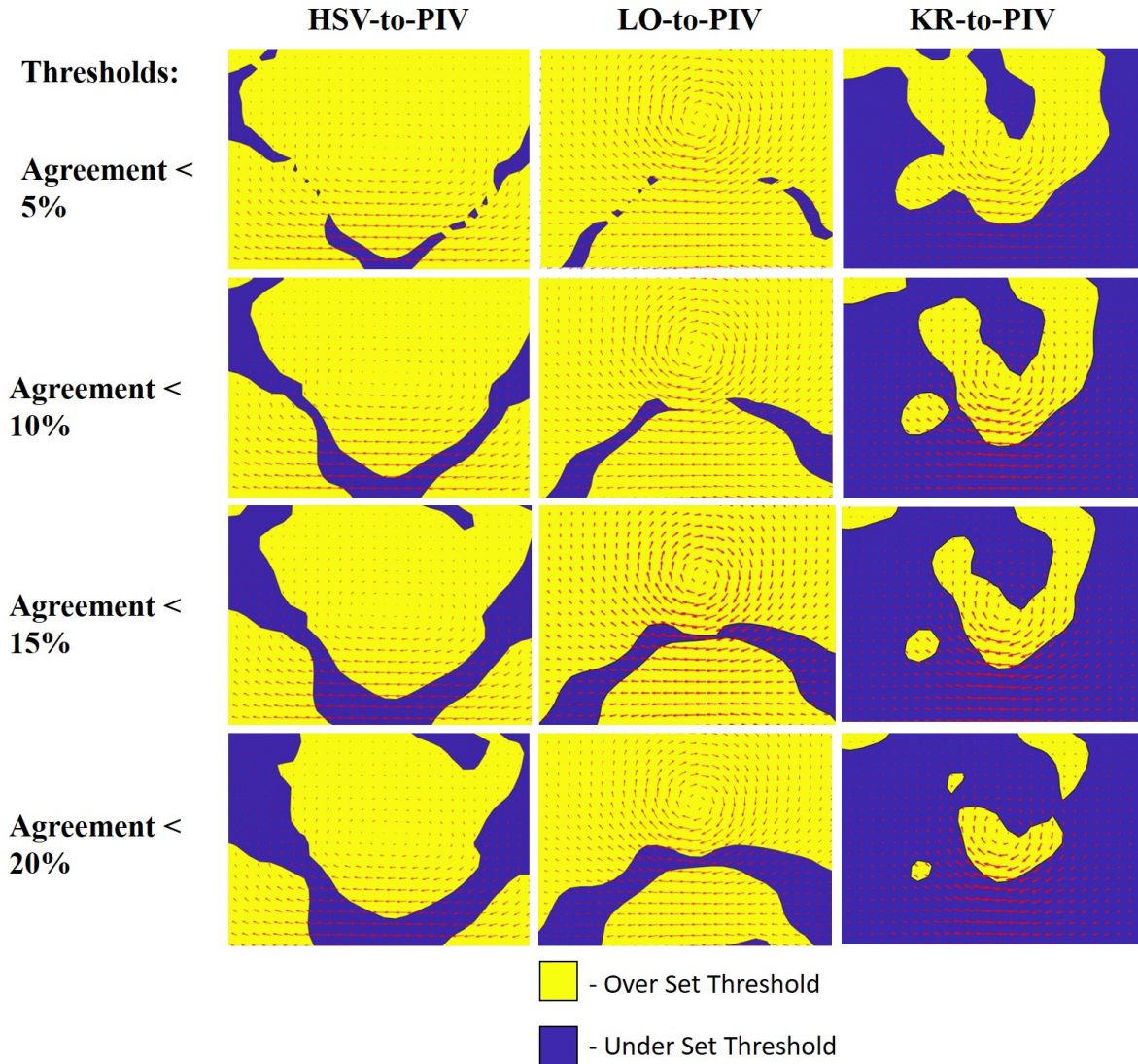


Figure 5.11: Maps demonstrating where analytical vector lengths lie ‘in bounds’ when compared to an average experimental map. Yellow regions lie over the set threshold, and blue regions lie under the set threshold. Thresholds are varied between 5-20%.

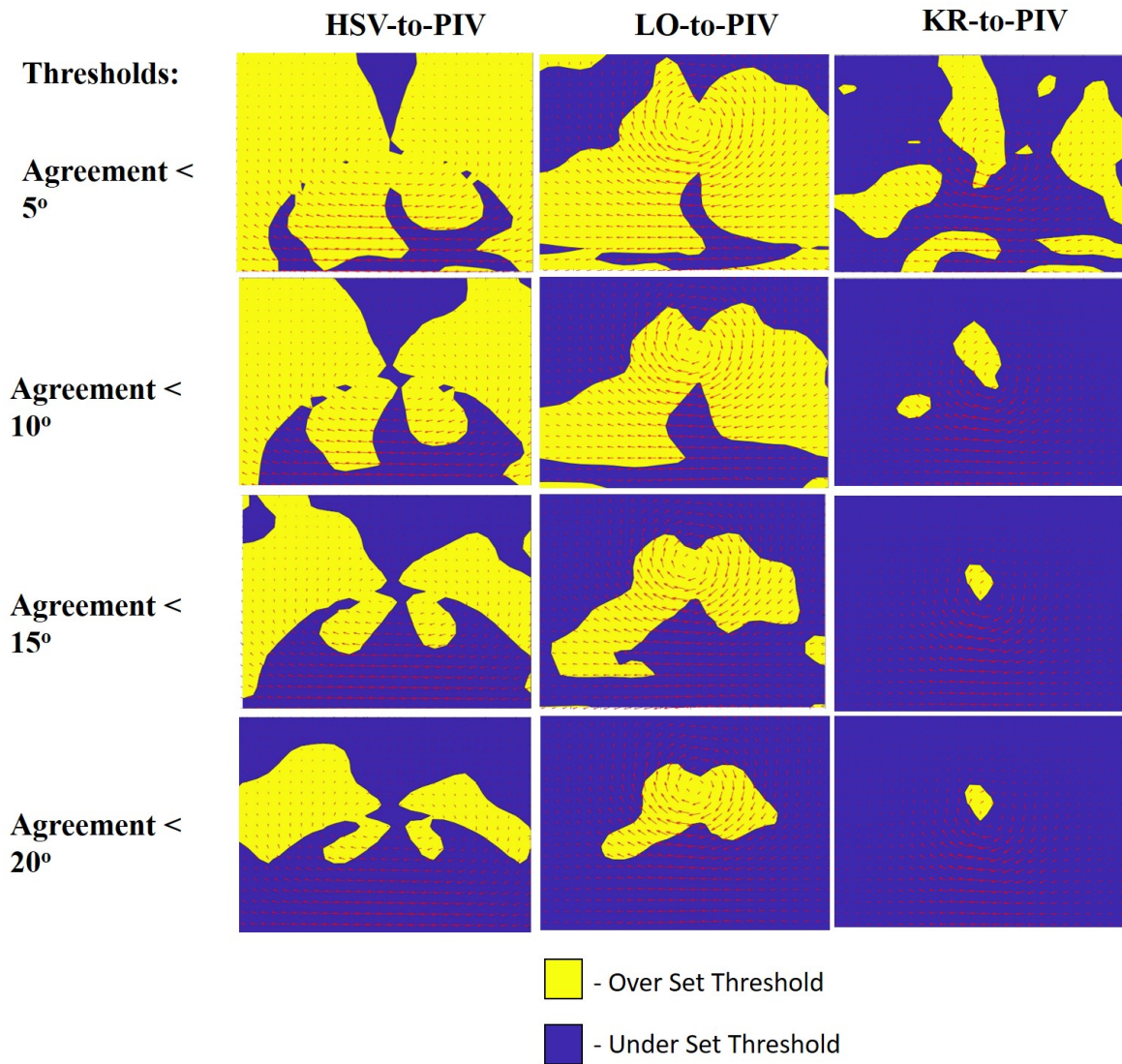


Figure 5.12: Maps demonstrating where analytical vector angles lie 'in bounds' when compared to an average experimental map. Yellow regions lie over the set threshold, and blue regions lie under the set threshold. Thresholds are varied between 5-20°.

The maps above visualise the vectors which lie 'in bounds' and 'out of bounds' with varying thresholds for both vector length and angle. KR vortices have a significant proportion of vectors which lie within bounds across all thresholds, whilst LO and HSV show lower agreement in both length and angle. These maps are useful to visualise where the models deviate from experimental behaviour.

### 5.4.3 Method C: Streamline Spherical Harmonics

The final method to compare experimental and theoretical vortices used the streamlines for each ring vortex in the laboratory reference frame. Streamlines are used extensively

in fluid visualisation, as they display the path followed by a small fluid element, allowing intuitive visualisation of how the flow behaves. Ring vortex model validation has used streamlines qualitatively [135], and this work expanded on these findings through quantitative comparison using spherical harmonics. The following method was used to generate consistent streamlines for each ring vortex vector plot. See Figure 5.14 for a method flowchart.

1. Identify the location of maximum vorticity the ring vortex - this is the centre of the top core.
2. Identify the bubble streamline which encloses the entire ring.
3. The distance between max vorticity (core centre) and bubble streamline (the top of the ring) is found, denoted ' $d$ '.
4. Five streamlines are generated, starting at  $\frac{d}{5}$  above the core centre and separated by increments of  $\frac{d}{5}$  until the 5th streamline is met, signifying the top of the ring.

These streamlines were generated for each ring, for PIV, HSV, LO and KR. Example streamlines are presented below.

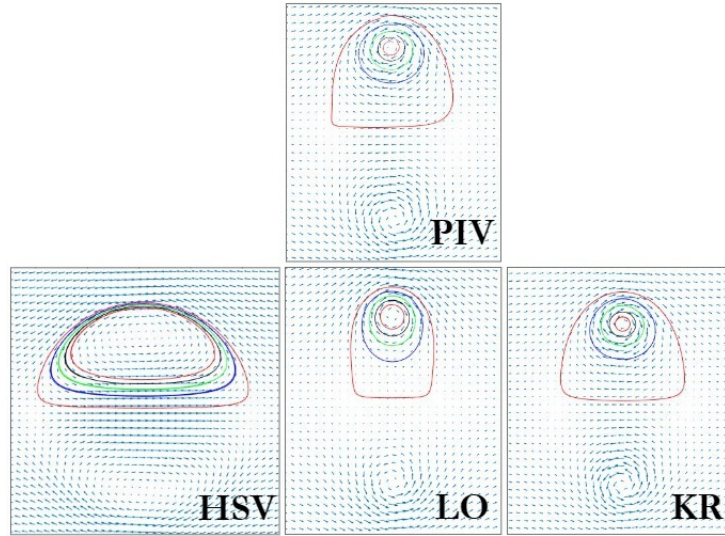


Figure 5.13: Example streamlines for ring vortex formulations. Experimental (Laser PIV), HSV, LO and KR formulations are included. An artefact in the PIV streamlines is apparent at the bottom left and is a result of PIV discretisation and the streamline seeding point.

The streamlines visually differ between formulations, particularly different between HSV and PIV. HSV has a wide, ‘semi-circle’ shape with deformed cores, and LO has a more compact aspect ratio when compared to PIV. The KR streamlines are visually the most similar to the PIV. These visual observations were further confirmed by quantitative comparison. Once the streamlines are generated, the following analysis takes place (summarised in Figure 5.14) to quantify these visual comparisons:

1. The distance  $R$  from the core centre to the streamline was found for  $[0-360^\circ]$ , and plotted as a plot of  $R$  vs  $\theta$
2. This line function was fit to a Fourier model, resulting in eight coefficients that describe the line. Coefficients were saved for this streamline
3. The process was repeated across all five streamlines and all coefficients saved, resulting in a  $[5 \times 8]$  matrix for this ring.
4. The process was repeated for each ring vortex.

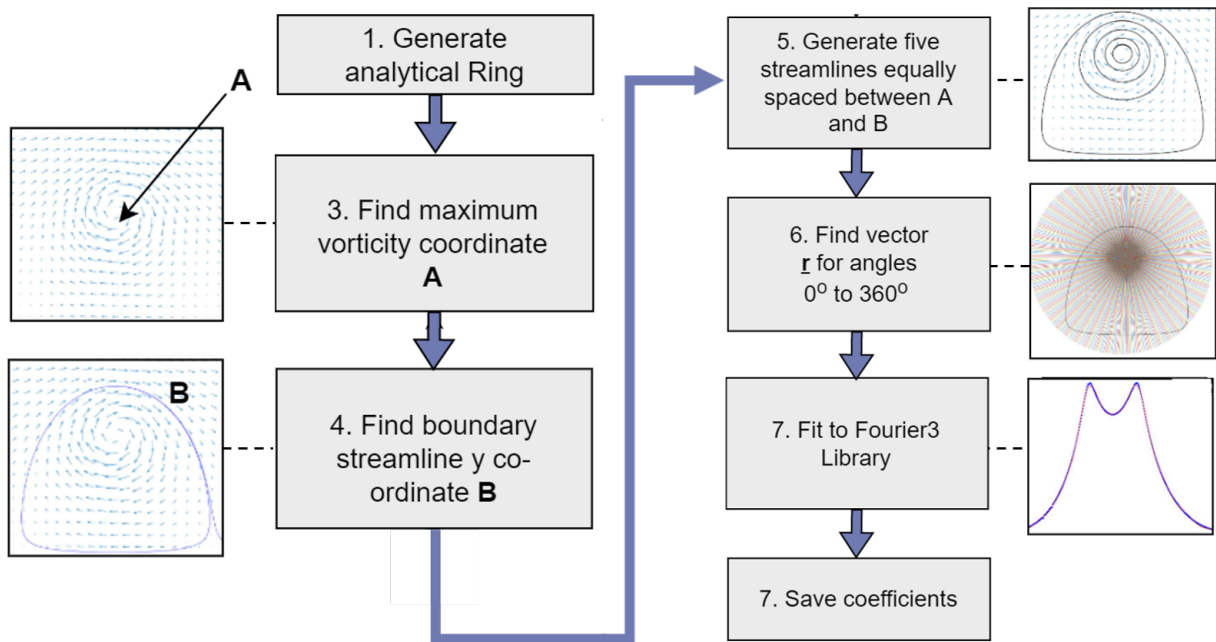


Figure 5.14: Flowchart for calculating spherical harmonics for ring vortex streamlines

This analysis was chosen as a quantitative mechanism for summarising streamline shapes with minimal user-reliance. Different coefficients (Fourier ‘signatures’) were generated from each of the streamlines. The visually different streamline shapes observed in Figure 5.13 are consequently reflected in the relative coefficients for each. Example coefficients are presented below for a sample ring, with clear similarity between the PIV and KR formulations, reflecting the visual streamline behaviour.

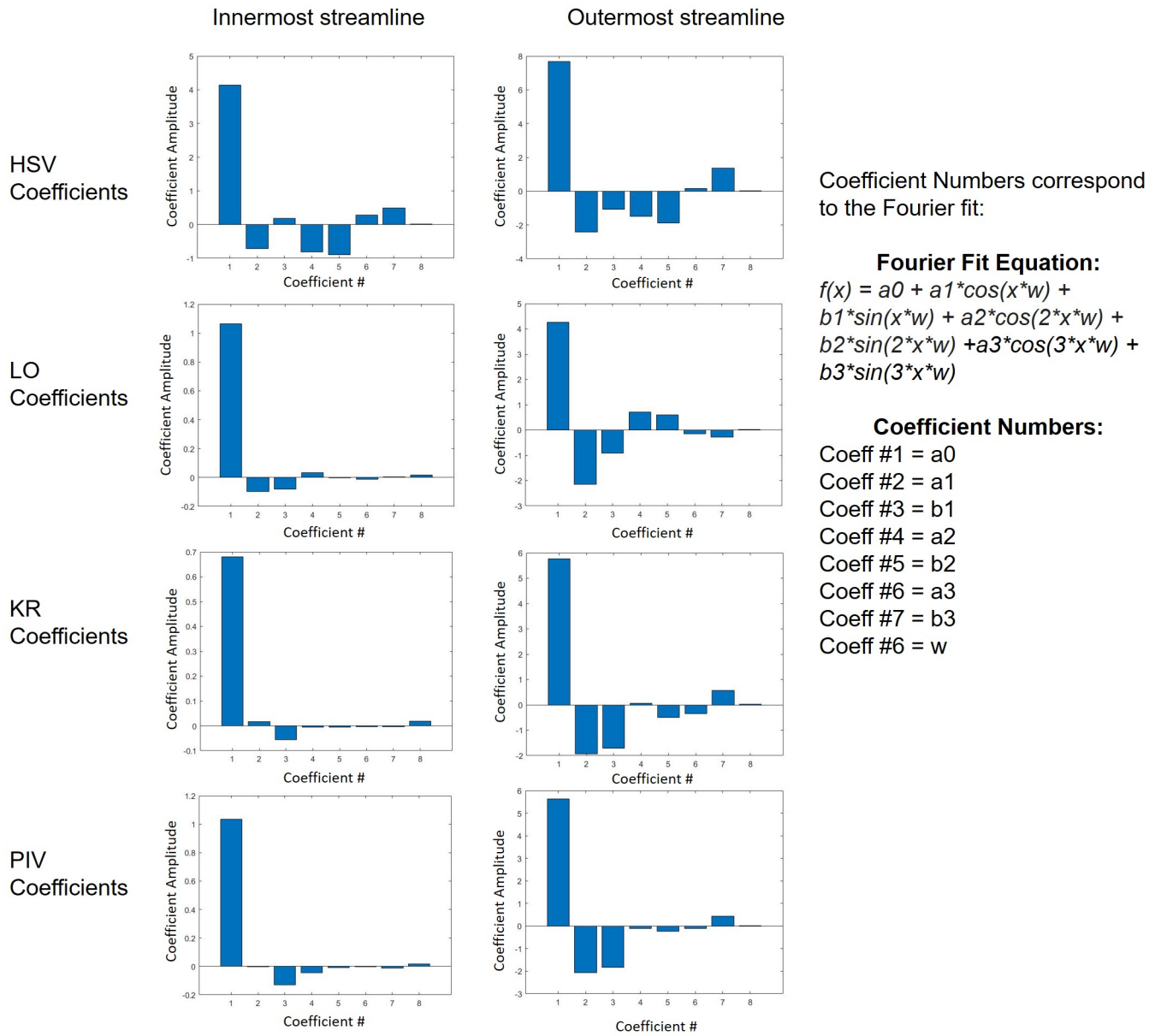


Figure 5.15: Example streamline harmonics coefficients for different ring vortex formulations.

The difference between coefficients in different formulations was quantified using experimental bounds. The streamline coefficients were found for all experimental rings, and averaged for each configuration. The standard deviation was also found, and a range was set for each coefficient, where inside the range [mean-STD:mean+STD] was deemed as ‘in bounds’ and outside the range as ‘out of bounds’. A sample ring’s streamlines were processed, and its coefficients deemed to lie in or out of these bounds. There were 40 coefficients (8 coefficients per streamline and 5 streamlines per ring) for each ring vortex. The percentage of coefficients lying within experimental bounds was calculated for each

ring vortex to indicate the level of agreement in streamline shape.

## 5.5 Results

### 5.5.1 Method A: Ring Vortex Properties

The results in this section compare the ring vortex properties for each formulation. Datapoints represent the average value across ten rings, whether experimental or theoretical. Error bars represent 1SD, and the variation of each property between individual rings.

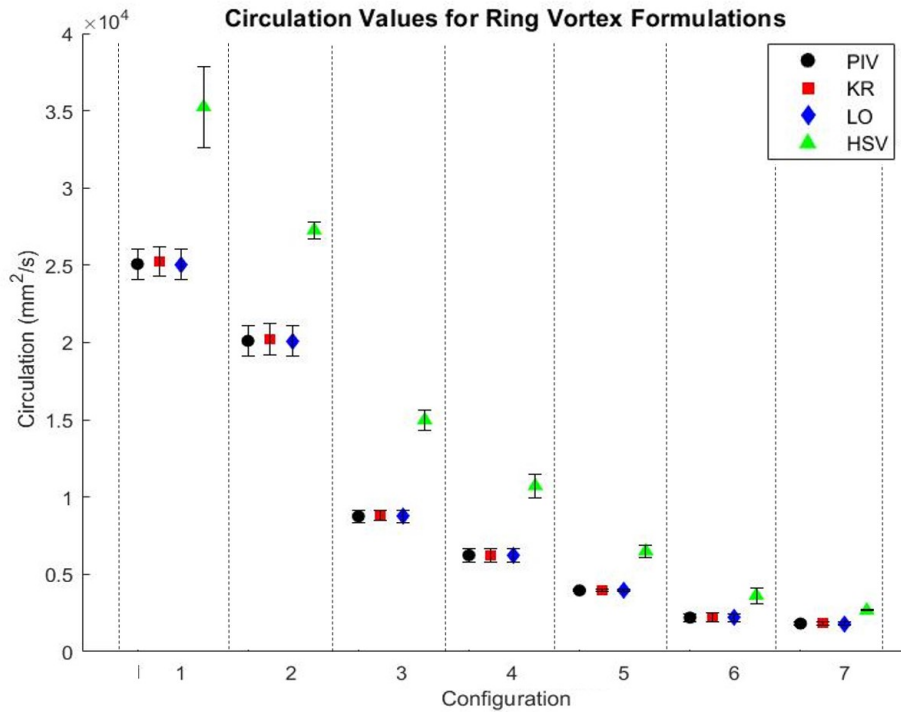


Figure 5.16: Comparison between circulation values for post-formation ring vortices of different formulations for configurations listed in Table 2.1. Datapoints represent the average of ten vortices and error bars 1SD

Figure 5.16 plots the circulation values for each formulation. It is immediately evident that HSV circulation is significantly higher than experimental values, whilst both LO and KR closely match the PIV. This is expected as both LO and KR use circulation as an input, and this preliminary analysis indicates that their formulation was correct.

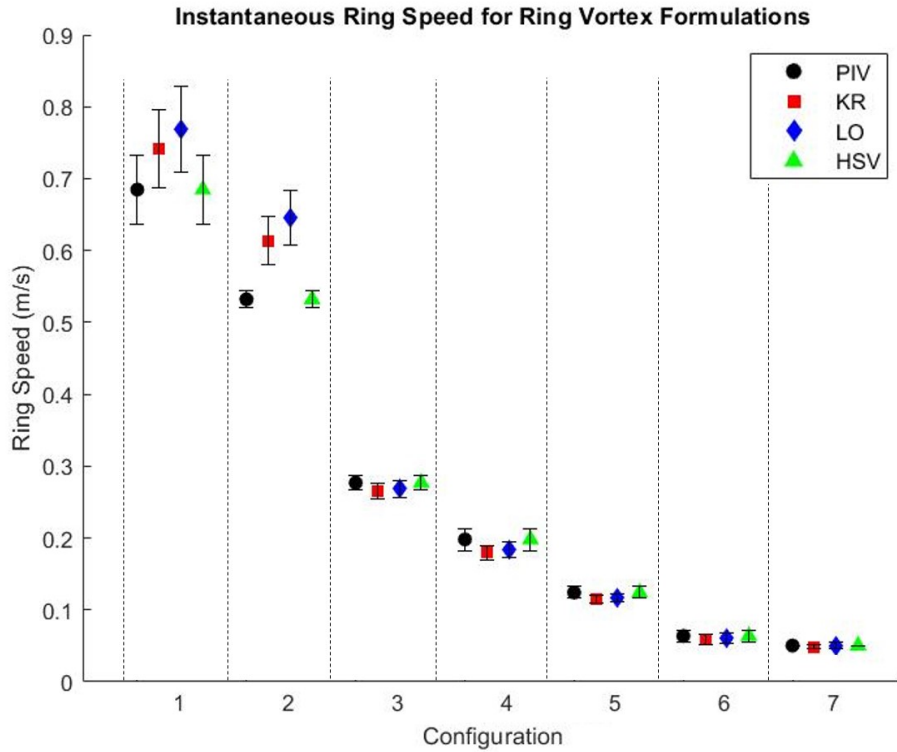


Figure 5.17: Comparison between ring speed values for post-formation ring vortices of different formulations for configurations listed in Table 2.1. Datapoints represent the average of ten vortices and error bars 1SD

This graph plots the instantaneous ring speed values for each formulation at 15cm from the orifice. There are mixed results, with LO and KR values varying from PIV measurements across the configurations. The HSV model uses ring speed as an input parameter, thus is not assessed here, and is only for validation. It is particularly notable that for the faster rings (configurations 1,2), the theoretical rings (KR, LO) are faster.

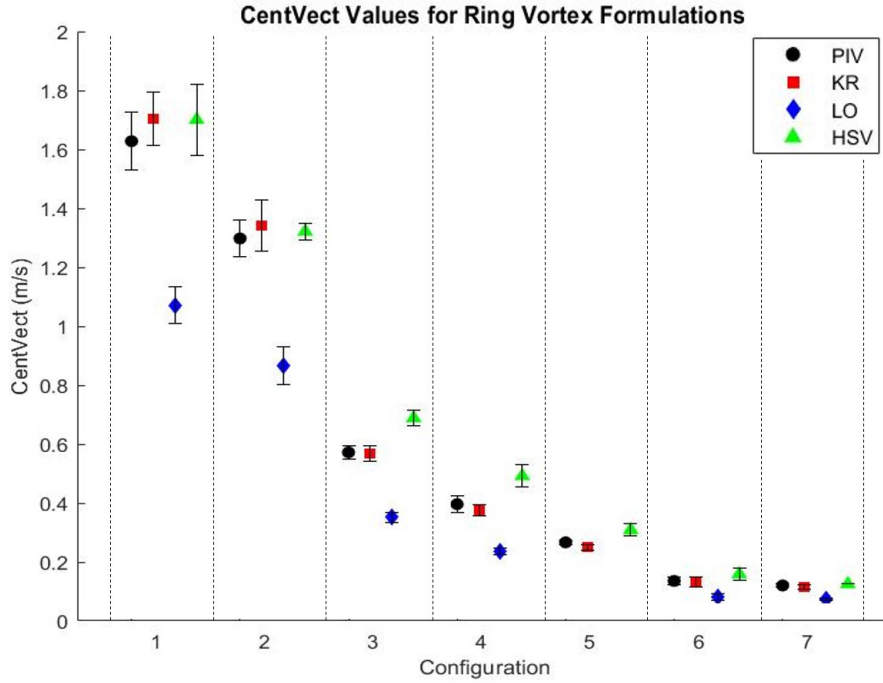


Figure 5.18: Comparison between CentVect values for post-formation ring vortices of different formulations for configurations listed in Table 2.1. Datapoints represent the average of ten vortices and error bars 1SD

The CentVect measurements for each model and experimental vortices are compared here. This measurement is taken directly from velocity vector plots, so reflects the micro-flow accuracy. LO values are consistently lower than PIV, HSV values are too high in most configurations, whilst KR lies within experimental tolerances across all tested ring vortices.

These results will be reviewed in the Discussion Section 5.6 along with results from Methods B and C.

### 5.5.2 Method B: Local Velocity Vector Agreement

The graphs in this section present the results for Method B, the comparison between velocity vectors of experimental and theoretical rings. These graphs display the **percentage of vectors that lie within 10% (for vector length) or 10° (for vector angle) of the average experimental vector at that location**. Individual PIV rings are also compared to the PIV averages to determine variation between individual runs. Both velocity vector length and angle are assessed, and details are listed in the captions.

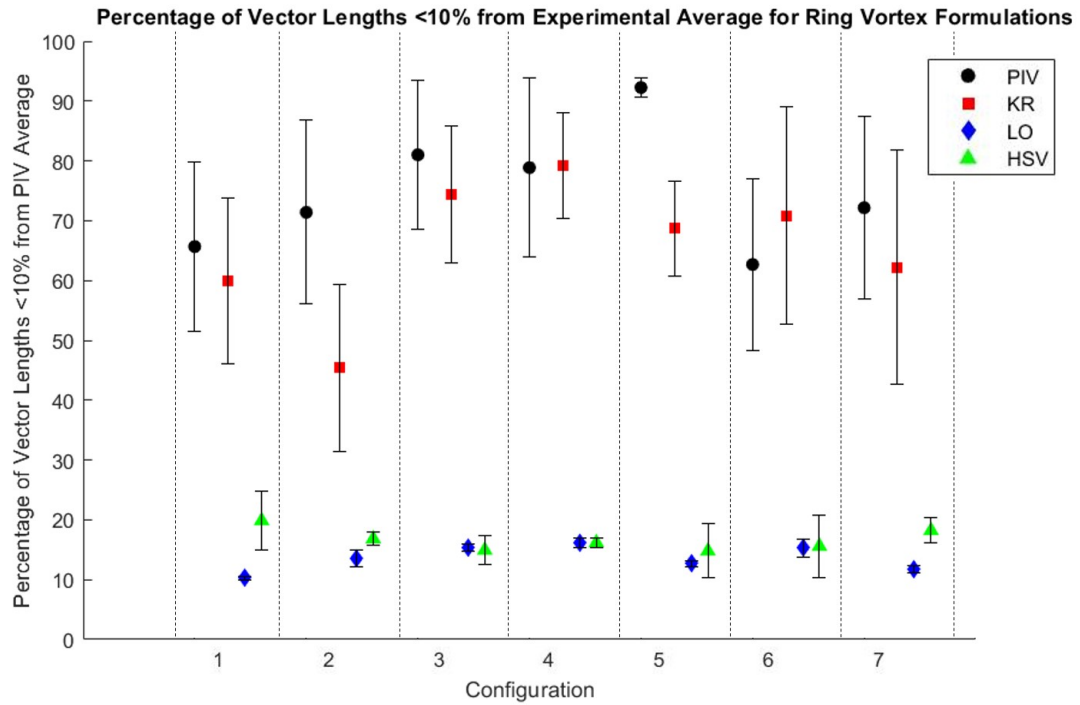


Figure 5.19: Graph presenting the similarity in vector lengths between analytical and experimental ring vortices. Y axis values correspond to the percentage of sample ring velocity vectors whose lengths lie within 10% of the experimental average at that point. Datapoints represent the average of ten vortices and error bars 1SD.

This graph present PIV-to-PIV agreement of 60-80%, with an anomaly of 90%. For analytical rings to act similarly to experimental rings, they must therefore have agreement of at least 60-80%. There was notably low agreement between HSV-to-experimental and LO-to-experimental comparisons. In all configurations, both models have less than 20% of vectors lying within experimental bounds of 10%. Meanwhile, the KR model had 60-80% of vectors lying in bounds, largely matching the experimental agreement. A notable exception was Configuration 2, where the KR agreement was only at 50%.

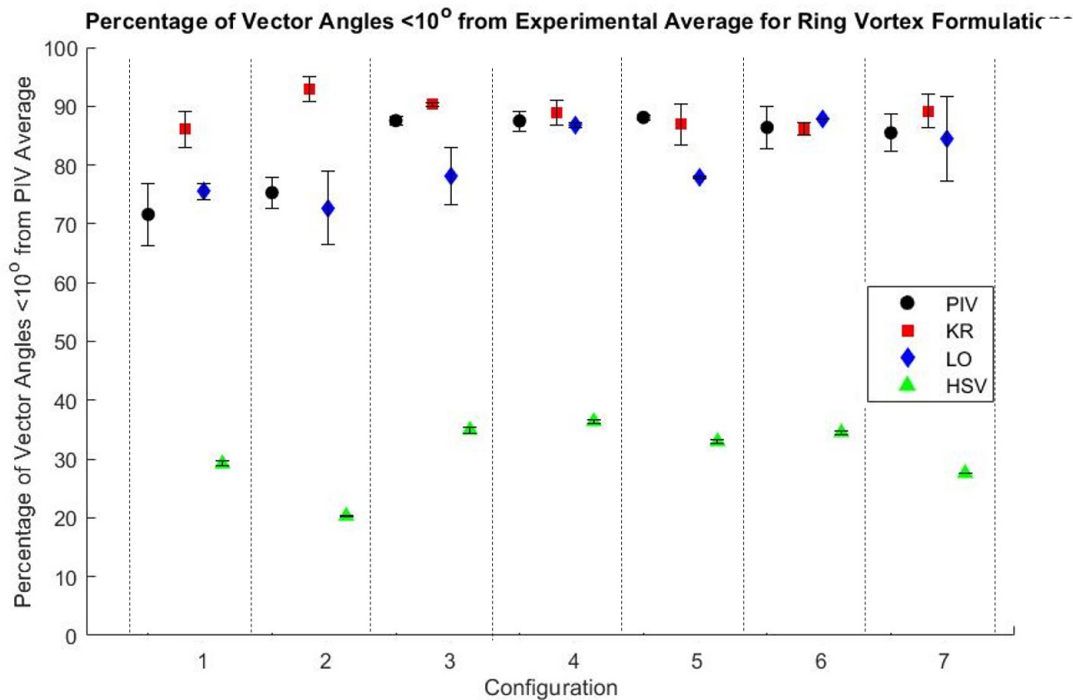


Figure 5.20: Graph presenting the similarity in vector angles between analytical and experimental ring vortices. Y axis values correspond to the percentage of sample ring velocity vectors whose angles lie within  $10^\circ$  of the experimental average at that point. Datapoints represent the average of ten vortices and error bars 1SD.

This graph presents the agreement of vector angle between formulations. PIV-to-PIV agreement is high in this analysis also, with values ranging from 70-90%. HSV has low agreement, with only 30-40% of vectors lying within 10 degrees of experimental averages for all configurations. Meanwhile, The LO agreement matches consistently with PIV agreement, from 70-90. KR agreement is the highest, ranging from 80-95% agreement with experimental rings.

### 5.5.3 Method C: Spherical Harmonics

Finally, this section lists results for the quantitative comparison between streamline spherical harmonics. For each configuration, the percentage of streamline coefficients that lie within experimental tolerances are presented. Datapoints represent the average of ten vortices and error bars represent 1SD.

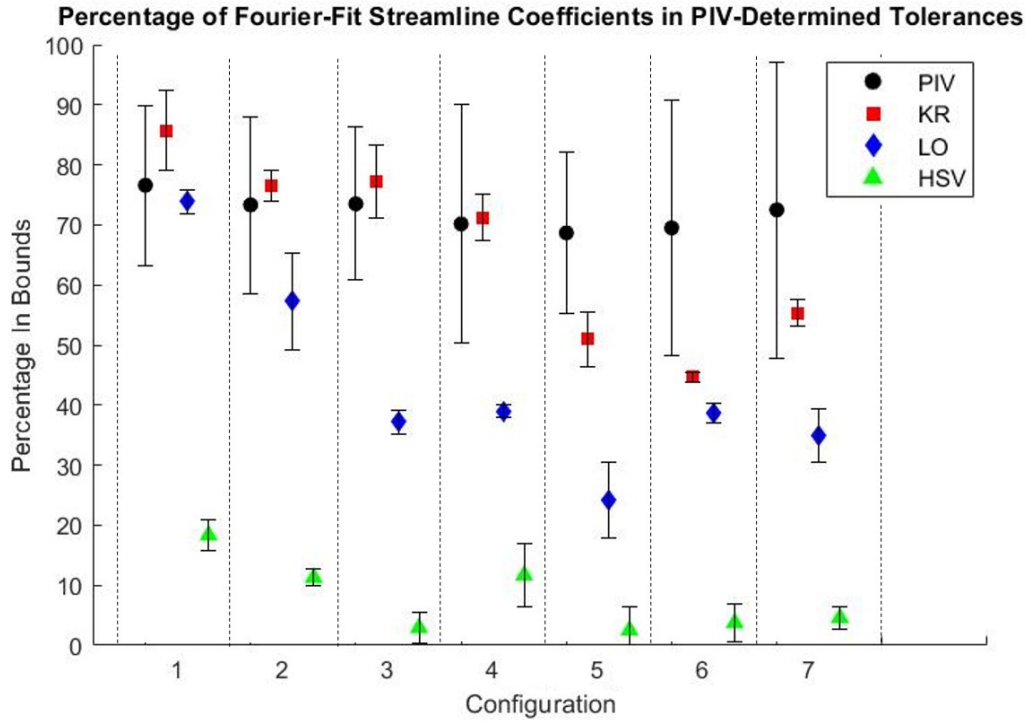


Figure 5.21: Graph presenting the similarity in streamline Fourier coefficients between analytical and experimental ring vortices. Y axis values correspond to the percentage of Fourier components for the sample ring that lie within experimental bounds of the experimental average. Datapoints represent the average of ten vortices and error bars 1SD.

This graph presents the agreement between streamline coefficients for each formulation. PIV-to-PIV agreement ranges from 70-80%. The HSV model has the lowest agreement across all configurations, with 5-20% of coefficients lying within experimental bounds. The LO model shows high agreement for faster rings, however slower rings (configurations 3-7) show a significant reduction in agreement. Finally, KR has good agreement for configurations 1-4, which again drops off for slower configurations.

## 5.6 Discussion

### 5.6.1 Results Analysis

The experimental ring vortices have been compared to each analytical vortex using a number of methods. To establish the level of agreement between the phantom rings and the theoretical KR rings it is useful to collate the results and assess them together. This section will discuss the results from Methods A, B and C and consider the limitations for each, before determining whether the experimental rings can be described using the KR analytical model.

## Method A: Ring Property Comparison

|      | Config | Speed |   |   | Circ |   |   | CentVect |   |   |
|------|--------|-------|---|---|------|---|---|----------|---|---|
|      |        | K     | L | H | K    | L | H | K        | L | H |
| Fast | 1      | ✓     | ✗ | ✓ | ✓    | ✓ | ✗ | ✓        | ✗ | ✓ |
|      | 2      | ✗     | ✗ | ✓ | ✓    | ✓ | ✗ | ✓        | ✗ | ✓ |
|      | 3      | ✓     | ✓ | ✓ | ✓    | ✓ | ✗ | ✓        | ✗ | ✗ |
|      | 4      | ✓     | ✓ | ✓ | ✓    | ✓ | ✗ | ✓        | ✗ | ✗ |
|      | 5      | ✓     | ✓ | ✓ | ✓    | ✓ | ✗ | ✓        | ✗ | ✗ |
|      | 6      | ✓     | ✓ | ✓ | ✓    | ✓ | ✗ | ✓        | ✗ | ✓ |
| Slow | 7      | ✓     | ✓ | ✓ | ✓    | ✓ | ✗ | ✓        | ✗ | ✓ |

Table 5.3: Table listing the results from comparing parameters of different ring vortex formulations. ✓ indicates that the analytical value lies within experimental tolerances, and ✗ that they lie without

### *Circulation*

Comparing circulation values validates the vector fields derived from the models, as both K-R and L-O require circulation as an input parameter. Across the seven configurations, L-O and K-R circulation values agree closely with experimental averages, indicating correct numerics. The HSV model doesn't use circulation as an input, and when measured, displays a circulation at approximately 50% higher than the experimental average, far outside of experimental bounds.

### *Ring Speed*

HSV speeds can't be compared to PIV speeds as they are used as the HSV input parameter. There is good agreement between L-O and PIV, with configurations 3-7 lying within experimental bounds. Similar results are found for KR, with KR speeds lying within experimental bounds for configurations 1,3-7. Configuration 2 has a significant disagreement with KR. Disagreement in higher speed rings implies a mechanism not considered in the model, such as the disturbance/turbulence observed at these speeds. Overall, both LO and KR models accurately calculate ring speeds for speeds up to 30cm/s.

### *CentVect*

The HSV CentVect measurement lies within experimental tolerances for most configurations (1,2,6,7). The LO measurements, however, have CentVect values at approximately half the experimental values, outside of experimental tolerances for all configurations. All KR values lie within tolerances across the configurations, with comparable error bars. CentVect is influenced by ring speed/circulation, core radius and ring radius, thus is a good indicator of general agreement between formulations' vector plots. It is also a direct measurement from velocity plots rather than derived expressions. The high KR-to-PIV agreement is positive, as it demonstrates higher similarity to PIV than other models.

**Method A Conclusions** Overall, the KR model most accurately estimates ring vortex properties for post-formation laminar rings. The only KR value not in agreement is the speed for configuration 2, which is a notable anomaly. The L-O model has good

agreement in speed and circulation, but is consistently wrong in CentVect. HSV gives incorrect values for both circulation and CentVect. The discrepancy between HSV, LO and the experimental bounds highlights their employment as secondary models.

### Method B: Vector Comparison Maps

Vector comparison was performed in two steps: comparison of vector lengths then of vector angles, providing information about the models' accuracy for both flow speeds and directions within the ring vortex. PIV-to-PIV agreement covered a range of 60-80% (ignoring the configuration 2 anomaly at 90%), defining the level at which a vortex is of sufficient agreement. Under this range, KR rings act as experimental vortices for configurations 1-7. Both LO and HSV compared negatively to PIV, as only 10-15% of vectors lay within experimental bounds across all configurations.

Secondly, the vector angles were compared, which indicated the similarity in ring shape and flow direction. PIV-to-PIV agreement was between 70-90% here. As expected, HSV agreement is very low, with <35% of vector angles lying within 10% of the experimental average due to its spherical shape. L-O agreement is variable, lying in experimental tolerances for configurations 1,2,4,6,7. KR is also variable, lying in experimental bounds for configurations 4,5,6,7. Those configurations where the KR agreement is not in experimental bounds has the KR agreement *higher* than experimental agreement. Overall, KR exhibits high agreement (90%) to averages for all configurations, thus it can be considered that KR vector angles are a good approximation of PIV, typically within a 10% tolerance.

### Method C: Spherical Harmonics

The final method compared the shape of streamlines through spherical harmonics. The PIV agreement to its own average was consistent at approximately 70-80% in this analysis. The HSV agreement was low across all configurations, with <20% of coefficients lying in experimental bounds, reflecting the visual difference in streamlines. LO agreement was again variable, with only configuration 1 lying in experimental bounds and low agreement for all other configurations. Finally, KR agrees with experiment for configurations 1-4. Configurations 5,6,7 has low agreement at around 50%. This analysis indicates that the KR model will accurately represent experimental streamlines for configurations 1-4. This analysis gave valuable information about the experimental ring shape. The KR model was inaccurate for slower rings, indicating a change in experimental behaviour.

## 5.6.2 Are the Phantom Ring Vortices Kaplanski-Rudi?

The objective of this work was to determine whether the experimental phantom rings could be described using a published analytical model, specifically the Kaplanski-Rudi model. As a range of methods have been used the results may vary. The summarised findings are tabulated below.

|          | Speed |   |   | Circ.n |   |   | CentVect |   |   | S. Harm |   |   | Vel Ang |   |   | Vel Len |   |   |
|----------|-------|---|---|--------|---|---|----------|---|---|---------|---|---|---------|---|---|---------|---|---|
|          | K     | L | H | K      | L | H | K        | L | H | K       | L | H | K       | L | H | K       | L | H |
| <b>1</b> | ✓     | ✗ | ✓ | ✓      | ✓ | ✗ | ✓        | ✗ | ✓ | ✓       | ✓ | ✗ | ✓       | ✓ | ✗ | ✓       | ✗ | ✗ |
| 2        | ✗     | ✗ | ✓ | ✓      | ✓ | ✗ | ✓        | ✗ | ✓ | ✓       | ✗ | ✗ | ✗       | ✓ | ✗ | ✓       | ✗ | ✗ |
| <b>3</b> | ✓     | ✓ | ✓ | ✓      | ✓ | ✗ | ✓        | ✗ | ✗ | ✓       | ✗ | ✗ | ✓       | ✗ | ✗ | ✓       | ✗ | ✗ |
| 4        | ✓     | ✓ | ✓ | ✓      | ✓ | ✗ | ✓        | ✗ | ✗ | ✓       | ✗ | ✗ | ✓       | ✓ | ✗ | ✓       | ✗ | ✗ |
| 5        | ✓     | ✓ | ✓ | ✓      | ✓ | ✗ | ✓        | ✗ | ✗ | ✗       | ✗ | ✗ | ✗       | ✗ | ✗ | ✓       | ✗ | ✗ |
| 6        | ✓     | ✓ | ✓ | ✓      | ✓ | ✗ | ✓        | ✗ | ✓ | ✗       | ✗ | ✗ | ✓       | ✓ | ✗ | ✓       | ✗ | ✗ |
| <b>7</b> | ✓     | ✓ | ✓ | ✓      | ✓ | ✗ | ✓        | ✗ | ✓ | ✓       | ✗ | ✗ | ✓       | ✓ | ✗ | ✓       | ✗ | ✗ |

Table 5.4: Table listing the agreement between ring vortex formulations for parameter comparison, velocity vector similarity and quantitative streamline similarity. Rows in bold present conditions where agreement is found with the Kaplanski-Rudi model across all methods.

This table presents the range of results from these analyses. In respect of secondary models of HSV and LO. These models were known to exhibit different behaviours to the phantom’s experimental vortices so their results stand to validate whether each method truly assesses the vortices. HSV was incorrect on most assessments, with the incorrect circulation, CentVect, spherical harmonics and vector values on most, if not all configurations. LO agreement was slightly better, with mostly correct speeds, and vector angles, but had incorrect CentVect values and vector lengths across all configurations. This low agreement was expected and reinforces the visual differences observed between vortices.

The K-R model exhibited high agreement with experimental vortices across the different methods. It agreed with configurations 1,3,4,7 on all metrics, signifying that a KR ring from these configurations is indistinguishable from an experimental ring. Configuration 2 had agreement in CentVect, streamlines and vector lengths. Configurations 5,6 have agreement on all methods except the streamline shape and velocity angles. Configuration 5 also included the anomalous point where the PIV agreement was very high, whilst the KR agreement was consistent with other KR readings which are in bounds (see Figure 4.13).

### 5.6.3 Agreement in Phantom Context

These analyses have explored whether the experimental vortices act according to the KR model at a fundamental level and offer increased rigour. In the context of this flow phantom, this level of detail may not be necessary. The ring vortex phantom flow fields have been historically expressed as velocity vector plots. If a ring vortex velocity plot were presented for a configuration 6 ring, the user wouldn’t be able to determine if it were a PIV or KR plot. Whilst the experimental vortex may not be fundamentally Kaplanski-Rudi behaving (resulting in low streamline agreement), the vector plots are indistinguishable between the two formulations within tolerances. There are therefore two conclusions from this analysis: in terms of fundamental mathematics, the phantom vortices act as KR vortices for configurations 1,3,4,7. In terms of velocity vector plots, the PIV and KR

rings are the same for configurations 1,3,4,6,7. The user may choose their required level of agreement if applying this model. This will be explored further in Chapter 6 in the context of phantom application.

### 5.6.4 Method Limitations

Due to their novelty, the methods applied here deserve particular critique. A noteworthy observation is the PIV streamline behaviour. All analytical ring streamlines close, however the experimental streamlines don't, following a spiralling pattern instead, from entrainment and energy loss mechanisms. The opening can be reduced by a smaller step-size in the post-processing (0.001), however further reducing this step size results in a computationally expensive code that takes too long to complete the angular analysis. The 0.001 step-size streamlines were chosen for analysis as they were nearly closed (See Figure 5.22), and the angular analysis took <1 minute per ring on a high-specification desktop.

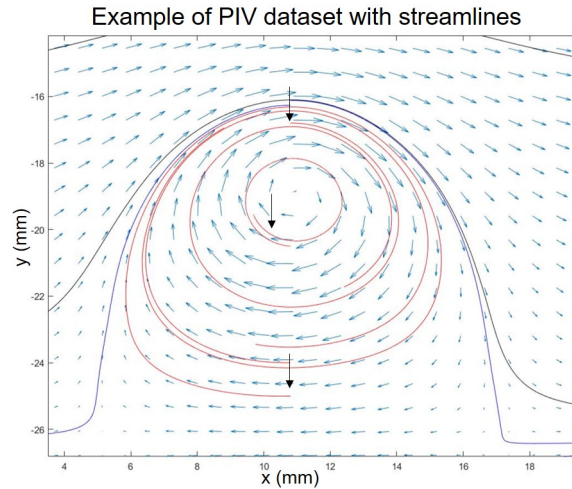


Figure 5.22: Example PIV dataset with superimposed streamlines in the moving ring reference frame. The open streamlines are visible, annotated by arrows.

Secondly is the issue of registration/ring alignment. This is particularly involved with Method B, for comparing local velocities. The individual vortices were aligned through the core centres, defined as the point of maximum vorticity, as this was found to be more consistent than the velocity centre (where all 4 surrounding vectors point in different quadrants). This was then followed by testing different alignments both axially and radially and observing the change in vector angle similarity at the vortex core, with the alignment of best similarity and vortical matching chosen. The data are discretised at 0.7193mm, a significant length-scale for 1cm wide rings. The discretisation is at 7% of the average ring width, so an axial mismatch in core alignment of up to 3.5% is possible. Incorrect alignment of rings will result in an incorrect report of low vector agreement when they are in truth identical, so this should be taken into account. This is perhaps the

cause of the relatively low PIV-to-PIV agreement, with only 60-80% agreement in length and 70-90% agreement in angle. This could be improved through increased resolution in analytical vortex representation to ensure a better-matched fit, but would remain limited by the discretisation.

## 5.7 Conclusions

This chapter has assessed the phantom vortices in the context of published analytical formulations. Three models of note were compared to the PIV datasets, known as Hill's Spherical Vortex, Lamb-Oseen model and Kaplanski-Rudi model. They were compared to the phantom vortices in terms of ring properties, streamline shape and velocity vector plots. HSV showed low agreement on all methods for all configurations, largely due to its spherical vortex assumption. The LO model had low agreement for micro-velocity (CentVect), streamline shape and velocity vector lengths. The Kaplanski-Rudi model, however, had high agreement across a number of configurations. If comparing them at the base level quantitatively, the phantom generates KR vortices under configurations 1,3,4,7 settings. If not requiring the detail of streamline components, and only vector plots/ring vortex properties, the KR model describes the vortices for configurations 1,3,4,5,7, within stated tolerances.

This integration of models into the phantom development is beneficial for a number of reasons. Classifying the rings as KR vortices strategically improves our understanding of the vortices at a fundamental level and its components. Integrating analytical ground-truth datasets into regular phantom use would enable flexibility of generating conditions and reduce reliance on limited experimental datasets. To establish whether the KR model can be used as a permanent feature on the phantom, more information is required. It is confirmed here that the old, OR piston vortices act according to KR under some conditions, but the new optimised vortices remain unaddressed. A broader range of rings is also required, to determine under what conditions experimental rings do not follow the KR model, and to establish boundaries for its use. This will be addressed in the next Chapter.

# Chapter 6

## Micro-Analysis of the Unit-1 US-Compatible Ring Vortex Phantom

### 6.1 Introduction

To this point, this thesis has characterised the phantom and its vortices in its 2019 state (Unit-0) and performed optimisations to establish more efficient working protocols and generated flows (defining Unit-1). The importance of accurate ground-truth datasets to characterise flow behaviour has been emphasised in the literature for phantom development. The ring vortex phantom (Unit-0) has experimental Laser PIV datasets which have shown significant agreement with the Kaplanski-Rudi model for analytical supplementation, but this is limited to the old, OR piston vortices. To achieve the objective of combined experimental and analytical ground-truth datasets for the optimised Unit-1 phantom using the NOR piston, the optimised vortices proposed in Chapter 3 need to be imaged. These refined vortices have demonstrated encouraging stability and reproducibility at the macro-scale, however to demonstrate their suitability for long-term use in research and clinical settings a characterisation of the micro-flow is warranted. This chapter will therefore fill this gap in the knowledge, by collecting up-to-date visualisation data of these vortices. This experiment and its analysis will fulfil the following objectives:

1. Empirically characterise the new ring vortices, determine their stability and reproducibility at the micro-scale and ensure they are suitable for phantom flow use
2. Explore the ring vortex space in terms of stability and reproducibility
3. Explore whether the new ring vortices behave according to analytical classification and under what conditions.

The 2019-PIV datasets used throughout this work have provided rich detailed information on the vortex dynamics, so a similar method was used to visualise the refined vortices. This chapter will therefore detail a Laser-PIV experiment performed on the

optimised phantom (2023) and the ensuing analysis. Positive results in this analysis will evidence the device’s readiness for clinical imaging experiments. For clarity, the two datasets will be named as follows: ‘ $PIV'_{19}$ ’ represents the 2019 PIV datasets, using the O-ring piston and the non-optimised phantom (Unit-0). ‘ $PIV'_{23}$ ’ represents the 2023 PIV datasets, using the non O-ring piston and the optimised phantom (Unit-1).

## 6.2 Methods

### 6.2.1 Ring Selection Procedure for Laser PIV

The ring vortex maps from Chapter 3 offer a framework for characterising the revised rings, based on variation in orifice size, piston speed and piston displacement. For the 2023 experiment, approximately 100 vortices were visualised and processed, so a range of generating conditions were selected accordingly. Two datasets were collected here: ‘Reference’ datasets and ‘Sample’ datasets. Reference datasets were comprised of 10 ring vortices per generating condition and were assessed for their **stability** and **reproducibility**, evaluating their suitability for flow phantom use at the micro-scale. There were 5 conditions in this dataset, which are listed in the table below. Configurations 6,12,15,20 were selected as they have a consistent stroke ratio of 1.5 and exhibited high stability and reproducibility at the macro-scale from video analysis. An anomalous configuration here is config 3, with a stroke ratio of 3.4. This set exhibited high reproducibility but low stability at the macro-level. Its inclusion here is two-fold: (a) it will determine whether macro-scale instability is reflected at the micro-scale, and (b) its high speed is desirable for clinical imaging experiments (See Chapter 8). Analysing configuration 3 enables valuable comparison with the more stable reference datasets.

|      | Config | Orifice | Piston Disp | Piston Max Spd | Av. Ring Spd | Stroke Ratio |
|------|--------|---------|-------------|----------------|--------------|--------------|
| Fast | 3*     | 10mm    | 0.7mm       | 2cm/s          | 28.5cm/s     | 3.4          |
|      | 6      | 15mm    | 0.1mm       | 2.5cm/s        | 12.9cm/s     | 1.5          |
|      | 12     | 15mm    | 0.1mm       | 1.3cm/s        | 8.01cm/s     | 1.5          |
|      | 15     | 20mm    | 1.22mm      | 2.5cm/s        | 8.86cm/s     | 1.5          |
| Slow | 20     | 20mm    | 1.22mm      | 1.3cm/s        | 4.67cm/s     | 1.5          |

Table 6.1: List of ‘reference’ datasets for the 2023 Laser-PIV experiment. Ten vortices of each configuration were visualised. \* - low stability condition.

The remaining vortices, known as ‘Sample’ datasets aimed to collect the widest range of ring vortices for assessment. A small sample (2-3 per condition) were imaged, and were analysed for their analytical behaviour, to offer broad classification of the phantom vortices across a broad range of behaviour. This diverse range of rings was also selected to understand the ring vortex ‘landscape’ in terms of energy and ring behaviour.

| Config | Orifice | Piston Displacement | Max Piston Speed | Average Ring Speed | Stroke Ratio | No. of Vortices |
|--------|---------|---------------------|------------------|--------------------|--------------|-----------------|
| 1      | 10mm    | 0.56mm              | 2cm/s            | $19.6 \pm 6.7\%$   | 2.7          | 3               |
| 2      | 10mm    | 0.62mm              | 2cm/s            | $27.6 \pm 3.82\%$  | 3.0          | 3               |
| 3***   | 10mm    | 0.7mm               | 2cm/s            | $28.0 \pm 2.97\%$  | 3.4          | 10              |
| 4      | 10mm    | 0.9mm               | 2cm/s            | $31.9 \pm 4.4\%$   | 4.4          | 3               |
| 5      | 15mm    | 0.8                 | 2.5cm/s          | $10.0 \pm 2.18\%$  | 1.3          | 3               |
| 6***   | 15mm    | 1.02mm              | 2.5cm/s          | $12.9 \pm 1.96\%$  | 1.5          | 10              |
| 7†     | 15mm    | 1.02mm              | 2.5cm/s          | $12.9 \pm 1.96\%$  | 1.5          | 5               |
| 8      | 15mm    | 1.66                | 2.5cm/s          | $17.3 \pm 2.86\%$  | 2.4          | 3               |
| 9      | 15mm    | 2.88mm              | 2.5cm/s          | $19.6 \pm 3.4\%$   | 4.2          | 3               |
| 10     | 15mm    | 1.02mm              | 2cm/s            | $11.9 \pm 3.27\%$  | 1.5          | 3               |
| 11     | 15mm    | 1.66mm              | 2cm/s            | $15.2 \pm 3.1\%$   | 2.4          | 3               |
| 12***  | 15mm    | 1.02mm              | 1.3cm/s          | $8.5 \pm 3.0\%$    | 1.5          | 10              |
| 13     | 15mm    | 1.66mm              | 1.3cm/s          | $9.5 \pm 3.22\%$   | 2.4          | 2               |
| 14     | 20mm    | 1.9mm               | 2.5cm/s          | $8.27 \pm 1.23\%$  | 1.2          | 2               |
| 15***  | 20mm    | 2.44mm              | 2.5cm/s          | $8.9 \pm 2.1\%$    | 1.5          | 10              |
| 16     | 20mm    | 3.9mm               | 2.5cm/s          | $11.4 \pm 4.2\%$   | 2.4          | 2               |
| 17     | 20mm    | 5.6mm               | 2.5cm/s          | $12.5 \pm 6.6\%$   | 3.2          | 2               |
| 18     | 20mm    | 2.44mm              | 2cm/s            | $6.9 \pm 3.8\%$    | 1.5          | 2               |
| 19     | 20mm    | 3.9mm               | 2cm/s            | $8.92 \pm 2.56\%$  | 2.4          | 2               |
| 20***  | 20mm    | 2.44mm              | 1.3cm/s          | $4.67 \pm 3.73\%$  | 1.5          | 10              |
| 21     | 20mm    | 3.9mm               | 1.3cm/s          | $6.26 \pm 5.9\%$   | 2.4          | 2               |

Table 6.2: List of all experimental conditions imaged in the 2023 Laser PIV experiment. † - Configurations 6 and 7 are identical, with these rings produced before and after the experiment to ensure phantom consistency. \*\*\* denotes a ‘reference’ dataset

## 6.2.2 PIV Methodology

The visualisation of the vortices was performed in collaboration with LaVision UK, with the author controlling the phantom throughout. The phantom was set up as described in Chapter 3 using the non O-ring piston and reinforced motor base (Unit-1). A double-pulse Nd:YAG laser plane (523nm wavelength, 1mm plane thickness) was placed below the tank, oriented along the vortices’ axis of travel. The laser was positioned in the centre of the tank using a calibration rig which allowed manual alignment to the tank’s central axis with an error of  $\pm 1$ mm. Two stereoscopic HFR cameras were mounted on an orthogonal tripod to capture 3-D velocity information, and the fluid volume was seeded with  $60\mu\text{m}$ -diameter polyamide particles (1g polyamide in 8L of water). The scattering particles are neutrally buoyant and fluoresce under laser illumination.

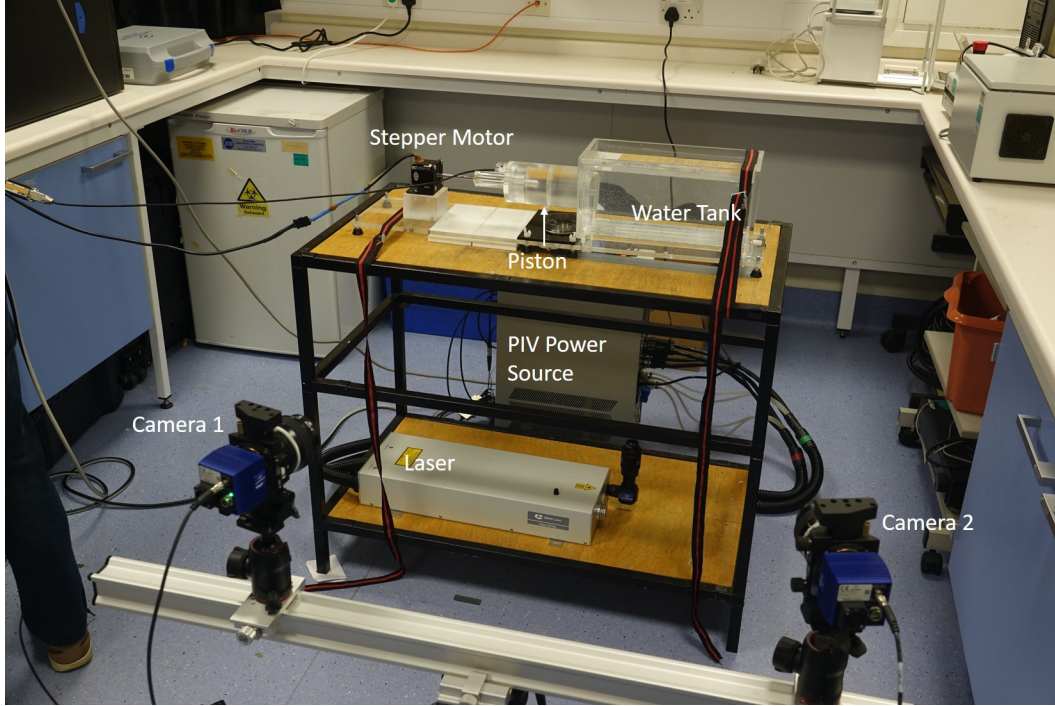


Figure 6.1: Photo of the 2023 Laser PIV experiment visualising the ring vortex phantom.

To image the vortex flow field, the laser delivered a double pulse (separated by a time delay of  $450\text{-}3000\mu\text{s}$ ) and the cameras captured the particles' positions in each pulse. The inter-pulse delay was selected for each condition related to the ring vortex speed, as the method is most accurate if particles move approximately 5 pixels on-screen between pulses. Correlation software then generated vector plots of the fluid motion from the particles' displacements. This process was repeated at  $15\text{Hz}$  to capture the vortices as they travelled across the field-of-view. To maintain efficient processing times, slower rings were captured at  $30\text{Hz}$ , capturing a minimum of 10 frames with the ring in view.

The phantom was used according to the regulations set in Chapter 3, with the NOR piston and refined input code profiles employed. The instrumentation pack's linear encoder tracked piston motion to ensure the piston was working to specification for each vortex. The phantom performed well over the 6-hour experiment with no malfunctions, with a reference dataset taken twice throughout the day indicating a ring vortex change in speed of 3%, well within tolerances. Velocity vector data were collected over a domain of  $12.83\text{cm(H)}\times 15.81\text{cm(W)}$ , mapping from  $7.2\text{cm}$ - $23\text{cm}$  from the orifice exit plane. The vectors are discretized to  $0.794\text{mm(W)}$  and  $0.8525\text{mm(H)}$ . The horizontal imaging domain is the width of the calibration grid presented below. This grid was used to relate real-world position to the PIV coordinate system, with the reference triangle located at the  $[0,0]$  origin in-software.

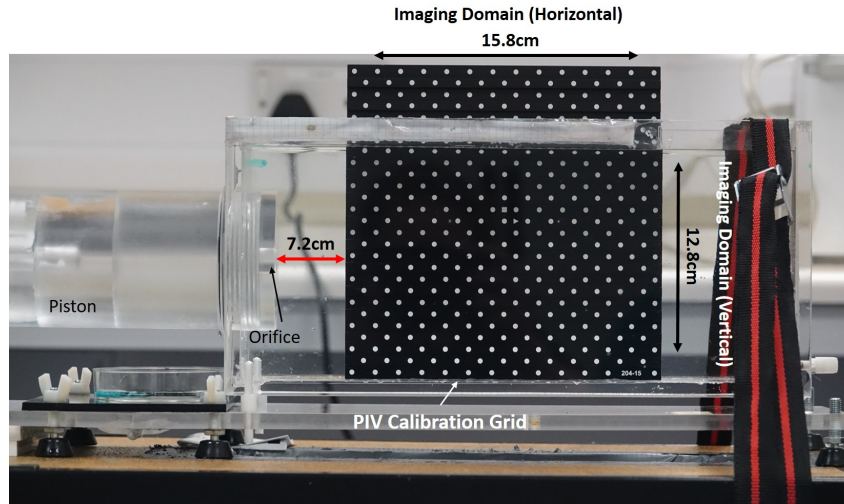


Figure 6.2: Photo of the calibration grid used for the 2023 Laser PIV experiment using the ring vortex phantom. The triangle on the grid correlates to the  $[0,0]$  origin in the PIV coordinate system.

## 6.3 Results I - Suitability as a Phantom Reference Flow

As discussed, analysis of these datasets relied on two approaches. This section presents the first, where reproducibility and stability of the reference conditions were assessed, to compare to previous analyses and ensure the phantom's viability. Methods were adopted from Chapter 2, where circulation, core radius, ring radius and vector agreement were assessed for reproducibility and stability.

### 6.3.1 Circulation - Stability and Reproducibility

The first evaluated property was circulation. Circulation was calculated through a line integral of the velocity vectors around a domain of 24mm(W) x 26mm(H) projecting up from the ring vortex' central axis. This is equal to an area integral over the same domain of the vorticity through Stokes' Law (see Chapter 2). Circulation was calculated for individual vortices across their journey through the PIV field-of-view, with the relative evolution plotted below.

a. Progression of Circulation for Reference Ring Vortex Phantom Configuration:

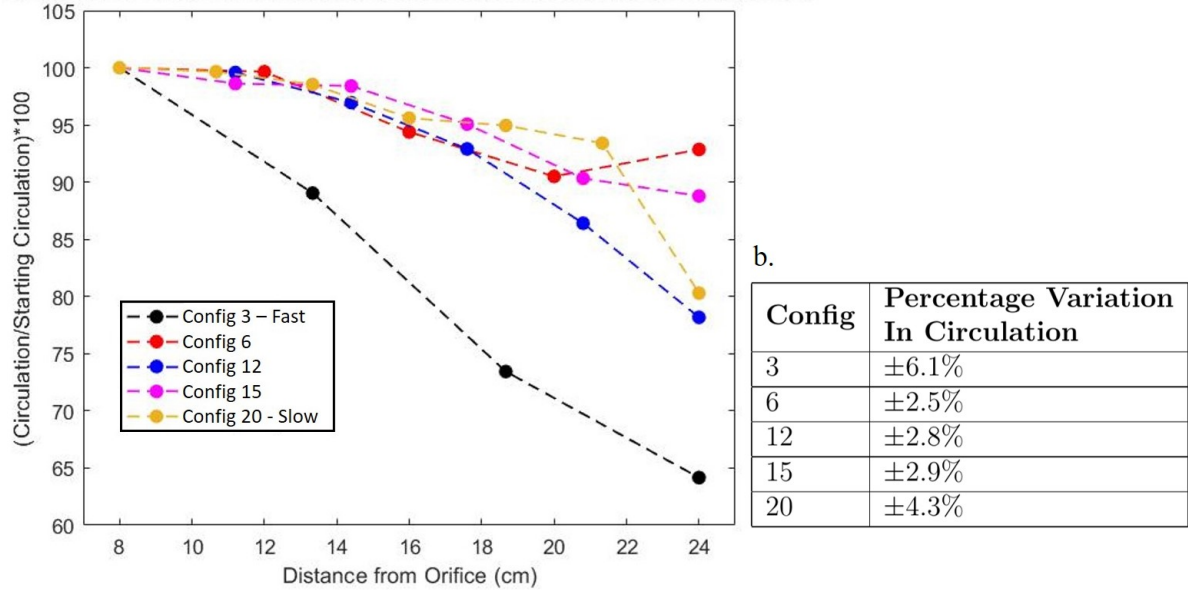


Figure 6.3: (a.) The evolution of circulation of reference ring vortices from  $PIV_23$  data, relative to starting circulation at 7cm from the orifice. Datapoints represent the average of ten vortices. Error bars are not shown, but is typically  $\sim 5\%$  as listed in (b.)

Figure 6.3a presents the evolution of circulation for the reference ring vortices throughout their journey, visualising their **stability**. Circulation is plotted as a percentage of its starting value. Every configuration loses circulation as expected, however Config 3 exhibits the highest loss of 37% over 15cm. Configurations 6,12,15,20 all experience less than 25% circulation loss on average.

Figure 6.3b lists the coefficient of variation for each reference configuration, representing the vortices' **reproducibility**. The average circulation across the journey was found for each ring vortex, averaged and the CoV calculated for each configuration. High reproducibility was found for all configurations, with configurations 6,12,15,20 exhibiting variation under 5%.

### 6.3.2 Ring Radius - Stability and Reproducibility

Ring radius was the second key parameter for ring vortex assessment, and is defined here as half the vertical distance between locations of maximum and minimum vorticity in the vortex cross section. Both stability and reproducibility were assessed. The relative evolution of ring radius is plotted below along with variability.

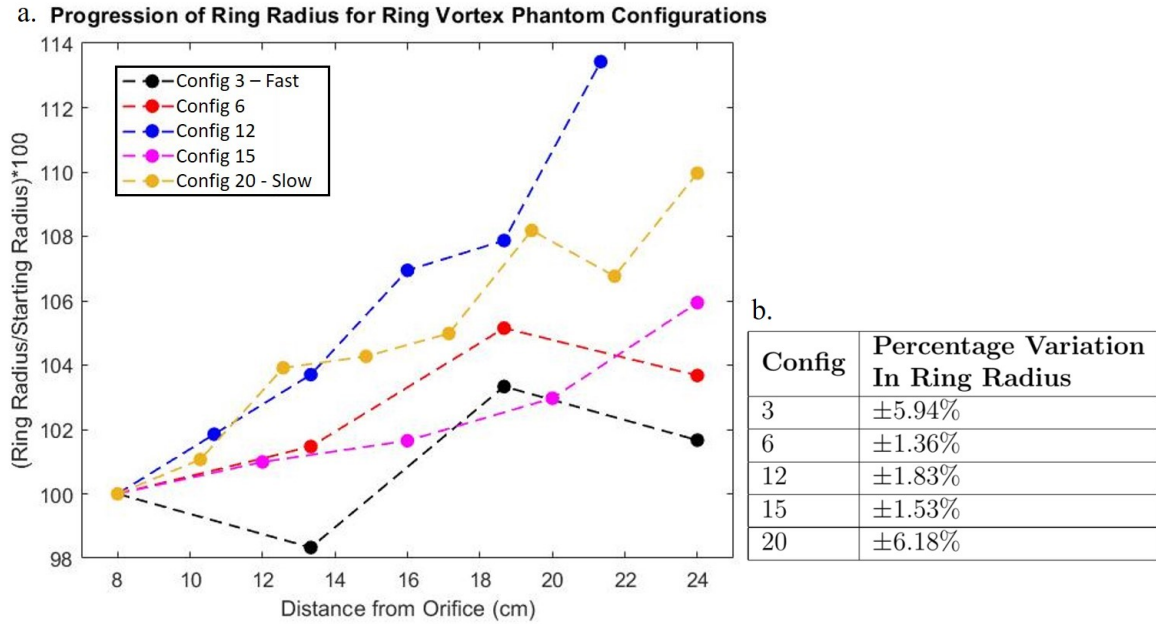


Figure 6.4: (a.) The evolution of ring radius of reference ring vortices from  $PIV_{23}$  data, relative to starting values at 7cm from the orifice. Datapoints represent the average of ten vortices. Error bars are not shown, reproducibility is listed in (b.) as coefficient of variability.

Figure 6.4a presents the progression of the ring radius across the tank, visualising ring radius **stability** for the reference datasets. An increase in ring size is expected and observed, as fluid is ingested into the ring as it travels [99]. The ring radii are all stable to within 15% for all configurations, and all are stable to within 10% except for configuration 12. It is notable that the slower rings (configurations 15,20) have a slightly larger relative increase in ring radius than faster rings.

Figure 6.4b presents the coefficient of variation for ring radius for the rings' journey, representing the **reproducibility**. Ring radius values are averaged across the journey and the CoV found for each configuration. A variability of  $\pm 5\%$  or lower is obtained by configurations 6,12,15 only, with configurations 3 and 20 slightly above the threshold. A measurement error of  $\sim 5\%$  is also introduced through the PIV dataset discretisation to 0.72mm.

### 6.3.3 Core Radius - Stability and Reproducibility

The third parameter was core radius, defined here as half the distance between maximum and minimum tangential velocities over the core centre. Axial and radial measurements were taken from both top and bottom cores and averaged for this analysis. The evolution of relative core radius is plotted below.

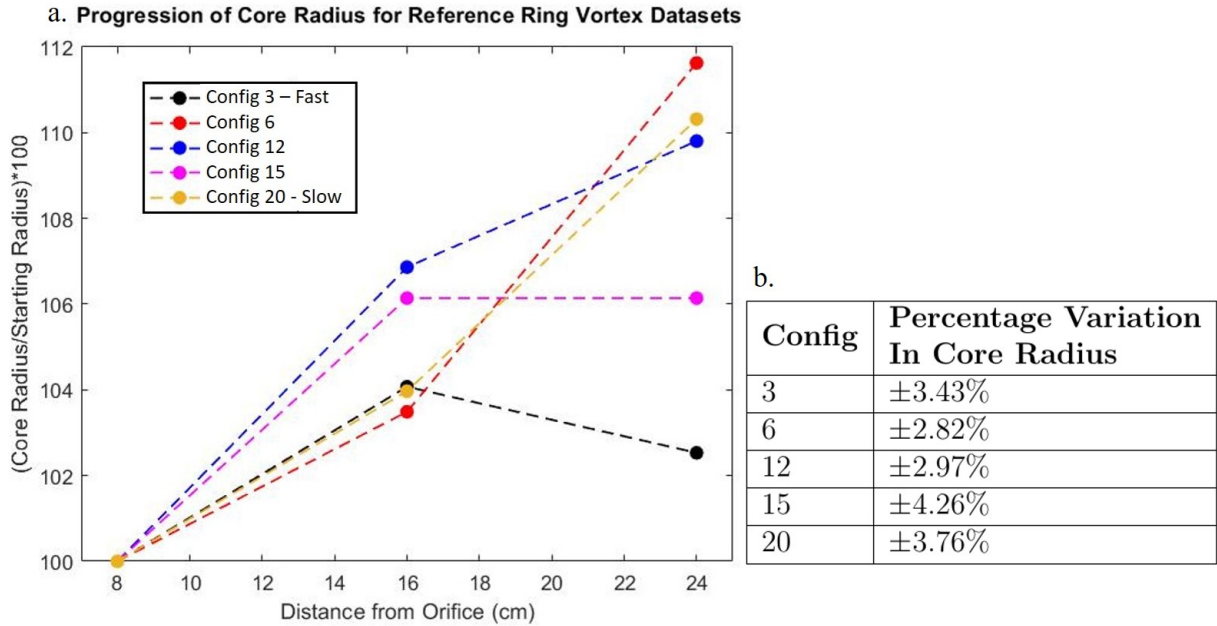


Figure 6.5: The evolution of core radius of reference ring vortices from  $PIV_23$  data, relative to starting values at 7cm from the orifice. Datapoints represent the average of ten vortices. Error bars are not shown, reproducibility is listed in (b.) as coefficient of variability.

Figure 6.5a presents the evolution of the core radius as the rings propagate across the tank, visualising their **stability**. Measurements are calculated as a percentage of their starting value. Across all configurations the core radii increase as expected due to entrainment. Similar to the ring radius evolution, all core radii increase by less than 15% across their propagations.

Figure 6.5b presents the coefficient of variation for core radius for each reference dataset, showing the **reproducibility** of the torus' minor radius. Core radius across the rings' journey was averaged and the CoV calculated. All configurations exhibited variance of less than 5%. An error of up to 20% could be introduced through the PIV discretisation of 0.72mm and the small core length-scale. These results will be collated along with the following vector analysis in the Discussion.

### 6.3.4 Vector Agreement - Stability and Reproducibility

The final assessment is more comprehensive than select parameters, assessing the entire flow field of each configuration. Chapter 2 demonstrated the usefulness of quantifying reproducibility of micro-scale flow-fields, as this truly gives a measure of how individual rings from the same condition vary. Tolerance maps were produced for each configuration, both for angle and length, and at the start and end of the imaging domain. To achieve this, velocity vector fields (22mm(W)x40mm(H) domain size) from each condition were overlaid, and their vector lengths and angles calculated at each coordinate. These values

were then compared across the ten vortices in each configuration with the average and variation calculated (CoV for vector length, SD for vector angle). Plotting the variation across the flow field generated a ‘tolerance map’, which visualise how reproducible each point in a ring vortex was for that condition. These maps are presented below for visual analysis, demonstrating where in the flow field individual vortices differ.

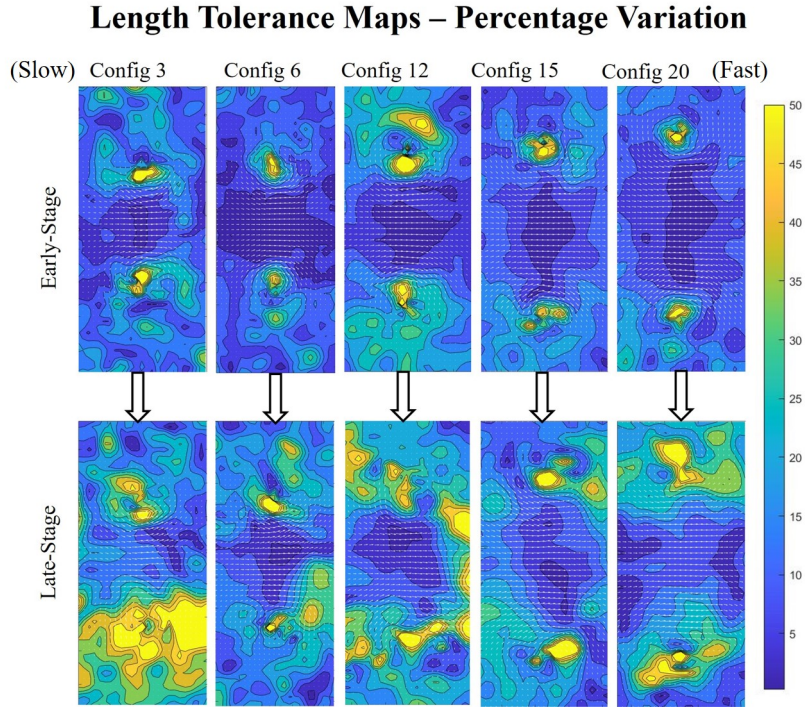


Figure 6.6: Tolerance Maps for the reference datasets of the 2023 Laser PIV experiment for vector lengths. Regions are colour-coded according to the colourbar, with values representing the local coefficient of variation in vector length between ten vortices.

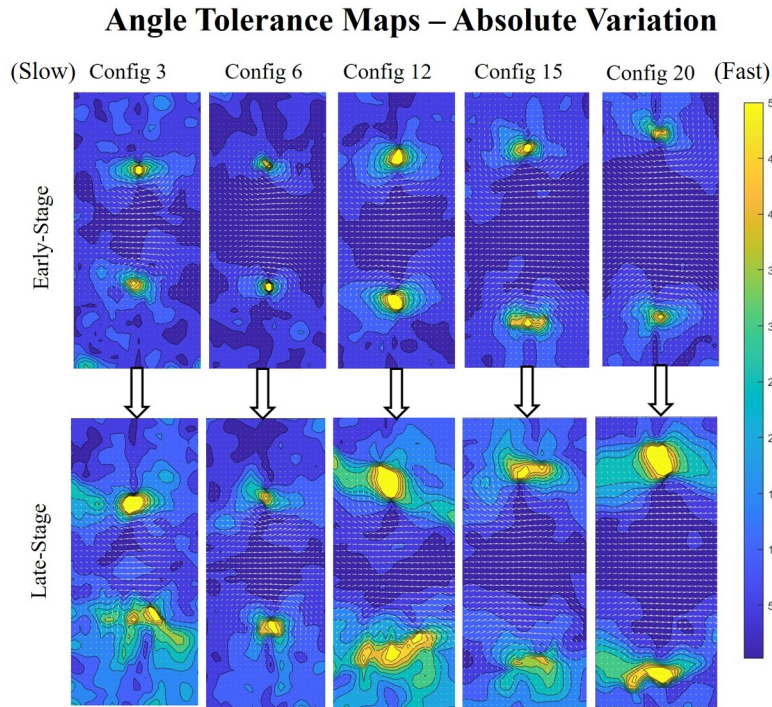


Figure 6.7: Tolerance Maps for the reference datasets of the 2023 Laser PIV experiment for vector angles. Regions are colour-coded according to the colourbar, with values representing the local standard deviation in vector angle between ten vortices.

These tolerance maps show an increase in variability as the rings travel from early-stage to late-stage and become susceptible to mechanisms which will affect each vortices uniquely. Length is more variable than angle by colour, and angular reproducibility notably decreases with distance from the core centre. As seen in Chapter 2, the ring vortex centre-point remains the most reproducible region in both vector length and vector angle. Each tolerance map visualises the condition’s **reproducibility**, and the difference between early-stage image and late-stage image is indicative of the **stability**. Suitable ring vortices will have a high agreement percentage in both vector length and angle at the start *and* end of their journey. Quantification is achieved through thresholding - the percentage of vector lengths that vary by less than  $\pm 10\%$ , and the percentage of vector angles that vary by less than  $\pm 5^\circ$ , respectively. These values are plotted below for both measurements, at the start, middle and end of the PIV imaging domain to show stability.

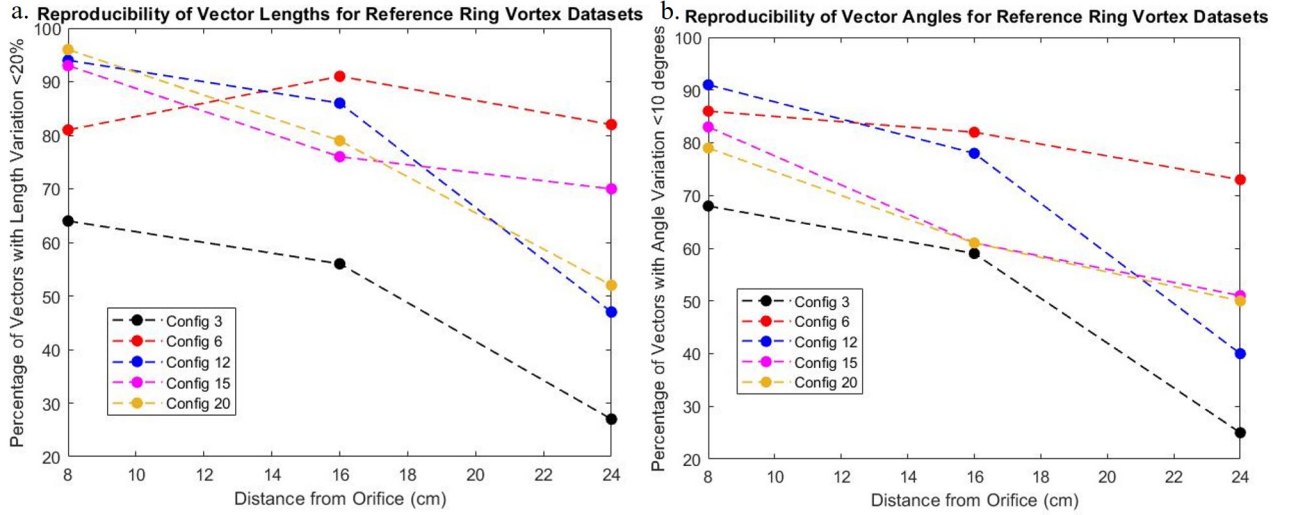


Figure 6.8: (a.) The reproducibility of velocity vector lengths for reference ring vortex datasets, both at the start and throughout the journey. The y axis represents the % of vectors whose lengths vary by less than  $\pm 10\%$  (1SD) across the ring and its immediate surroundings. (b.) The reproducibility of velocity vector angles for reference ring vortex datasets, both at the start and throughout the journey. The y axis represents the % of vectors whose angles vary by less than  $\pm 5^\circ$  (1SD) across the ring and its immediate surroundings.

Figure 6.8a presents the reproducibility of vector lengths for each reference condition in  $PIV_{23}$  datasets. All configurations except configuration 3 exhibit reproducibility of  $>80\%$  of lengths varying by less than  $\pm 10\%$  at the start of the domain. Reproducibility decreases as the rings propagate, but configurations 6,15,20 all retain over 50% high reproducibility vectors by end-of-domain. Configuration 3 is below 50% from its conception, indicating low reproducibility between rings throughout. Configuration 12 starts reproducible but falls below 50% reproducibility by the end of the domain.

Figure 6.8b presents the reproducibility of vector angles within the ring vortex reference datasets. Similarly to the vector angles, configuration 3 never achieves 80% reproducibility. All other configurations start with reproducibility over 78%, and configurations 12,20 are below 50% by the late-stage measurement.

### 6.3.5 Discussion - Phantom Flow Suitability

This analysis explored the reproducibility and stability of the  $PIV_{23}$  reference datasets, in terms of isolated micro-flow parameters and overall flow-fields. These findings were collated to characterise the vortices' overall behaviour. Chapter 2 retrieved reproducibility and stability metrics for OR piston vortices, demonstrating what this phantom can generate. These optimised vortices will be compared to the thresholds established in 2019 analysis, to determine the impact that phantom optimisation has had on the vortex' stability and reproducibility. The thresholds used are as follows:

- Ring vortex parameters **reproducible** to within  $\pm 10\%$ . Core radius can be reproducible to  $\pm 15\%$  due to discretization.
- Ring vortex parameters **stable** to within 20% over 14cm.
- For vector comparison, a starting value of  $>60\%$  high reproducibility vectors is reached.
- For vector comparison, a finishing value of  $>50\%$  high reproducibility vectors is reached.

Using these thresholds, each condition was assessed, and the results tabulated below:

| Cfg | Circ<br>Reprod. | Circ<br>Stab. | R.Rad<br>Reprod | R.Rad<br>Stab. | C.Rad<br>Reprod | C.Rad<br>Stab. | Ang<br>Start | Ang<br>End | Len<br>Start | Len<br>End |
|-----|-----------------|---------------|-----------------|----------------|-----------------|----------------|--------------|------------|--------------|------------|
| 3   | ✗               | ✗             | ✓               | ✗              | ✓               | ✓              | ✗            | ✗          | ✗            | ✗          |
| 6   | ✓               | ✓             | ✓               | ✓              | ✓               | ✓              | ✓            | ✓          | ✓            | ✓          |
| 12  | ✓               | ✗             | ✓               | ✓              | ✓               | ✓              | ✓            | ✓          | ✓            | ✗          |
| 15  | ✓               | ✓             | ✓               | ✓              | ✓               | ✓              | ✓            | ✓          | ✓            | ✓          |
| 20  | ✓               | ✓             | ✓               | ✓              | ✓               | ✓              | ✓            | ✓          | ✓            | ✓          |

Table 6.3: Metrics of reference datasets for phantom flow requirements at the micro-scale. Abbreviations are used in the headings: ‘*Circ*’ is circulation, ‘*R. Rad*’ is ring radius, ‘*C. Rad*’ is core radius, ‘*Ang*’ is the vector angles with high reproducibility, ‘*Len*’ is the vector lengths with high reproducibility, ‘*Reprod*’ is the reproducibility, and ‘*Stab*’ the stability.

Table 6.3 presents where each configuration either exceeded the designated threshold (✓), or fell below it (✗). Configuration 3 failed to meet the thresholds on all parameters except for core radius, indicating low stability and reproducibility in a number of metrics. This result was expected given its low stability at the macro-scale.

The remaining configurations perform well, with configurations 6,15, 20 surpassing the thresholds on all metrics.

The remaining configuration is config 12, which has insufficient circulation stability and vector length/angle stability. This is surprising given its macro-stability and is an interesting find. Its circulation stability is at 77% ( $\pm 2\%$ ) rather than the designated 80% but its late-stage vector angle agreement is 38% , which is very low. This indicates that this configuration has differently-acting rings at the end-stage of the domain. It is notable that in the vector graphs the rings are reproducible in both vector length and angle in the mid stage ( 17cm from orifice) as is the circulation, so if high reproducibility were needed at the micro-stage, configuration 12 could be imaged up to this location. It is suitable at the start of journey, so modalities such as Ultrasound could use the rings with a probe located between the 10-17cm locations.

In conclusion, the reference datasets of configuration 6,15,20 deliver reference micro-flows which meet established tolerances for propagation over the 7-22cm domain originating at the orifice. These configurations demonstrate the **same** stability and reproducibility

as the previous phantom iteration. Configuration 12 loses its stability after 17cm, and configuration 3 exhibits low reproducibility and stability across its journey. The thresholds employed here were to enable comparison between the  $PIV_{19}$  and  $PIV_{23}$  datasets, as three configurations met these thresholds using the OR piston and 2019 configurations. Three configurations meet the thresholds in this exercise. The previous phantom demonstrated 3/7 tested configurations which met the thresholds, and this phantom version demonstrated 3/5 conditions with the same attributes. This demonstrates that the change in phantom conditions has not removed the vortex' suitability. It is worth noting that configurations that don't meet the set tolerances aren't unusable - these can be employed, with more relaxed tolerances cited.

## 6.4 Results II - Agreement with Kaplanski-Rudi Model

The reference datasets were appraised for their suitability in flow phantom use, allowing analysis to proceed to a second stage, which was determining whether the  $PIV_{19}$  vortices and  $PIV_{23}$  vortices were fundamentally in the same 'family' of rings, which was determined analytically. The more stable  $PIV_{19}$  ring vortices were found to behave according to the Kaplanski-Rudi model within tolerances, so performing the same analyses with the  $PIV_{23}$  datasets would determine whether the change in generating conditions has changed the rings' analytical behaviour. Analysing a larger set of vortices with the KR model would also increase understanding of when experimental vortices are KR-like, which wasn't achievable with the limited  $PIV_{19}$  datasets. HSV and LO were not compared to the  $PIV_{23}$  rings in this instance due to their low performance in Chapter 5.

The rings were processed according to the methods presented in Chapter 5, with three procedures used to compare analytical and experimental vortices: (a) Comparison of basic parameters (ring speed and CentVect), (b) Comparison of velocity vectors and (c) Comparison of streamlines through Fourier analysis. A Kaplanski-Rudi ring was generated to mimic every PIV-imaged ring vortex listed in Table 6.2 by using the core radius, ring radius and circulation in their formulation (See Chapter 5 for detailed methods) and used for this comparison.

### 6.4.1 Integral Parameters

The first method compares the ring speeds and CentVect values for both the PIV rings and their Kaplanski-Rudi counterparts. KR ring speeds were calculated and CentVect values were measured as the axial velocity along the ring vortex' central axis. These parameters were chosen as circulation, ring radius and core radius were discounted due to their role in KR vector plot production.

# Ring Speed

**Correlation between Experimental and Theoretical Ring Vortex Speeds using the Kaplanski-Rudi Model**

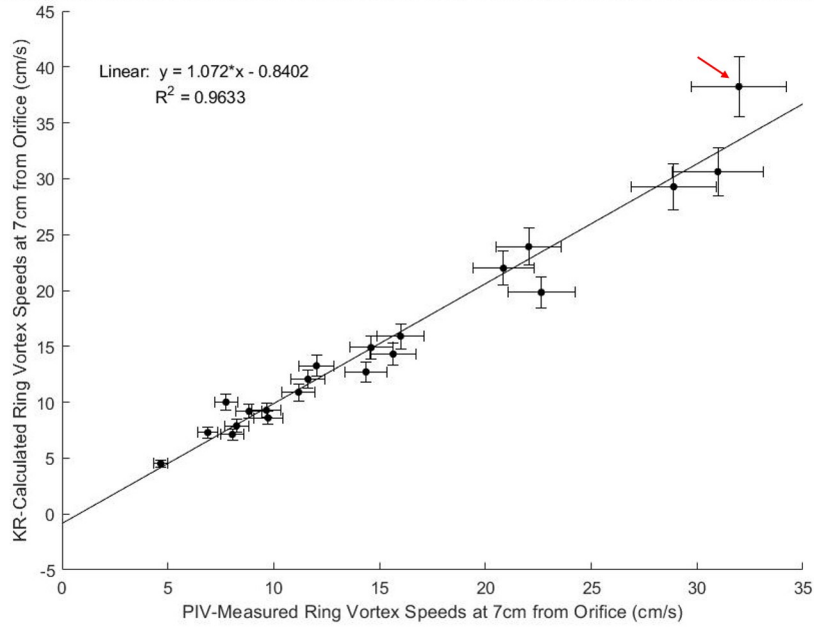


Figure 6.9: Correlation between experimental ring speeds and KR ring speeds calculated from 2023 PIV datasets. Error bars represent 1SD and are the variation between individual vortices. An outlier is annotated with the red arrow.

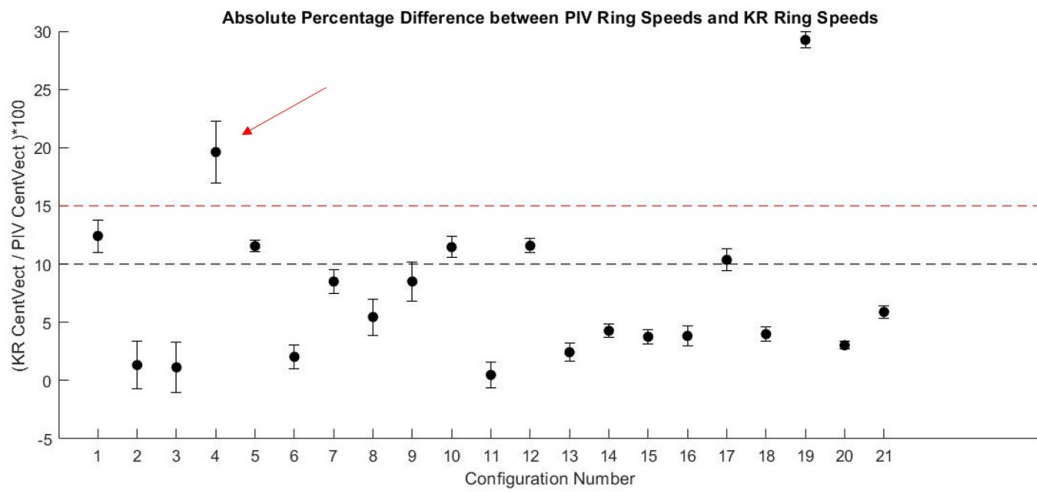


Figure 6.10: Relative percentage error between PIV ring speed values and KR ring speed values for 2023 PIV datasets. Thresholds are set at 10% and 15% and an outlier is annotated with a red arrow.

Figure 6.9 presents the correlation between experimental PIV-calculated ring vortex speeds and theoretical KR-calculated ring vortex speeds for the reference datasets. Datapoints represent the average of 10 ring vortices, and the error bars represent 1SD. The data are fit to a linear model, resulting in a gradient and intercept of 1.07 and -0.84 respectively. These values demonstrate a close-to-equal linear relationship between the KR and PIV values across all conditions, with an  $R^2$  value of 0.993 demonstrating very strong correlation and clarifies that the Kaplanski-Rudi model accurately calculates ring speeds for these ring vortices as a whole. These statistics are further improved with the removal of the annotated anomaly (condition 4), giving a gradient and intercept of 0.99 and 0.03, with an  $R^2$  of 0.97. Data from individual configurations are presented in Figure 6.10, demonstrating the spread of agreement between experimental and theoretical values. Most configurations agree within 10%, but configurations 4 and 19 have a difference of >20% between PIV and KR speed values.

## CentVect

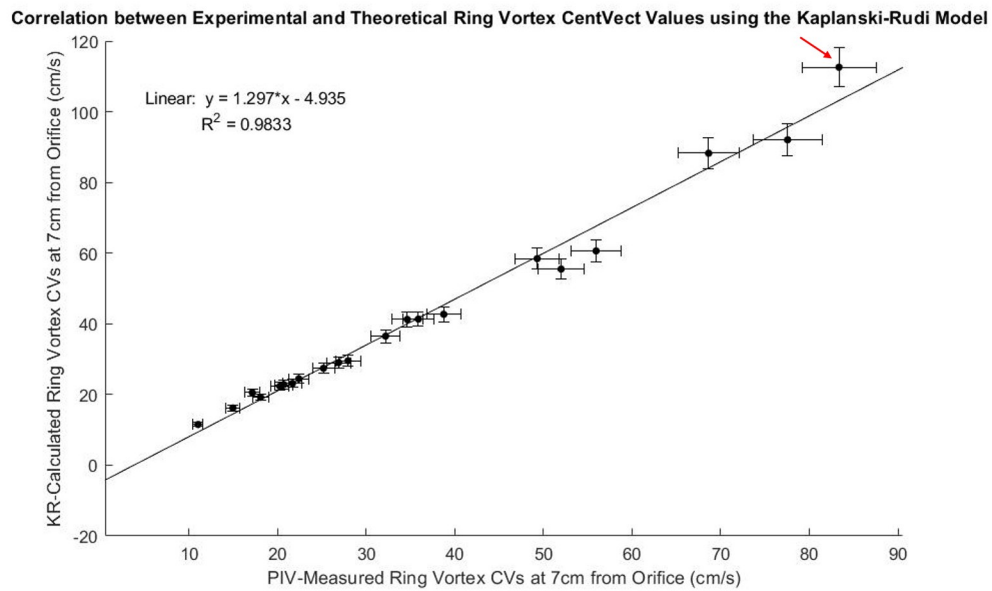


Figure 6.11: Correlation between experimental CentVect values and KR CentVect values, calculated from 2023 PIV datasets. Error bars represent 1SD and are the variation between individual vortices. An anomaly is annotated with the red arrow.

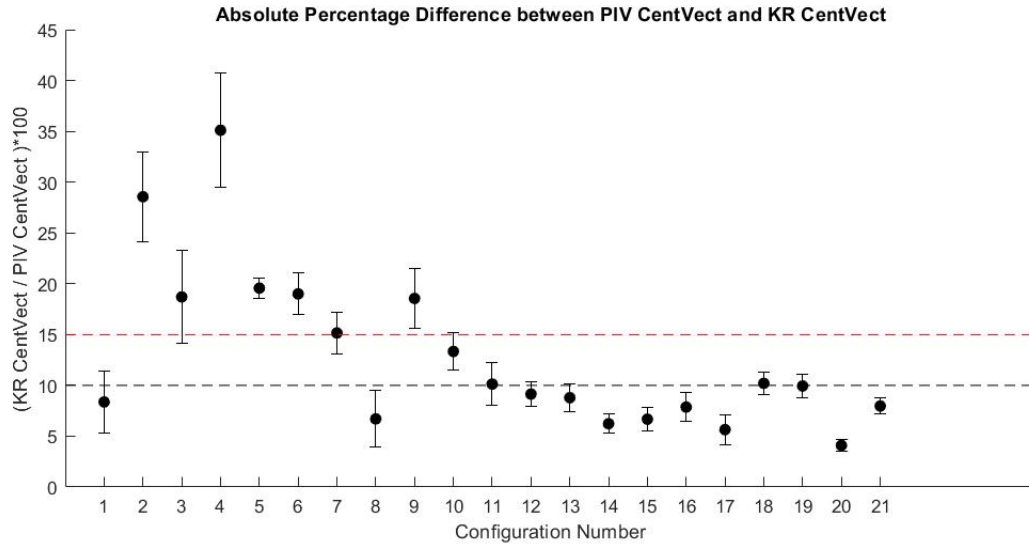


Figure 6.12: Relative percentage error between KR CentVect values and PIV CentVect values for 2023 PIV datasets. Thresholds are set at 10% and 15%.

Figure 6.11 presents the correlation between PIV-measured CentVect values and KR-calculated CentVect values. When fit to a linear model a gradient and intercept of 1.30 and -4.94 were reached respectively ( $R^2$  value of 0.96), indicating that the KR-calculated CentVect values were consistently 20-30% higher than the PIV-measured values. If the annotated anomaly (condition 4) was removed, the gradient and intercept became 1.22 and -3 respectively, and the  $R^2$  value was 0.99. This significant change from one anomaly showed that the agreement varies between different conditions. Individual configurations can be assessed in Figure 6.12 where the agreement between formulations varies from 1% to 30%. Most experimental rings had a CentVect within 10% of their analytical counterparts, with conditions 2,4 exhibiting CentVect values at >20% from the KR value.

## 6.4.2 Local Vector Agreement

The second method compared velocity vectors from the PIV and KR ring vortex flow fields. The KR ring was overlaid onto its PIV counterpart and vector lengths and angles were calculated for each coordinate. The KR vector angles were then compared to the PIV vectors, with those lying within  $10^\circ$  of the PIV identified. This was repeated for vector lengths, with the vectors lying within 20% of the PIV value identified. These results are plotted below.

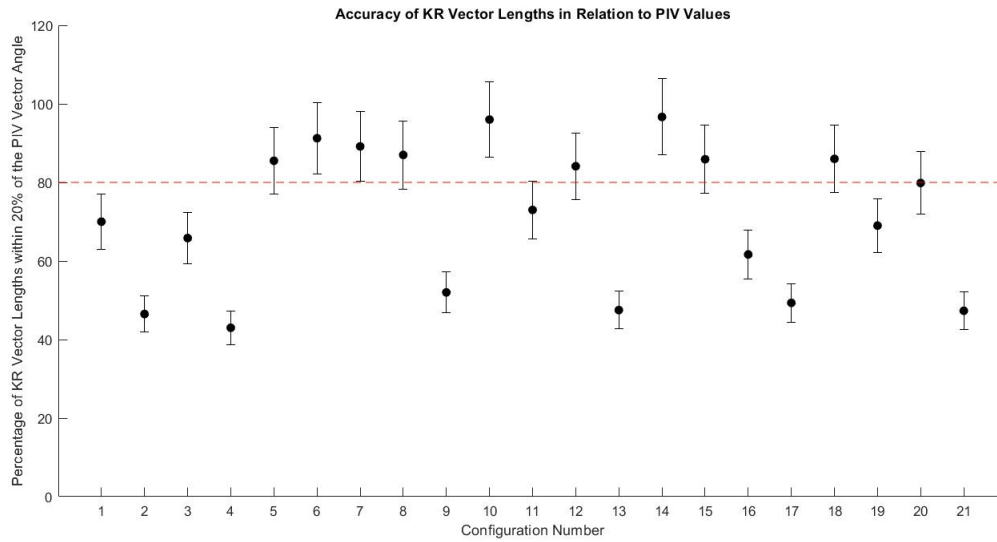


Figure 6.13: Agreement of KR and PIV velocity vector lengths for 2023 PIV datasets. Y axis values represent the percentage of KR vectors whose lengths lie within 20% of the corresponding PIV length. Error bars represent 1SD.

This graph presents the agreement between KR and PIV ring vortex flow fields in terms of vector lengths. The y axis here represents the percentage of KR vectors whose lengths lie within 20% of the corresponding PIV vector length. All sampling and reference datasets are plotted here. Error bars represent 1SD and are fixed at 6%, corresponding to the maximum CoV calculated from reference datasets. A threshold of 80% agreement is annotated on the graph.

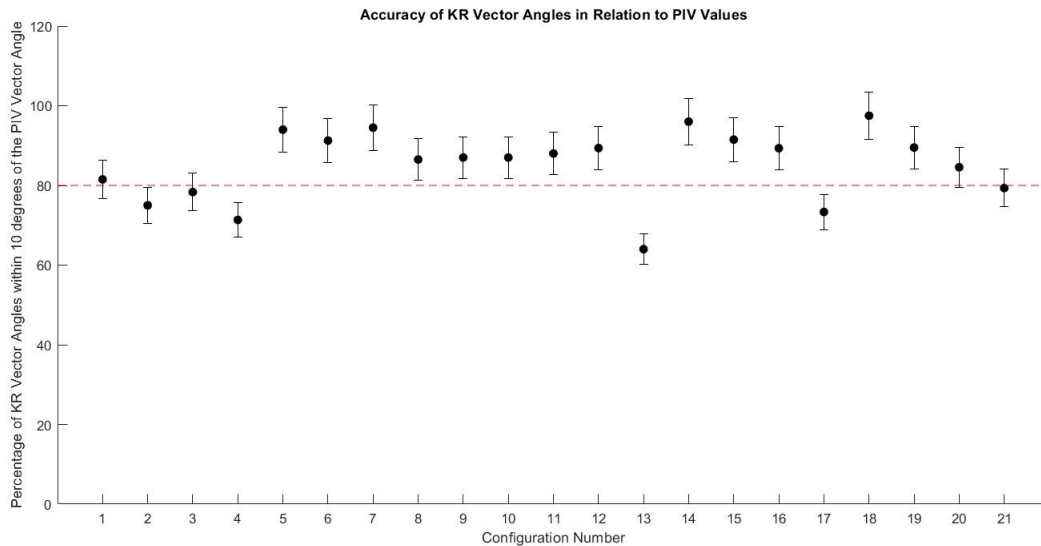


Figure 6.14: Agreement of KR and PIV velocity vector angles for 2023 PIV datasets. Y axis values represent the percentage of KR vectors whose angles lie within  $10^\circ$  of the corresponding PIV angle. Error bars represent 1SD.

The graph above presents the agreement between the PIV ring vortices and the corresponding KR vortices. The y axis represents the percentage of KR vector angles that lie within  $10^\circ$  of the corresponding PIV vector angle. The results are consistently high, with most configurations exhibiting  $>80\%$  of vectors close to KR vector direction. Sample datasets are insufficient to calculate tolerances, so error bars are fixed at  $\pm 10\%$ , calculated as the maximum CoV in the reference datasets with ten vortices. A threshold of 80% agreement is annotated on the graph. It is notable that the KR-to-PIV agreement is higher in this method than in Chapter 5. This is likely due to the fact that this analysis compares a single KR to its single PIV counterpart, rather than comparing a KR ring to an averaged PIV vector set.

### 6.4.3 Streamline Harmonics

The final method compared streamlines generated by the KR and PIV rings respectively. Streamlines were generated at equal intervals from the core centre to the bubble streamline in the radial direction, and plotted in  $r, \theta$  form. These plots were then fit to a Fourier model and the eight corresponding coefficients found for each. See Chapter 5 for a more detailed method. Chapter 5 then classified each KR coefficient as ‘within experimental bounds’ for each configuration, but this is not possible for this analysis. The sample datasets only have 2-3 rings apiece, which is insufficient data to create a ‘bounds’ (previously mean-STD:mean+STD). To quantify streamline coefficients here, experimental bounds were established for the reference datasets with ten vortices, and these standard deviations used for the sample datasets in lieu of condition-specific variation. The percentage of KR coefficients that lie within the experimental bounds was calculated for every condition,

and is plotted below.

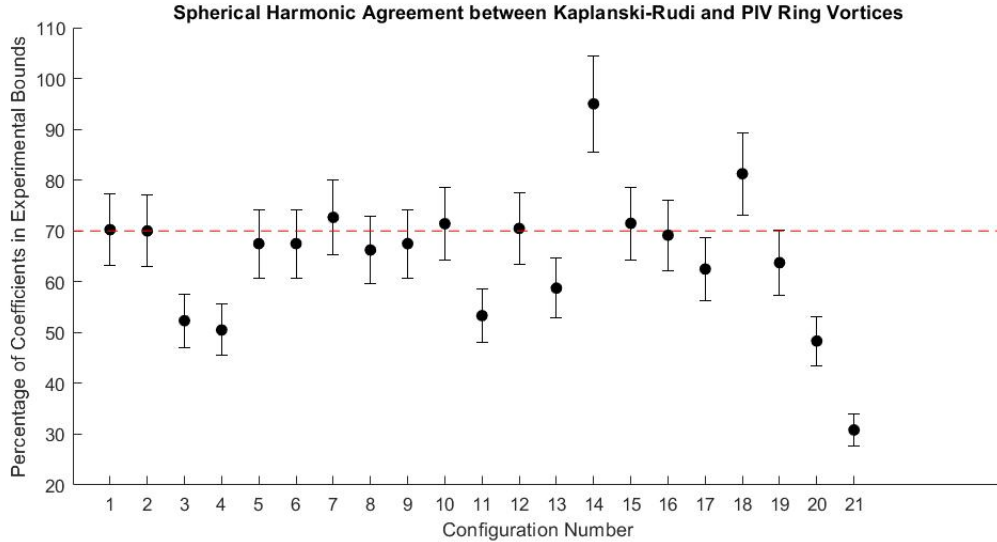


Figure 6.15: Agreement of KR and PIV streamline coefficients for 2023 PIV datasets. Y axis values represent the percentage of KR coefficients who lie within pre-established bounds around the PIV coefficients. Error bars represent 1SD.

This graph presents the percentage of spherical harmonic coefficients which lie within experimental bounds. Error bars are fixed at 10%, which is the maximum variation from reference datasets with 10 vortices, due to insufficient data for true variation. A threshold of 70% agreement is set on this graph, which will be discussed below.

#### 6.4.4 Discussion - Are the Rings Kaplanski-Rudi?

The primary objective of this analysis was to determine whether any of the  $PIV_{23}$  vortices behaved according to the Kaplanski-Rudi model within similar tolerances to the  $PIV_{19}$  vortices as analysed in Chapter 5. To quantify this, thresholds will be established, based on the tolerances of the most KR-like vortices assessed in Chapter 5. These are listed below:

- KR ring speed is within 10% of the PIV ring speed - set from Chapter 5 similarity
- KR CentVect is within 10% of the PIV CentVect - set from Chapter 5 similarity
- Vector agreement (length or angle) is over 80% - set from Chapter 5 where PIV-to-PIV comparison was at the 80-90% range.
- Streamline agreement is over 70% - set from Chapter 5 analysis where PIV-to-PIV agreement in streamlines was within the 70-75% range.

These thresholds are the tolerances under which previous phantom vortices were defined as KR-like. To determine whether the optimised vortices behave in the same way, the same thresholds will be applied. Whether each of these conditions are met by each configuration is listed in the table below.

| Config     | CV | Speed | Vector Length | Vector Angle | Streamline |
|------------|----|-------|---------------|--------------|------------|
| 1          | ✓  | ✗     | ✗             | ✓            | ✓          |
| 2          | ✗  | ✓     | ✗             | ✗            | ✓          |
| 3          | ✗  | ✓     | ✗             | ✓            | ✗          |
| 4          | ✗  | ✗     | ✗             | ✗            | ✗          |
| <b>5*</b>  | ✗  | ✓     | ✓             | ✓            | ✓          |
| <b>6*</b>  | ✗  | ✓     | ✓             | ✓            | ✓          |
| <b>7*</b>  | ✗  | ✓     | ✓             | ✓            | ✓          |
| <b>8</b>   | ✓  | ✓     | ✓             | ✓            | ✓          |
| 9          | ✗  | ✓     | ✗             | ✓            | ✓          |
| <b>10*</b> | ✗  | ✓     | ✓             | ✓            | ✓          |
| 11         | ✓  | ✓     | ✗             | ✓            | ✗          |
| 12         | ✓  | ✗     | ✓             | ✓            | ✓          |
| 13         | ✓  | ✓     | ✗             | ✗            | ✗          |
| <b>14</b>  | ✓  | ✓     | ✓             | ✓            | ✓          |
| <b>15</b>  | ✓  | ✓     | ✓             | ✓            | ✓          |
| 16         | ✓  | ✓     | ✗             | ✓            | ✓          |
| 17         | ✓  | ✓     | ✗             | ✗            | ✗          |
| <b>18</b>  | ✓  | ✓     | ✓             | ✓            | ✓          |
| 19         | ✓  | ✗     | ✗             | ✓            | ✓          |
| 20         | ✓  | ✓     | ✓             | ✓            | ✗          |
| 21         | ✓  | ✓     | ✗             | ✗            | ✗          |

Table 6.4: Agreement of 2023 PIV ring vortices with the Kaplanski-Rudi model for ring parameters, velocity vector dynamics and streamline coefficients. Lines in bold denote conditions where all conditions are met. Asterisks denote conditions where all thresholds are met except for CentVect similarity within 10%.

The table gives informative results, some of which are decidedly mixed across the different metrics. The only configurations which act as Kaplanski-Rudi across all metrics are 8,14,15 and 18. Four other configurations were determined to be KR under the same thresholds in Chapter 5. This analytical agreement indicates that four of the optimised  $PIV_{23}$  vortices are analytically the same ‘family’ as the  $PIV_{19}$  vortices under this assessment.

The second objective of this KR analysis was to determine whether the KR model can be used to plot vector analytical vector flow-fields that mirror the experimental visualisations. This has more superficial requirements, where the *similarity of velocity vector field* is the key assessment. When considering only the flow-field methods (comparing vector angle/length and streamline coefficients), configurations 5,6,7,8,10,12,14,15,18 act

as Kaplanski-Rudi vortices. All speed and centvect values for these configurations are within 15% and 20% of PIV values respectively, so the analytical approximation is fairly close to reality, but do not reach the 10% similarity of previous vortices. The thresholds can be adjusted accordingly. The low number of configurations acting as Kaplanski-Rudi rings is not a concern, as the range of vortex configurations was selected to image diverse rings. It was expected that only some would act as KR, which would define the boundaries in which the model is valid for this device.

These results generate **two primary outcomes** that are relevant to the phantom development. (a) four configurations show the same adherence to the Kaplanski-Rudi model as vortices visualised in 2019. This implies that the change in generating conditions doesn't implicitly remove the KR-like behaviour, but it is sensitive to the conditions, as before. (b) Nine conditions reach the established thresholds for the *flow-field* behaviour and *streamline agreement*, where within tolerances the KR flow field is indistinguishable from the experimental flow-field. This indicates that the KR model is a suitable candidate for use as ground-truth datasets for flow characterisation in these experimental conditions. The speeds and CentVects from these conditions are accurate to within 15% and 20% respectively.

#### 6.4.5 Discussion - Relation to Generating Conditions

It is useful to relate these findings to the ring vortex generating conditions, to establish any relationship between how the rings are made and how closely they adhere to KR. A significant ring vortex parameter which has been discussed throughout this thesis is 'Stroke Ratio' - the ratio between jet length and orifice diameter. As introduced in Chapter 3, the stroke ratio is a metric of how much energy has been injected into the ring vortex in relation to its maximum possible value for its size. A too-high stroke ratio will result in a 'shedding' ring vortex where there is too much circulation for the ring and it consistently sheds vortices throughout its journey. When selecting the rings for this PIV experiment, the stroke ratio was varied, allowing exploration of whether stroke ratio affects the rings' adherence to the KR model. Using the thresholds discussed above (including a Speed and CentVect agreement of 20%), the following data can be presented:

| Config | Kaplanski-Rudi? | Stroke Ratio if KR | Stroke Ratio if not KR |
|--------|-----------------|--------------------|------------------------|
| 1      | No              | /                  | 2.7                    |
| 2      | No              | /                  | 3                      |
| 3      | No              | /                  | 3.4                    |
| 4      | No              | /                  | 4.4                    |
| 5      | Yes             | 1.3                | /                      |
| 6      | Yes             | 1.5                | /                      |
| 7      | Yes             | 1.5                | /                      |
| 8      | Yes             | 2.4                | /                      |
| 9      | No              | /                  | 4.2                    |
| 10     | Yes             | 1.5                | /                      |
| 11     | No              | /                  | 2.4                    |
| 12     | Yes             | 1.5                | /                      |
| 13     | No              | /                  | 2.4                    |
| 14     | Yes             | 1.2                | /                      |
| 15     | Yes             | 1.5                | /                      |
| 16     | No              | /                  | 2.4                    |
| 17     | No              | /                  | 3.2                    |
| 18     | Yes             | 1.5                | /                      |
| 19     | No              | /                  | 2.4                    |
| 20     | No              | /                  | 1.5                    |
| 21     | No              | /                  | 2.4                    |

Table 6.5: List of ring vortex configurations and their adherence to the Kaplanski-Rudi analytical model according to declared tolerances. Their stroke ratios are also listed

Visualising the data in this manner allows a pattern to emerge. For the majority of rings acting as Kaplanski-Rudi rings, they have a stroke ratio of 1.2-1.5, excepting configuration 8. The rings which do not act as Kaplanski-Rudi have stroke ratios of 2.4-4.4, excepting configuration 20. These two anomalies are annotated in red. A higher stroke ratio not agreeing with the Kaplanski-Rudi model would indicate that the model doesn't take into account shedding or turbulent behaviour, which is noted in the original paper [137]. Interestingly with configuration 20 the rings act as KR rings on all metrics except for the streamline coefficients. This anomaly could be a result of flawed processing, the limited dataset or, more likely, a different mechanism becoming dominant that isn't taken into account in the KR model. Configuration 20 is the second slowest ring vortex.

Beyond these anomalies however, in the context of the phantom the Kaplanski-Rudi model can be used to estimate ring vortices in this energy space with a stroke ratio of 1.2-1.5 across the variety of orifice sizes used. The implications of this application will be discussed below.

## 6.5 Discussion - Phantom Context

Characterising the  $PIV_{23}$  datasets has established the connection between the optimised phantom vortices and those formulated from the Kaplanski-Rudi model at the micro-scale. Under the set thresholds of parameter, vector and streamline agreement it has been concluded that rings from a stroke ratio of 1.2-1.5 in this energy space can be approximated as Kaplanski-Rudi. Although this is mathematically noteworthy for ring vortex research, it also has significant implications in the context of this imaging phantom. An overarching target is to establish accurate, flexible ground-truth datasets for the ring vortex phantom to ensure high confidence in its flow profile during future development. This was the initial reasoning for establishing whether ring vortex analytical models in the literature are sufficiently similar to the phantom vortices. A characterisation tool is therefore proposed for the ring vortex phantom using the findings of this thesis, which will provide analytically derived flow characterisation for every generated vortex, using real-time device and flow QA measurements from the instrumentation pack. Time constraints limited this tool's development during this project but software has been written and undergone preliminary testing, with results indicating very strong depiction of experimental vortices. Once in regular use, this tool would essentially act as a 'virtual-PIV' - generating PIV-level flow-fields for every vortex in real-time, based on real-time measurements and the KR model.

## 6.6 Conclusions

This chapter has detailed the collection and analysis of Laser PIV datasets for the refined US-compatible ring vortex phantom (Unit-1). Both reference datasets (5 configurations of 10 vortices a-piece) and sampling datasets (16 configurations with 2-3 vortices a-piece) were visualised. The reference datasets were analysed for their stability and reproducibility at the micro-level, with 4 conditions found to be suitable for phantom use with updated tolerances. Following this, all configurations were investigated for their adherence to the Kaplanski-Rudi viscous ring vortex model. Three methods were used, comparing ring parameters, vector agreement and streamline Fourier coefficients. Requirements of speed accuracy to  $<15\%$  and CentVect accuracy to  $<20\%$ , vector agreement  $>80\%$  and streamline agreement of  $>70\%$  were set as thresholds to be deemed as Kaplanski-Rudi. Under these conditions 9 configurations can be summarised by Kaplanski-Rudi, with the remaining 12 not Kaplanski-Rudi. A connection to the stroke ratio was found in the data, as 19/21 of the configurations showed Kaplanski-Rudi behaviour for stroke ratios 1.3-1.5, and non Kaplanski-Rudi vortices for stroke ratio  $>2.4$ .

Overall, this chapter has demonstrated the phantom's readiness for more widespread use. Combining the micro-flow analysis with the macro-flow analysis presented in Chapter 3 demonstrates the tolerances for each configuration and sets the phantom's tolerances across the vortex space. The accordance with Kaplanski-Rudi rings also has potential for prediction of ring vortex micro-flows, using a proposed predictive tool.

# Chapter 7

## Design and Development of an MRI-Compatible Phantom

### 7.1 Introduction

Throughout this thesis, the ring vortex phantom has been optimised for use in an ultrasound environment, assessed for its analytical properties and expanded to perform real-time quality assurance on its functionality. The phantom is therefore ready for systematic testing and validation using US modalities in clinical and research environments. The review of current and next-generation quantitative flow imaging modalities in Chapter 1 included the prominent position of MRI technologies, such as MRA and 4D-MRI. These technologies are arguably the current and future gold-standard for flow imaging, thus any phantoms designed for comparison of these technologies would be well placed to be compatible with an MRI environment. The ring vortex phantom's current inability to assess this modality limits its potential, restricted as it is to US modalities. There are many benefits to expanding the phantom to MRI. This chapter will present adaptation of the current US-compatible model to an MRI-compliant prototype. Requirements for MRI-safe devices, concept design and manufacturing will be presented, followed by an assessment of both device and flow functionality. Throughout this chapter the ring vortex phantom developed from Chapters 1-7 is referred to as the 'US-phantom' for clarity.

### 7.2 Background - MRI Considerations for Phantom Design

#### 7.2.1 MRI Clinical Safety Regulations

The clinical MRI environment is unique and subject to strict regulations to ensure safety of both patients and staff. The primary hazard is the high-strength magnetic field generated by the scanner (typical clinical values range from 1.5-3.0T), sufficient to cause grave injury or death in the surrounding environment if not strictly controlled. As a result, the American College of Radiology has defined certain safety zones (See Figure 7.1) for

environments containing an MRI scanner. These zones, or a similar classification method, are used in clinical MRI environments, with the levels defined by the local magnetic field strength. Each zone is accompanied by increasingly strict site-access regulations to ensure minimal risk of injury [146].

- **Zone 1** is freely accessible to members of the public and no specific screening is required for access. Zone 1 is used for reception areas and waiting rooms, where patients first enter the MRI environment for their scan. Magnetic effects here are negligible and pose little danger.
- **Zone 2** is more controlled, with site access granted to trained clinicians, approved patients and companions only. Patients undergo pre-scan checks in Zone 2, such as medical history coverage and gowning. Screening for ferromagnetic objects takes place for all personnel here.
- **Zone 3** is accessible only to authorised, screened personnel. Zone 3 contains the control room, from which clinicians and technologists control the scanner and observe the acquisition.
- **Zone 4** is the final zone and is subject to the highest field strength. This is inside the scanner room, where only the patient is allowed during the scan, and clinicians only during scan preparation [147].

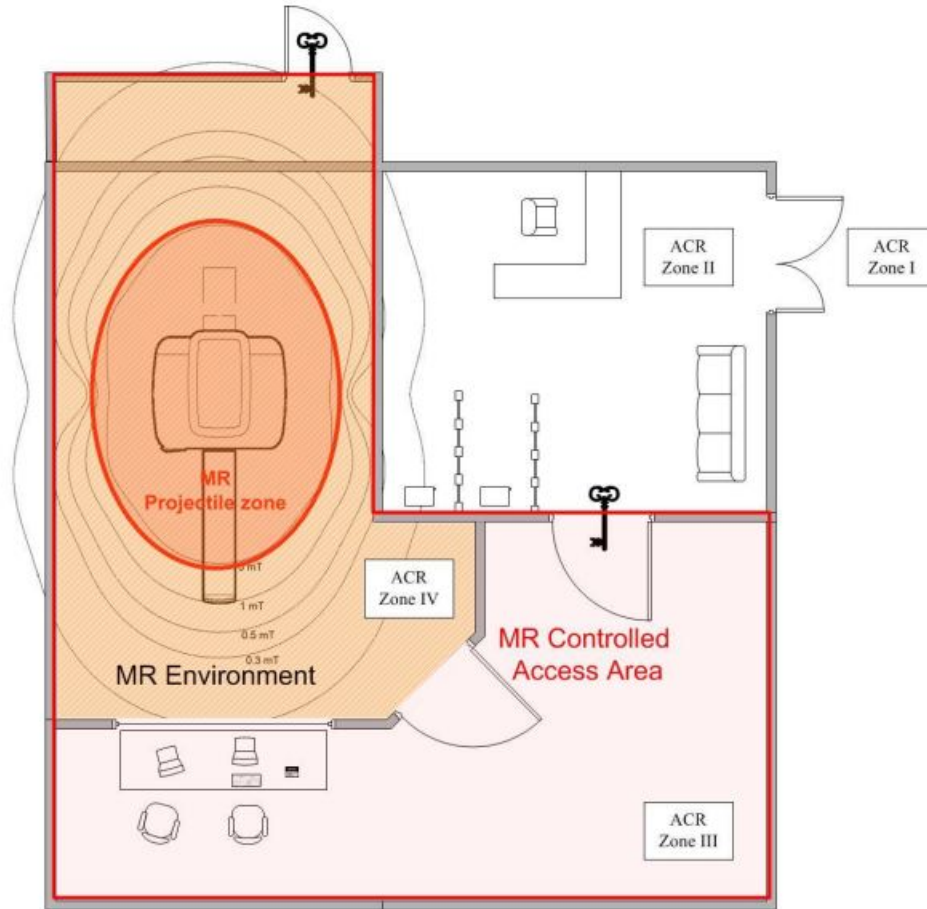


Figure 7.1: Diagram of typical MRI safety zones as defined by the American College of Radiology. [147]

These zones are dictated in clinical environments where MRI scanners are in operation, and must be considered when designing an MRI-compatible flow phantom. A common floor plan for the clinical MRI environment is presented above, with the zones annotated. Included on this schematic is the ‘5G line’, a safety boundary encompassing the scanner, at which the field strength is 5 Gauss (or 0.5mT), below which is safe for ferromagnetic components. The control room is located outside of this contour, allowing for electronic equipment such as computers and ECG machines to be used. The 5G line is of utmost importance for screening, as inside of this boundary devices such as pacemakers are at risk of being affected [148].

These zones are significant during the development of clinical MRI-related devices, as each zone has corresponding equipment regulations. Namely, Zone 4 may contain no ferromagnetic materials during scanner use. Safety definitions are assigned to all objects in the clinical environment, partitioned into three categories (See Figure 7.2): MRI-safe (safe in all MRI environments - no ferromagnetic components), MRI-conditional (approved for use in MRI environment under certain regulations - variable materials) and MRI-unsafe (not suitable for MRI environment- ferromagnetic components present) [147]. The US-

compatible ring vortex phantom is classified as ‘MRI-unsafe’, as it contains ferromagnetic materials which would be placed within the 5G boundary. To allow this phantom to be used in the environment, a re-design will make the phantom either MRI-safe or MRI-compatible.

| <b>MRI-Relevant Criteria: Definitions from ASTM international standard F2503-13</b> |  |
|---|--|
|    | <p style="text-align: center;"><b>MRI-Safe</b></p> <p>‘an item that poses no known hazards resulting from exposure to any MR environment. MR Safe items are composed of materials that are electrically nonconductive, nonmetallic, and nonmagnetic.’</p>  |
|    | <p style="text-align: center;"><b>MRI-Conditional</b></p> <p>‘an item with demonstrated safety in the MR environment within defined conditions. At a minimum, address the conditions of the static magnetic field, the switched gradient magnetic field and the radiofrequency fields. Additional conditions, including specific configurations of the item, may be required.’</p> |
|   | <p style="text-align: center;"><b>MRI-Unsafe</b></p> <p>‘an item which poses unacceptable risks to the patient, medical staff or other persons within the MR environment.’</p>   |

Figure 7.2: Classifications for devices when used in an clinical MRI-environment. [147]

## 7.2.2 Standard Clinical Phantoms

A number of MRI-compatible flow phantoms are available or in development, with different approaches to overcome the magnetic field restrictions. One common approach is to construct fully MRI-safe devices where non-magnetic pumps or motors are employed to generate the flow, often using piezoelectric (PZ) components [149],[150]. This approach was considered for the phantom, however limitations in power [150] and varied reports of interference with scanner images [151],[152] are identified as problems for these relatively new components. PZ motors are used in commercial phantoms but their relative infancy brings into question their reliability and robustness, along with the high cost. As a result, the stepper motor used throughout the ring vortex phantom’s development remains as the actuation component for the MRI-compatible system.

The second design approach is founded in hydraulics, which is also evident in the literature [153],[154] (See Figure 7.3). For these phantoms, the motor/pump is removed from the phantom section where the flow is generated. The motor is placed in the control room (Zone 3, suitable for electronic equipment) and connected via fluid-filled pipes to the scanner bed where the flow component is placed. These devices are classified as ‘MRI-conditional’, as the motors (MRI-unsafe) and flow section/pipes (MRI-safe) must be placed in their designated zones to be safe. Whilst more cumbersome than the fully MRI-

safe option, this removes reliance on piezoelectric motors and their limitations. Hydraulic systems are reliable, cost-effective and proven in the clinical context. By design control rooms share a wall with scanner rooms to allow the scan to be observed, incorporating a port/hole that allows connection of components between the scanning and control room. Connecting the motor to the flow section is therefore achievable through the port. The ring vortex phantom will accommodate this concept for MRI-compatibility.

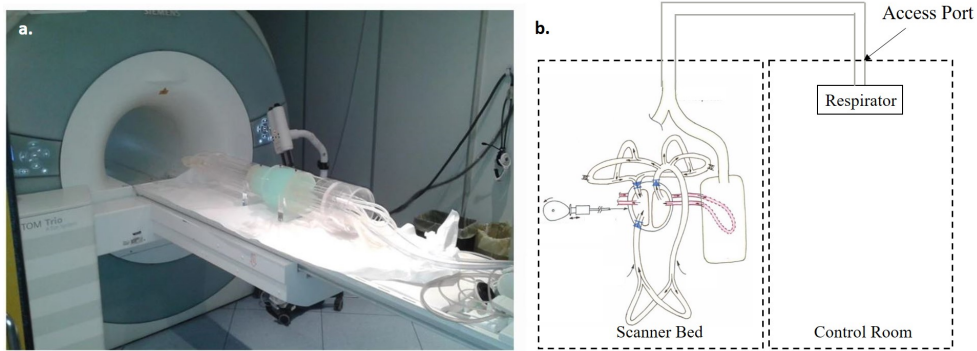


Figure 7.3: Example MRI-compatible flow phantoms which use hydraulic systems connecting the scanner bed to the adjoining control room [153][154].

## 7.3 Design Concepts for the MRI-Compatible Ring Vortex Phantom

### 7.3.1 Concepts and Hydraulic System

With the basis for MRI-adaptation established, a revised design for the ring vortex phantom was proposed. The only ferromagnetic components of the phantom are the stepper motor and attached lead screw, along with peripheral devices such as the Arduino electronics box, laptop and linear encoder. These components should therefore be located in the control room. The remaining components (water tank, piston cylinder, piston and phantom base) are manufactured from Perspex thus are MRI-safe. Crucially, all components in contact with the water are MRI-safe, so provided that generating conditions replicate those of the US-phantom, the ring vortex should remain undisturbed.

Employing the hydraulic concept, the revised phantom design separates the phantom into two components: ‘Motor/Piston Input’ and ‘Plate/Tank Output’, placed in the control room and scanner respectively. The two components will be coupled via a flexible fluid-filled pipe. The concept design for this is presented below in Figure 7.4.

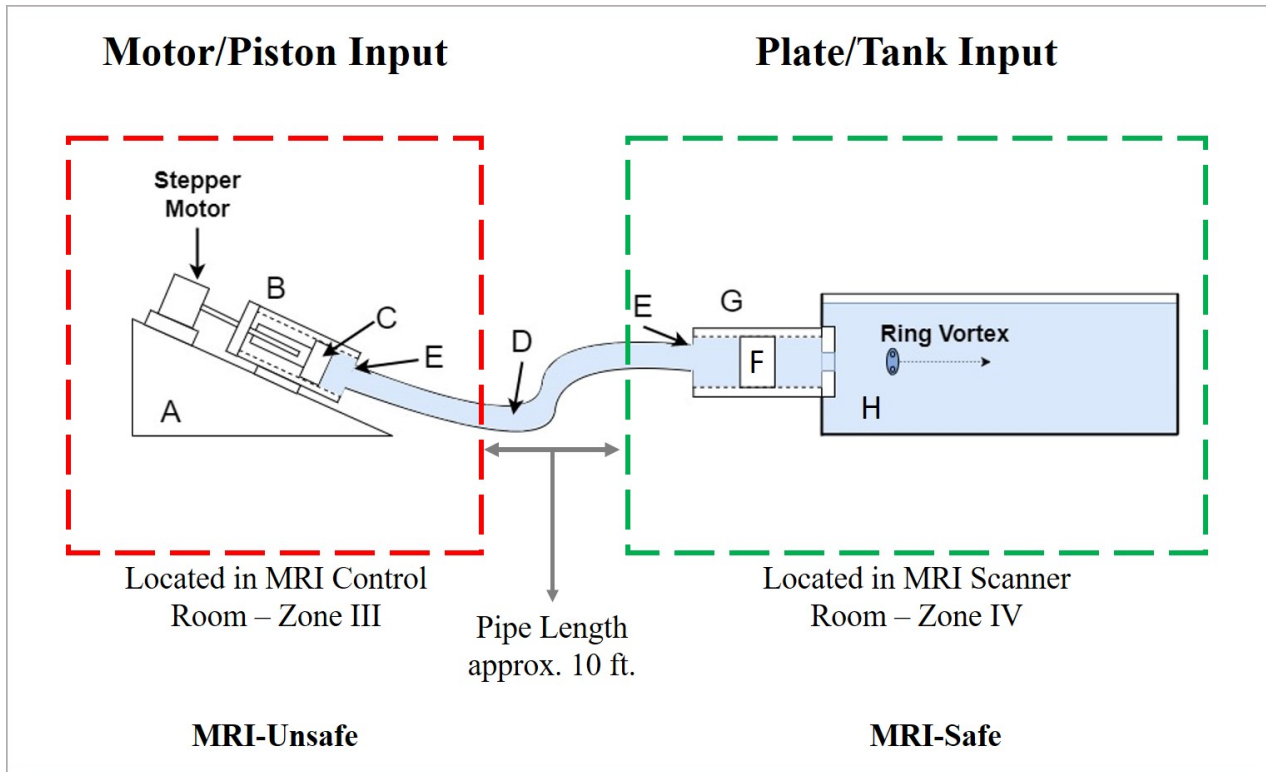


Figure 7.4: Concept Design for the MRI-Compatible ring vortex phantom

The key components are listed below, along with their function:

- (A) **Motor Mount**- This angled structure supports the motor, piston and piston cylinder. The angle aims to reduce water leakage through the rear-end of the piston cylinder.
- (B) **Piston Cylinder**- This hollow cylindrical chamber contains the piston and eliminates lateral motion as the piston is propelled.
- (C) **Piston**. This is driven by the stepper motor via the lead screw and expels a jet/slug of fluid through the orifice into the pipe.
- (D) **Hydraulic Pipe**- The fluid impulse propagates along the length of this pipe into the scanner bed component. The pipe must be flexible, stiff-walled, watertight and translucent. The fluid is considered incompressible.
- (E) **Couplers**- These connectors join the hydraulic pipe to the tank cylinder and piston cylinder respectively. The phantom needs to be portable so these couplers are detachable and watertight.
- (F) **Plate**- The piston-generated jet propagates through the pipe then into the tank cylinder, propelling the plate forward. The plate in turn expels fluid through the orifice and generate a ring vortex.

- (G) **Tank Cylinder**- The cylinder is reminiscent of the piston cylinder used in the US-phantom, with an air-hole to ensure ease of assembly. A plate covers the back to retain a water-tight seal.
- (H) **Water Tank**- The ring vortex propagates across the length of the tank, supported by the base.

Mechanically, the phantom ought to fulfil the same basic requirements as the US-compatible phantom for commercial viability. It must be portable (thus components should be detachable), safe and cost-effective. The significant design change will likely impact the dynamics of the phantom, so characterisation of device functionality will take place once manufactured. The vortices will also be characterised, to assess their **controllability, stability and reproducibility**, proving their suitability for use in this phantom.

### 7.3.2 Previous work

Previous work used a proof-of-concept device to explore whether the hydraulic concept design could be used to generate ring vortices [155]. A proposed design was used to manufacture the motor mount and piston cylinder, and a hosepipe used for the coupling pipe. Preliminary experiments were undertaken to test the device, and ring vortices were successfully generated. No plate was used here, with the generating slug of fluid propelled by the motor-actuated piston alone. The generated vortices were visually deformed and unstable. It was hypothesised that turbulence in the pipe distorted the rings and caused instabilities at the orifice. No quantitative assessment was performed on the rings, and the phantom was not imaged beyond camera recordings. This proof-of-concept exercise demonstrated that ring vortices can be generated in a hydraulic system based on the US-phantom. The addition of the plate (F on Figure 7.4) in this design is designed to stabilise the flow through the orifice.

## 7.4 Materials and Methods - MRI Phantom Manufacturing

### 7.4.1 MRI-Unsafe Motor/Piston Input

The first portion of the device (Motor/Piston Assembly) is designed to be located in the control room, and is comprised of a mount, motor mount, piston cylinder, piston and piston guide (See Figure 7.5). These components were all manufactured using Perspex. The mount was angled on two vertical struts topped with a 20mm-thick horizontal base, on which a solid Perspex block was attached to support the motor. The piston cylinder was attached to two vertical struts, which is in turn screwed into the mount during assembly. The piston cylinder was closed at the bottom end, with a threaded 20mm diameter orifice to connect to the hydraulic coupling pipe. The piston was identical to the US-phantom, with the non O-ring piston used due to its reliability seen in earlier

experiments. The stepper motor was screwed onto the motor mount through a vertical bracket and connected to a neighbouring laptop.

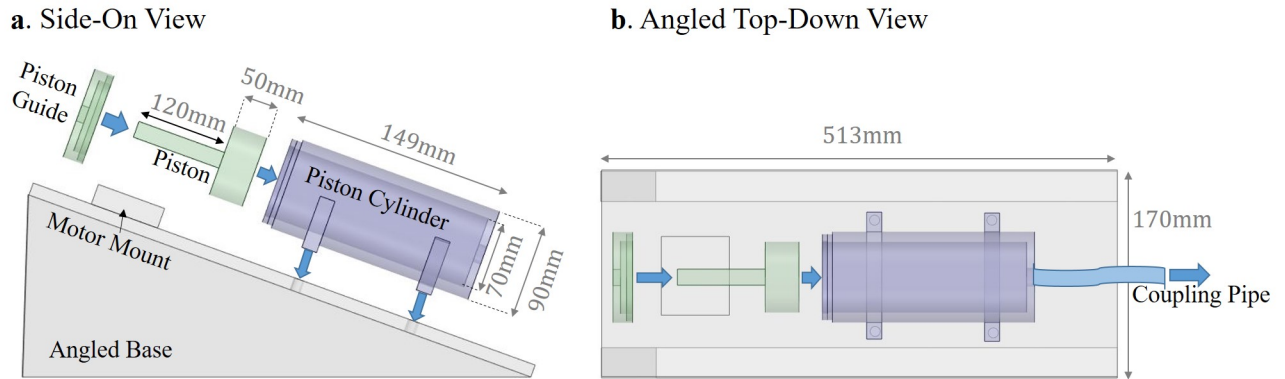


Figure 7.5: Schematic of the Motor/Piston Input portion of the MRI phantom design.

When testing this device, it became clear that the piston was not truly watertight. In the US-phantom a small amount of water ( $\sim 5\text{ml}$  every 15 mins) leaked past the piston head during experiments. The increased weight of water increased this  $\sim 5\text{ml}$  build up to  $\sim 50\text{ml}$  during the same amount of time when the motor is placed below the level of the water tank, which can quickly accumulate during lengthy experiments. Placing the motor on the same level as the tank stops this leakage, but allows air to enter the system past the piston head. Introducing air into the system compromises the hydraulic system and affects the vortices, so the experiments detailed in this chapter took place with the motor/piston input component on the floor. As for widespread future use the phantom will need to be usable at any relative motor-to-tank height difference.

## 7.4.2 MRI-Safe Plate/Tank Output

The second portion (Plate/Tank Assembly) was designed to be placed in the scanner bed and has no metallic or electronic components. It is comprised of the water tank, phantom base, plate cylinder and plate (Figure 7.6). The water tank and phantom base were unchanged from the US-phantom design, with the tank measuring  $370\text{mm(L)} \times 175\text{mm(H)} \times 175\text{mm(W)}$  externally, with walls of  $10\text{mm}$  thickness. The plate cylinder, attached to the tank via a threaded  $70\text{mm}$ -diameter orifice has dimensions of  $90\text{mm(D)} \times 145\text{mm(L)}$  with a wall thickness of  $10\text{mm}$ . A  $1\text{mm}$ -diameter air-hole was made in the cylinder's upper wall to allow removal of trapped air during assembly. The piston cylinder back-end (not attached to the tank) was closed using a  $90\text{mm}$ -diameter plate. This plate was attached permanently onto the cylinder and has a  $20\text{mm}$  diameter circular cut-out, onto which the coupling pipe was attached. The final component is the push-plate, which is propelled by the piston-generated impulse in the control room. To ensure a tight fit and minimal friction with the cylinder interior, this followed the non O-ring piston design,

which had demonstrated low friction with the cylinder's inner walls during US-phantom development.

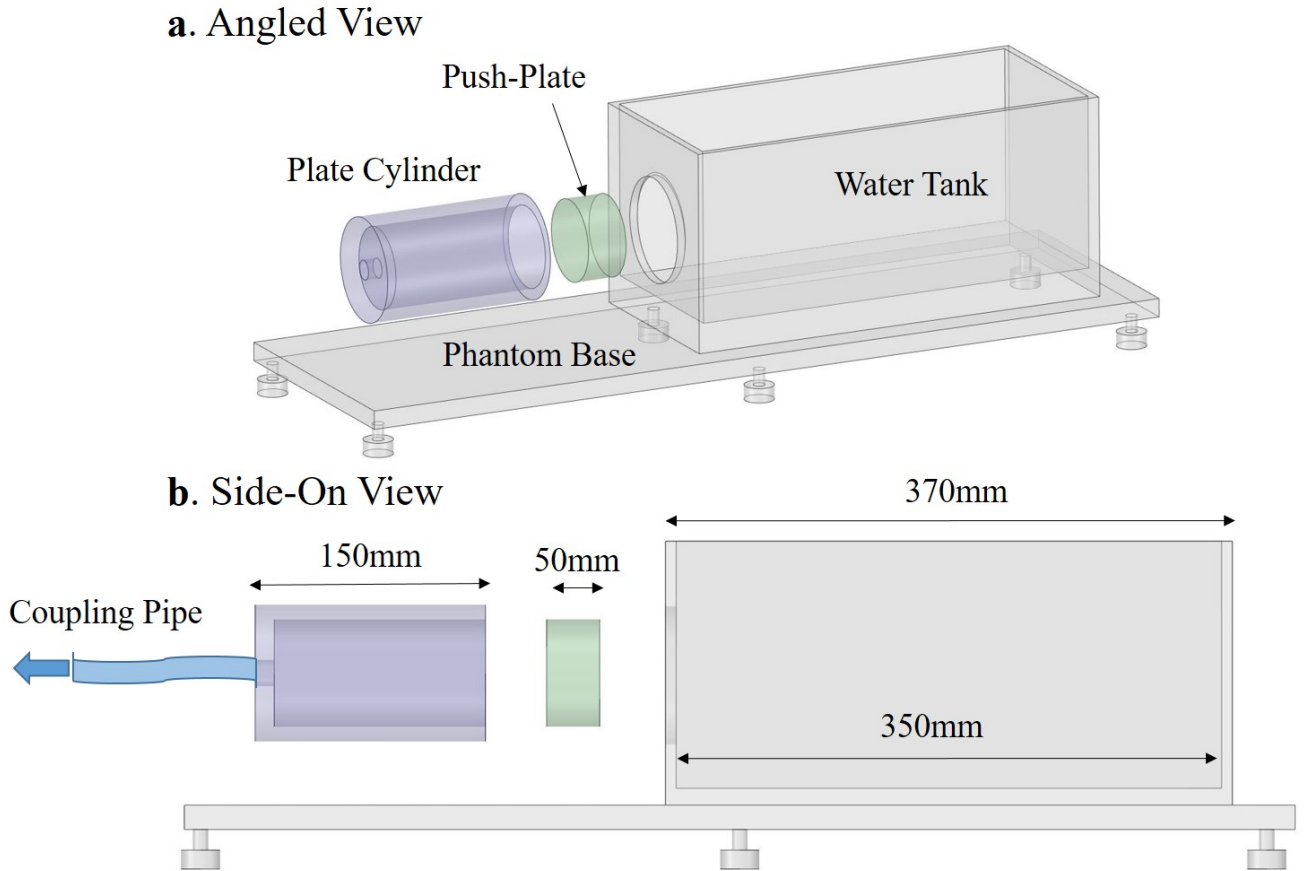


Figure 7.6: Schematic of the Plate/Tank Output component of the MRI ring vortex phantom

During testing this component held up well to the pressures exerted by the piston propulsion. The component as a whole is watertight, with any leaking the result of user error during setup, for example not connecting the cylinder to the tank correctly.

### 7.4.3 Coupling Pipe and Connectors

The two assemblies described above are connected by a fluid-filled hydraulic pipe. Choice of pipe is paramount, as its properties will impact both the flow and phantom practicality. It must be sufficiently flexible to navigate around corners and traverse any motor-to-tank height difference, but sufficiently stiff to minimise energy loss from pipe expansion as the flow is propelled. A flexible PMMA pipe reinforced with an embedded stiff PMMA helix was selected. It has a smooth interior, is easily manipulated, is adequately stiff, is translucent, and cost-effective.

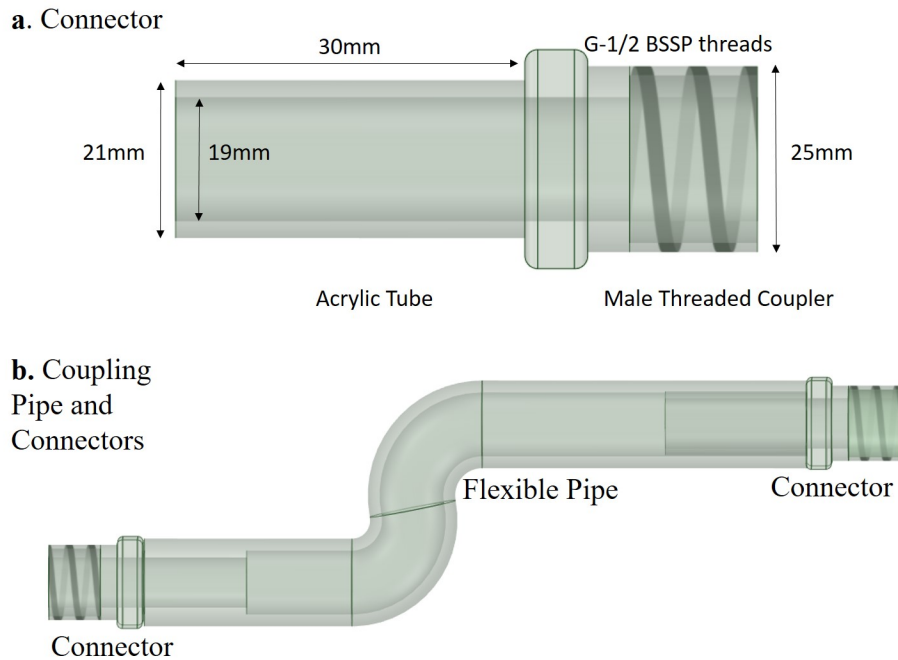


Figure 7.7: Schematic of the pipe couplers for the MRI-compatible ring vortex phantom. The couplers insert into each end of the pipe and attach to the plate cylinder and piston cylinder respectively.

This pipe is connected to both the piston cylinder and the tank cylinder via couplers. The piston cylinder has a G-1/2 BSSP female threading, however the tank cylinder has no threading. A G-1/2 female connector was therefore attached to its back-plate. Custom pipe-connectors were manufactured by attaching short 19mm external-diameter acrylic tubes (matching the pipe internal diameter) to G-1/2 male-threaded hollow connectors (See Figure 7.7a). The tube-end was attached permanently into the pipe to form a water tight seal. The threaded ends can then be attached and detached from the piston and plate cylinders respectively during assembly, disassembly or transport. These connectors are robust, withstand extended experiments with no leakage and are resistant to the applied pressures, so are suitable for use in the prototype at this stage.

#### 7.4.4 Full Device and Initial Observations

The assembly of this phantom is straightforward in the laboratory environment. To assemble the phantom, the user inserts the piston of the motor/piston assembly into the piston cylinder and screws the cylinder onto the motor mount. The pipe is attached onto both the tank and piston cylinders, and the tank cylinder subsequently screwed onto the water tank. The tank is elevated and filled with dyed water (dark blue/black), allowing for the water to fill the piston cylinder and coupling pipe in turn. It is imperative that air bubbles are removed from the system as this will compromise the incompressibility and affect the piston-to-plate energy transfer relationship. Air bubbles

can be easily seen due to the dark fluid and translucent pipe, and manual manipulation is used to remove these via the open tank. The plate is inserted into the tank cylinder by pushing it in from the tank entrance and releasing water from the air-release hole. Finally, the water tank is emptied of the dyed water, refilled with clean distilled water and the orifice attached. The phantom is now ready for use (See Figure 7.8) With an experienced user, set up of the MRI-compatible phantom takes 25-30 minutes.

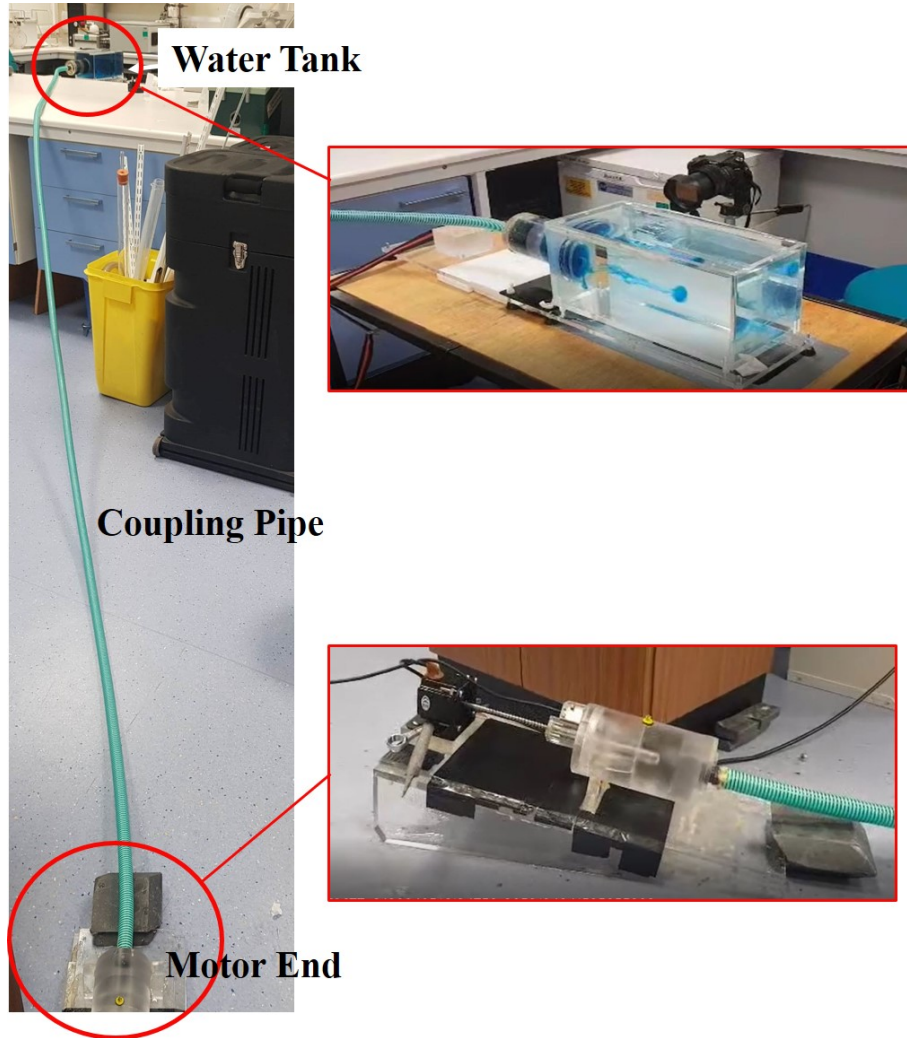


Figure 7.8: Photograph of the MRI-compatible phantom prototype in a laboratory environment.

A range of ring vortices were generated for visual assessment and refinement of the device. It was noted that the plate moved in active response to the piston motion, and the generated rings were not visually distorted. They emerged circular from the orifice and propagated as expected, with the diffusive, laminar and turbulent regimes observable as from the US-phantom. An initial observation identified that the motor was ‘flexing’ from the amount of force required to propel the piston. The added water weight of the hydraulic

pipe increases the system inertia, thus more force is required to propel the piston. This displaced the motor and induced oscillatory motion in the piston. This was observed in the US-phantom during development and should be minimised to ensure reproducible motion and minimal strain on the components. The motor was therefore supported with metal inserts, to prevent the bracket deformation. Future design refinements will eliminate this issue.

## 7.5 Device Assessment - Characterising Device Functionality

Manufacture of the MRI-compatible system produced a device capable of ring vortex generation in an MRI environment. For this device to be assessed as a potential phantom device, characterisation was required to quantify its functionality. In a similar fashion to the US-phantom, this characterisation took place at two levels: device behaviour and flow behaviour. The device dynamics were assessed first, followed by an assessment of the generated vortices which is detailed in Section 7.6.

For characterisation of the device functionality, the dynamic components' motion were examined to explore its **controllability** and **reproducibility**. In the US-phantom this involved tracking the piston displacement and speed in response to certain motor pulse sequences. The MRI-compatible design has three dynamic components - the motor, piston and plate. Understanding the relationship between the input motor code, the piston response and the plate response in this device is significant, as the three profiles will likely differ depending on the conditions. In an ideal scenario with no energy losses and an infinitely long stiff pipe the plate velocity profile would match the piston profile, which would in turn match the input code for the motor. This would entail zero energy loss, zero jet effects and no friction on the piston and plate, therefore is unrealistic for the experimental device. This section will therefore establish these relationships, and clarify any sensitivities or dependencies present.

### 7.5.1 Method - Tracking Plate Motion

Predicting the plate motion from the motor pulse sequence was unachievable without previous characterisation of its velocity profiles. Encoding the piston with the linear encoder has provided valuable information for ring vortex generation throughout this work, proving the importance of tracking the dynamic components. Tracking the plate through the encoder was not possible as the plate is fully submerged, so an alternative was sought. A long-term commercial tracking tool will be MRI-compatible however at this development stage a camera-operated visual processing tool was sufficient. To track the plate, a SONY RX10 camera was mounted at approximately 15cm from the tank cylinder at a zoom of x4 so the cylinder filled the entire frame. As the plate was propelled by the piston, the propulsion was recorded at 500fps, manually triggered by the user. This was then exported to MATLAB for post-processing, with one video for each plate propulsion.

Once loaded in MATLAB, some simple post-processing was employed (See Figure 7.9). In this algorithm, a sample frame is loaded and the user draws a line across the plate length from the left-wall (LW) to the right-wall (RW), identifying 5cm in terms of pixel units. A point either side of the plate is then selected. MATLAB sets a line between these points and measures the pixel intensities along the line. As the fluid is dyed dark each side of the piston, a large increase in intensity is observed at the LW, and a large decrease at the RW, coinciding with the plate edges. The intensity profile is found between the points for every subsequent frame and the LW and RW location detected for every frame. These pixel locations are converted to centimetres using the initial LW-RW 5cm calibration, and the plate position is plotted against time for both LW and RW. These are averaged to remove any fluctuations or anomalous readings (for example from a water droplet or flash from ambient lighting) to calculate the plate velocity profile.

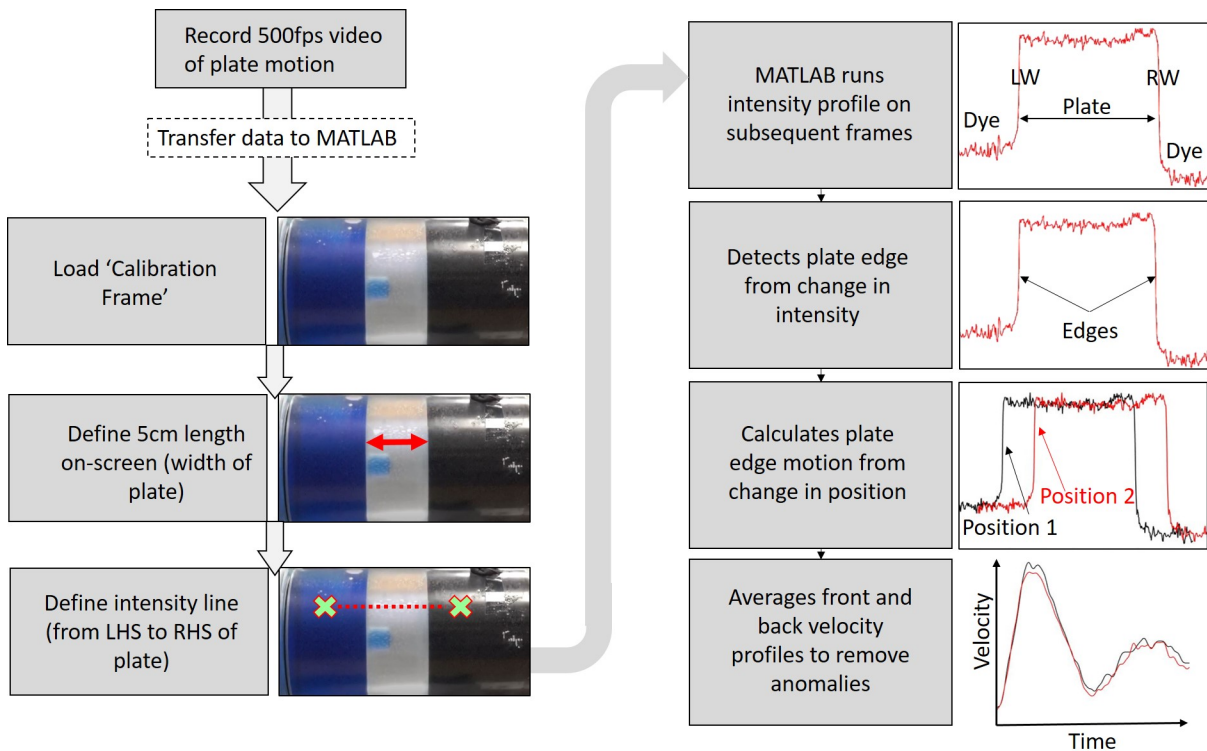


Figure 7.9: Flowchart explaining the post-processing methods used in tracking the plate in the MRI-Compatible Ring Vortex Phantom.

This method required validation to determine the errors borne from its use. An experiment was performed where the piston was tracked using the encoder (deemed the ‘gold-standard’ method in this exercise) and the camera. Three displacements were used with five instances on each. The average displacement and speed were measured using both encoder and camera data using the method described above. The average % difference between the encoder and camera results and the associated variability was found for each condition. These results are listed below.

| <b>ProgDisp</b> | <b>Distance Error</b> | <b>Average Speed Error</b> |
|-----------------|-----------------------|----------------------------|
| 0.5mm           | 1.1-5.3%              | 2.6-9.8%                   |
| 3mm             | 3.7-4.3%              | 1.1-9.1%                   |
| 4mm             | 0.5-2.75%             | 0.1-7.9%                   |

Table 7.1: Experimental errors in the measurement of plate displacement and plate average speed

Non-zero errors were present in both displacement and speed measurements. Distance measurements using the camera-encoding method deviated from the encoder’s value by 5.3% or less, giving an accurate answer. The speed measurements had a higher associated error of up to 9.8% error. These errors were integrated into plate measurements throughout this chapter.

## 7.5.2 Results - Piston Profiles

The first stage of device characterisation was to understand the piston motion in this setup. Piston motion can be easily tracked using the LM10 linear encoder, as demonstrated in Chapters 3,4. The piston motion in the US-phantom was subject to motor oscillation, stiffness of the phantom base and tightness of the lead screw. These factors were true in the MRI-device also, and exacerbated due to the increased inertia of the water. Particularly with the motor positioned lower than the water tank, the increased opposing force was likely to affect the piston propulsion.

To characterise the piston motion, a variety of impulses were generated and tracked using the encoder. Programmed piston speeds of 2cm/s and 1.2cm/s were selected, with programmed displacements ranging from 0.5-2mm. A top-hat function motor pulse sequence was used. For visualisation, a range of the tracked piston profiles are presented below:

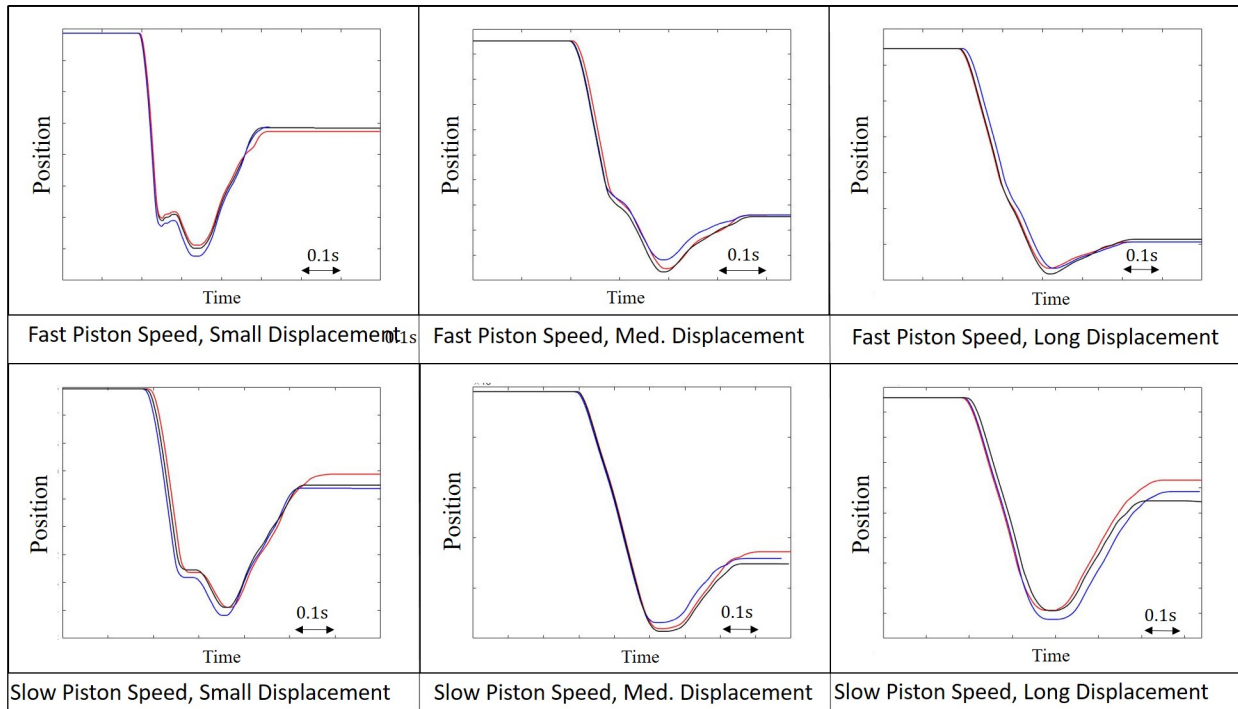


Figure 7.10: Example piston velocity profiles for speeds of 2cm/s and 1.2cm/s for the MRI-Compatible ring vortex phantom. Each line represents an individual run.

These profiles are distinctly different to the programmed motor pulse sequences, where the piston is propelled forward by the requested displacement and stops with no oscillation. A notable universal response is observed where the piston continues moving before stopping and reversing direction, drawing back to an intermediate position where it remains steady. This was not from motor oscillation as the piston visibly moves back up the lead screw as it reverses direction, rather than the motor itself moving. The large mass of water above the piston pushes the piston as it stops moving, propelling it backwards up the lead screw until it settles at an interim position. It was clear that the piston displacement differed from the programmed motor displacement.

To characterise these profiles, the acceleration, average piston speed and piston displacement were examined. For each parameter the **reproducibility** and **controllability** were assessed - controllability being the relationship to the user-defined input conditions defining the motor pulse sequence. The parameters calculated below assessed the initial forward motion and did not take into account the drawback.

### Piston Acceleration

In Chapter 3, the piston profiles were analysed for the US-phantom, with the ‘threshold acceleration’ found - the acceleration achieved by the motor with an input of infinite acceleration (top-hat function). The US-phantom achieved values of  $\sim 200\text{cm}/\text{s}^2$ . It was expected that the MRI-compatible device would achieve a lower threshold acceleration due to increased inertia, so this was measured. A range of piston impulses were generated

over two piston speeds and ten displacements, with the acceleration calculated for each. These accelerations are presented below.

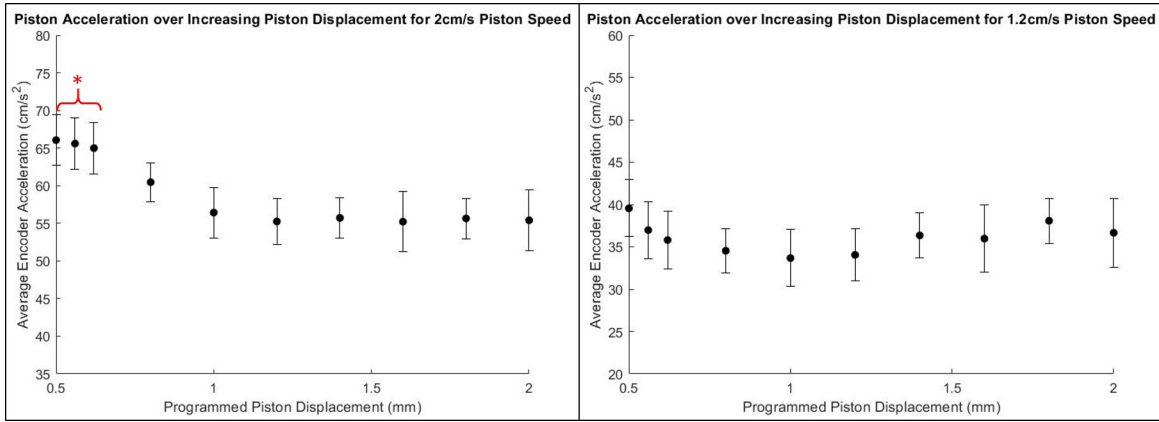


Figure 7.11: Graphs presenting the average piston accelerations for 2cm/s and 1.2cm/s piston speeds in the MRI-Compatible Phantom Prototype. Anomalies are annotated. Datapoints represent the average of ten impulses and error bars represent 1SD.

Two features are significant in these results: the acceleration average values (to characterise controllability) and the error bars (for reproducibility). As expected the acceleration is considerably lower than the US-phantom, with a value of  $55 - 65\text{cm}/\text{s}^2$  for fast piston profiles and  $35 - 40\text{cm}/\text{s}^2$  for slow piston profiles. Anomalous readings are observed for displacements below 0.6mm with the fast 2cm/s piston speed (annotated with \* on Figure 7.11). These profiles have higher accelerations, indicating the piston ‘jumping’ forward. This can place the motor under strain so these conditions are not recommended for extended use. The consistency of acceleration for profiles over 0.6mm, however, indicates good controllability/predictability of the piston functionality under these conditions.

Overall the reproducibility in acceleration is high across all conditions, with CoV values ranging from 3-10%. This variability is sufficient for reliable piston use.

## Piston Displacement

The second parameter to assess was the piston displacement, a key parameter for controlling and predicting the generated vortices. This parameter was assessed for its reproducibility and relation to the programmed placement (controllability). These results are presented below.

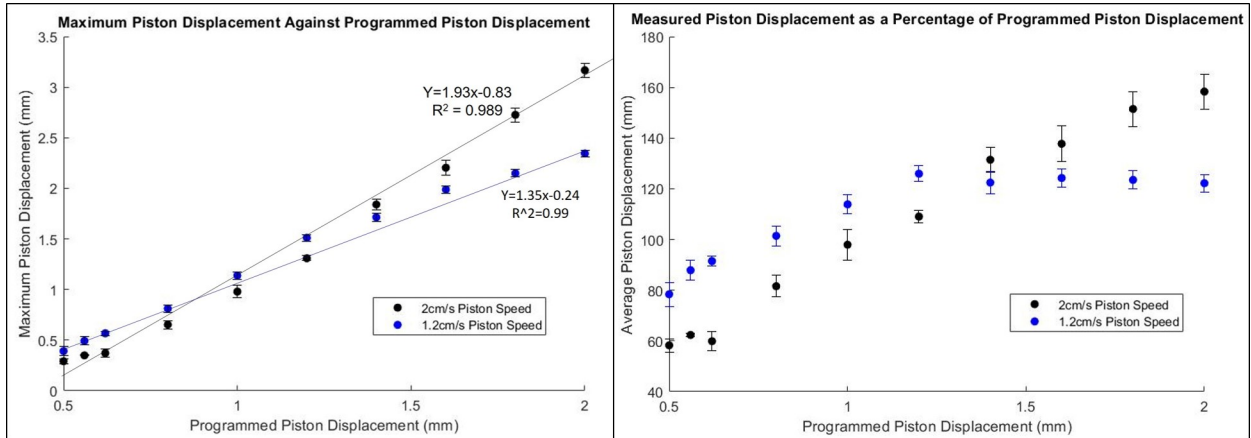


Figure 7.12: Graphs presenting the average piston displacements for 2cm/s and 1.2cm/s piston speeds in the MRI-phantom prototype. Datapoints represent the average of ten impulses and error bars represent 1SD.

Graph (a) presents the absolute values of piston displacements over a range of displacements. When compared to the programmed distances, both fast and slow piston speed profiles exhibit strong linear relationships with  $R^2$  over 0.985, demonstrating high controllability. The fast speed profiles has a steeper gradient at 1.93, with piston distance approximately 93% higher than the programmed value. Slow profiles are only 35% higher than the programmed displacement with a gradient of 1.35. These linear relationships can be used to predict piston response to the programmed value, but values don't all lie on the linear graphs, thus a case-by-case prediction would be prudent - using the averaged datapoints of each experimental condition to predict likely piston response.

Reproducibility is high across the conditions for this parameter, with CoV values of  $<6\%$  across the range of conditions. It is noteworthy that when plotted as percentages of the programmed displacement (Graph b), the slow piston speed displacements level out at approx. 120%, indicating an equilibrium of sorts in its underlying mechanics. This could be interpreted in terms of initial force and damping factor in a harmonic oscillator model but will not be further investigated in this project. The key outcomes from this analysis is that the piston displacements are reproducible to within 10% and the displacements are well-characterised with respect to experimental conditions.

### Piston Average Speed

Finally, the piston speed was assessed for the test conditions. Anomalous values here would indicate the piston jumping, getting stuck or unpredictable oscillation in the motor/piston component. It is expected that longer displacements will have higher average speeds, as shorter impulses spend a more significant time in the acceleration/deceleration phase. Results are presented below for a variety of conditions.

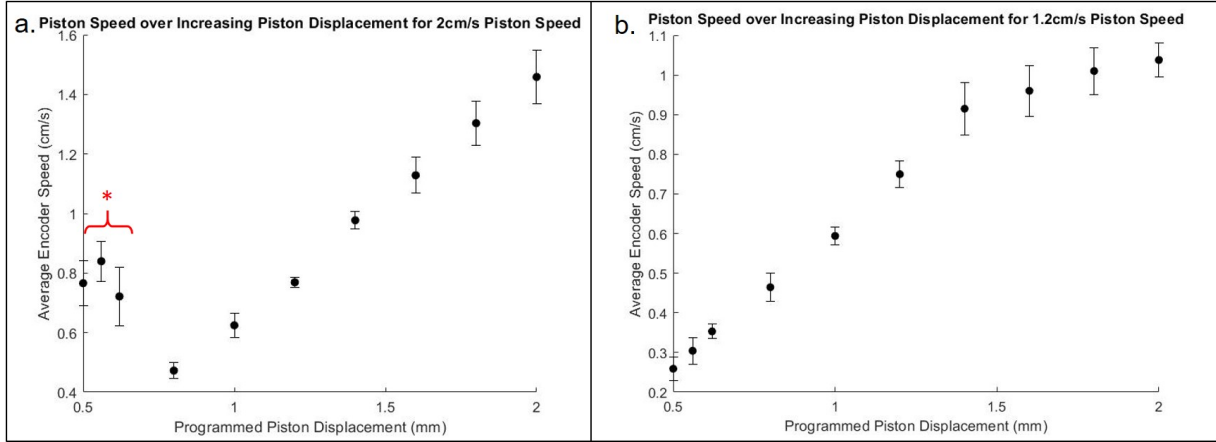


Figure 7.13: Graphs presenting the average piston velocities for 2cm/s and 1.2cm/s piston speeds in the MRI-phantom Prototype. Datapoints represent the average of ten impulses and error bars represent 1SD.

A clear relationship is observed in this data, where higher displacements results in higher average speeds, as expected. This relationship is non-linear, particularly in the slow piston profiles in Graph (b). Anomalous results are present in impulses under 0.6mm for the fast piston speeds in Graph (a) (annotated with \*) where the piston is moving faster than would be expected. These anomalies are present in the acceleration analysis also, implying that the piston is jumping forward. These conditions are therefore not recommended for use.

Reproducibility is high for both piston speeds, with all CoV values under 10% for the non-anomalous readings. This implies that the piston is moving reliably under the motor impulse and ejecting a consistent amount of energy towards the plate with tight tolerances. Overall, this analysis demonstrates that the piston speeds are both reproducible, and are characterised using these graphs, thus can be controlled by the user. Future work should refer to these values to predict piston motion from certain experimental conditions.

### 7.5.3 Results - Plate Profiles

The piston response to the motor conditions has been characterised. The ring vortices, however, are generated by the plate impulse, so plate motion was also explored to determine its response to the piston impulse and motor conditions. Profiles visually exhibited similar behaviour to the piston profiles (See Figure 7.14), with an initial forward push followed by a drawback to an interim position. This demonstrated that the plate actively responded to the piston's impulse through the coupling pipe.

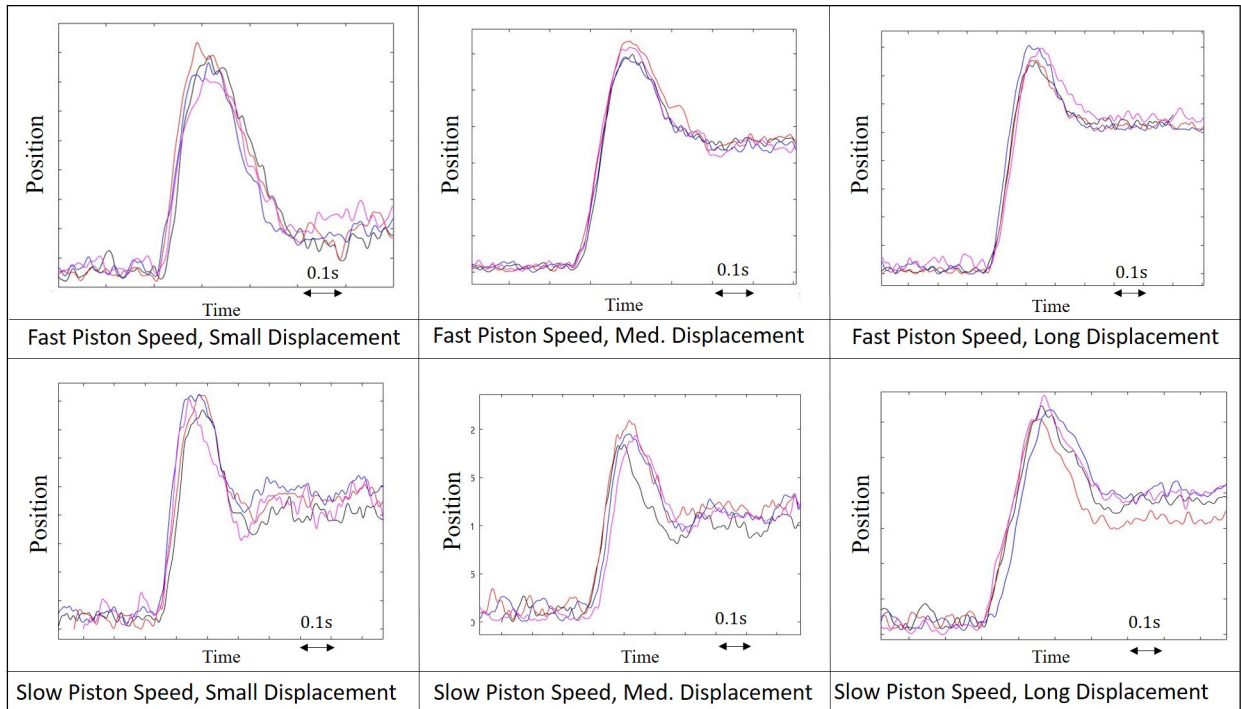


Figure 7.14: Graphs presenting the average plate profiles for 2cm/s and 1.2cm/s piston speeds in the MRI-Compatible Phantom Prototype. Each line represents an individual run.

The plate impulse was quantitatively assessed in a similar fashion to the piston analysis, analysing controllability and reproducibility of each condition. Restrictions are imposed by the limited tracking method described in Section 7.5.2. The limited spatial resolution removes the possibility of quantifying acceleration, so only plate displacement and speed were quantified. Noise is visible on the plate profiles, which is not present on piston results, a result of the automated optical analysis.

### Plate Displacement

The first key parameter is plate displacement. The relationship between the programmed displacement and plate displacement (controllability) and reproducibility were clarified. The drawback portion of the profile was assessed, these results reflect the *maximum* displacement for each condition. Multiple experiments were recorded for each displacement on different days to assess variability between experiments, with notable results.

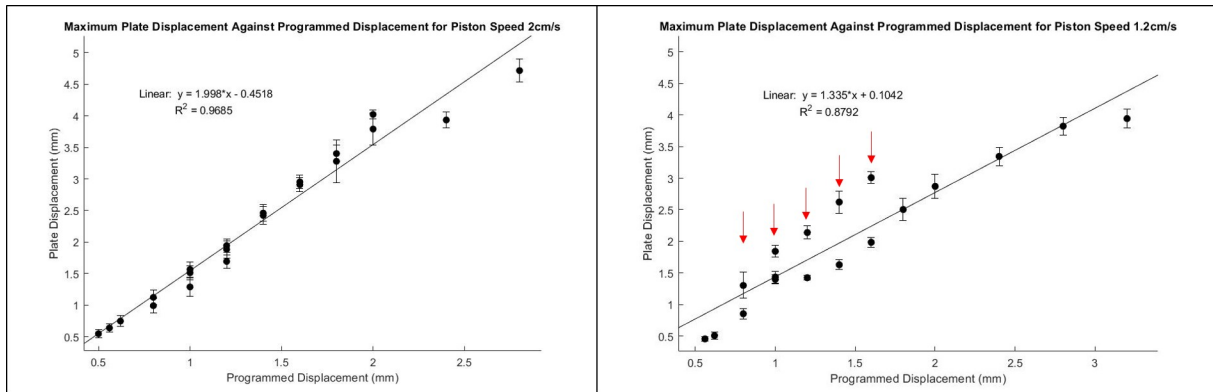


Figure 7.15: Maximum plate displacements for a range of programmed displacements for the MRI-phantom. Datapoints represent the average of ten impulses and error bars represent 1SD. Anomalies are annotated

Analysis of reproducibility, expressed in error bars in Figure 7.15, indicated high reproducibility despite more variation than the piston displacements. CoV values ranged from 4-11% for the fast piston impulses, and 3-11% for the slower piston impulses. These values were suitable for use and indicate that the plate moved a similar distance for each individual impulse. The method-borne error of up to 5% must be considered on top of these results.

Secondly the relationship between programmed displacement and plate displacement was quantified through linearity. Graph A demonstrates a strong linear relationship between the two, with the gradient inferring that the plate moves over  $\sim 199\%$  of the programmed displacement. Results from different days are all plotted here and show minimal variability, with the  $R^2 = 0.97$ . This very strong relationship allows for confident prediction of plate displacement from programmed displacement for a piston speed of 2cm/s.

The slower piston speed of 1.2cm/s displayed a different relationship. A gradient of 1.335 indicates that the plate moves over  $\sim 133\%$  of the programmed displacement, less than the fast impulses. Notable anomalies are present in this data with 5 datapoints (indicated by arrows) lying significantly above the other data and the linear fit. This resulted in an  $R^2$  value of 0.88. Whilst this is classified as a strong relationship, the anomalies compromised the quality of these results. The anomalies are further investigated in Section 7.5.6. Overall, plate displacement from both programmed piston speeds exhibited high reproducibility. The plate displacement is controllable through the linear relationships, but less confidence is evident in the slow piston profiles.

## Plate Average Speed

The second parameter for plate motion characterisation was the average speed. This measurement was derived from the camera encoding method. The results are plotted below.

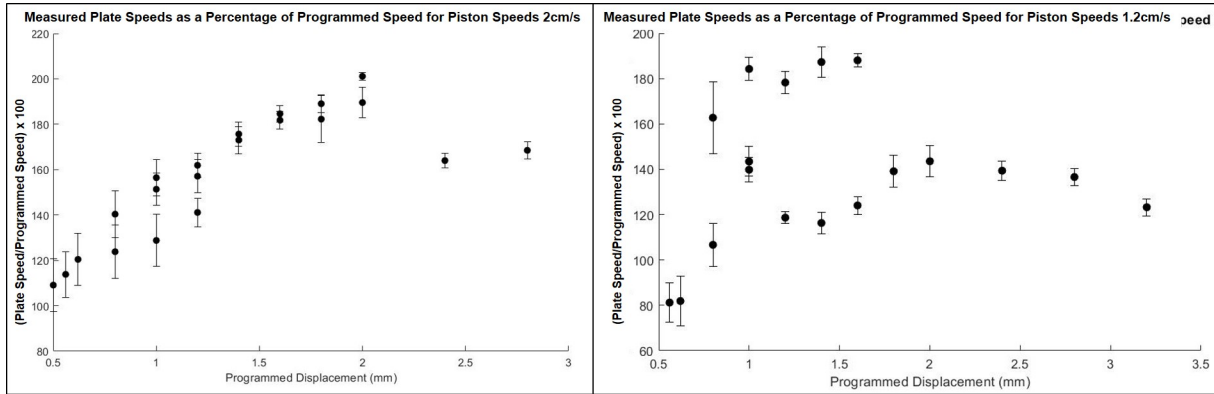


Figure 7.16: Average Plate Speeds for a range of programmed displacements for the ring vortex phantom. Datapoints represent the average of ten impulses and error bars represent 1SD.

As expected, the variability was increased from plate displacement, ranging from 5-17% for the fast impulses and 3-19% for the slow impulses. However, despite the large error bars an increase in plate average speed can be seen for the fast impulses. This is expected, as the further the plate moves, the longer it will spend in the high-speed ‘plateau’ phase, rather than the low-speed sections of the acceleration and deceleration. The slow impulses show higher variability, and the clear anomalies are once again present in Graph (b). Their reappearance indicates that these measurements are anomalous in plate displacement *and* plate speed. Reproducibility is decreased when the error of 10% from the analysis is included.

Overall the plate analysis has provided information about its motion and clarified the profiles’ relationship to motor sequence parameters. Increase in both displacement and average speed was found with respect to increasing programmed speed. Reproducibility is lower than previous phantom functionality partially from analysis method variation.

#### 7.5.4 Piston-to-Plate Relationship

The piston and plate motion have been analysed in terms of their displacements and speeds in relation to the programmed motor input. This is useful but for long-term experiments it is advantageous to understand the piston-to-plate relationship. Knowledge of this relationship is useful as the piston can be tracked in real-time during data collection, through use of the linear encoder. If the piston dynamics are known, the plate response can be predicted without use of the camera (which is unsuitable for the MRI environment).

In an ideal system with incompressible water, zero compliance and zero energy loss the plate and piston motion would be identical. The discrepancy from ideal behaviour was characterised for the experimental setup used in this chapter to understand the magnitude of difference between piston and plate motion. Difference between the two profiles is visualised in Figure 7.17. Both plate and piston experienced the drawback behaviour, and interestingly the plate was drawn back almost to its initial position in the fast piston speed (Figure 7.18a).

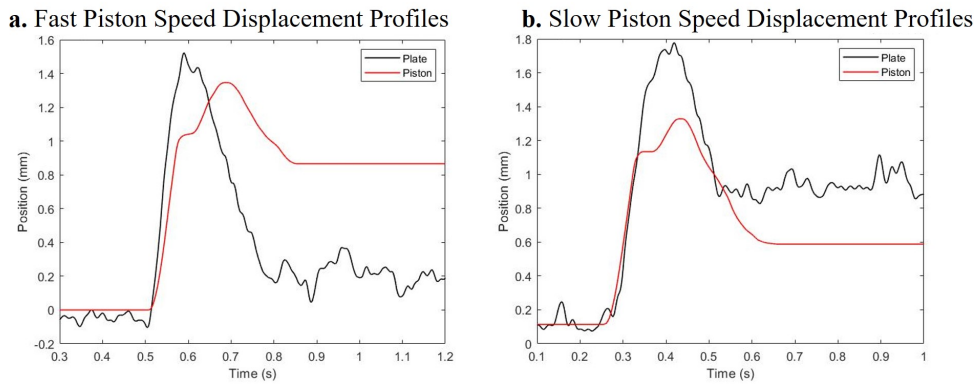


Figure 7.17: Example piston and plate velocity profiles from the MRI-compatible ring vortex phantom. 'Fast' piston speed refers to 2cm/s programmed piston speed and 'slow' piston speed refers to 1.2cm/s programmed piston speed.

### Piston-to-Plate Displacement

Similarly to the previous section, the displacement and average speed of each condition was assessed for characterisation. For these analyses however the plate motion was plotted with respect to the piston motion, rather than the input programmed values. These relationships are presented below.

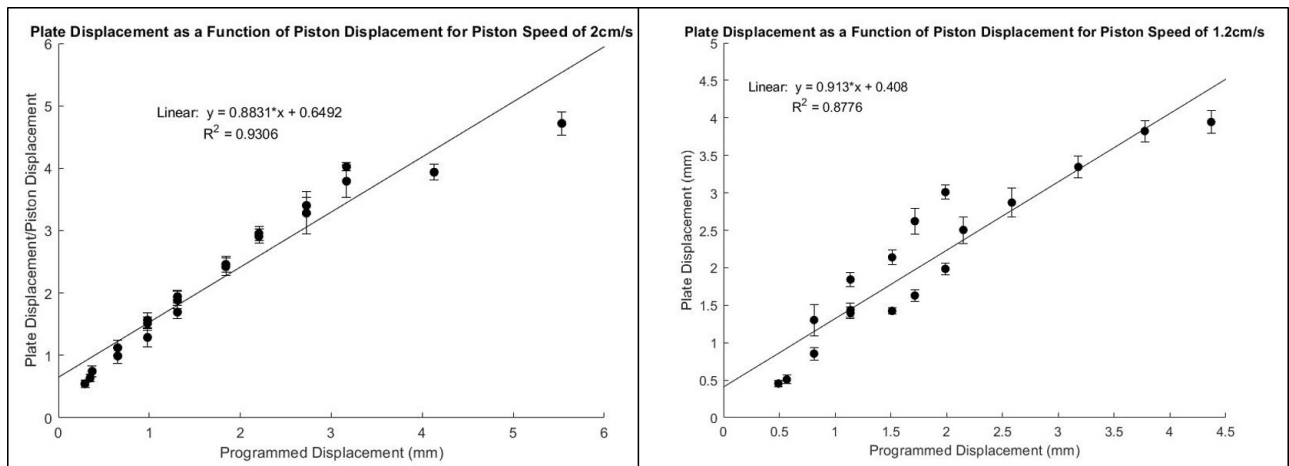


Figure 7.18: Piston and Plate displacements for a range of programmed displacements. Datapoints represent the average of ten impulses and error bars represent 1SD.

Strong linearity was observed between the piston and plate displacements, with  $R^2$  values of 0.93 and 0.88 for the fast and slow piston speeds respectively (Figure 7.18). The linear graph equations allow prediction of the plate motion from the plate displacement under each piston speed.

The anomalous readings were observed again in Graph (b) with the slow piston speed, which distorts the piston-to-plate relationship followed by all other measurements. It is

clear that these anomalies distorted the linear fit and that their removal (Figure 7.19) would result in a stronger correlation, similar to the fast piston data.

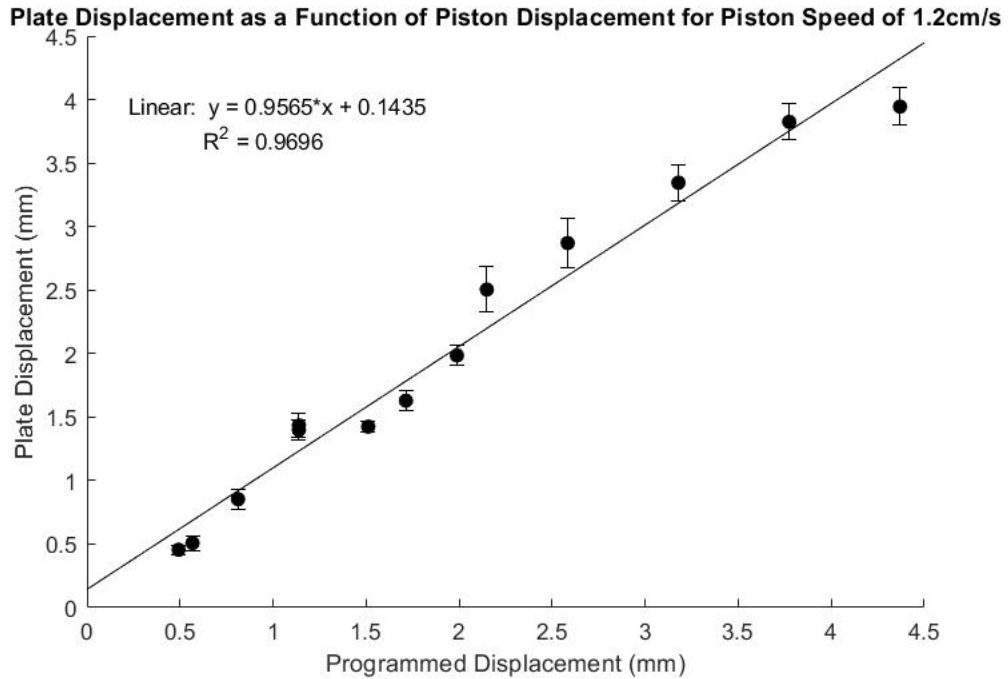


Figure 7.19: Plate displacements for slow piston speeds. Datapoints represent the average of ten impulses and error bars represent 1SD. Anomalies identified in Figure 7.18 have been removed.

Figure 7.19 presents Figure 7.18b without the anomalies. Here the correlation relationship was clearly stronger with a  $R^2$  value of 0.97. All points are within close bounds of the line. The removed anomalous readings were all collected in a single session and differed significantly from other measurements. The reason for these anomalies will be investigated in Section 7.5.6.

### Piston-to-Plate Speed

The second parameter to characterise the piston-to-plate relationship is the average speed. Plate and piston values are plotted in the figure below.

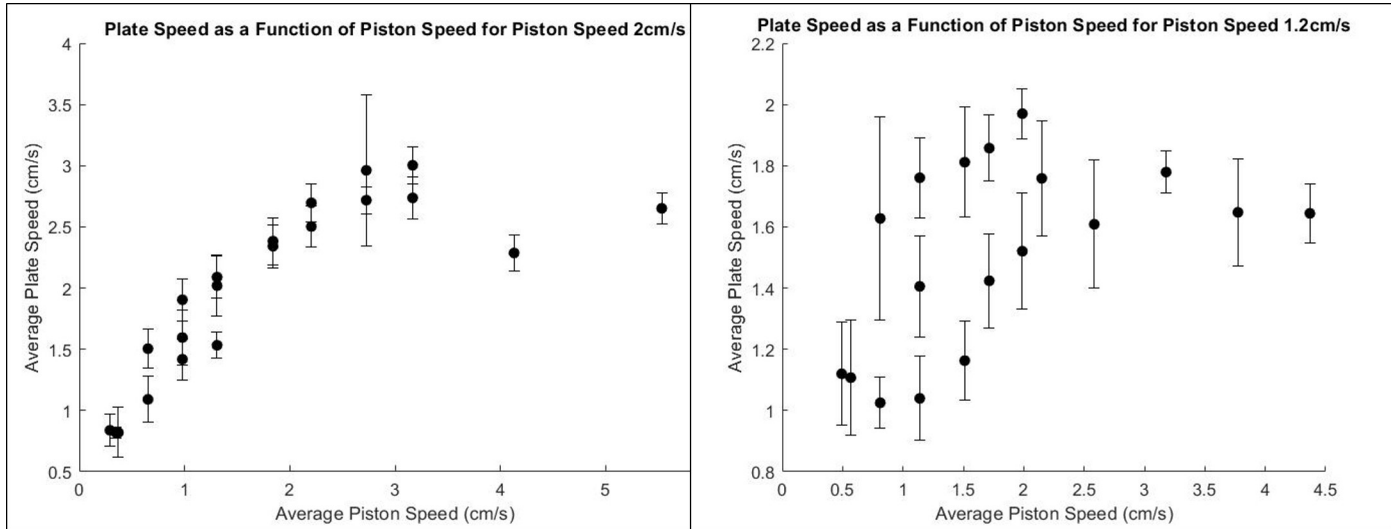


Figure 7.20: Average plate speed as a function of average piston speed on the MRI-compatible ring vortex phantom. Measurements from the fast piston speed (2cm/s programmed speed) and slow piston speed (1.2cm/s programmed speed) are presented.

Overall, strong relationships exist between the piston and plate motion in terms of speed and distance. Graph (a) shows higher reproducibility of the plate speeds when generated by a faster programmed piston speed. The relationship is close to linear but experiences a fall-off in higher speeds. Graph (b) shows a higher variability between plate speeds, with the anomalies also present. Using these graphs (and the tabulated results in Section 7.5.7) the user will be able to predict plate motion, and therefore ring vortex behaviour, from piston motion tracked by the linear encoder.

### 7.5.5 Discussion - Phantom Sensitivity

It has been observed that there was an anomalous set of readings throughout this data analysis. It was noted that these results were all from one experiment, implying a systematic complication for that session. Upon reflection of the raw camera data, it became clear that the position of the plate for this collection varied significantly from its position during other experiments. Experimental protocol positions the plate halfway down the piston barrel, and is repositioned here for each new data collection sequence. However, the videos indicate that the plate was too far towards the hydraulic pipe connection during this collection - clearly a delay occurred during the experiment which pulled its position backwards from leakage. This incorrect positioning with anomalous results indicates a sensitivity in the phantom design which warrants further investigation.

Analysis of unused test data from preliminary collection sessions exposed a similar sensitivity. Data were analysed from two data collection sessions where the plate was towards the pipe-end and towards the tank-end respectively. The displacements and speeds for these plate impulses are plotted alongside the correct-placement values below.

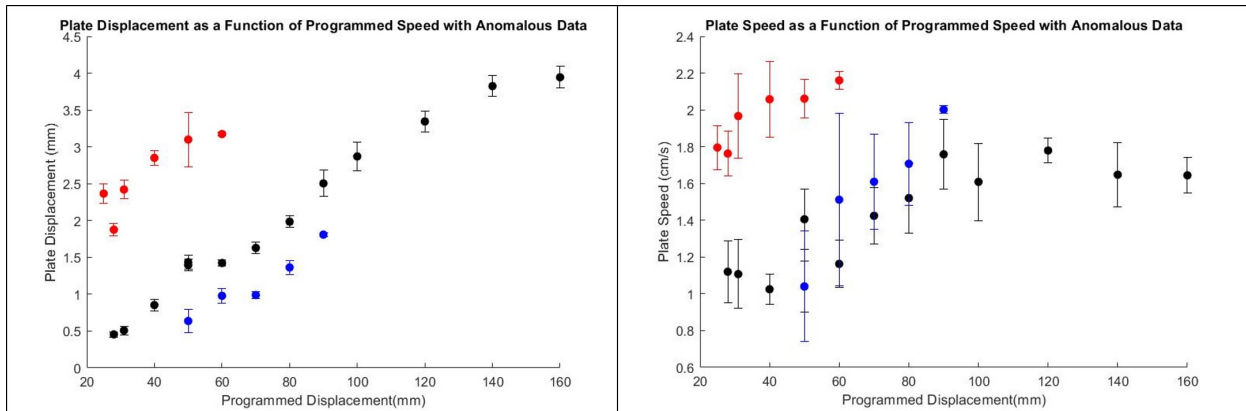


Figure 7.21: Plate displacement and average speed as a function of programmed piston displacement for the ring vortex phantom. Certain abnormal trends are identified through red and blue datapoints. Datapoints represent the average of ten impulses and error bars represent 1SD.

The red datapoints are derived from the experiment where the plate is  $\sim 3.5\text{cm}$  from the pipe-opening. These results show a higher displacement *and* higher average speed than the centrally-placed plates. It is hypothesised that the plate's proximity to the pipe's jet pushes it further and faster than when placed in a more central position. Conversely, blue datapoints represent when the plate was  $\sim 2.5\text{cm}$  from the tank end of the cylinder, further away from the jet. These impulses show the plate not moving far enough and moving with highly variable speed. This is hypothesised to be due to the distance from the pipe jet. Visual analysis of all available datasets indicated that when the plate centre was within **6.5cm** of the pipe connection or within **6.5cm** of the tank, these anomalous readings occurred. A more systematic experiment would be required to confirm these findings and clarify the boundaries but there is a clear zone which will generate plate displacements according to the relationship in Figure 7.19. These boundaries are illustrated in Figure 7.22.

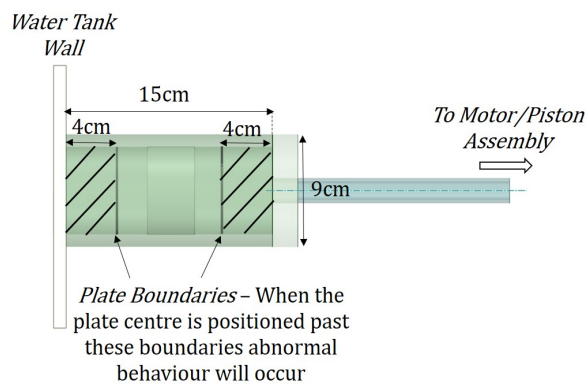


Figure 7.22: Schematic showing the boundaries in the plate cylinder beyond which the plate velocity profile will exhibit abnormal dynamics.

Future experiments described in this chapter took place using the central plate position, and QA on the phantom in the long-term will highlight any anomalous readings due to plate positioning. This clearly demonstrates the need for encoding the plate in every impulse.

### 7.5.6 Discussion - Phantom Functionality

This section has aimed to characterise the MRI-phantom’s dynamic components during use. Reproducibility remained high in both the piston and plate despite the hydraulic system inclusion, with displacements varying by <10% over a range of conditions. Piston speeds vary by less than 10% also, and plate speed varied by up to 20% . These variabilities are higher than expected, but more reproducible plate motion is evident with variability of ~10%, which is more suitable for phantom use. These values are valid when the phantom is assembled correctly with the plate’s centre more than 6.5cm away from either extreme end of the tank cylinder. Characterisation is possible between the programmed conditions, piston behaviour and plate behaviour, using the values listed in the reference table below.

| Prog.Dist | Prog.Speed | Piston.Dist  | Piston.Spnd  | Plate.Dist   | Plate.Spnd   |
|-----------|------------|--------------|--------------|--------------|--------------|
| 0.5mm     | 2cm/s      | 0.29 ± 9.0%  | 0.77 ± 9.9%  | 0.54 ± 11.7% | 0.84 ± 15%   |
| 0.56mm    | 2cm/s      | 0.35 ± 1.6%  | 0.84 ± 8.0%  | 0.64 ± 10.1% | 0.82 ± 5.4%  |
| 0.62mm    | 2cm/s      | 0.37 ± 10%   | 0.81 ± 13.6% | 0.75 ± 11.5% | 0.82 ± 19%   |
| 0.8mm     | 2cm/s      | 0.65 ± 6.5%  | 0.47 ± 5.8%  | 1.06 ± 10.3% | 1.29 ± 17%   |
| 1.0mm     | 2cm/s      | 0.98 ± 6.1%  | 0.62 ± 6.4%  | 1.40 ± 7.2%  | 1.67 ± 12%   |
| 1.2mm     | 2cm/s      | 1.31 ± 1.9%  | 0.77 ± 2.1%  | 1.82 ± 5.3%  | 1.81 ± 7.1%  |
| 1.4mm     | 2cm/s      | 1.84 ± 2.2%  | 0.98 ± 2.9%  | 2.44 ± 3.9%  | 2.36 ± 7.1%  |
| 1.6mm     | 2cm/s      | 2.2 ± 2.7%   | 1.13 ± 5.3%  | 2.93 ± 3.86% | 2.60 ± 6.2%  |
| 1.8mm     | 2cm/s      | 2.73 ± 3.2%  | 1.30 ± 5.7%  | 3.34 ± 2.99% | 2.84 ± 4.1%  |
| 2.0mm     | 2cm/s      | 3.17 ± 5.2%  | 1.46 ± 6.1%  | 3.91 ± 1.67% | 2.87 ± 6.22% |
| 2.4mm     | 2cm/s      | 3.61 ± 2.5%  | 1.61 ± 4.9%  | 3.34 ± 2.22% | 1.78 ± 3.9%  |
| 0.5mm     | 1.2cm/s    | 0.39 ± 12.1% | 0.26 ± 11.1% | 2.36 ± 5.52  | 1.80 ± 6.7%  |
| 0.56mm    | 1.2cm/s    | 0.49 ± 8.1%  | 0.30 ± 10.9% | 1.88 ± 4.65% | 1.76 ± 6.8%  |
| 0.62mm    | 1.2cm/s    | 0.57 ± 3.6%  | 0.35 ± 5.3%  | 2.42 ± 5.31% | 1.97 ± 11.0% |
| 0.8mm     | 1.2cm/s    | 0.81 ± 4.8%  | 0.46 ± 7.6%  | 1.30 ± 3.52  | 1.63 ± 10.1% |
| 1.0mm     | 1.2cm/s    | 1.14 ± 3.3%  | 0.59 ± 3.7%  | 1.24 ± 7.22% | 1.40 ± 5.4%  |
| 1.2mm     | 1.2cm/s    | 1.51 ± 2.1%  | 0.75 ± 4.6%  | 1.56 ± 8.9%  | 1.66 ± 2.26% |
| 1.4mm     | 1.2cm/s    | 1.71 ± 2.6%  | 0.91 ± 7.2%  | 1.81 ± 4.55% | 1.73 ± 5.8%  |
| 1.6mm     | 1.2cm/s    | 1.99 ± 1.8%  | 0.96 ± 6.6%  | 2.19 ± 5.4%  | 1.84 ± 4.13% |
| 1.8mm     | 1.2cm/s    | 2.15 ± 1.6%  | 1.01 ± 5.8%  | 3.28 ± 6.79% | 1.71 ± 2.3%  |
| 2.0mm     | 1.2cm/s    | 2.34 ± 1.5%  | 1.04 ± 4.1%  | 3.79 ± 1.3%  | 2.01 ± 6.3%  |

This table is useful for future experiments if the plate is not tracked in real-time.

In the long-term a MRI-compatible QA tool ought to track the plate motion to high accuracy, but for interim experiments predictions can be made from the piston values when tracked using the encoder in the control room. This table also accentuates the main outcome from this analysis: the MRI-compatible phantom is able to generate reproducible and controllable plate impulses using the stepper motor and hydraulic system prototype. This proves the device functionality and potential for generating reproducible, controllable ring vortices in turn.

## 7.6 Flow Assessment - Characterising the MRI-Phantom Vortices

The revised phantom design displayed plate impulses with high reproducibility and controllability under certain conditions. The next stage of phantom assessment was capturing and examining the ring vortices to ensure their suitability for phantom flows. The inclusion of the hydraulic pipe impacts the jet energy exiting the orifice, and the acceleration also. The vortices being generated would therefore differ from those in the US-phantom and require re-assessment. This was performed in a similar manner to Chapter 3, using maps to present the **stability** and **reproducibility** of the vortices as a function of their orifice size and stroke ratios. This was largely performed at the macro-scale using camera recordings, and a small sample of Laser PIV-visualised vortices was assessed at the micro-scale.

### 7.6.1 Methods - Ring Vortex Analysis

To characterise the ring vortices, a diverse range of generating conditions were required, over a number of orifice sizes, piston/plate speeds and stroke ratios. The conditions under examination are listed in the table below.

| Orifice | Programmed Speed | Stroke Ratios                                 |
|---------|------------------|---|
| 10mm    | 1.2cm/s          | 2.4,2.7,3,3.3,4.9                             |
| 10mm    | 2cm/s            | 2.4,2.7,3,3.3,4.9                             |
| 15mm    | 1.2m/s           | 1.2,1.5,1.8,2.1,2.4,2.7                       |
| 15mm    | 2cm/s            | 1.2, 1.5, 1.8, 2.1, 2.4, 2.7                  |
| 20mm    | 1.2cm/s          | 0.6, 0.75, 0.85, 1.01, 1.14, 1.26, 1.47, 1.71 |
| 20mm    | 2cm/s            | 0.6, 0.75, 0.85, 1.01, 1.14, 1.26, 1.47, 1.71 |

The MRI phantom was set up as described in Section 7.2, with the motor on the floor below the tank height. The pipe was held taut around a corner to minimise energy loss through pipe motion and avoid any kinks or sharp corners. The SONY RX10 camera was mounted at 15cm from the plate to measure the plate profiles at 500fps, and a NIKON D3500 camera mounted at approximately 2m from the phantom wall recording at 60fps

to capture the vortex propagation. Fifteen rings were generated for each configuration, and analyses were performed in MATLAB.

## 7.6.2 Results - Ring Vortex Analysis

A ring vortex ‘map’ was produced when analysing the US-phantom vortices, to characterise the space over which the phantom can generate vortices. This map varied stroke ratio, piston speed and orifice diameter, and plotted stability, initial reproducibility and overall journey reproducibility for each setting. This was repeated for the MRI-phantom in this section, to determine whether the generated vortices remain suitable reference flows for a phantom device. Thresholds of ‘suitability’ were defined according to the stabilities and reproducibilities achieved by the US-phantom in Chapter 3. At the macro-scale, these are as follows:

- **Reproducibility** - Ring speed has a reproducibility (both initially and averaged over the journey) of <10%.
- **Stability** - Rings show a 70% stability lifetime of over 15cm.

### Initial Reproducibility at 5cm

The first macro-parameter under review was the rings’ initial speeds, defined as the speed of the ring at 5cm from the orifice. Variability of this speed (listed as CoV values in Figure 7.23 and in-text) was related to the reproducibility of the plate motion and the reproducibility of the ring generation for this condition. Values for these maps are generated using the MATLAB ring-tracking algorithm used throughout this project.

## Coefficient of Variability in Initial Ring Speed for MRI-Phantom

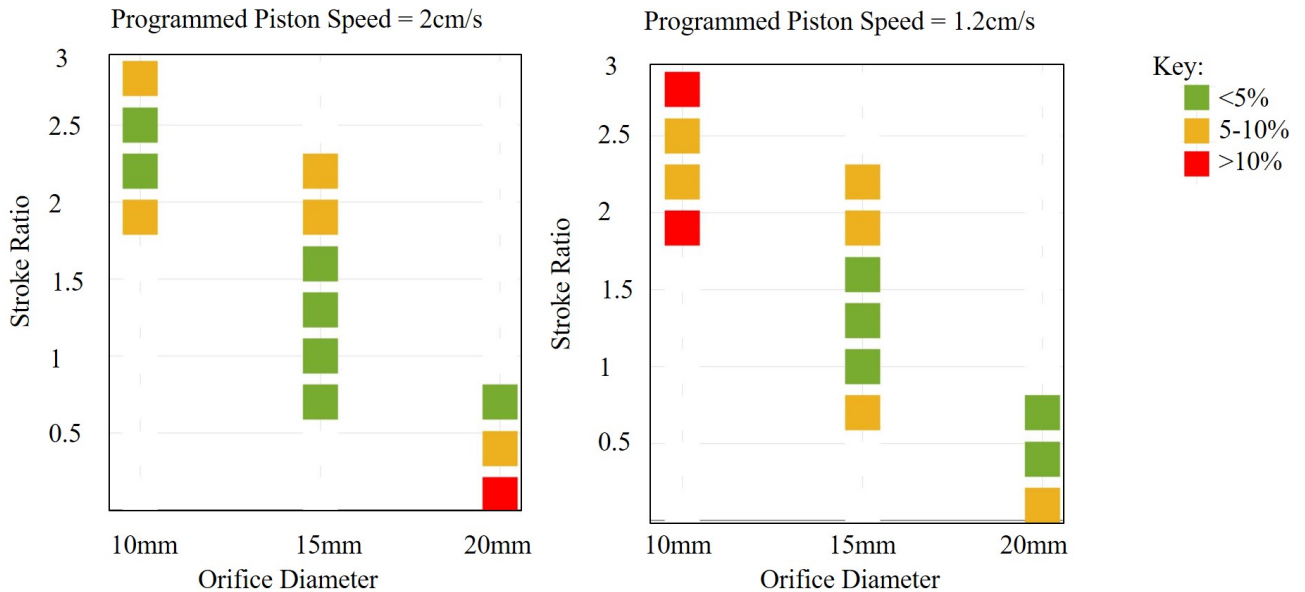


Figure 7.23: 2-D map of MRI-ring vortex initial reproducibility. Stroke ratio, orifice diameter and piston speed are varied. Datapoints represent the CoV in each condition's initial speed, colour coded according to the in-figure key.

Figure 7.23 presents the reproducibility exhibited by the MRI-phantom vortices. The 10mm orifice fails to generate sufficiently reproducible rings using the slow piston speed, with mixed results on the fast piston speed. Larger orifices are successful across both piston speeds. There is high reproducibility evident in these vortices, with 12 vortices exhibiting variability under 5% and reaching the threshold (green datapoints).

### Reproducibility over Journey

The second metric was the reproducibility of the rings' average speeds over their journeys (from 5-20cm from the orifice). This would give an indication of whether the rings' propagation and mechanisms (i.e. diffusion and shedding) hamper the rings' reproducibilities. Values listed are CoV on the map and in-text.

## Coefficient of Variability in Average Ring Speed for MRI-Phantom

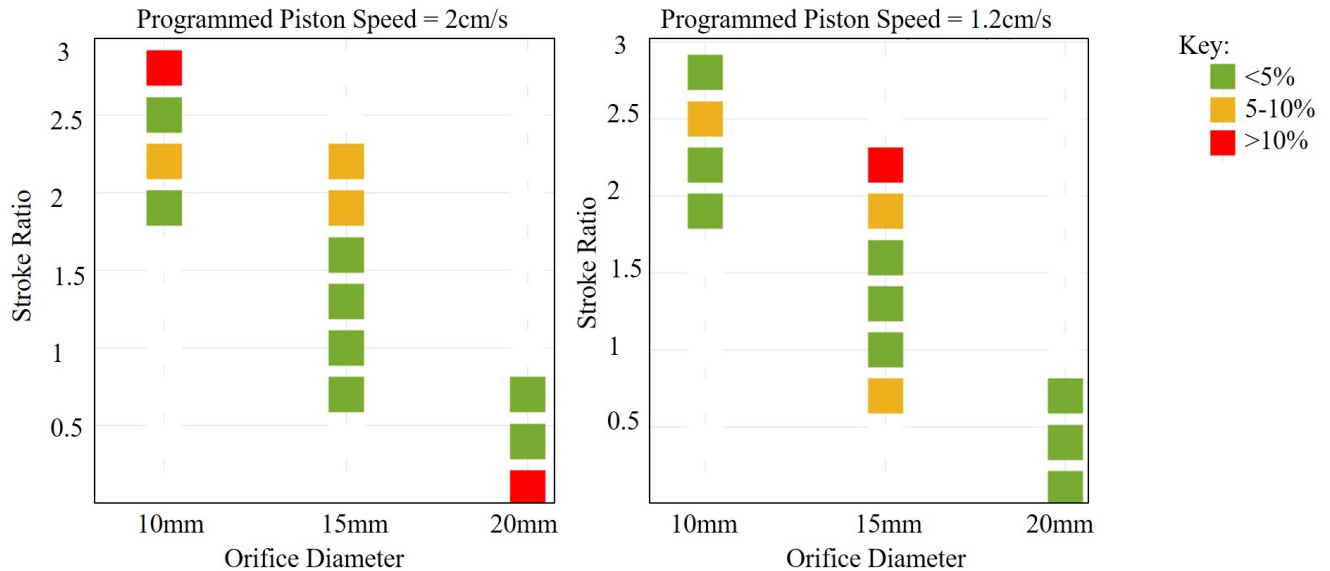


Figure 7.24: 2-D map of MRI-ring vortex journey-long reproducibility. Stroke ratio, orifice diameter and piston speed are varied. Datapoints represent the CoV in each condition's average speed, colour coded according to the in-figure key.

Initial observations indicated a similarity to the starting speed maps, as could be expected. All three orifices are able to generate vortices with sufficient journey-long reproducibility. 17 vortex conditions achieved the threshold reproducibility (green datapoint) in this map.

### Ring Stability

Finally, the ring stability was analysed. This is a key parameter, and was calculated by the rings' deceleration relative to their initial speeds. '70% Stability lifetime' was the stability metric as introduced in Chapter 3, defined as the distance over which the rings travel and lose 30% of their translational speed. A lifetime of >15cm is ideal, as it indicates a stable ring not susceptible to large scale diffusion or shedding. Colour coding in this map correspond to the 70% Stability Lifetime for each generation setting, not the CoV values.

## 70% Stability Lifetime in Ring Speed for MRI-Phantom

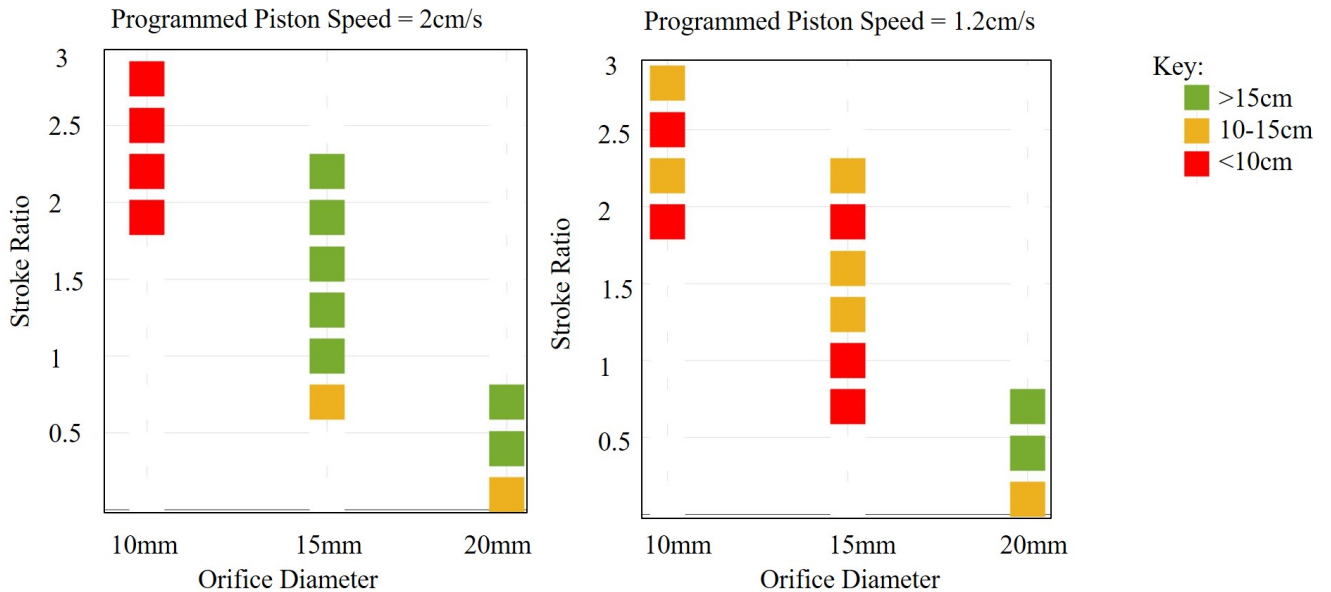


Figure 7.25: 2-D map of MRI-ring vortex stability. Stroke ratio, orifice diameter and piston speed are varied. Datapoints represent the 70% Stability lifetime for each condition, colour-coded according to the in-figure key.

Figure 7.25 shows the varying stability under different conditions. Green datapoints indicate a lifetime of >15cm, yellow a 10-15cm lifetime and red a <10cm lifetime. All measurements start from 5cm from the orifice, i.e. a ring vortex with a lifetime of 14cm will have 70% stability (lose 30% of its speed) as it travels from 5cm to 19cm from the orifice. It is clear that vortices generated from the small 10mm orifice are unstable, as they are all yellow or red. Higher stability vortices are generated by the larger orifices for the faster ring speeds. Nine vortices exhibit stability over the threshold (green datapoints), across the two larger orifices.

### 7.6.3 Discussion I - Suitability of MRI-P ring vortices as reference phantom flow

The rings were assessed at the macro-scale for their suitability on three different metrics: initial speed reproducibility, average speed reproducibility and stability. Visualising these datasets in one plot is helpful for determining the suitability of each generating condition for phantom flow use. Suitable vortices were classed 'green' on all three metrics - high reproducibility both in initial and average speed and high stability. These conditions reach the thresholds achieved by US-phantom vortices at the macro-scale in Chapter 3.

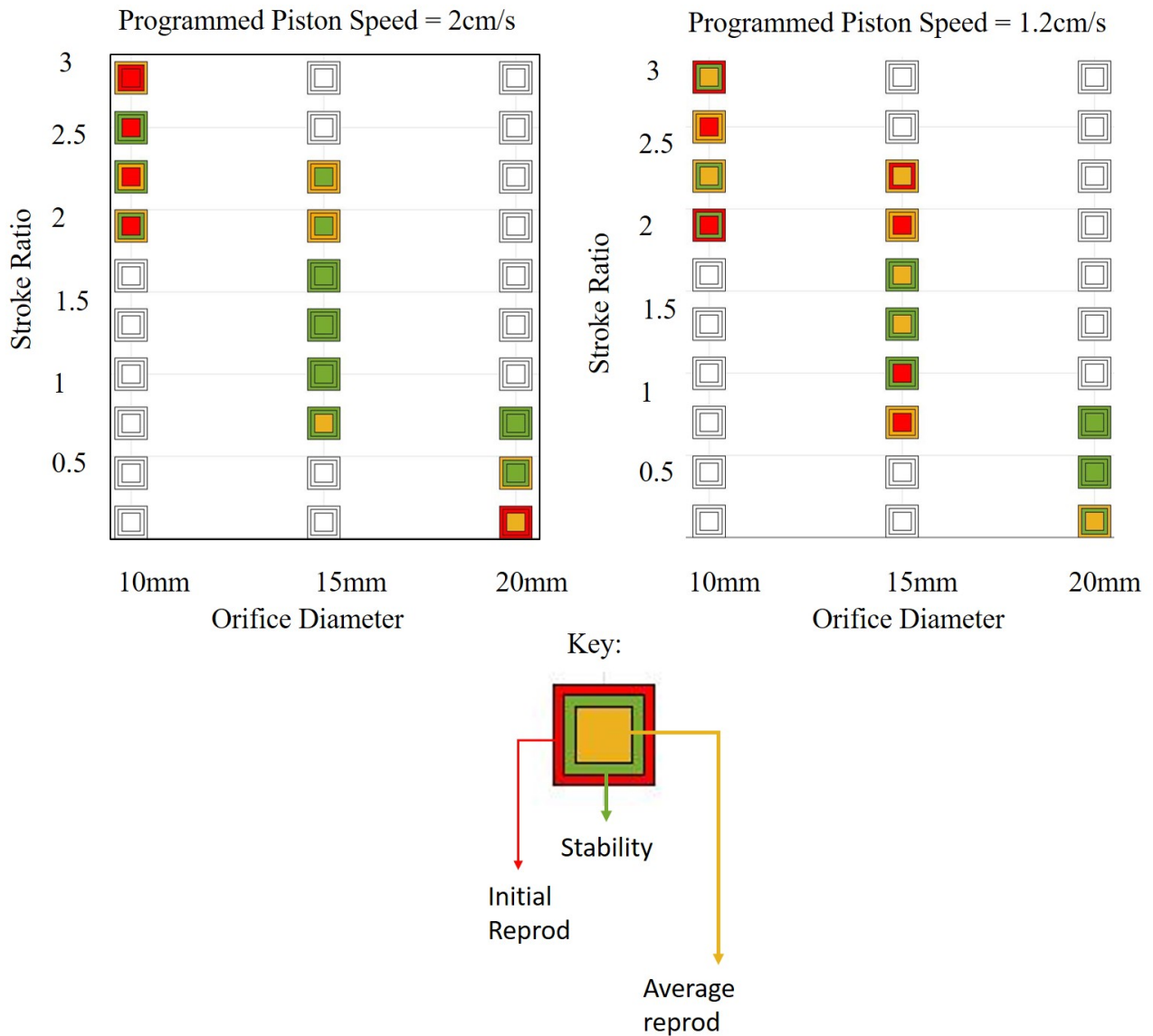


Figure 7.26: 2-D map of MRI-ring vortex phantom flow stability and reproducibility. Stroke ratio, orifice diameter and piston speed are varied. Datapoints represent the stability, initial reproducibility and average reproducibility of each conditions.

This cumulative dataset neatly describes each experimental condition in terms of the key reference flow parameters. There are 5 configurations which fulfil all requirements (all green datapoints). These are listed in the table below as M1-M6. Unfortunately 3/6 of these use the same piston speed and same orifice size, resulting in rings with limited diversity - the speeds range from 6.7-16.7cm/s with limited size variation. To thoroughly assess imaging modalities a more diverse range is needed both in speed and size. To achieve this, the option of high-reproducibility, low-stability rings can be explored. 4D-MRI is a time-resolved technique where the rings will be imaged across their journey.

Other MRA modalities, however, are not time-resolved and will require a single snapshot of the vortices early in their journey. In this scenario only high reproducibility is required to ensure predictable vortices.

The threshold for suitable vortices was therefore expanded to high reproducibility in both initial and average speeds, with no stability requirement. Included configurations are listed in the table below (M6-M11) which results in **11** suitable vortex settings. These are more diverse in size as all three orifices are used. 'Suitable' vortices would be selected based on the end-users requirements.

|     | <b>Orifice</b> | <b>Piston Dist</b> | <b>Piston Spd</b> | <b>Stroke Rat</b> | <b>High R</b> | <b>High S</b> | <b>Av. Spd</b> |
|-----|----------------|--------------------|-------------------|-------------------|---------------|---------------|----------------|
| M1  | 15mm           | 0.8mm              | 2cm/s             | 1.2               | Y             | Y             | 10.13          |
| M2  | 15mm           | 1mm                | 2cm/s             | 1.4               | Y             | Y             | 13.40          |
| M3  | 15mm           | 1.2mm              | 2cm/s             | 1.8               | Y             | Y             | 16.17          |
| M4  | 20mm           | 1.2mm              | 2cm/s             | 0.8               | Y             | Y             | 7.49           |
| M5  | 20mm           | 0.8mm              | 1.2cm/s           | 0.6               | Y             | Y             | 6.70           |
| M6  | 20mm           | 1mm                | 1.2cm/s           | 0.8               | Y             | Y             | 7.08           |
| M7  | 10mm           | 0.56mm             | 2cm/s             | 2.7               | Y             | N             | 16.06          |
| M8  | 15mm           | 0.8mm              | 2cm/s             | 0.8               | Y             | N             | 10.63          |
| M9  | 15mm           | 0.8mm              | 1.2cm/s           | 1.2               | Y             | N             | 10.63          |
| M10 | 15mm           | 1mm                | 1.2cm/s           | 1.4               | Y             | N             | 12.43          |
| M11 | 15mm           | 1.2mm              | 1.2cm/s           | 1.7               | Y             | N             | 13.02          |

#### 7.6.4 Discussion II - Micro-Analysis

In addition to their bulk behaviour as phantom flows, it was important to determine whether the MRI-phantom vortices exhibit similar dynamics as the US-phantom vortices, and whether the addition of the hydraulic component inherently changed their behaviour. This was achieved through comparison to the Kaplanski-Rudi model, as performed in Chapters 5,6. It was shown in Chapter 6 that the US-phantom generates KR vortices when the stroke ratio is 1.2, so by performing the same analysis on MRI-phantom vortices it could be determined whether the rings were still KR-like.

To achieve this, a small sample size of vortices from 4 generation settings were visualised using Laser PIV in the data acquisition described in Section 6.3. To determine whether the MRI-phantom vortices act according to KR the experimental rings were measured for their properties (circulation, ring radius and core radius), and these values were used to generate KR ring vortices of the same properties. Three methods were used to compare the experimental and KR vortices, mirroring those used throughout Chapter 6. These methods were as follows: (a) ring speed and CentVect was compared between the experimental and theoretical rings to find the % difference. (b) Vector plots were compared in terms of both angle and length at each coordinate, and (c) streamline harmonics were calculated for experimental and theoretical rings and compared. Results are listed in the table below.

|    | Orifice | Piston Spd | StrokeR | Speed Diff | CV Diff | Angle | Length | Strmln |
|----|---------|------------|---------|------------|---------|-------|--------|--------|
| M1 | 15mm    | 2cm/s      | 1.2     | 8.5%       | 7.6%    | 91%   | 90%    | 60%    |
| M2 | 15mm    | 1.2cm/s    | 1.4     | 1%         | 14%     | 81%   | 61%    | 23%    |
| M3 | 20mm    | 2cm/s      | 1.8     | 3.5%       | 2.4%    | 89%   | 94%    | 57%    |
| M4 | 20mm    | 1.2cm/s    | 0.8     | 1.8%       | 12.9%   | 86%   | 94%    | 27%    |

Table 7.2: Configurations tested using the MRI-Phantom for their accordance to the Kaplanski-Rudi model, along with results comparing the KR rings to PIV-imaged experimental rings. ‘Diff’ refers to the % difference between experimental and theoretical rings for that parameter.

To determine whether these rings act similarly to the US-phantom rings in terms of analytical model adherence, thresholds from the US-phantom analytical analysis were considered. KR-like vortices in the Chapter 6 analysis were found to meet the following agreement thresholds:

- The analytical speed is within 15% of the experimentally-measured ring speed
- The analytical ring’s CentVect is within 20% of the experimentally-measured CentVect
- Vector agreement stands at >80% in both vector length and vector angle
- Streamline coefficient agreement of >70% is achieved.

The MRI-phantom vortices were assessed for whether they met these conditions in turn. Firstly, parameter agreement between experimental and theoretical vortices was high, with all four configurations agreeing within tolerances for ring speed and CentVect. For vector agreement, M1,3,4 meet the requirements for both vector length and angle, but M2 has poorer vector angle agreement of 61%. Unfortunately no configurations meet the streamline coefficient agreement in this analysis, as at least 70% of analytical coefficients must lie within experimental bounds. The experimental bounds here are adapted in terms of CoV from US-phantom experimental bounds in Chapter 6, due to insufficient data. Therefore, according to the thresholds set in Chapter 6, no MRI-configurations are deemed KR-like within the same tolerances. Their flow-fields and parameters exhibit high agreement but at the fundamental level their streamlines differ. Two configurations show higher KR-like behaviour, with streamline agreement of 60% and 57%, which are **M1** and **M3**. These configurations’ experimental flow fields are indistinguishable from their theoretical counterparts, so can be considered KR-like but with different tolerances than the US-phantom. Interestingly, these KR-behaving vortices are generated using the faster piston speed of 2cm/s. These results suggest that the inclusion of the hydraulic pipe into the phantom design affects the KR-like behaviour but only at a fundamental, quantitative level, the flow fields and parameters remain KR-like to the same degree as the US-phantom vortices.

## 7.7 Conclusion

This chapter has presented the latest generation of the ring vortex phantom - the MRI-compatible prototype. Developing from a proof-of-concept device from previous work, components were manufactured according to a revised design suitable for use in an MRI clinical environment. This design integrated a hydraulic pipe into the phantom, where the motor propels a piston and hydraulically coupled to a plate to generate the ring vortices. This device proved its ability to generate vortices in the laboratory environment.

The device was characterised for its dynamic components, investigating the relationship between the motor pulse sequence, the piston motion and the plate motion to determine the device's controllability and reproducibility. Both the plate and piston overshoot the programmed displacement and drawback to an interim position, arising from the pipe water-weight pushing the piston backwards. Despite this, the piston acceleration, displacement and average speed demonstrated high reproducibility over a range of input conditions. The plate displacement correlated strongly to input conditions generally, allowing for high-confidence estimates of plate motion for each input condition. The relationship between piston and plate was then assessed, with high reproducibility and a strong relationship observed for displacement. Plate speed showed elevated variability on some configurations but a number of conditions demonstrated high reproducibility. These conditions allow for high-confidence predictions of the plate motion when the piston is tracked by the encoder. Under the condition that the plate is placed in the centre portion of the cylinder these relationships remain valid, and a reference table was provided for both displacements and speeds. This would be improved through encoding of the plate in an MRI-compatible manner, providing real-time device QA on the phantom in both piston and plate.

The ring vortices generated by this device were then assessed for their viability as phantom reference flow in terms of reproducibility and stability. Maps were generated with varied piston speed, orifice diameter and stroke ratio. Once analysed together, 5 configurations were deemed suitable for all metrics. Expanding the requirements to high-reproducibility but medium-to-low stability produces 11 suitable configurations for non time-resolved modalities. A reference table was provided of these settings.

Finally, a small sample of vortices were analysed at the micro-scale using Laser PIV datasets. The rings were found to act according to the Kaplanski-Rudi model in terms of parameter agreement and vector flow-field agreement for three conditions, according to agreement achieved by US-phantom vortices. Their streamlines differed from the theoretical rings so require lower thresholds to be considered KR-like. An agreement of 60% in streamline coefficient would result in two MRI-phantom conditions whose vortices are indistinguishable from their analytical counterparts. In summary, a prototype device has been manufactured that is suitable for use in MRI clinical environments. This phantom generates ring vortices suitable for application as a reference flow, and under certain circumstances behaves according to the KR model. Future work using this device is detailed further in Chapter 8.

# Chapter 8

## Future Work and Thesis Conclusions

### 8.1 Review of the Thesis

This thesis has presented the latest phase of the development of the ring vortex complex flow phantom. This project started with a prototype device which functioned correctly in a research environment and was able to generate ring vortices which were reproducible and stable at a macro-scale. This device had undergone preliminary visualisation through ultrasound and Laser PIV but a definitive characterisation of the flow profile was not achieved. This project therefore had two primary objectives to advance the device: the *characterisation* of the phantom and its flows, and the *optimisation and expansion* of the phantom device. These objectives has been fulfilled through a range of methods.

Firstly, the ring vortices generated by the device were empirically characterised using the  $PIV_{19}$  datasets on the Unit-0 phantom. Analysis was performed at the micro-scale to establish the stability and reproducibility that the phantom was able to achieve. Results indicated that the range of imaged vortices achieved different levels, calling into question the suitability of less stable vortices.

The phantom was then optimised in Chapter 3 by upgrading the dynamic piston component, optimising the motor pulse sequences and eliminating oscillatory motion. This was followed by the macro-scale assessment of a wide range of ring vortices, to characterise the optimised phantom reference flows. Suitable stability and reproducibility was evidenced in these analyses, with a number of conditions able to reproduce the stability and reproducibility of the  $PIV_{19}$  vortices. This defined Unit-1 of the phantom.

The phantom was then expanded through an instrumentation pack. The aim of this exercise was to increase confidence in the device through integrating real-time QA feedback on device and flow functionality. Three components collected key information during phantom use, allowing for immediate identification of any anomalous behaviour. Flow phantom QA is integrated into many phantoms in the literature, and this tool elevates the ring vortex phantom above most options by providing real-time information and validating the use of experimental ground-truth datasets for flow characterisation.

This was followed by an analytical characterisation of the experimental vortices in Chapter 5. This characterisation aimed to explore the potential of using analytical models

to characterise the flow in place of, or to supplement, the more limited experimental datasets. This potential was explored through comparing the experimental ring vortices to analytical models from the literature. Results were positive with three configurations acting as KR-like vortices under set thresholds, but slower and faster rings acted otherwise. This proved the potential of analytical model use under certain circumstances but required a larger breadth of experimental data for confirmation.

These experimental data were collected in Chapter 6, where a Laser PIV experiment took place to characterise the optimised vortices first explored in Chapter 3. These vortices were analysed for their stability and reproducibility for phantom flow use, and for their accordance to the Kaplanski-Rudi model. Stability and reproducibility remained high. A number of vortices were classed as KR-like using the thresholds established in Chapter 5. A connection was found between stroke ratio and KR-like behaviour, implying that the higher stroke ratio rings were acting as non KR ring vortices.

Finally, the ultrasound phantom was expanded to be MRI-compatible and enable visualisation through MRI-based imaging modalities. Chapter 7 presented the design concepts and manufacture of a hydraulically coupled ring vortex phantom design. Similarly to Chapter 3, this phantom was assessed for its functionality in both device and generated flows. The device's dynamic components demonstrated reproducible and controllable motion, with the plate showing some sensitivity related to position. Vortices generated by this device were analysed at the macro-scale for their stability and reproducibility, with a number of suitable configurations identified, using the thresholds imposed during the US-phantom development. Finally, evidence of KR-like behaviour was found in two PIV-imaged vortex conditions. This chapter proved the concept and proposed a design concept for the MRI-compatible phantom, from which a multimodal concept could be manufactured.

This thesis' main contributions towards ring vortex phantom development is the increase in *confidence* in the ring vortex and the device, achieved largely thorough experimental and analytical characterisation of its flow fields under a wide range of generating conditions. The US-phantom is ready for more widespread imaging of its reference flows in research and clinical settings to demonstrate its suitability. The MRI-phantom aptly demonstrates the robustness of the ring vortex to varying generating conditions, and shows potential for a future multimodal phantom.

## 8.2 Future Work - Phantom Refinement

The phantom is currently laboratory-suitable, and not refined for commercial use. There are a number of improvements that are required before the device is ready for commercialisation. Recommendations for these improvements are listed below.

### 8.2.1 US-Phantom Redesign

The phantom device has proven to be robust and suitable for long-term use, showing little degradation over the project and highly predictable, characterised dynamics. The

device is, however, limited by its current motor, restricting the range of vortices that can be generated. IPEM 102 [156], the clinically-used IPEM recommendations for clinical QA of ultrasound equipment, requires speeds of 50cm/s to be used (typically through string phantoms) to test clinical systems. The US-phantom currently generates rings up to 31cm/s but these rings are unstable. A future, more clinically viable device would therefore generate rings which propagate at 50cm/s and exhibit high stability. Intra-ring velocities are higher than bulk speeds so can reach this requirement, but a bulk speed of 50cm/s would be beneficial for assessment of clinical ultrasound-based Doppler modalities.

Faster rings could be achieved through faster jet propulsion through the orifice. Whilst a more powerful motor capable of higher speeds could be implemented, this could cause skipping or overheating during longer experiments. A design change in the piston/piston cylinder components would increase jet propulsion speed (and therefore ring speed) without changing the motor pulse sequence. Increasing the jet speed would generate faster rings from the larger orifices, which have historically generated higher stability rings. Further characterisation would ensure the increase in stroke ratio doesn't decrease ring vortex stability or reproducibility.

Other basic device improvements would entail more orifice sizes (e.g. 12.5mm and 17.5mm diameter options) to increase the diversity of rings, particularly as those from the 10mm orifice were often unstable. Finally, the motor should be attached directly to the phantom in such a way as to minimise any oscillation during propulsion.

## 8.2.2 Phantom Commercialisation

In addition to the above recommendations which would directly impact the flow profile, other changes would be made to commercialise the phantom, readying it for more widespread clinical use and improving its accessibility.

Currently the phantom is controlled by a user selecting parameters in Arduino software, sending the code to the Arduino board where a push-button starts the sequencing. In the final product, a more streamlined procedure would be implemented where the user can select what rings are required, how many, at what time delay and the phantom would start. To increase usability this should be on a non-coding software interface such as a touchscreen (achievable with Arduino compatibility) or a virtual UI in a custom software which is provided with the phantom. Arduino is free and open-source but not currently used widely in clinic.

The assembly of the phantom is straightforward, with the most difficult task the levelling of the device to ensure good motor-to-piston alignment, as this has significant effects on the ring vortices. The phantom currently remains on a table for all experiments but requires re-alignment (taking <3 minutes) before experiments. The threaded feet are useful for this, but misalignment can occur. A revised method to ensure correct alignment is needed, potentially through the addition of spirit levels onto the motor and piston components. The phantom has manufactured with a custom carry-case which can be wheeled for good portability, and no issues have arisen from this when transporting the phantom for experiments.

Finally, the phantom currently uses water as its fluid. Other phantoms, particularly

those for use with ultrasound, use blood-mimicking fluid (such as an Orgasol/water solution) to mimic the viscosity of blood and more closely mimic physiological flows. This phantom doesn't aim to mimic any particular flow, and the vortices travel well in water, but there is certainly potential to expand to include BMF as an option to align with clinical QA standards. In this scenario the rings would require re-classification at the macro and micro-level due to the change in viscosity. The Kaplanski-Rudi model uses viscosity as a variable so this could be changed and the rings' adherence to its equations assessed.

More specific commercialisation of the phantom device would vary depending on the intended end-user. The phantom has a range of potential uses, in both fluid dynamics research to clinical practice. It is likely that each user would demand specific designs, such as device size, range of vortex speed and materials used (such as the MRI-phantom). This work has demonstrated that the ring vortex is suitable as a phantom reference flow at the micro-scale, therefore the design can now be refined for each end-user as required, without doubt cast on the device's feasibility.

### 8.2.3 Instrumentation Pack Commercialisation

A separate focal point for commercialisation is the instrumentation pack developed throughout Chapter 4. Infrastructure to combine the phantom and QA-performing components was manufactured using rapid prototype 3D-printing, intended for short-term laboratory use. These components are not robust enough to undergo extensive transport and use, thus would require replacement with CNC-machined components, similar to the core phantom components.

The linear encoder is paramount for phantom characterisation and confidence in its continued functionality, and is certainly the most important component of the instrumentation pack. It is a commercial product and costs  $\sim$ £400 at the time of writing, providing detailed information regarding the piston motion. Motors with built-in encoding are available but they wouldn't necessarily reflect the piston motion with high accuracy, so direct encoding of the piston is recommended. The encoder works through MATLAB (requiring a paid subscription) but control could be sought through Python or LabVIEW. This also extends to the user interface which is currently in MATLAB. A limitation of the encoder is that it requires a high-spec laptop to achieve a high sampling frequency, which could limit accessibility once commercialised.

The laser-photodiode component is comprised of a custom-built photodiode circuit and high-power Class 3D pencil lasers. Refinement of these would entail swapping the pencil lasers to lower-power laser diodes, improving the safety and reducing the current need for filters. Embedding the laser diodes and photodiodes in the tank wall as permanent features would be more efficient for phantom setup with minimal inter-experiment variability from user-performed setup. A concern for this component is the electronics' close proximity to the open water tank, so fully enclosing the diodes in the wall would be recommended, or closing part of the water tank.

Finally, the Doppler probe has proven useful for this application, but could certainly be refined for use. The probe contains a transducer which would ideally be embedded into the tank wall and subsequently powered and controlled through the Arduino board.

This would be more space-efficient and integrate it into the core phantom components. The probe beam would require high-precision characterisation of its beam width and focal distance.

#### 8.2.4 MRI-Compatible Phantom Improvements

There are a number of recommended improvements for the MRI-compatible ring vortex phantom, as the current device was manufactured in-laboratory. Particular changes would be:

- **Coupler Connections** - The current connectors are custom-manufactured from two components. Custom-designed couplers would be simple to manufacture using the current design. Currently threads are used to attach the pipe but a simpler, more accessible design would involve clips, similar to hose clamps. High-strength and watertight designs would be required to withstand the pressures present within the pipe.
- **Piston/Piston Cylinder**- The current piston used is the non O-ring piston, adapted from the US-compatible phantom. This is suitable as it experiences minimal friction with the piston cylinder interior wall and responds to the motor pulse sequence. However, neither the piston cylinder nor the piston are fully watertight, meaning that as it is placed on a higher surface, air enters the system. For long-term use the motor would be placed on an elevated surface, but this would require a fully air- and water-tight design for the piston cylinder.
- **Motor Stand**- Finally, the motor stand requires an in-built weight. The Perspex components are lightweight and suitable for transportation, but tension in the pipe and thrust from the motor required that weights (5-10kg) were placed on the stand to stop it moving. A weighted base would eliminate this issue.

Beyond these recommendations, the current proof-of-concept system works effectively and is able to generate reproducible vortices in an MRI-compatible setup. To improve characterisation of the device, a form of QA would be beneficial, particularly given the increased possibility of incorrect setup. A design incorporating fibre optic cables into the phantom was proposed throughout this project, using a control room-located circuit with fibre optic cables to track the plate displacement and ring speed, mirroring the linear encoder and laser-photodiode array from the US-phantom QA tool. This was tested in laboratory and found to function well, but refinement is required.

### 8.3 Future Work - Imaging

With the scientific basis of the phantom well-established, the next key component of its development is achieved through imaging. The phantom has been visualised using camera and Laser PIV methods in a laboratory setting but its true purpose is to image and assess clinical imaging modalities. Experiments performed in varied clinical environments will

prove the phantom’s usefulness and viability on traditional, well-trusted flow imaging techniques. This will be furthered through imaging state-of-the-art technologies to assess their quantitative abilities.

### 8.3.1 Clinical Ultrasound Experiments

To test the phantom on well-established clinical imaging modalities, preliminary experiments were performed with clinical colleagues in Sheffield Teaching Hospitals on a range of ultrasound techniques. The phantom was imaged using a GE LOGIQ-E9 scanner used regularly in Royal Hallamshire Hospital. A linear transducer (2D 9L-D, bandwidth 2-8MHz, 5cm length) was selected for its frequent application in vascular work. The probe was oriented along the vortices’ paths and suspended over the water tank with the elements submerged. A polyurethane acoustic absorber was placed angled on the base of the tank to reduce reverberation in the image.

B-mode was performed as a cine loop to visualise the rings’ cross sections as they propagated across the imaging domain. Ten rings of each configuration for the Unit-0 phantom were imaged. The vortices were visualised well, with the vortex atmosphere and cores clearly visible on most instances. An example dataset is presented below, for both B-mode and PW Doppler.

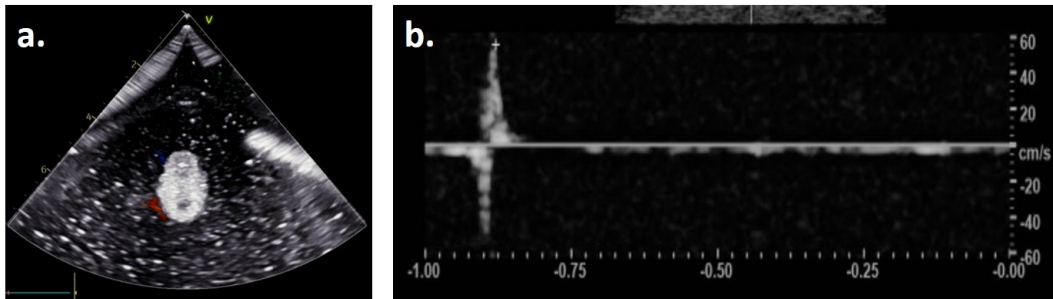


Figure 8.1: a. Example scan of the ring vortex using B-mode ultrasound with CDI to visualise the rings, saved as a cine loop. b. Example PW Doppler trace, measuring radial velocities across the centre of the top core.

B-Mode scans were used to calculate bulk ring speed, through calculating the inter-frame ring displacement and dividing by the frame time duration. PW Doppler can be used for a more in-depth analysis of the intra-ring micro-flow velocities. To achieve this, a 1mm sample gate was initiated on the scanner and moved incrementally down the ring. The ring propagates through the domain and generates a trace of the detected axial velocities. This can be observed in the data below, where PIV and PW Doppler traces are compared. As the domain is located at the vortex core, a clear bi-phasic signature is produced, as axial velocities are both parallel and anti-parallel to the beam. Outside of the core, a monophasic signature is observed for both PIV and PW Doppler.

This initial agreement between the probe and phantom is promising, as it indicates the ability of the ring vortex to be imaged by Doppler ultrasound, giving a basis for

future modality assessment. This work is ongoing and represents the first of a number of proposed experiments which will clarify the phantom’s viability for regular clinical QA practice. A preliminary conference poster is presented in Appendix C.

### 8.3.2 Proposed Experiments

These ultrasound experiments produced interesting and positive results, with the scanner able to visualise vortical behaviour to the micro-scale. Further experiments will comprise the next, and final, pre-commercialisation stage of the ring vortex phantom development. For clinical imaging, imaging the phantom flows using 2D PC MRA and standard 4D-MRI protocol would establish its usefulness in MRI QA protocols. Extension to pre-clinical, state of the art technologies such as VFI, speckle tracking and pre-clinical versions of these techniques (e.g. HFR VFI, high resolution 4D-MRI) would be possible after the assessment of clinical modalities.

These imaging experiments are of top priority in the next stage of phantom development - significant advancements have been achieved in phantom development and refinement and there is heightened confidence with the limited amount of current users. Expanding the roster of collaborations will widen its potential, identify limitations, and increase the phantom’s presence in the field. Prioritisation should be given to its application on various techniques, to highlight its multimodal capabilities.

## 8.4 Thesis Conclusion

This thesis presents the further development of the ring vortex complex flow phantom, compatible with ultrasound and MRI quantitative flow imaging technologies. Characterisation has been performed on the device and its generating flow profiles to ensure high confidence in the device from new users. The phantom generates ring vortices which behave according to the analytically-derived Kaplanski-Rudi viscous vortex ring model, and demonstrates potential for integration of analytical ring vortex visualisations into the phantom’s use. This will provide high-confidence ground-truth datasets which are refined to each individual flow using real-time QA measurements. An MRI-compatible version of this device has been proposed to enable imaging in an MRI environment.

The ring vortex phantom functions well in the laboratory environment and has proven its viability as a clinical device in ultrasound experiments. The true core of this thesis was improving confidence in the phantom’s viability as a test object. Unit-0 was functioning correctly at the commencement of this project and was proposed as reliable ring vortex generator, but understanding of its mechanics and confidence in the ring vortices was low. This project has therefore strove to improve confidence, with the importance of the piston/plate behaviour clarified. The ring vortex behaviour is *directly* related to the piston velocity profile, so by tracking the piston (or plate) profile in real-time, trust in the flow profile is improved.

This will form a central concept in further phantom development, and should be the primary focus in any re-designs or further development. Interest has been shown

from external parties for involvement in its future development, from both clinical and industrial connections. The ring vortex phantom offers a novel approach to quantitative flow imaging QA and could make a noted impact on clinical QA procedures in the future.

# References

1. *British Heart Foundation UK Factsheet* <https://www.bhf.org.uk/-/media/files/for-professionals/research/heart-statistics/bhf-cvd-statistics-uk-factsheet.pdf?> Accessed: 26-04-23.
2. *WHO Cardiovascular Disease Factsheet* [https://www.who.int/news-room/factsheets/detail/cardiovascular-diseases-\(cvds\)](https://www.who.int/news-room/factsheets/detail/cardiovascular-diseases-(cvds)). Accessed: 26-04-23.
3. Schuijf, J., Shaw, L., Wijns, W., Lamb, H., de Roos A Poldermans, D., van der Wall, E. & Bax, J. Cardiac imaging in coronary artery disease: differing modalities. *Heart (British Cardiac Society)* **91**, 1110–1117 (2005).
4. Rehman, R., Yelamanchili, V. & Makaryus, A. Cardiac Imaging (2022).
5. *RSNA Quantitative Imaging Biomarker Alliance Statement* <https://www.rsna.org/research/quantitative-imaging-biomarkers-alliance>. Accessed: 20-04-23.
6. Wang, Y. & Ng, C. The impact of quantitative imaging in medicine and surgery: Charting our course for the future. *Quant Imaging Med Surg* **1**, 1–3 (2011).
7. Ghekiere, O., Salgado, R., Buls, N., Leiner, T., Mancini, I., Vanhoenacker, P., Dendale, P. & Nchimi, A. Image quality in coronary CT angiography: challenges and technical solutions. *Br J Radiol.* **90** (1072 2017).
8. Tavakol, M., Ashraf, S. & Brener, S. Risks and complications of coronary angiography: a comprehensive review. *Glob J Health Sci.* **4**, 65–93 (2012).
9. Rauf, A., Denny, S., Pierres, F., Jackson, A., Papamichail, N., Pavlidis, A. & Al-fakih, K. Current diagnostic yield of invasive coronary angiography at a district general hospital. *British Journal of Cardiology* **24** (2017).
10. Prevrhal, S., Forsythe, C., Harnish, R., Saeed, M. & Yeh, B. CT angiographic measurement of vascular blood flow velocity by using projection data. *Glob J Health Sci.* **261**, 923–929 (2011).
11. Meola, M., Ibeas, J., Lasalle, G. & Petrucci, I. Basics for performing a high-quality color Doppler sonography of the vascular access. *J Vasc Access* **21**, 18–31 (2021).
12. Cardullo, P. Continuous-Wave Doppler Ultrasound. *Journal for Vascular Ultrasound* **35**, 201–207 (2011).
13. Deane, C., Nicolaidis, K., Rizzo, G., Hecher, K. & Ximenes, R. *Doppler in Obstetrics* (The Fetal Medicine Foundation, 2002).

14. Carroll, D., Howden, W. & Murphy, A. Spectral Doppler (Ultrasound). *Radiope-dia.org*. Accessed 12-10-22 (2023).
15. Anavekar, N. & Oh, J. Doppler Echocardiography: A Contemporary Review. *Journal of Cardiology* **54**, 347–358 (2009).
16. Terslev, L., Diamantopoulous, A., Dohn, U., Schmidt, W. & Torp-Pedersen, S. Settings and artefacts relevant for Doppler ultrasound in large vessel vasculitis. *Arthritis Research Therapy* **19** (2017).
17. Evans, D., Jensen, J. & Nielsen, M. Ultrasonic colour Doppler imaging. *Interface focus*. **1**, 490–502 (2011).
18. Andranikian, A. Validating Color Doppler Ultrasound Performance Via A Quanti-tative Comparison with Particle Image Velocimetry. *Proceedings* **1** (2016).
19. Kruskal, J., Newman, P., Sammons, L. & Kane, R. Optimizing Doppler and color flow US: application to hepatic sonography. *Radiographics* **24**, 657–675 (2004).
20. Jensen, J., Nikolov, S., Yu, A. & Garcia, D. Ultrasound Vector Flow Imaging-Part I: Sequential Systems. *IEEE Trans Ultrason Ferroelectr Freq Control*. **63**, 1704–1721 (2016).
21. Baun, J. Emerging Technology: Ultrasound Vector Flow Imaging—A Novel Ap-proach to Arterial Hemodynamic Quantification. *Journal of Diagnostic Medical Sonography* **37**, 599–606 (2021).
22. Goddi, A., Fanizza, M., Bortolotto, C., Raciti, M., Fiorina, I., He, X., Du, Y. & Calliada, F. Vector flow imaging techniques: An innovative ultrasonographic technique for the study of blood flow. *J Clin Ultrasound* **45**, 582–588 (2017).
23. Hansen, K., Udesen, J. & Thomsen, C. In Vivo validation of a blood vector velocity estimator with MR angiography. *IEEE Transactions on ultrasonics, ferroelectrics and frequency control* **56**, 91–100 (2009).
24. Swillens, A., Degroote, J. & Verendeels, J. A simulation environment for validating ultrasonic blood flow and vessel wall imaging based on fluid structure interaction simulations. *Medical Physics* **37**, 4318–5330 (2010).
25. Udesen, J., Nielsen, M. & Nielsen, K. Examples of In Vivo blood vector velocity estimation. *Ultrasound in Medicine and Biology* **33**, 541–548 (2007).
26. Hur, B., Lee, J., Chu, A., Kim, S., Han, J. & Choi, B. UltraFast Doppler ultra-sonography for hepatic vessels of liver recipients: preliminary experiences. *Ultra-sonography* **34**, 58–65 (2015).
27. Hansen, K., Møller-Sørensen, H. & Pedersen, M. First report on intraoperative vector flow imaging of the heart among patients with healthy and diseased aortic valves. *Ultrasonics* **56**, 243–250 (2015).
28. Zhou, M., Yu, Y., Chen, R., Liu, X., Hu, Y., Ma, Z., Gao, L., Jan, W. & Wang, L. Wall shear stress and its role in atherosclerosis. *Frontiers in Cardiovascular Medicine* **10** (2023).

29. Qiu, Y., Yang, D., Zhang, Q., Chen, K., Yi, D. & Wang, W. V Flow technology in measurement of wall shear stress of common carotid arteries in healthy adults: Feasibility and normal values. *Clinical Hemorheology and Microcirculation* **74**, 453–462 (2020).
30. Qiu, Y., Cheng, J., Zhang, Q., Yang, D., Zuo, D., Mao, F., Liu, L., Dong, Y., Cao, S. & Wang, W. Clinical Application of High-Frame-Rate Vector Flow Imaging in Evaluation of Carotid Atherosclerotic Stenosis. *Diagnostics* **13**, 519 (2023).
31. Haniel, J., Yiu, B., Chee, A., Huebner, R. & Yu, A. Efficacy of ultrasound vector flow imaging in tracking omnidirectional pulsatile flow. *Medical Physics* **50**, 1699–1714 (2023).
32. Yiu, B. & Yu, A. Spiral Flow Phantom for Ultrasound Flow Imaging Experimentation. *IEEE Trans Ultrason Ferroelectr Freq Control* **64**, 1840–1848 (2017).
33. Currie, S., Hoggard, N., Craven, I., Hadjivassiliou, M. & Wilkinson, I. Understanding MRI: basic MR physics for physicians. *Postgrad Med J* **89**, 209–23 (2013).
34. Grover, V., Tognarelli, J., Crossey, M., Cox, I., Taylor-Robinson, S. & McPhail, M. Magnetic Resonance Imaging: Principles and Techniques: Lessons for Clinicians. *J Clin Exp Hepatol* **5**, 246–255 (2015).
35. Seeger, L. Physical Principles of Magnetic Resonance Imaging. *Clinical Orthopaedics and Related Research* **244**, 7–16 (1989).
36. McDonnell, C., Herfkens, R., Norbash, A. & Rubin, G. Magnetic resonance imaging and measurement of blood flow. *West J Med.* **160**, 137–242 (1989).
37. Willinek, W., Born, M., Simon, B., Tschampa, H., Krautmacher, C., Gieseke, J., Urbach, H., Textor, H. & Schild, H. Time-of-flight MR angiography: comparison of 3.0-T imaging and 1.5-T imaging—initial experience. *Radiology* **229**, 913–920 (2003).
38. Edelman, R. & Koktzoglou, I. Non-Contrast MR Angiography: An Update. *Journal of Magnetic Resonance Imaging* **49**, 355–373 (2019).
39. Mostbeck, G., Caputo, G. & Higgins, C. MR measurement of blood flow in the cardiovascular system. *American Journal of Roentgenology* **159**, 453–461 (1992).
40. Stankovic, Z., Allen, B., Garcia, J., Jarvis, K. & Markl, M. 4D flow imaging with MRI. *Cardiovasc Diagn Ther* **4**, 173–192 (2014).
41. Ibrahim, M., Hazhirkarzar, B. & Dublin, A. Gadolinium Magnetic Resonance Imaging. *Treasure Island (FL): StatPearls Publishing;* (2022).
42. Costelloe, C., Amini, B. & Madewell, J. Risks and Benefits of Gadolinium-Based Contrast-Enhanced MRI. *Seminars in Ultrasound, CT and MRI* **41**, 170–182 (2020).
43. Wymer, D., Patel, K., Burke, W. & Bhatia, V. Phase-Contrast MRI: Physics, Techniques, and Clinical Applications. *RadioGraphics* **40**, 122–140 (2020).
44. Ebberts, T. Flow Imaging: Cardiac Applications of 3D Cine Phase-Contrast MRI. *Current Cardiovascular Imaging Reports* **4**, 127–133 (2020).

45. Dyverfeldt, P., Bissell, M. & Barker, A. 4D flow cardiovascular magnetic resonance consensus statement. *Cardiovasc Magn Reson* **17**, 72 (2015).
46. Juffermans, J., van Assen, H., te Kiefte, B., Ramaekers, M., van der Palen, R., van den Boogaard, P., Adriaans, B., Wildberger, J., Dekkers, I., Scholte, A., Schalla, S., Lamb, H. & Westenberg, J. 4D Flow MRI in Ascending Aortic Aneurysms: Reproducibility of Hemodynamic Parameters. *Applied Sciences* **12**, 3912 (2022).
47. Gabbour, M., Rigsby, C., Markl, M., Schnell, S., Jarvis, K., de Freitas, R., Popescu, A. & Robinson, J. Comparison of 4D flow and 2D PC MRI blood flow quantification in children and young adults with congenital heart disease. *Cardiovasc Magn Reson* **15**, 72 (2013).
48. Sieren, M., Berlin, C., Oechtering, T., Hunold, P., Drömann, D., Barkhausen, J. & Frydrychowicz, A. Comparison of 4D Flow MRI to 2D Flow MRI in the pulmonary arteries in healthy volunteers and patients with pulmonary hypertension. *PLoS ONE* **14** (2019).
49. Bock, J., Töger, J., Bidhult, S., Markenroth, B., Arvidsson, P., Kanski, M., Arheden, H., Testud, F., Greiser, A., Heiberg, E. & Carlsson, M. Validation and reproducibility of cardiovascular 4D-flow MRI from two vendors using 2×2 parallel imaging acceleration in pulsatile flow phantom and in vivo with and without respiratory gating. *Acta Radiol.* **60**, 327–337 (2019).
50. Zhang, Y., Tang, X., Ma, Y., Shi, H., Wang, X. & Pan, C. A test-retest multisite reproducibility study of cardiovascular four-dimensional flow MRI without respiratory gating. *Clin Radiol.* **76**, 236 (2021).
51. Westenberg, J., Roes, S., Ajmone, M., Binnendijk, N., Doornbos, J., Bax, J., Reiber, J., de Roos, A. & van der Geest, R. Mitral valve and tricuspid valve blood flow: accurate quantification with 3D velocity-encoded MR imaging with retrospective valve tracking. *Quant Imaging Med Surg* **249**, 792–800 (2008).
52. Ng, A. & Swanevelder, J. Resolution in ultrasound imaging. *Continuing Education in Anaesthesia Critical Care Pain* **11**, 186–192 (2011).
53. Keane, P., Ruiz-Garcia, H. & Sadda, S. *Advanced Imaging Technologies* (Retina, 2013).
54. Sharma, M., Hollerbach, S., Fusaroli, P., Löwe, A., Koch, J., Ignee, A., Jenssen, C. & Dietrich, C. General principles of image optimization in EUS. *Endoscopic ultrasound* **10**, 168–184 (2021).
55. Du, Y., Goddi, A., Bortolotto, C., Shen, Y., Dell’Era, A., Calliada, F. & Zhu, L. Wall Shear Stress Measurements Based on Ultrasound Vector Flow Imaging: Theoretical Studies and Clinical Examples. *Journal of Ultrasound in Medicine* **39** (2020).

56. Leinan, P., Grønli, T., Skjetne, P., Wigen, M., Urheim, S., Lovstakken, L. & Dahl, S. Comparison of ultrasound vector flow imaging and CFD simulations with PIV measurements of flow in a left ventricular outflow tract phantom - Implications for clinical use and in silico studies. *Comput Biol Med* **146** (2022).
57. Bollache, E., van Ooij, P., Powell, A., Carr, J., Markl, M. & Barker, A. Comparison of 4D flow and 2D velocity-encoded phase contrast MRI sequences for the evaluation of aortic hemodynamics. *Int J Cardiovasc Imaging* **32**, 61–72 (2016).
58. Markl, M., Frydrychowicz, A., Kozerke, S., Hope, M. & Wieben, O. 4D flow MRI. *J Magn Reson Imaging* **36**, 1015–1036 (2001).
59. Jackson, E. Quantitative Imaging: The Translation from Research Tool to Clinical Practice. *Radiology* **286**, 499–501 (2018).
60. NIST. *What are Imaging Phantoms* Accessed on 24-12-22. 2021. <https://www.nist.gov/physics/what-are-imaging-phantoms>.
61. Hoskins, P. *Flow Phantoms* 231–253. ISBN: 978-3-319-46405-3 (2017).
62. Shalbi, S., Oglat, A., Albarbar, B., Elkut, F., Qaeed, M. & Arra, A. A brief review for common doppler ultrasound flow phantoms. *Journal of Medical Ultrasound* **28**, 138–142 (2020).
63. Kenwright, D., Laverick, N., Anderson, T., Moran, C. & Hoskins, P. Wall-less Flow Phantom for High-Frequency Ultrasound Applications. *Ultrasound Med Biol.* **41**, 890–897 (2015).
64. Poepping, T., Nikolov, H., Thorne, M. & Holdsworth, D. A thin-walled carotid vessel phantom for Doppler ultrasound flow studies. *Ultrasound Med Biol.* **30**, 1067–1078 (2004).
65. Urbina, J., Sotelo, J., Springmuller, S., Montalba, C., Letelier, K., Tejos, C., Irarrazaval, P., Andia, M., Razavi, R., Valverde, I. & Uribe, A. Realistic aortic phantom to study hemodynamics using MRI and cardiac catheterization in normal and aortic coarctation conditions. *Journal of Magnetic Resonance Imaging* **44** (2016).
66. Brunette, J., Mongrain, R., Laurier, J., Galaz, R. & Tardif, J. 3D flow study in a mildly stenotic coronary artery phantom using a whole volume PIV method. *Medical Engineering and Physics* **30** (2008).
67. Cagney, N. & Balabani, S. Taylor-Couette flow of shear-thinning fluids. *Physics of Fluids* **31** (2019).
68. Moser, K., Raguin, L., Harris, A., Morris, H., Georgiadis, J., Shannon, M. & Philpott, M. Visualization of Taylor-Couette and spiral Poiseuille flows using a snapshot FLASH spatial tagging sequence. *Magnetic Resonance Imaging* **18** (2000).
69. Zhou, X., Kenwright, D., Wang, S., Hossack, J. & Hoskins, P. Fabrication of Two Flow Phantoms for Doppler Ultrasound Imaging. *IEEE Trans Ultrason Ferroelectr Freq Control.* **64**, 53–65 (2017).

70. Inc, S. N. *Doppler Ultrasound Phantoms* Accessed on 24-11-22. <https://www.sunnuclear.com/products/doppler-ultrasound-phantoms>.
71. Grice, J., Pickens, D. & Price, R. Technical Note: A new phantom design for routine testing of Doppler ultrasound. *Medical Physics* **43**, 4431 (2016).
72. Nordell, B., Ståhlberg, F., Ericsson, A. & Ranta, C. A rotating phantom for the study of flow effects in MR imaging. *Magn Reson Imaging* **6**, 695–705 (1988).
73. Vali, A., Schmitter, S., Ma, L., Flassbeck, S., Schmidt, S., Markl, M. & Schnell, S. Development of a rotation phantom for phase contrast MRI sequence validation and quality control. *Magn Reson Imaging* **84** (2020).
74. Meagher, S., Poepping, T., Ramnarine, K., Black, R. & Hoskins, P. Anatomical flow phantoms of the nonplanar carotid bifurcation, part II: experimental validation with Doppler ultrasound. *Ultrasound Med Biol.* **33**, 303–310 (2007).
75. Köhler, U., Marshall, I., Robertson, M., Long, Q., Xu, X. & Hoskins, P. MRI measurement of wall shear stress vectors in bifurcation models and comparison with CFD predictions. *J Magn Reson Imaging* **14**, 563–573 (2001).
76. Summers, P., Holdsworth, D., Nikolov, H., Rutt, B. & Drangova, M. Multisite trial of MR flow measurement: Phantom and protocol design. *Journal of Magnetic Resonance Imaging* **21** (2005).
77. Chee, A., Ho, C., Yiu, B. & Yu, A. Walled Carotid Bifurcation Phantoms for Imaging Investigations of Vessel Wall Motion and Blood Flow Dynamics. *IEEE transactions on ultrasonics, ferroelectrics, and frequency control* **63**, 1852–1864 (2016).
78. Smith, R., Rutt, B. & Holdsworth, D. Anthropomorphic carotid bifurcation phantom for MRI applications. *J Magn Reson Imaging* **10**, 533–544 (1999).
79. Lai, S., Yiu, B., Poon, A. & Yu, A. Design of anthropomorphic flow phantoms based on rapid prototyping of compliant vessel geometries. *Ultrasound Med Biol.* **39**, 1654–1664 (2013).
80. Chee, A., Ishii, T., Yiu, B. & Yu, A. Helical toroid phantom for 3D flow imaging investigations. *Phys Med Biol* **66** (2007).
81. Ebel, S., Hubner, L., Kohler, B., Kropf, S., Preim, B., Jung, B., Grothoff, M. & Gutberlet, M. Validation of two accelerated 4D flow MRI sequences at 3T: a phantom study. *European Radiology Experimental* **3** (2019).
82. Thomson, W. II. On vortex atoms. *The London, Edinburgh, and Dublin Philosophical Magazine and Journal of Science* **34**, 15–24 (1867).
83. Meleshko, V., Gourjii, A. & Krasnopolskaya, T. Vortex rings: History and state of the art. *Journal of Mathematical Sciences* **187** (2012).
84. Marten, K., Shariff, K., Psarakos, S. & White, D. Ring bubbles of dolphins. *Scientific American* **275** **2**, 82–7 (1996).
85. Johnson, W. *Model for Vortex Ring State Influence on Rotorcraft Flight Dynamics* in (2013).

86. Lim, T. & Nickels, T. *Vortex Rings* (Fluid Vortices, 1995).
87. Ahkmetov, D. *Vortex Rings* (Springer Berlin, Heidelberg, 2009).
88. Saffman, P. Dynamics of Vorticity. *Journal of Fluid Mechanics* **106**, 49–58 (1981).
89. Sun, Z. & Brücker, C. Investigation of the vortex ring transition using scanning Tomo-PIV. *Exp Fluids* **58**, 36 (2017).
90. Fernandez, J. & Sesterhenn, J. Axial and radial dynamics of compressible vortex rings. *European Journal of Mechanics* **76**, 303–315 (2019).
91. Katopodes, N. *Free-Surface Flow* 516–565 (Butterworth-Heinemann, 2019).
92. Dabiri, J. & Gharib, M. Fluid entrainment by isolated vortex rings. *Journal of Fluid Mechanics* **511**, 311–331 (2004).
93. Shariff, K. & Leonard, A. Vortex Rings. *Annual Review of Fluid Mechanics* **24**, 235–279 (1992).
94. Didden, N. On the formation of vortex rings: Rolling-up and production of circulation. *Journal of Applied Mathematics and Physics* **30**, 101–116 (1979).
95. Pullin, D. Vortex ring formation at tube and orifice openings. *Physics of Fluids* **22**, 401–403 (1979).
96. Saffman, P. The number of waves on unstable vortex rings. *Journal of Fluid Mechanics* **84**, 625–639 (1978).
97. Fang, T., Yang, L. & Qin, L. A theoretical model on vortex ring formation based on the roll-up of a vortex sheet with finite thickness. *Physics of Fluids* **32** (2020).
98. De Guyon, G. & Mulleners, K. Estimating the non-dimensional energy of vortex rings by modelling their roll-up. *Journal of Fluid Mechanics* **940**, R2 (2022).
99. Maxworthy, T. The structure and stability of vortex rings. *Journal of Fluid Mechanics* **51**, 15–32 (1972).
100. Reynolds, O. On the Resistance Encountered by Vortex Rings and the Relation between Vortex Rings and the Stream-Lines of a Disc. *Nature* **14**, 477–479 (1876).
101. Maxworthy, T. Some experimental studies of vortex rings. *Journal of Fluid Mechanics* **81**, 465–495 (1977).
102. Baird, M., Wairegi, T. & Loo, H. Velocity and momentum of vortex rings in relation to formation parameters. *Canadian Journal of Chemical Engineering* **55**, 19–26 (1977).
103. Archer, P., Thomas, T. & Coleman, G. Direct numerical simulation of vortex ring evolution from the laminar to the early turbulent regime. *Journal of Fluid Mechanics* **598**, 201–226 (2008).
104. Adhikiri, D. *Some experimental studies on vortex formation and interaction* Accessed 02-12-22. MA thesis (National University of Singapore, 2009).
105. Gharib, M., Rambod, E. & Shariff, K. A universal time scale for vortex ring formation. *Journal of Fluid Mechanics* **360**, 121–140 (1998).

106. Hussain, K. & Jothi, T. Vortex Ring Propagation and Interactions Studies. *Sādhanā* **43**, 99 (2018).
107. Linden, P. & Turner, J. The formation of ‘optimal’ vortex rings, and the efficiency of propulsion devices. *Journal of Fluid Mechanics* **427**, 61–72 (2001).
108. Bellhouse, B. Fluid mechanics of a model mitral valve and left ventricle. *Cardiovascular Research* **6**, 199–210 (1972).
109. Reul, H., Talukder, N. & Muller, E. Fluid mechanics of the natural mitral valve. *Journal of Biomechanics* **14**, 361–372 (1981).
110. Kim, W., Bisgaard, T., Nielsen, S., Poulsen, J., Pedersen, E., Hasenkam, J. & Yoganathan, A. Two-dimensional mitral flow velocity profiles in pig models using epicardial Doppler echocardiography. *Journal of the American College of Cardiology* **24**, 532–545 (1994).
111. Pedrizzetti, G., Canna, G. L., Alfieri, O. & Tonti, G. The vortex—an early predictor of cardiovascular outcome? *Nature reviews* **11**, 545–553 (2014).
112. Kheradvar, A. & Pedrizzetti, G. *Vortex Formation in the Cardiovascular System* (Springer, 2012).
113. Falahatpisheh, A., Pahlevan, N. & Kheradvar, A. Effect of the Mitral Valve’s Anterior Leaflet on Axisymmetry of Transmitral Vortex Ring. *Annals of biomedical engineering* **43**, 2349–2360 (2015).
114. Töger, J., Kanski, M., Carlsson, M., Kovács, S., Söderlind, G., Arheden, H. & Heiberg, E. Vortex ring formation in the left ventricle of the heart: analysis by 4D flow MRI and Lagrangian coherent structures. *Annals of biomedical engineering* **40**, 2652–2662 (2012).
115. Ardivissson, P., Kovacs, S., Toger, J., Borgquist, R., Heiberg, E., Carlsson, M. & Arheden, H. Vortex ring behavior provides the epigenetic blueprint for the human heart. *Scientific Reports* **6** (2016).
116. Pedrizzetti, G., Domenichini, F. & Tonti, G. On the left ventricular vortex reversal after mitral valve replacement. *Annals of biomedical engineering* **38**, 769–773 (2010).
117. Kheradvar, A., Assadi, R., Falahatpisheh, A. & Sengupta, P. Assessment of transmitral vortex formation in patients with diastolic dysfunction. *Journal of the American Society of Echocardiography* **25**, 220–227 (2012).
118. Ferrari, S., Ambrogio, S., Walker, A., Narracott, A. & Fenner, J. The Ring Vortex: A Candidate for a Liquid-Based Complex Flow Phantom for Medical Imaging. *VipIMAGE* **25** (2017).
119. Ambrogio, S., Walker, A., Narracott, A., Ferrari, S., Verma, P. & Fenner, J. A complex flow phantom for medical imaging: ring vortex phantom design and technical specification. *Journal of Medical Engineering & Technology* **43**, 190–201 (2019).

120. Components, R. *LM10 Linear Encoder Datasheet* Accessed on 10-12-22. 2022. <https://www.rls.si/eng/lm10-linear-and-rotary-magnetic-encoder-system>.
121. Durand, E., Jolivet, O., Itti, E., Tasu, J. & Bittoun, J. Precision of magnetic resonance velocity and acceleration measurements: theoretical issues and phantom experiments. *Journal of Magnetic Resonance Imaging* **13**, 445–451 (2001).
122. Tuncay, V., Zijlstra, J., Oudkerk, M. & van Ooijen, P. Design, Implementation, and Validation of a Pulsatile Heart Phantom Pump. *Journal of Digital Imaging* **33**, 1301–1305 (2020).
123. Matthews, A., Simatwo, K., Narracott, A., Amrogio, S., Walker, A. & Fenner, J. Quality Assuring a Ring Vortex Flow Phantom in Real-Time. *Open Journal of Medical Imaging* **13**, 11–29 (2023).
124. Helmholtz, H. Über Integrale der hydrodynamischen Gleichungen, " welche der Wirbelbewegung entsprechen. *J. für die reine und angewandte Mathematik* **55**, 25–55 (1858).
125. Batchelor, G. *An Introduction to Fluid Dynamics* (1970).
126. Lamb, H. Hydrodynamics. 6th Edition. *Cambridge University Press* (1932).
127. Danaila, I., Kaplanski, F. & Sazhin, S. *Vortex Ring Models* (Springer Nature, 2021).
128. Saffman, P. *Vortex Dynamics* ISBN: 9780511624063 (1993).
129. Hill, M. J. M. On a Spherical Vortex. *Physiological Transactions of the Royal Society A* **185** (1894).
130. Tryggesson, H. *Analytical Vortex Solutions to the Navier-Stokes Equation* Accessed 02-12-22 (Växjö University, 2007).
131. Fraenkel, L. On Steady Vortex Rings of Small Cross-Section in an Ideal Fluid. *Proceedings of the Royal Society of London. Series A, Mathematical and Physical Sciences* **316**, 29–62 (1970).
132. Norbury, J. A steady vortex ring close to Hill's spherical vortex. *Mathematical Proceedings of the Cambridge Philosophical Society* **72**, 253–284 (1972).
133. Norbury, J. A family of steady vortex rings. *Journal of Fluid Mechanics* **57**, 417–431 (1973).
134. Krieg, M. & Mohseni, K. On Approximating the Translational Velocity of Vortex Rings. *Journal of Fluids Engineering* **135** (Dec. 2013).
135. Daniele, I. & Helie, J. Numerical simulation of the postformation evolution of a laminar vortex ring. *Physics of Fluids* **20** (2008).
136. Yehoshua, T. & Seifert, A. Empirical Model for the Evolution of a Vortex-Pair Introduced into a Boundary Layer. *Aerospace Lab* **6**, 1–12 (2013).
137. Kaplanski, F. & Rudi, U. Dynamics of a viscous vortex ring. *International Journal of Fluid Mechanics Research* **26** (1999).

138. Kaplanski, F. & Rudi, Y. Evolution of a viscous vortex ring. *Fluid Dynamic* **36**, 16–25 (2001).
139. Berezovski, A. & Kaplanski, F. Vorticity distributions for thick and thin viscous vortex pairs and rings. *Archives of Mechanics* **47** (1995).
140. Stanaway, S., Cantwell, B. & Spalart, P. *A numerical study of viscous vortex rings using a spectral method* in (1988).
141. Weigand, A. & Gharib, M. On the evolution of laminar vortex rings. *Experiments in Fluids* **22**, 447–457 (1997).
142. Cater, J., Soria, J. & Lim, T. The interaction of the piston vortex with a piston-generated vortex ring. *Journal of Fluid Mechanics* **499**, 327–343 (Jan. 2004).
143. Yattori, H. & Hijiya, K. Short-wavelength stability analysis of Hill’s vortex with/without swirl. *Physics of Fluids* **22**, 074104–074104 (2010).
144. Shadden, S., Dabiri, J. & Marsden, J. Lagrangian analysis of fluid transport in empirical vortex ring flows. *Physics of Fluids* **18** (2006).
145. Thürey, N., Sadlo, F., Schirm, S., Müller, M. & Gross, M. *Real-time simulations of bubbles and foam within a shallow-water framework* in (2007), 191–198.
146. Sammet, S. Magnetic Resonance Safety. *Abdominal Radiology* **41**, 444–451 (2016).
147. Of Radiology, A. C. *ACR Manual on MR Safety* Accessed on 20-12-22. 2020. <https://www.acr.org/-/media/ACR/Files/Radiology-Safety/MR-Safety/Manual-on-MR-Safety.pdf>.
148. Sammet, C., Yang, X., Wassenaar, P., Bourekas, E., Yuh, B., Shellock, F., Sammet, S. & Knopp, M. RF-related heating assessment of extracranial neurosurgical implants at 7T. *Magnetic resonance imaging* **31**, 1029–1034 (2013).
149. Tavallaei, M., Johnson, P., Liu, J. & Drangova, M. Design and evaluation of an MRI-compatible linear motion stage. *Medical Physics* **43**, 62–71 (2016).
150. Jung, J., Seo, D., Lee, Y. & Kang, C. MRI-Compatible Microcirculation System Using Ultrasonic Pumps for Microvascular Imaging on 3T MRI. *Sensors* **22**, 6191 (2022).
151. Wendt, O., Oellinger, J., Luth, T., Felix, R. & Boenick, U. The effects of the use of piezoelectric motors in a 1.5-Tesla high-field magnetic resonance imaging system (MRI). *Biomed Tech* **45**, 20–25 (2000).
152. Wang, Y., Cole, G., Su, H., Pilitsis, J. & Fischer, G. MRI compatibility evaluation of a piezoelectric actuator system for a neural interventional robot. *Annual International Conference of the IEEE Engineering in Medicine and Biology Society*, 6072–6075 (2009).
153. Gadda, G., Cocozza, S., Gambaccini, M., Taibi, A., Tedeschi, E., Zamboni, P. & Palma, G. NO-HYPE: a novel hydrodynamic phantom for the evaluation of MRI flow measurements. *Medical Biological Engineering Computing* **59**, 1889–1899 (2021).

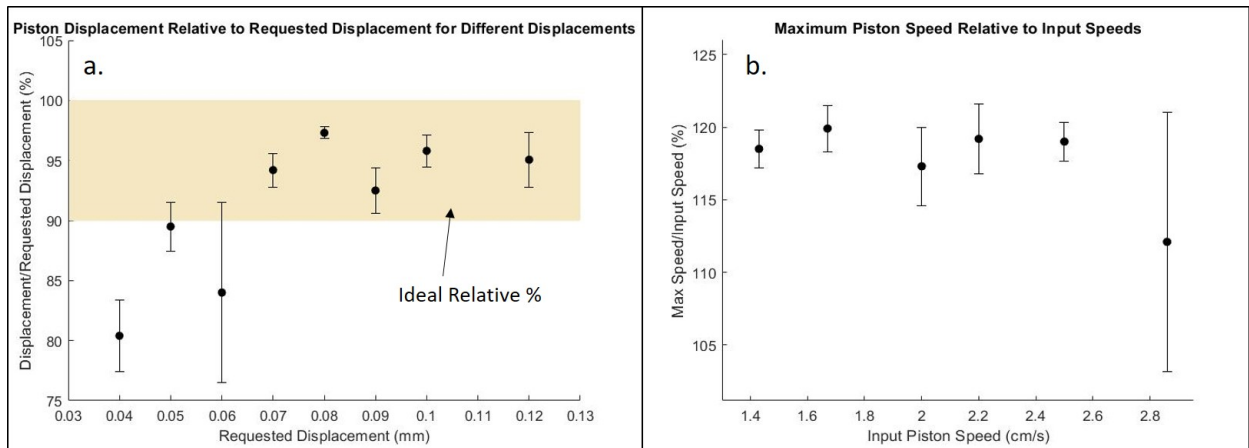
154. Swailes, N., MacDonald, M. & Frayne, R. Dynamic phantom with heart, lung, and blood motion for initial validation of MRI techniques. *Journal of Magnetic Resonance Imaging* **34**, 941–946 (2011).
155. Ambrogio, S. *Development of a Complex Flow Phantom for Diagnostic Imaging* PhD thesis (University of Sheffield, 2019).
156. IPEM. *Report 102 Quality Assurance of Ultrasound Imaging Systems* (IPEM Report Series Editor, 2010).

# Appendices

## A. Motor Limitations

Safety of the device is top priority for future use, which requires effective and appropriate use of the motor and knowledge of its boundaries and limits. Historically the phantom has moved the motor over 0.8mm at speeds of 2cm/s and 1.33cm/s. Further work on the phantom and its vortices demands a more diverse range of distances and speeds. Driving the motor too fast will result in skipped steps and potentially overheating, whilst requesting too short a displacement will cause skipping and unpredictable piston motion. Experiments will be undertaken to establish the conditions under which the piston moves reproducibly and predictably.

Two experiments took place to determine these limits. The phantom was filled with water and set up as previously described. Using a simple top-hat input code and piston speed of 2cm/s, the piston displacement was varied from 0.04mm-1.3mm in increments of 0.1mm. Fifteen impulses were recorded for each using the encoder. Analysis of the encoder profiles found the average displacement for each condition, and the ratio between the measured and programmed displacements. A second experiment was also performed to find the maximum suitable speed, where the displacement was fixed at 1mm and the piston speed varied between 1.4-2.7cm/s in increments of 0.4cm/s. These profiles were assessed for their maximum piston speed. The results for both experiments are presented below.



Graphs presenting the limits of the motor in the ring vortex phantom. Graph (a) presents the relative value of the measured piston displacement (in relation to requested displacement) for different displacements, and Graph (b) the relative maximum piston speed to the requested speed for different speeds.

Results from both experiments reveal behaviours which imply thresholds in effective motor use with the phantom. For piston displacement, the measured distance should be within 10% of the requested value, with minimal variation to ensure reproducibility. It is clear that for distances below 0.07mm, there is a steep drop-off

in expected-to-measured relative displacements, and variation increases rapidly. Therefore, no piston displacements under 0.07mm should be used. Use of these displacements would introduce variability and place strain on the motor. Audibly, at displacements at 0.07mm the user can hear the motor sticking, or sounding different on each impulse.

Secondly, the maximum piston speed was assessed for varying PS values. This is expected to be above the input speed, due to the oscillation. However, as the speed is increased, there is a steep change between PS=2.5cm/s and PS=2.86cm/s, from  $\sim 120\%PS$  to  $\sim 112\%PS$ , accompanied by a significant increase in variability (1.5% CoV to 9% CoV). This indicates that the motor is no longer moving reproducibly, either through skipping or getting stuck. Either way, the maximum reliable input speed is at 2.5cm/s. These are clear limits imposed by the device which will be followed for all future experiments.

## B. Streamfunction Background - Mathematics

The streamfunction is used extensively in Chapter 5 as the derivation basis for calculating velocity components. The mathematical background of this function is tangential to the phantom project but important to understand for the context of fluid dynamics.

Fundamentally, all matter must conserve mass to be physical, and fluid motion is no different. Fluid conservation of mass is represented by the continuity equation, which is a central construct of fluid dynamics. This is derived below.

$$M_v = \int_V \rho dV \quad (8.1)$$

Where  $M_v$  is the mass inside the volume, and  $\rho$  the fluid density Fluid is moving through the volume surface, which can be quantified as follows:

$$\frac{dM_v}{dt} = - \int_S \rho \mathbf{u} \cdot \mathbf{n} dS \quad (8.2)$$

Where  $S$  is the surface covering the volume,  $\mathbf{u}$  the velocity and  $\mathbf{n}$  the unit vector normal to the surface Volume is fixed thus non-varying with respect to time:

$$- \int_S \rho \mathbf{u} \cdot \mathbf{n} dS = \frac{d}{dt} \int_V \rho dV = \int_V \frac{\partial \rho}{\partial t} dV \quad (8.3)$$

It is at this stage useful to represent the expression only in terms of volume, so the divergence theorem is applied: Divergence Theorem:

$$- \int_S \rho \mathbf{u} \cdot \mathbf{n} dS = - \int_V \nabla \cdot (\rho \mathbf{u}) dV \quad (8.4)$$

In words, 'the surface integral of a vector field ( $\rho \mathbf{u}$  in this instance) over a closed surface is equal to the volume integral of the divergence of this field over the volume bounded by the surface Applying this to Equation 8.3 gives the following expression:

$$\int_V \frac{\partial \rho}{\partial t} dV = - \int_V \nabla \cdot (\rho \mathbf{u}) dV \quad (8.5)$$

Therefore

$$\int_V \left[ \frac{\partial \rho}{\partial t} + \nabla \cdot (\rho \mathbf{u}) \right] dV = 0 \quad (8.6)$$

This can be applied to all  $V$ , thus the continuity equation can be derived:

$$\frac{\partial \rho}{\partial t} + \nabla \cdot (\rho \mathbf{u}) = 0 \quad (8.7)$$

### 8.4.1 Incompressible Fluids

This thesis considers incompressible fluids, where the density is not variant with respect to time, thus the continuity equation reduces to:

$$\nabla \cdot (\rho \mathbf{u}) = 0 \quad (8.8)$$

This, by definition, imposes a restraint of  $\nabla \cdot \mathbf{u} = 0$  for incompressible fluids.

### 8.4.2 Streamfunction and Velocity Components

The velocity field,  $\mathbf{u}$  can be expressed as the curl of a scalar field:  $\mathbf{u} = \nabla \times \mathbf{S}$ . This scalar field is known as the 'streamfunction' ( $\psi$ ).

When working in two-dimensional fields (as throughout this thesis), the velocity components will be in  $x, y$  directions. The streamfunction is therefore only in the  $z$  direction:  $\psi = (0, 0, \psi)$ . Taking the curl of the scalar function derives the orthogonal velocity components, as shown below:

$$\nabla \times \mathbf{F} = \left( \frac{\partial \psi_x}{\partial y} - \frac{\partial \psi_y}{\partial z} \right) \mathbf{i} + \left( \frac{\partial \psi_x}{\partial z} - \frac{\partial \psi_x}{\partial x} \right) \mathbf{j} + \left( \frac{\partial \psi_y}{\partial x} - \frac{\partial \psi_x}{\partial y} \right) \mathbf{k} \quad (8.9)$$

$\psi_x$  and  $\psi_y$  are zero, so the expression cancels, and the velocity components are as follows:

$$u = u_i = \frac{\partial \psi}{\partial y} \quad (8.10)$$

$$v = u_j = -\frac{\partial \psi}{\partial x} \quad (8.11)$$

These expressions present the relationship between the streamfunction and velocity components in a Cartesian coordinate system ( $x, y$ ) for an incompressible, two-dimensional fluid.

### 8.4.3 Stokes Streamfunction

The Stokes streamfunction is employed for axisymmetric three-dimensional flows such as the ring vortex. The streamfunction is defined as follows:

$$\mathbf{S} = \frac{1}{r}\psi(r, z, t)e_{\theta} \quad (8.12)$$

This introduces a factor of  $1/r$  into the velocity component expressions, where  $r$  is the distance from the axis of rotation (radial coordinate).

# C. Conference Poster

## ULTRASOUND IMAGING AND THE RING VORTEX PHANTOM: AN INITIAL EXPERIENCE

A. S. Matthews<sup>1</sup>, J. Lister<sup>2</sup>, P. Verma<sup>2</sup>, A. Walker<sup>3</sup>, J. W. Fenner<sup>1</sup>

[1] – Medical Physics, Mathematical Modelling in Medicine, Division of Clinical Medicine, University of Sheffield, Sheffield

[2] – Medical Physics, Sheffield Teaching Hospitals NHS FT, Sheffield

[3] – Leeds Test Objects, Boroughbridge

### Introduction

The ring vortex complex flow phantom is a prototype device designed to challenge quantitative flow imaging technologies. The device employs the ring vortex as its reference flow, producing complex yet well-characterized flows over a range of generating conditions. Ring vortices are generated by propelling a slug of fluid through a circular orifice into an ambient fluid volume. An axisymmetric toroidal circulating core forms around the orifice before detaching and propagating across the tank at a steady translational velocity. These vortices have demonstrated high predictability, stability and reproducibility to within 10%. This study explored the performance of established clinical ultrasound techniques (B-mode and PW Doppler) in the context of the flow phantom.

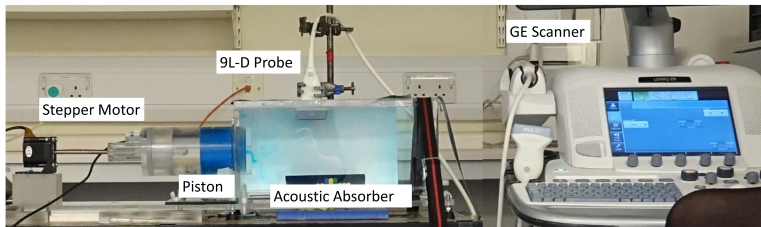


Figure 1: Annotated experimental setup of the ring vortex phantom and Ultrasound scanner

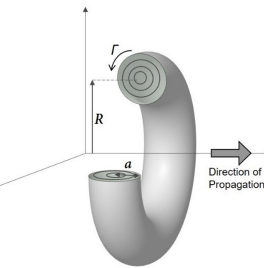


Figure 2: Schematic of the Ring Vortex

### Methods

A selection of ring vortices were generated over 5 generating conditions, with translational ring speed ranging from 5cm/s-40cm/s. The flow was seeded with neutrally buoyant 10µm diameter nylon particles to ensure sufficient visualization through scattering, and ten vortices of each condition were generated and analyzed.

The vortices were visualized using a GE LOGIQ E9 scanner with 9L-D probe. Firstly, B-Mode images were taken of the rings in a cine loop, imaging the rings as they travelled. The rings' translational speeds were calculated through measurement of the inter-frame displacement and compared to real-time camera recordings.

Secondly, PW Doppler was used to interrogate the intra-ring micro-flow velocities, using a 1mm gate positioned down the ring's cross-section in 1mm increments. Five measurements were taken for each position with maximum values averaged. These were then compared to Laser-PIV datasets.

### B-Mode Results – Bulk Measurements

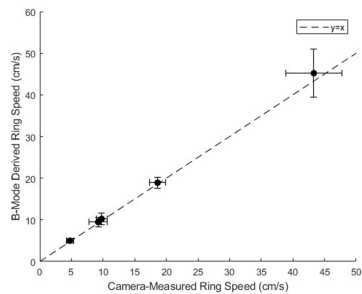


Figure 3: Graph presenting the agreement between ring speed when measured using B-Mode datasets and camera data respectively

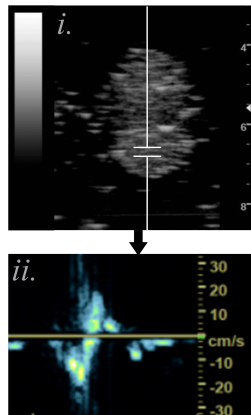


Figure 4: (i) Example B-Mode image with example annotated PW-D gate  
(ii) Example PW-D trace when measured over the vortex core

### PW Doppler Results – Micro Measurements

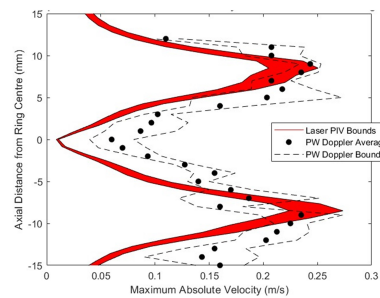


Figure 5: Graph presenting the maximum local velocities measured down the ring, using Laser PIV and PW-D respectively.

### Conclusions

The results indicate that B-Mode-derived velocity values at the macro-scale are accurate to within 10% when compared to the phantom benchmark datasets. More notably, PW Doppler consistently detects the expected velocity profiles from intra-ring micro-flow velocities, which are quantitatively comparable to the Laser PIV datasets also. This initial study shows promise for the ring vortex phantom in Doppler US QA, with further work required to compare inter-scanner and inter-probe variation.

### Acknowledgements

This project was supported by EPSRC and carried out in collaboration with Leeds Test Objects.

